12-2020

Discontinuous Recycled and Repurposed Carbon Fiber Reinforced Thermoplastic Organosheet Composites

Philip R. Barnett
University of Tennessee, Knoxville, pbarnet3@vols.utk.edu

To the Graduate Council:

I am submitting herewith a dissertation written by Philip R. Barnett entitled "Discontinuous Recycled and Repurposed Carbon Fiber Reinforced Thermoplastic Organosheet Composites." I have examined the final electronic copy of this dissertation for form and content and recommend that it be accepted in partial fulfillment of the requirements for the degree of Doctor of Philosophy, with a major in Energy Science and Engineering.

Dayakar Penumadu, Major Professor

We have read this dissertation and recommend its acceptance:

Uday Vaidya, David P. Harper, Brett G. Compton

Accepted for the Council:

Dixie L. Thompson

Vice Provost and Dean of the Graduate School

(Original signatures are on file with official student records.)

Discontinuous Recycled and Repurposed Carbon Fiber Reinforced Thermoplastic Organosheet Composites

A Dissertation Presented for the
Doctor of Philosophy
Degree
The University of Tennessee, Knoxville

Philip Raymond Barnett
December 2020

To Mom, Dad, Jacob, and Zachary, for encouraging me to always give my all, remain curious, and give back to others.

To Daniela, for your love, support, and patience.

To all of my friends and family, thank you.

ACKNOWLEDGEMENTS

This work was only possible through the contributions of numerous individuals. I will forever be grateful for the assistance of my family, friends, colleagues, advisors, mentors, mentees, and support staff. Thank you to my parents, Stephen and Nancy, for instilling in me the inherent value of education, curiosity, and the willingness to try new things without fear of mistakes. To my brothers, Jacob and Zachary, thank you for reminding me to have fun and for looking up to me to keep me grounded. Daniela, thank you for your never-ending love and encouragement as you have been by my side throughout this graduate school journey.

I thank my committee, led by Dr. Dayakar Penumadu, for their encouragement, support, and never-ending commitment to excellence. Dr. Penumadu, thank you for fostering a family atmosphere within our research group and seeing that we always keep the most important things in life at the forefront. Dr. Vaidya, thank you for opening your lab to me and treating me as if I were your own student. Dr. Harper, thank you for getting your hands dirty in the lab when I needed it and pushing me to have no fear when it comes to maintaining and fixing laboratory equipment. Dr. Compton, thank you for your mentorship throughout my research and preparations for post-graduate life.

I think all of my labmates and colleagues for their hard work that has led to my successful completion of this degree. To all of my outstanding undergraduates, Damon Vance, Brett Hulett, Zach Cook, Colby Gilbert, Alban Robin, Nalin Varma, and Bryce Stubbings, thank you for your hard work and dedication. I hope you learned as much from my mentorship as I did from becoming a mentor. To my colleagues in the research group, Stephen Young, Marton Kardos, Stephen Puplampu, Zach Arwood, Hannah Maeser, William Henken, Vivek Chawla, Mohsin Thakur, Aashish Sharma, Andrew Patchen, Matt Seals, Matt Kant, Neel Patel, Kamlesh Bornani, Javier Garcia, JC Chin, and the rest of the Penumadu group, thank you for your friendship, collaboration, and expertise that enabled me to complete this work.

Thank you to Andy Baker, Ken Thomas, and Larry Roberts in the Civil Engineering machine shop for their expertise and guidance in developing and crafting custom test fixtures. Thank you to Dr. Suresh Babu and Dr. Lee Riedinger for your guidance as Bredesen Center Directors who have fostered leadership and excellence in our amazing program. Thank you to my friends and colleagues in other labs, including Dr. Mi Li, Alex Stiles, Hicham Ghossein, and Nadim Hmeidat for your friendship. Thank you to the Bredesen Center, Civil Engineering, and other support staff who have ensured that the logistics of my research were never a hindrance. And finally, thank you to the Institute for Advanced Composites Manufacturing Innovation (IACMI) and Oak Ridge National Laboratory (ORNL) for providing the university with world-class facilities and ample opportunities for industry collaboration.

ABSTRACT

There is a significant need for low cost, high volume composites in the automotive industry to aid in vehicle lightweighting and safety. The current state-of-the-art severely compromises the mechanical properties of composites to achieve cost and cycle time goals. In this dissertation, a novel composite format, termed discontinuous carbon fiber organosheets, using recycled and repurposed carbon fibers in a thermoplastic matrix is developed and studied. Unlike traditional composites, the long fiber length and rapid processing time yield mechanical properties and cycle times competitive with automotive metals.

Several studies were performed to characterize this new material format. First, samples were manufactured from carded recycled carbon fiber and wet deposited virgin carbon fiber preforms infiltrated with a polyphenylene sulfide (PPS) matrix. The orientation-dependent tensile and shear properties of these composites were characterized. It was found that classical laminate theory in combination with statistical methods could accurately describe their mechanical behavior. Next, the effects of varying processing time and atmosphere, as well as post-process annealing, were studied using dynamic mechanical analysis, differential scanning calorimetry, tensile testing, and nano-indentation. Due to the stochastic nature of discontinuous fiber composites, statistical methods were applied to evaluate changes. Then, a model based on the stochastic microstructure of the composites was developed to predict their strength and modulus. Composites with an acrylonitrile butadiene styrene and a common structural epoxy matrix were also produced and tested to validate the applicability of the model to a range of composites. An ensuing study of the infiltration behavior of the preforms was used to optimize the processing conditions for rapid production. Here, fluid permeability and preform compression were studied to evaluate an existing model of composite infiltration, which was validated by in-situ compression molding experiments.

Finally, the composites were used to produce complex geometry samples for a study on their crashworthiness. Sinusoidal specimens were produced from PPS, ABS, and epoxy composites and tested at a range of temperatures and loading rates relevant to automotive applications. The results showed that discontinuous fiber organosheet composites not only achieve competitive mechanical properties but also exceed the crashworthiness of traditional composite materials.

TABLE OF CONTENTS

LIST OF TABLES

LIST OF FIGURES

CHAPTER I. INTRODUCTION

Composites in the Automotive Industry

Fiber-reinforced polymer composite materials consist of a fiber reinforcement embedded in either a thermosetting or thermoplastic polymeric matrix. Traditionally, composites have been utilized heavily in the aerospace industry. In such applications, composites serve as primary structures including the airframe and stringers, as well as thin-shell structures such as the skin. Typical production routes in the aerospace industry include vacuum-assisted resin transfer molding (VARTM), automated tape placement, and autoclave processing. In each case, laminated composites are used to minimize material weight through optimal laminate orientation. In such composites, a lamina refers to a single layer of composite material, while a laminate refers to a stack of lamina that is used to build a structure. Typically, mechanical properties increase with decreasing lamina thickness, while manufacturing time increases with the number of laminae. Additionally, lamina orientation has a strong effect on the mechanical properties, where small misalignment from the longitudinal fiber axis can yield dramatically reduced strength and modulus. Typical laminae are in the form of unidirectional fibers or woven fabrics. Laminates made of thin unidirectional lamina offer better performance than woven fabrics, due in part to an increased number of laminae and lessened fiber misorientation due to fiber crimp induced by the weave. However, these lamination processes often yield slow production rates, high scrap rate, and high cost that is not conducive to automotive applications. In response, many existing carbon fiber-reinforced automotive components utilize high areal weight woven fabrics to increase production rates. Despite these improvements, high cost and slow production rates still limit automotive composites to low-volume, high-performance applications.

Fiber-reinforced composites have long been the state-of-the-art in high-performance automotive applications. For example, the Chevrolet Corvette has utilized composite materials since its inception in 1953 in which the body panels were constructed of fiberglass sheet molding compound (SMC). SMC materials consist of chopped fiberglass in a polyester or vinyl ester matrix containing significant mineral filler content. SMC parts are produced via compression molding, in which a charge of SMC is placed in a heated mold and held under pressure as it cures in typically less than two minutes[1]. The SMC charge typically flows in the mold, thereby making charge placement simple and cost-effective. However, the performance and weight savings of SMC materials are severely limited when compared to continuous fiber composites. For extreme performance applications, Formula 1 vehicles and other supercars have long used composites manufactured using more traditional lamination methods in applications such as the driveshaft, body panels, and crashworthy body frames[2]. The low production volume and high cost of these high-performance vehicles make such manufacturing methods

economically feasible, but the same methods cannot be applied to consumer performance vehicles.

Consumer performance vehicles stand to benefit from lightweighting made possible by composite materials. For example, a 10% reduction in vehicle weight has been shown to provide a 6-8% improvement in fuel economy for a traditional internal combustion engine vehicle and up to a 13.7% range increase in range for battery electric vehicles[3]. Only recently have fiber-reinforced polymer composites been used extensively in medium volume, consumer performance applications. An example is the BMW i3 electric vehicle, which utilizes extensive continuous fiber composites in the frame, floor assembly, and front doors, as well as manufacturing waste in the roof and rear seat structures[4]. However, the bulk of fiber-reinforced automotive composites has been evident in the form of thermoplastic composites produced through processes such as compression molding of long fiber thermoplastics (LFT) and injection molding[5]. The composites produced by these processes incorporate discontinuous fibers and offer low to medium performance capabilities. As such, there is a clear need for low-cost, high-performance automotive composites.

A consortium of automotive manufacturers has set forth a goal for 2025 in which vehicle mass is reduced 25% relative to a comparable 2012 vehicle at less than $5.00 per pound of mass saved[6]. To achieve this goal, significant incorporation of composite materials will be necessary. They have designated the following target properties for automotive composites: cycle time less than 3 minutes, greater than 700 MPa tensile strength, and greater than 100 GPa tensile modulus. For a quasi-isotropic layup, this translates to 41 GPa modulus and 215 MPa strength using a first-ply failure criterion. While the target material properties can already be achieved using existing technologies, the cost must be reduced significantly. There are many ways to reduce the cost of composites, including reductions in fiber precursor cost, lowering fiber oxidation and stabilization energy requirements, reducing composites manufacturing equipment cost, shortening cycle time, and relaxing material storage requirements. The recovery of post-production waste and end-of-life recycled material is also a feasible route toward reducing the cost of automotive composites that is explored in this dissertation.

Composite Waste Utilization

It is estimated that the scrap rate for carbon fiber in typical manufacturing is in the range of 10-30%[7]. As such, thousands of tons of scrap fiber waste are landfilled each year. To mitigate this waste stream, some companies repurpose dry scrap material by producing nonwovens. For example, the BMW i3 uses high-pressure resin transfer molding to consolidate nonwoven mats with an epoxy resin to produce seat and roof structures[4]. Scrap material containing epoxy resins (e.g., scrap prepreg) typically must undergo recycling processes before it can be repurposed. A variety of recycling processes are used to recover fibers, with the

most common being mechanical grinding, pyrolysis, chemical solvolysis, and fluidized bed processing[8]. In general, mechanical grinding significantly degrades the fiber length, thereby rendering it as only a low-value filler material. Meanwhile, pyrolysis, chemical solvolysis, and fluidized bed processing retain fiber length to a maximum of a few inches with mechanical properties close to those of the virgin fiber. As such, these long recycled fibers can be used in high-value structural applications. Furthermore, fiber recycling is economically-viable, where the cost of recycling is approximately 15% of the cost of producing virgin carbon fibers[9]. As such, the use of repurposed and recycled carbon fibers offers a solution to reducing the cost of automotive composites.

State-of-the-Art in Discontinuous Fiber Composites

Discontinuous fiber composites are produced using a variety of manufacturing methods that yield a range of mechanical properties that are strongly dependent on the fiber length, fiber volume fraction, and fiber orientation. Each of these variables is strongly influenced by the chosen processing route. Here, we will discuss two primary fiber architectures: aligned and random.

Aligned carbon fiber composites can be produced using a variety of methods including, compounding/extrusion, dynamic alignment, commingling, carding, and prepreg slitting[5,10–12]. In compounding/extrusion processes, the discontinuous fibers are compounded with molten polymer and then extruded to form a final geometry. In this case, extrusion may be done into a mold cavity (injection molding) or onto a print bed to build parts using additive manufacturing. During the extrusion process, fibers are aligned in the flow direction. The fiber length is typically severely degraded by shear forces that break the fibers during the compounding and extrusion processes, thereby reducing the final mechanical properties. Conversely, dynamic alignment processes retain fiber length through reduced shear during alignment. Fibers are typically dynamically aligned using either pneumatic or hydrodynamic forces as the fibers are deposited through a converging geometry onto a moving surface[13]. The aligned preforms can then be infused with resin using methods such as compression molding, resin transfer molding, or wet layup. Through retained fiber length, the mechanical properties of dynamically aligned fibers are typically much higher than compounding/extrusion processes. Commingling processes involve the mechanical entanglement of carbon and polymeric fibers to form a yarn[14]. The yarn can then be processed using compression molding to melt the polymeric fibers into the entangled reinforcement. Another processing method that produces aligned composites is carding, in which a series of combs separates and opens fiber bundles, which are drawn along a roller[11]. The preform can then be impregnated with a matrix resin using methods similar to the dynamically aligned fibers. Prepreg slitting involves cutting continuous fiber prepregs to introduce regularly repeating discontinuities. These discontinuities improve the formability of the material over the initial prepreg. In general, dynamically aligned fibers and prepreg slitting provide the highest axial mechanical properties for aligned discontinuous fiber composites.

Random discontinuous fiber composites typically consist of SMCs, glass mat thermoplastics (GMT), platelet composites, long fiber thermoplastics (LFT), and wet deposition[5]. SMCs are typically produced as fiber tows are chopped and allowed to randomly fall onto a thermoset resin film. A series of rollers then partially consolidate the material, which is later placed in a heated press for molding. Based on the flow of the charge in the mold, random or aligned orientation can be achieved. Platelet composites are produced by cutting unidirectional prepreg into platelets followed by compression molding. As with SMCs, flow can be induced by mold geometry and charge placement. GMTs are produced from needled chopped fibers that are impregnated with a thermoplastic film or powder in a compression molding process. The blanks can then be formed to the desired final part shape. Long fiber thermoplastics are typically produced by compounding long-fiber pellets in a low shear extruder to produce a molten charge that is subsequently compression molded. Much like SMCs, the flow of the charge in the mold can lead to aligned orientation. Wet deposition processes are based on the principle of papermaking, in which fibers are mixed in a slurry of water, drained, and dried to form nonwoven mats. Alignment can be induced by adjusting the drain location to induce hydrodynamic forces, though random orientation is typically desired.

Table I-1 provides example tensile strength and modulus values for composites produced using the methods described. In general, the mechanical properties of random discontinuous fiber composites are considerably lower than aligned discontinuous fiber composites. However, in the direction transverse to alignment, the mechanical properties of aligned discontinuous fiber composites tend to be much lower. As a result, random discontinuous fiber composites are more appropriate for structures that undergo multidirectional loading and require rapid processing that is not conducive to careful laminate layup.

Modeling Discontinuous Fiber Composite Properties

Many models have been developed to predict the modulus and strength of discontinuous fiber composites with in-plane fiber orientation. Generally, modulus estimates have been acceptable, while strength estimates are often inaccurate. There are two main model types used to predict the mechanical properties of short fiber composites: micromechanical and empirical models. A few of the existing models are considered here. The material properties used in the models are found in Table I 2. Typical values of T300 carbon fiber were used for the reinforcing fiber and typical values of PPS were used for the matrix[22].

The shear lag micromechanical model developed by Cox considers a single fiber encased in a shell of matrix[23]. The fibers are assumed to be perfectly bonded with perfectly elastic behavior for both the fiber and matrix. The longitudinal modulus of the micromechanical representative volume element is:

$$E_{11} = E_f \left[1 - \frac{\tanh(\frac{\beta L_f}{2})}{\frac{\beta L_f}{2}} \right] V_f + E_m(1 - V_f) \quad (1)$$

Table I-1. Typical properties of discontinuous fiber composites

Format	Fiber Type	Matrix Material	Modulus (GPa)	Strength (MPa)	Fiber Volume Fraction (%)	Reference
Injection molding	Virgin Carbon	Polyphenylene Sulfide	30.5	174	32.8	[15]
Additive manufacturing	Virgin Carbon	ABS	13.5	67	27	[16]
Dynamic alignment	Virgin Carbon	Epoxy	115	1509	55	[13]
Commingling	Recycled Carbon	Polypropylene	31.5	160	27.7	[14]
Carded	Recycled Carbon	Polypropylene	17.5	150	20	[11]
Prepreg slitting	Virgin Carbon	Epoxy	119	950	58	[12]
SMC	Virgin Carbon	Epoxy	28.8	143	51.4	[17]
GMT	Glass	Polypropylene	5.5	37	20	[18]
Platelet composite	Virgin Carbon	Epoxy	42.8	240	64	[19]
LFT	Glass	Polypropylene	7.9	100	19	[20]
Wet deposition	Recycled carbon	Polypropylene	11.0	75	20	[11]
Wet deposition	Virgin Carbon	PA6/PA66	19.5	170	25	[21]

Table I-2. Material properties used in prediction of 2D random composite properties

Parameter	Value
Fiber Longitudinal Modulus (GPa), E_{f1}	230
Fiber Transverse Modulus (GPa), E_{f2}	15
Fiber Shear Modulus (GPa), G_{f12}	27
Fiber Strength (MPa), σ_f	3700
Fiber Poisson's Ratio, v_{12f}	0.20
Matrix Modulus (GPa), E_m	3.4
Matrix Strength (MPa), σ_m	80
Matrix Poisson's Ratio, v_m	0.38
Fiber Length (mm), L_f	25.4
Fiber Diameter (μm), d_f	7
Interfacial Shear Strength (MPa), τ_s	30

where V_f is the fiber volume fraction and β is given by:

$$\beta = \left[\frac{2\pi G_m}{E_f\left(\pi r_f^2\right)\ln\left(\frac{R}{r_f}\right)}\right]^{\frac{1}{2}} \tag{2}$$

Here, R refers to the radius of the matrix sheath, which is a function of the fiber packing. Cox defined the ratio of radii as:

$$\frac{R}{r_f} = \sqrt{\frac{2\pi}{\sqrt{3}\,V_f}} \tag{3}$$

Then, for a planar randomly oriented material, Cox defined the modulus as:

$$E_c = \frac{1}{3}E_{11} \tag{4}$$

The Halpin-Tsai equations are an empirical set of equations developed to predict the longitudinal, transverse, and shear moduli of short fiber composites[24]. The equations are formulated as:

$$\frac{p_c}{p_f} = \frac{1+\zeta\eta V_f}{1-\eta V_f} \tag{5}$$

where:

$$\eta = \frac{\frac{p_f}{p_m}-1}{\frac{p_f}{p_m}+\zeta} \tag{6}$$

The variable p corresponds to the modulus property, while the subscripts f, m, and c correspond to the fiber, matrix, and composite properties respectively. The variable ζ is a measure of reinforcement geometry which is equal to 1 for shear modulus, 2 for the transverse modulus, and twice the fiber aspect ratio for the longitudinal modulus. Once the properties in the principal directions are estimated, the properties of a random laminate can be calculated[25] as follows:

$$E_c = \frac{4U_5(U_1-U_5)}{U_1} \tag{7}$$

where:

$$U_1 = \frac{3Q_{11} + 3Q_{22} + 2Q_{12} + 4Q_{66}}{8} \tag{8}$$

$$U_5 = \frac{Q_{11} + Q_{22} - 2Q_{12} + 4Q_{66}}{8} \tag{9}$$

with:

$$Q_{11} = \frac{E_{11}}{1 - \upsilon_{12}\upsilon_{21}} \tag{10}$$

$$Q_{22} = \frac{E_{22}}{1 - \nu_{12}\upsilon_{21}} \tag{11}$$

$$Q_{12} = Q_{11}\upsilon_{21} \tag{12}$$

$$Q_{66} = G_{12c} \tag{13}$$

Here, ν_{12} is estimated using the rule of mixtures, and ν_{21} is determined using symmetry of the compliance matrix in transversely orthotropic materials.
Other empirical models for the modulus of planar random discontinuous fiber composites are found in Table I-3. Each of these models was implemented across a range of fiber volume fractions from 1-65% to provide a baseline estimate for the properties that should be expected from randomly-oriented discontinuous fiber composites. The results are shown in Figure I-1. The Cox approximation serves as a lower bound, while the Manera serves as an upper bound. When compared with Table I-1, it is clear that some manufacturing processes yield good agreement with the model, though none at higher fiber volume fractions achieve the predicted moduli.

The strength of discontinuous fiber composites is much more difficult to predict than the modulus. As in the case of modulus predictions, there exist both empirical and micromechanics-based models. One of the most commonly used micromechanical models is the Tyson-Kelly model[29]:

$$\sigma_{cL} = V_f\sigma_f\left(1 - \frac{L_c}{2L_f}\right) + \left(1 - V_f\right)\sigma_m, \qquad for\ L_f > L_c \tag{14}$$

$$\sigma_{cL} = V_f\sigma_f\frac{1}{2L_c} + \left(1 - V_f\right)\sigma_m, \qquad for\ L_f \leq L_c \tag{15}$$

where σ_{cL} is the composite longitudinal strength and L_c is the critical fiber length, defined as:

Table I-3. Empirical models for the prediction of the elastic modulus of discontinuous fiber composites

Model Name	Modulus Estimate	Reference
Christensen-Waals	$E_c = \frac{V_f}{3}E_f + (1 + V_f)E_m, V_f < 0.2$	[26]
Manera	$E_c = V_f\left(\frac{16}{45}E_f + 2E_m\right) + \frac{8}{9}E_m,$ $0.1 < V_f < 0.4$	[27]
Pan	$E_c = E_f\frac{V_f}{\pi} + E_m(1 - \frac{V_f}{\pi})$	[28]

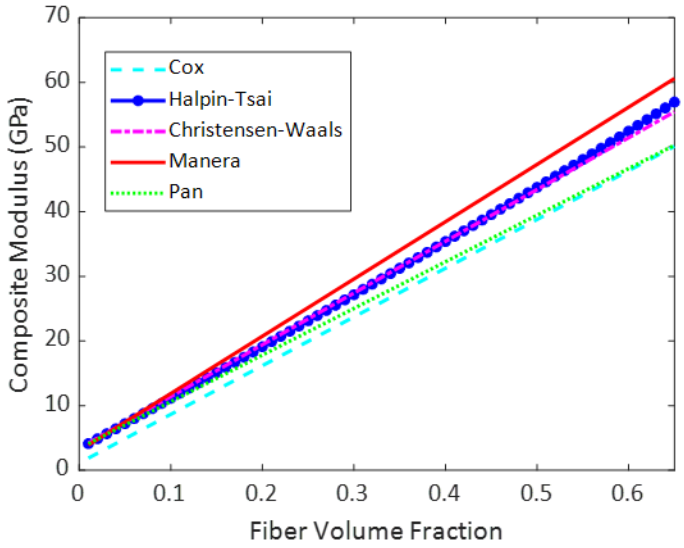

Figure I-1. Predicted composite modulus from models found in literature

$$L_c = \frac{\sigma_f d_f}{2\tau_s} \tag{16}$$

This model only accounts for unidirectionally-aligned fibers. To account for random alignment, an empirical fiber orientation factor is often applied. Equation (14) or (15) is multiplied by this term, which is typically equal to 0.2[30].

The model proposed by Chen accounts for different failure types resulting from changes in fiber orientation[31]. The author proposes that there are three failure types apparent in unidirectional continuous fiber composites: fiber failure, matrix failure in shear, and matrix failure in plane-strain, which are also apparent in discontinuous fiber composites. Using this concept, they arrive at the following expression:

$$\sigma_c = \frac{2\tau_m}{\pi}\left(2 + \ln\left(\frac{\xi \sigma_{cROM}\sigma_m}{\tau_m^2}\right)\right) \tag{17}$$

where:

$$\tau_m = \frac{\sigma_m}{\sqrt{3}} \tag{18}$$

$$\sigma_{cROM} = \sigma_f V_f + \left(1 - V_f\right)\sigma_m \tag{19}$$

The matrix shear strength, τ_m, is determined according to the von Mises yield criterion and the continuous fiber modulus, σ_{cROM}, is calculated according to the rule-of-mixtures. The strength efficiency factor, ξ, is dependent upon the reinforcing geometry, but typically takes values near 0.5.

The strength model proposed by Baxter can be applied to nonrandom fiber orientations, as well as random orientations[32]. In this model based on the Tsai-Hill failure criteria, the strength of an aligned discontinuous fiber composite at a given angle, θ, is given as:

$$\sigma(\theta) = \left[\frac{\cos^4\theta}{\sigma_{cL}} + \left(\frac{1}{\tau_m^2} - \frac{1}{\sigma_{cL}^2}\right)\sin^2\theta\cos^2\theta + \frac{\sin^4\theta}{\sigma_T^2}\right]^{-\frac{1}{2}} \tag{20}$$

Here, the Tyson-Kelly model is used to determine the longitudinal tensile strength of the composite, the shear strength of the matrix is assumed to represent the shear strength of the composite, and the transverse tensile strength is assumed to be either the strength of the matrix or follow:

$$\sigma_T = \sigma_m \left[1 - 2\left(\frac{V_f}{\pi}\right)^{\frac{1}{2}}\right] \tag{21}$$

The strength of a random composite can then be determined according to:

$$\sigma_c = \frac{1}{\pi}\int_0^{\pi} \sigma(\theta) d\theta \tag{22}$$

A more recently developed method of predicting the strength of discontinuous fiber composites has been proposed by Shokrieh[33]. This method relies on the concept of continuum damage mechanics to predict the strength of discontinuous fiber composites. First, the Halpin-Tsai equations are used to model the elastic stiffness of a unidirectional lamina of the composite. Then, classical lamination theory is used to determine the stiffness of a composite laminate containing plies at random angles. Next, a small increment of stress is applied to the composite laminate and the stress in each lamina is calculated. The Tsai-Wu failure criteria assuming that the tensile and compressive properties are equivalent is used to determine if the layer was damaged:

$$F = \left[\left(\frac{\sigma_x}{\sigma_L}\right)^2 + \left(\frac{\sigma_y}{\sigma_T}\right)^2 - \frac{\sigma_x \sigma_y}{\sigma_L \sigma_T} + \left(\frac{\tau_{xy}}{\tau_m}\right)^2\right]^{-\frac{1}{2}} \tag{23}$$

where the x and y subscripts refer to the local lamina stresses. When F is greater than 1, failure has occurred. The transverse tensile strength is calculated according to equation (21) and the shear strength is calculated according to equation (18). The longitudinal tensile strength is based on the tensile strength predicted via the shear-lag theory as:

$$\sigma_L = \frac{E_x}{E_f}\sigma_f \frac{1}{1 - \operatorname{sech}\left(\frac{L}{2}\sqrt{\frac{E_m}{E_f(r_f(R - r_f)(1 - \nu_m)}}\right)} \tag{24}$$

where L refers to the fiber length in the undamaged state or the critical length in the damaged state.

If the layer was damaged, it was determined if the damage type was fiber breakage or matrix cracking and debonding. Based on the type of damage, the stiffness of the layer was randomly degraded and the damage variable was updated. A small increment of stress was then applied to the damaged laminate,

where the effective stress was used to evaluate new damage. This process was repeated until all layers failed. Further details can be found in the cited paper. As a stochastic method, this prediction captures the variability typically shown in discontinuous fiber composites.

Each of these models was implemented across the same range of fiber volume fractions as was done for the modulus predictions. The results are shown in Figure I-2. There is significantly more variability in strength predictions than the modulus. For example, the Tyson-Kelly model predicts much higher strength at high fiber volume fractions. The Baxter and Chen models are nearly equivalent when the transverse strength is taken as the matrix strength. For the Baxter model based on equation (21) and the Shokrieh model that uses the same equation to estimate transverse tensile strength, the random fiber composite strength decreases above a limiting fiber volume fraction. This behavior occurs as the failure becomes dominated by transverse tension as the fiber volume fraction increases (i.e., the second term in equation (23) becomes dominant). When compared to the experimental data in Table I-1, it is clear that these models are in the right range for the material strength, but the wide range of measured properties makes it difficult to identify a model that best captures the behavior of all samples. As a result, there is a clear need for a highly adaptable model that can accurately predict the properties of a variety of discontinuous fiber composite formats.

Recycled and Repurposed Carbon Fiber Organosheets to Meet Automotive Needs

The automotive industry has clearly defined their needs for composite materials: a minimum performance of 41 GPa quasi-isotropic modulus and 215 MPa quasi-isotropic strength must be achieved at a cost of less than $5 per pound of mass offset. Existing continuous fiber composites can already meet the modulus and strength requirements, but are far too expensive. The use of recycled and repurposed fibers provides an opportunity to reduce material costs. From the literature included in Table I-1, it appears that platelet composites may be a viable option, though they are made of expensive chopped prepreg. If a similar end product with random microstructure can be achieved using recycled or repurposed fibers in alternate formats, it is expected that the target properties can be achieved at a much lower cost. Two promising fiber preform manufacturing techniques for recycled and repurposed fibers are carding and wet deposition. Though these techniques have thus far yielded subpar mechanical properties, optimized manufacturing processes may improve their viability.

This dissertation explores the manufacturing of discontinuous fiber composites in an organosheet format. An organosheet is simply a composite lamina made of a carbon fiber reinforced thermoplastic that can be stacked and molded to form thicker structures. Organosheets are often compression molded to form complex shapes. One of the primary benefits of organosheets is that they do not require careful material storage requirements since the matrix does not undergo a curing process. As such, the shelf-life of organosheets is not a limitation

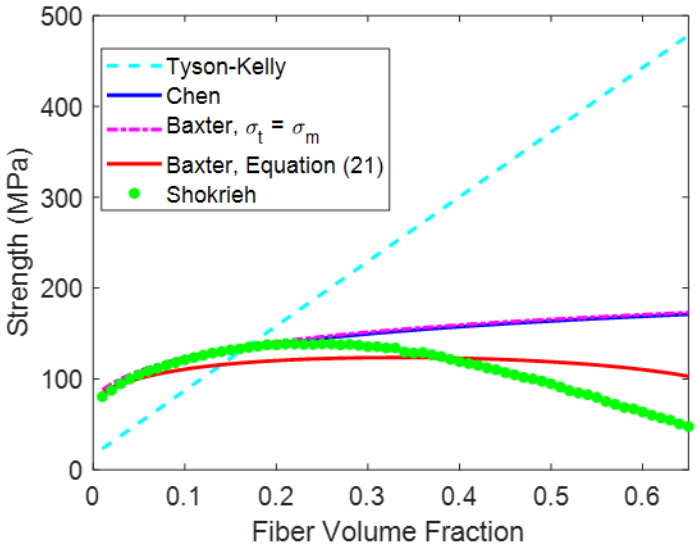

Figure I-2. Predicted composite strength from models found in the literature

for high volume manufacturing. Typically, organosheets use continuous fiber fabrics as the reinforcement. In this work, recycled fiber preforms made through a carding process and repurposed virgin fiber preforms made through a wet deposition process were studied. Organosheets were produced using a film stacking process, in which a preform was sandwiched by polymer films and then placed in a heated press for impregnation. The resulting organosheets were then stacked and molded to form test specimens.

The thermoplastic matrix studied in this work was polyphenylene sulfide (PPS). PPS is a semicrystalline thermoplastic with very good thermal and chemical resistance, low melt viscosity, and high strength and stiffness. PPS is nearly insoluble in organic solvents below 200 °C and is inherently flame resistant[34]. Carbon fiber/PPS laminates are rated for low-stress applications up to 240 °C and do not experience significant degradation in tensile properties at 120 °C[35]. These properties make it an especially attractive thermoplastic for automotive applications, where chemical and thermal resistance are important for under-the-hood parts that may be in contact with automotive fluids and extreme heat from internal combustion engines. The low melt viscosity of PPS makes it a good candidate for film infusion processes, which have been successfully demonstrated using traditional compression molding and a double belt press for continuous fiber composites[36]. However, any infusion process must occur quickly or in an inert atmosphere to limit degradation. It has been shown that the viscosity of PPS increases considerably when held at the melt temperature, due to a combination of oxidation, chain extension/chain branching, and eventual cross-linking[37]. In this dissertation, organosheet composites were produced using various dwell times and atmospheric conditions to determine optimal processing conditions. Additionally, x-ray radiographs of the compression molding process were taken in-situ to identify the minimum time for infiltration. Experiments were conducted to measure the permeability of the fiber preforms, the viscosity of the PPS melt, and the compressibility of the fiber preforms. These results were used as inputs to existing models of resin infiltration to determine their applicability to thermoplastic composite infiltration.

Once the composite laminate is produced, post-processing steps such as annealing can be used to further optimize the mechanical properties. Neat PPS is known to crystallize when cooled below the critical quench rate of approximately 20 °C min^{-1}[38]. As such, the structure of the solidified polymer is amorphous, yielding lower mechanical properties than crystallized PPS. Fibers have been shown to increase the crystallization rate of PPS[39], providing nucleation sites for crystal growth. This is of importance because the crystalline phase of PPS has a higher modulus and strength than the amorphous. Furthermore, it has been shown that annealing significantly improves the interfacial shear strength of carbon fiber/PPS composites in both microbond[40] and fiber push-out tests[41]. While the mechanism of this interface improvement is not well understood, the result is a significant improvement in mechanical properties. For example, the storage modulus of glass fiber/PPS composites was an order of magnitude higher when

annealed as opposed to quenched[42]. As part of this dissertation, carbon fiber/PPS organosheet composite specimens were annealed to optimize their mechanical properties. Tensile testing was used to quantify the effects of annealing on the composites.

In general, discontinuous fiber composites exhibit greater variation in mechanical properties than continuous fiber composites. This is due largely to the inhomogeneous microstructure, where there exist weak regions of low fiber volume fraction, poor fiber alignment, or high void content. As such, statistical methods must be used to identify differences induced by processing conditions and annealing. The bootstrap principle was applied to the tensile data to elucidate these effects. Similarly, this variation may serve to explain the lack of a good strength prediction model for discontinuous fiber composites. Recent progress has been made in which stochastic models have been developed to account for the variability in platelet composites[43]. However, no such stochastic model exists for discontinuous fiber composites containing long, curved fibers such as those found in preforms produced via carding and wet deposition methods. In this dissertation, a stochastic model based on the observed microstructure and constituent component properties of discontinuous fiber composites is presented. The model utilizes micromechanical estimates of composite properties, thereby limiting the number of experiments necessary for model inputs. In fact, most of the inputs can be found in material datasheets. The results show very good agreement with experiments for a variety of nonwoven formats and matrix materials, serving as a powerful tool for the prediction of the tensile and shear properties of discontinuous fiber composites.

One topic that has not been discussed thus far is the need for crashworthy automotive composite structures. Composites are utilized extensively in Formula 1 racing to protect drivers in crash scenarios with minimal weight[44]. Similarly, the BMW i3 uses a continuous carbon fiber composite monocoque frame to protect passengers. One of the biggest challenges preventing composites from wider adoption for crashworthy structures is the lack of understanding of the mechanisms governing energy absorption. In general, we know that tougher matrices provide greater energy absorption capabilities[45], fiber orientation strongly affects energy absorption[46], the energy absorption is affected by strain rate and temperature[47], and chopped-fiber systems perform comparably to continuous fiber composites[48]. As such, discontinuous fiber organosheet composites made with tough thermoplastic matrices may offer a good solution to automotive crashworthiness. As a part of this dissertation work, sinusoid crush specimens were manufactured and tested at a variety of rates and temperatures. Three matrices were considered: PPS, acrylonitrile butadiene styrene (ABS), and epoxy. These tests, along with the mechanical properties measured in other experiments, provide a baseline for future modeling of the crashworthiness of discontinuous fiber composite systems and clearly illustrate the crashworthiness of organosheet composites made with repurposed and recycled fibers.

In the remainder of this dissertation, the reader will learn how discontinuous recycled and repurposed carbon fiber organosheets are produced, optimized, and modeled. The effects of processing parameters such as time and processing atmosphere were considered, as well as post-process annealing. Statistical methods were used to evaluate the mechanical properties of such composites using micro-mechanical models and classical lamination theory to develop a robust model for the prediction of composite mechanical properties. Experiments measuring the infiltration of the preforms were conducted to optimize processing time. To elucidate the applicability of such materials to the automotive industry, a crashworthiness study was undertaken in which the energy absorption capability of the material was characterized over a range of matrix materials, strain rates, and temperatures. After reading this dissertation, one should have an adequate background to apply these findings to problems relevant to the automotive industry.

References

[1] E. Ghassemieh, Materials in Automotive Application , State of the Art and Prospects, InTech, 2011. https://doi.org/10.5772/1821.

[2] A.B. Strong, Fundamentals of Composites Manufacturing: Materials, Methods, and Applications, First, Society of Manufacturing Engineers, Dearborn, 1989.

[3] W.J. Joost, Reducing vehicle weight and improving U.S. energy efficiency using integrated computational materials engineering, Journal of The Minerals, Metals, and Materials Society. 64 (2012) 1032–1038. https://doi.org/10.1007/s11837-012-0424-z.

[4] M. Pervaiz, S. Panthapulakkal, B. KC, M. Sain, J. Tjong, Emerging Trends in Automotive Lightweighting through Novel Composite Materials, Materials Sciences and Applications. 07 (2016) 26–38. https://doi.org/10.4236/msa.2016.71004.

[5] U.K. Vaidya, K.K. Chawla, Processing of fibre reinforced thermoplastic composites, International Materials Reviews. 53 (2008) 185–218. https://doi.org/10.1179/174328008x325223.

[6] U.S. Driving Research and Innovation for Vehicle efficiency and Energy sustainability, Materials Technical Team Roadmap, 2017.

[7] J.P. Snudden, C. Ward, K. Potter, Reusing automotive composites production waste, Reinforced Plastics. 58 (2014) 20–27. https://doi.org/10.1016/S0034-3617(14)70246-2.

[8] S. Pimenta, S.T. Pinho, Recycling carbon fibre reinforced polymers for structural applications: Technology review and market outlook, Waste Management. 31 (2011) 378–392. https://doi.org/10.1016/j.wasman.2010.09.019.

[9] F. Meng, J. McKechnie, S.J. Pickering, An assessment of financial viability of recycled carbon fibre in automotive applications, Composites Part A: Applied Science and Manufacturing. 109 (2018) 207–220. https://doi.org/10.1016/j.compositesa.2018.03.011.

[10] M. Such, C. Ward, K. Potter, Aligned Discontinuous Fibre Composites: A Short History, Journal of Multifunctional Composites. 2 (2014) 155–168. https://doi.org/10.12783/issn.2168-4286/2/3/4/Such.

[11] J. Wölling, M. Schmieg, F. Manis, K. Drechsler, Nonwovens from Recycled Carbon Fibres - Comparison of Processing Technologies, Procedia CIRP. 66 (2017) 271–276. https://doi.org/10.1016/j.procir.2017.03.281.

[12] I. Taketa, T. Okabe, A. Kitano, A new compression-molding approach using unidirectionally arrayed chopped strands, Composites Part A: Applied Science and Manufacturing. 39 (2008) 1884–1890. https://doi.org/10.1016/j.compositesa.2008.09.012.

[13] H. Yu, K.D. Potter, M.R. Wisnom, A novel manufacturing method for aligned discontinuous fibre composites (High Performance-Discontinuous Fibre method), Composites Part A: Applied Science and Manufacturing. 65 (2014) 175–185. https://doi.org/10.1016/j.compositesa.2014.06.005.

[14] M.H. Akonda, C.A. Lawrence, B.M. Weager, Recycled carbon fibre-reinforced polypropylene thermoplastic composites, Composites Part A: Applied Science and Manufacturing. 43 (2012) 79–86. https://doi.org/10.1016/j.compositesa.2011.09.014.
[15] K. Stoeffler, S. Andjelic, N. Legros, J. Roberge, S.B. Schougaard, Polyphenylene sulfide (PPS) composites reinforced with recycled carbon fiber, Composites Science and Technology. 84 (2013) 65–71. https://doi.org/10.1016/j.compscitech.2013.05.005.
[16] H.L. Tekinalp, V. Kunc, G.M. Velez-Garcia, C.E. Duty, L.J. Love, A.K. Naskar, C.A. Blue, S. Ozcan, Highly oriented carbon fiber-polymer composites via additive manufacturing, Composites Science and Technology. 105 (2014) 144–150. https://doi.org/10.1016/j.compscitech.2014.10.009.
[17] Z. Chen, H. Tang, Y. Shao, Q. Sun, G. Zhou, Y. Li, H. Xu, D. Zeng, X. Su, Failure of chopped carbon fiber Sheet Molding Compound (SMC) composites under uniaxial tensile loading: Computational prediction and experimental analysis, Composites Part A: Applied Science and Manufacturing. 118 (2019) 117–130. https://doi.org/10.1016/j.compositesa.2018.12.021.
[18] N.-J.J. Lee, J. Jang, The effect of fibre content on the mechanical properties of glass fibre mat/polypropylene composites, Composites Part A: Applied Science and Manufacturing. 30 (1999) 815–822. https://doi.org/10.1016/S1359-835X(98)00185-7.
[19] P. Feraboli, E. Peitso, T. Cleveland, P.B. Stickler, F. Deleo, T. Cleveland, P.B. Stickler, Characterization of prepreg-based discontiuous carbon fibre/epoxy systems, Journal of Reinforced Plastics and Composites. 28 (2009) 1191–1214. https://doi.org/10.1177/0731684408088883.
[20] K. Balaji Thattaiparthasarathy, S. Pillay, H. Ning, U.K. Vaidya, Process simulation, design and manufacturing of a long fiber thermoplastic composite for mass transit application, Composites Part A: Applied Science and Manufacturing. 39 (2008) 1512–1521. https://doi.org/10.1016/j.compositesa.2008.05.017.
[21] K.H. Wong, T.A. Turner, S.J. Pickering, Challenges in Developing Nylon Composites Commingled With Discontinuous Recycled Carbon Fibre, ECCM16 - European Conference on Composite Materials. (2014) 22–26. https://doi.org/10.1007/s002030050525.
[22] I.M. Daniel, O. Ishai, Engineering Mechanics of Composite Materials, 2nd ed., Oxford University Press, New York, 2006.
[23] H.L. Cox, The elasticity and strength of paper and other fibrous materials, British Journal of Applied Physics. 3 (1952) 72–79. https://doi.org/10.1088/0508-3443/3/3/302.
[24] J.C. Halpin, J.L. Kardos, The Halpin-Tsai equations: A review, Polymer Engineering and Science. 16 (1976) 344–352. https://doi.org/10.1002/pen.760160512.
[25] J.C. Halpin, N.J. Pagano, The laminate approximation for randomly oriented fibrous composites, Journal of Composite Materials. 3 (1969) 720–724.

[26] R.M. Christensen, F.M. Waals, Effective stiffness of randomly oriented fibre composites, Journal of Composite Materials. 6 (1972) 518–535. https://doi.org/10.1177/002199837200600307.
[27] M. Manera, Elastic Properties of Randomly Oriented Short Fiber-Glass Composites, Journal of Composite Materials. 11 (1977) 235–247. https://doi.org/10.1177/002199837701100208.
[28] N. Pan, The Elastic Constants of Randomly Oriented Fiber Composites: A New Approach to Prediction, Science and Engineering of Composite Materials. 5 (1996) 63–72. https://doi.org/10.1515/SECM.1996.5.2.63.
[29] A. Kelly, W.R. Tyson, Tensile properties of fibre-reinforced metals: Copper/tungsten and copper/molybdenum, Journal of the Mechanics and Physics of Solids. 13 (1965) 329–350. https://doi.org/10.1016/0022-5096(65)90035-9.
[30] J.L. Thomason, M.A. Vlug, G. Schipper, H.G.L.T. Krikor, Influence of fibre length and concentration on the properties of glass fibre-reinforced polypropylene: Part 3. Strength and strain at failure, Composites Part A: Applied Science and Manufacturing. 27 (1996) 1075–1084. https://doi.org/https://doi.org/10.1016/1359-835X(96)00066-8.
[31] P.E. Chen, Strength properties of discontinuous fiber composites, Polymer Engineering & Science. 11 (1971) 51–56. https://doi.org/10.1002/pen.760110109.
[32] W.J. Baxter, Strength of metal matrix composites reinforced with randomly oriented discontinuous fibers, Metallurgical Transactions. A, Physical Metallurgy and Materials Science. 23 A (1992) 3045–3053. https://doi.org/10.1007/BF02646122.
[33] M.M. Shokrieh, H. Moshrefzadeh-Sani, A novel laminate analogy to calculate the strength of two-dimensional randomly oriented short-fiber composites, Composites Science and Technology. 147 (2017) 22–29. https://doi.org/10.1016/j.compscitech.2017.04.034.
[34] A.S. Rahate, K.R. Nemade, S.A. Waghuley, Polyphenylene sulfide (PPS): State of the art and applications, Reviews in Chemical Engineering. 29 (2013) 471–489. https://doi.org/10.1515/revce-2012-0021.
[35] B. Vieille, J. Aucher, L. Taleb, Influence of temperature on the behavior of carbon fiber fabrics reinforced PPS laminates, Materials Science and Engineering A. 517 (2009) 51–60. https://doi.org/10.1016/j.msea.2009.03.038.
[36] D. Liu, Y. Zhu, J. Ding, X. Lin, X. Fan, Experimental investigation of carbon fiber reinforced poly(phenylene sulfide) composites prepared using a double-belt press, Composites Part B: Engineering. 77 (2015) 363–370. https://doi.org/10.1016/j.compositesb.2015.03.062.
[37] D.R. Fagerburg, J.J. Watkins, P.B. Lawrence, Melt viscosity increase during rheological testing of poly(phenylene sulfide), Journal of Applied Polymer Science. 50 (1993) 1903–1907. https://doi.org/10.1002/app.1993.070501106.
[38] W.J.B. Grouve, G. Vanden Poel, L.L. Warnet, R. Akkerman, On crystallisation and fracture toughness of poly(phenylene sulphide) under tape

placement conditions, Plastics, Rubber and Composites. 42 (2013) 282–288. https://doi.org/10.1179/1743289812Y.0000000039.
[39] R. Zhang, Y. Huang, M. Min, Y. Gao, X. Yu, A. Lu, Z. Lu, Isothermal crystallization of pure and glass fiber reinforced poly(phenylene sulfide) composites, Polymer Composites. 30 (2009) 460–466. https://doi.org/10.1002/pc.
[40] B. Liu, X. Wang, S. Long, J. Yang, Interfacial micromechanics of carbon fiber-reinforced polyphenylene sulfide composites, Composite Interfaces. 21 (2014) 359–369. https://doi.org/10.1080/15685543.2014.878875.
[41] M. Greisel, J. Jäger, J. Moosburger-Will, M.G.R.R. Sause, W.M. Mueller, S. Horn, Influence of residual thermal stress in carbon fiber-reinforced thermoplastic composites on interfacial fracture toughness evaluated by cyclic single-fiber push-out tests, Composites Part A: Applied Science and Manufacturing. 66 (2014) 117–127. https://doi.org/10.1016/j.compositesa.2014.07.010.
[42] A. Arici, T. Sinmazcelik, L. Capan, I. Yilgor, E. Yilgor, Influence of Annealing on the Performance of Short Glass Fiber-reinforced Polyphenylene Sulfide (PPS) Composites, Journal of Composite Materials. 39 (2005) 21–33. https://doi.org/10.1177/0021998305046432.
[43] S.G. Kravchenko, D.E. Sommer, B.R. Denos, A.J. Favaloro, C.M. Tow, W.B. Avery, R.B. Pipes, Tensile properties of a stochastic prepreg platelet molded composite, Composites Part A: Applied Science and Manufacturing. 124 (2019) 105507. https://doi.org/10.1016/j.compositesa.2019.105507.
[44] H. Dirk, J.A. Lukaszewicz, Automotive composite structures for crashworthiness, in: Advanced Composite Materials for Automotive Applications: Structural Integrity and Crashworthiness, 2013: pp. 99–127. https://doi.org/10.1002/9781118535288.
[45] P. Feraboli, Development of a Corrugated Test Specimen for Composite Materials Energy Absorption, Journal of Composite Materials. 42 (2008) 229–256. https://doi.org/10.1177/0021998307086202.
[46] D. Hull, A unified approach to progressive crushing of fibre-reinforced composite tubes, Composites Science and Technology. 40 (1991) 377–421. https://doi.org/10.1016/0266-3538(91)90031-J.
[47] S. Ramakrishna, H. Hamada, Energy absorption characteristics of crash worthy structural composite materials, Key Engineering Materials. (1998) 585–620. https://doi.org/10.4028/www.scientific.net/kem.141-143.585.
[48] G.C. Jacob, J.F. Fellers, J.M. Starbuck, S. Simunovic, Crashworthiness of Automotive Composite Material Systems, Journal of Applied Polymer Science. 92 (2004) 3218–3225. https://doi.org/10.1002/app.20336.

CHAPTER II.
REPURPOSED/RECYCLED DISCONTINUOUS CARBON FIBER ORGANOSHEET DEVELOPMENT AND COMPOSITE PROPERTIES

A version of this chapter was originally prepared for publication in the journal Composites Part C: Open Access by Philip R. Barnett, Colby L. Gilbert, and Dayakar Penumadu:

P.R. Barnett, C. L. Gilbert, D. Penumadu, Repurposed discontinuous carbon fiber organosheet composites: Properties and laminate analogy, Composites Part C: Open Access, Submitted: October 16, 2020.

Abstract

The high cost of carbon fiber composites often limits their use in automotive applications. This paper describes the study of an emerging class of materials, chopped fiber reinforced thermoplastic (polyphenylene sulfide) organosheets that provide mechanical properties exceeding sheet molding compounds at low material and manufacturing cost with long shelf life at room temperature. The tensile and shear properties were found to be directionally-dependent, while the impact of void content on these properties was small. We showed that tensile testing of the dry preforms can serve as a method of screening the degree of anisotropy, reducing the need for extensive processing trials. Due to the anisotropy and microstructure variance of these materials, designs must encompass the laminate stacking sequence and the variability in mechanical properties. We showed that Monte Carlo simulations of composite lamination theory utilizing stochastic mechanical properties conservatively predict the mechanical properties of organosheet laminates. This paper offers one of the first in-depth evaluations of this novel new class of composite materials using repurposed/recycled carbon fiber.

Introduction

Carbon fiber-reinforced composites are popular within the aerospace industry due to their high specific strength and stiffness, corrosion resistance, and fatigue resistance. These properties are also desirable in the automotive industry, though carbon fiber composites have struggled to gain a large share of the automotive materials market due to high material costs, slow production rate, and concerns about recyclability. The integration of lightweight fiber-reinforced composites into vehicles offers significant weight savings that can lead to improved fuel efficiency. For example, a 10% reduction in vehicle weight is associated with a 6% reduction in fuel consumption for passenger vehicles[1]. The automotive industry has established a minimum benchmark for carbon fiber composites: 100 GPa unidirectional modulus and 700 MPa strength[2], which translates to 41 GPa modulus and 215 MPa strength in a quasi-isotropic layup. While these properties are easily attained using aerospace-grade composites, automotive manufacturers require lower material costs and more rapid production rates.

Thermoset matrices present a problem for vehicle recycling, which is becoming of greater importance to automotive manufacturers. Established legislation in the European Union requires that vehicles disposed of after 2015 be

85% recyclable, with the burden of disposal placed upon the component manufacturer[3]. As a result, thermoplastic composites appear to be the most viable option for future automotive composites. Thermoplastic matrix composites offer much promise due to enhanced impact properties, rapid cycle times, improved assembly and joining methods, and unlimited shelf life of raw materials, among other benefits[4]. When reinforced with repurposed or recycled carbon fibers, thermoplastics offer a cost-effective alternative to metal automotive structural components. For example, BMW reused post-process carbon fibers in the roof and rear seat structures of the i3 electric vehicle[5]. These fibers were recovered from waste generated in the production of woven fabrics and made into a nonwoven mat.

In addition to post-process dry fiber reuse, cured composite recycling has become a more feasible enterprise in recent years due to improved methods yielding better fiber length retention. Methods such as matrix pyrolysis, chemical solvolysis, and fluidized-bed processing have shown good mechanical property retention, approaching 98% virgin strength[6]. It is estimated that as much as 30% of the total material used in the manufacturing of carbon fiber parts is wasted, primarily in the form of scrap prepreg[7]. Therefore, there is considerable value to be recovered from carbon fiber manufacturing waste. Recycled fibers are currently used in relatively low-performance applications such as injection molding and 3-D printing due to the reduced fiber length resulting from the recycling and compounding processes. However, less aggressive processes such as carding or wet deposition used to create nonwoven preforms retain fiber length, thereby offering improved mechanical properties that could move recycled fiber composites into higher performance applications. Some work using these manufacturing methods has focused on intermingling recycled carbon fibers with polymer fibers to produce preforms that are then stacked in a mold and compression molded[8,9]. While high mechanical properties can be achieved, the cost of thermoplastic fibers makes this manufacturing route unattractive.

The present paper details the manufacturing and evaluation of a randomly oriented, discontinuous fiber thermoplastic matrix organosheet produced via compression molding. Organosheets refer to thin fiber preforms that are pre-impregnated with a thermoplastic resin and then stacked and molded to form laminated composites. In this study, polyphenylene sulfide (PPS) film was used as the matrix, offering high-temperature stability, inherent flame resistance, and good chemical resistance[10]. The use of a polymer film is more attractive than a fiber due to the reduced cost of conversion from pelletized polymer. The deformation behavior of the constituent dry fiber preforms made either from repurposed or recycled carbon fiber was studied to characterize the anisotropy before infusion. Organosheet laminae were produced and subsequently compression molded to form composite parts. The tensile properties of the composite were studied at both the organosheet lamina and composite laminate scale. V-notch shear specimens were also tested to determine the shear strength and modulus of the composite laminates. Digital image correlation (DIC) was used to measure spatially resolved

strain for observation of material inhomogeneity effects. These tests allow for the generation of a 2D stiffness matrix to model the composite stiffness and strength using a Monte Carlo simulation based on composite laminate theory. The density and void content of the composites were measured using optical microscopy and water displacement. The results of this study provide a multi-scale analysis of the mechanical properties from raw fiber preforms to laminated composites that highlights important considerations for designs with discontinuous fiber organosheets.

Materials and Methods

Polyphenylene Sulfide Matrix

Commercially-available polyphenylene sulfide (PPS) films of 0.127 mm nominal thickness and 1.34 g cm^{-3} density were obtained (Ryton QA200P, Solvay). The mechanical and chemical stability of PPS makes it a good candidate for automotive applications. Furthermore, PPS can be thermally bonded to additively build complex structures with reduced numbers of parts. These properties make PPS a good candidate for under-the-hood automotive applications, as well as corrosion-resistant exterior components.

Nonwoven Carbon Fibers

Repurposed virgin wet-laid and recycled carded nonwovens were studied. The virgin carbon fiber nonwovens obtained from Neenah Performance Materials were produced using a modified papermaking process to yield a nominal 300 g m^{-2} areal density (measured 310.0 ± 6.6 g m^{-2}). The nonwoven is produced by mixing fibers into a water-binder slurry, draining the water through a filter to prevent fiber loss, and drying the resulting mat to activate the binding agent[11]. The mixing and draining techniques can be used to control the fiber orientation, with most targeting in-plane random orientation for quasi-isotropic properties. Fiber burn off tests conducted in a furnace at 500 °C for 30 minutes showed that 1.1 ± 0.2% binder was used in the wet-laid nonwovens. Fiber length was measured to be 28.8 ± 13.5 mm. This process also tends to retain the fiber tow geometry, leading to regions of varying fiber density. Single fiber testing revealed that these fibers are likely standard modulus, with a strength of 3302 ± 238 MPa and modulus of 197 ± 10 GPa. Recycled carbon fiber nonwovens were obtained from ELG Carbon Fibre in the form of a nominal 200 g m^{-2} mat (measured 184.2 ± 11.2 g m^{-2}) produced using a carding process where a series of combs mechanically entangles and orients fibers. The recycled fiber nonwovens did not have any binder or sizing apparent in fiber burn off tests, likely due to the pyrolysis process used to recover the fibers. Unlike the wet-laid process, the carding process pulled the tows apart, yielding a more homogeneous microstructure. The carding process also led to a wider distribution of fiber lengths, measured to be 38.8 ± 22.2 mm. Single fiber testing revealed that these fibers are likely intermediate modulus, with a strength of 4426 ± 386 MPa and modulus of 206 ± 14 GPa.

Nonwoven preforms of these formats offer several benefits, including good formability, low material costs, and the ability to upcycle waste virgin fiber or recycled fibers to high strength applications. Typical discontinuous fiber composite manufacturing methods include injection molding, extrusion-compression, and compression molding of SMCs and chopped strand mats. The first two processing methods tend to significantly degrade fiber length and therefore reduce mechanical properties such as strength and stiffness. In the case of SMCs and chopped strand mats, the fiber length is typically controlled by the chopping speed of continuous fiber tows, which are much more costly than recycled or repurposed fibers. Additionally, the use of thermosetting resins in SMC materials requires material storage considerations that are not required for thermoplastic composites.

Compression Molding

Organosheets were produced via compression molding in a heated press (Carver model 3895) at 300 °C under 1 MPa pressure for 5 minutes, followed by cooling to 60 °C under pressure. These processing conditions were arrived at via differential scanning calorimetry and parallel plate rheological experiments that enabled the determination of the melting temperature and maximum allowable processing time before material degradation. A film infusion process, in which one layer of carbon fiber nonwoven was placed between two layers of PPS film in an aluminum mold, was used to form a 250 mm X 250 mm organosheet. The organosheets were cut into 100 mm X 100 mm sheets, stacked into a 1.6 mm thick aluminum mold, and molded using the same processing schedule to form a final laminate. The virgin composite had a nominal estimated void-free density of 1.563 g cm^{-3} and nominal fiber volume fraction of 41.7%, while the recycled composite had a nominal void-free density of 1.494 g cm^{-3} and nominal fiber volume fraction of 30.1% based upon the constituent materials. Virgin fiber composites were also made at 300 °C with 1 MPa pressure for 30 minutes under vacuum to evaluate the impact of processing time. Vacuum was used to limit the thermal degradation of the PPS matrix via oxidation. Rheological experiments showed no significant viscosity increase after 30 minutes in an inert argon atmosphere. Images of the constituent materials, organosheet, and resulting plate are shown in Figure II-1.

Nonwoven Tensile Testing

To characterize the orientation-dependent mechanical properties of the nonwoven preforms, tensile tests were performed on the un-infused fiber mats. Samples of 25.4 mm X 250 mm with a 200 mm gauge length were tested on an Instron 5667 load frame with a 500 N load cell at a rate of 100 mm min^{-1}. Tabs made of masking tape were applied to the top and bottom 25 mm of the sample to prevent failure at the grips. Previous work has shown that the isotropy of fibrous nonwovens can be studied using such tests[12]. It is expected that the maximum load achieved in both the machine and cross directions correlates to the level of anisotropy in the nonwoven preform.

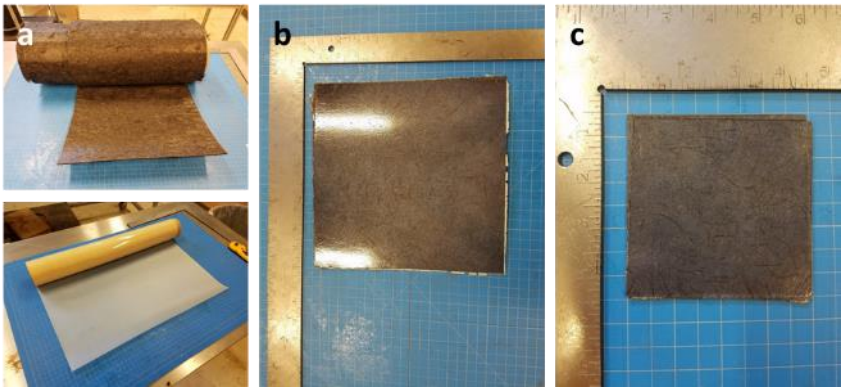

Figure II-1. a) Wet-laid carbon fiber mat and PPS film; b) Organosheet image; c) Consolidated panel image

Composite Tensile Testing

Tensile testing was completed at room temperature per the ASTM D3039 standard on an MTS 858 hydraulic load frame with a 25 kN load cell where true strain measurements were taken over a gauge length of 25.4 mm using an extensometer. The strain for a limited number of samples was measured on both sides using DIC (Correlated Solutions, VIC-3D), where the entire sample surface served as the region of interest. Sample dimensions were nominally 100 mm X 12.7, with the thickness depending upon the fiber type, but near 2.0 mm. 12.7 mm X 12.7 mm G-10 fiberglass tabs were adhered to the samples using a two-part epoxy (West System 105/206, cured for at least 24 hours) in the grip region to promote failure in the gauge length, and the gripping pressure was set to 5.5 MPa. Organosheet tensile sample dimensions were similar, with a thickness of approximately 0.5 mm, and 25.4 mm X 12.7 mm G-10 fiberglass tabs were utilized in the grip region, with a gripping pressure of 1.4 MPa. Samples prepared with all lamina oriented in the machine (MD) and cross directions (CD) of the nonwoven roll were tested. Unless noted, all other laminate samples were prepared using lamina where the laminate sequence was random.

Shear Testing

The shear modulus and shear strength of the composite laminates were determined according to ASTM D5379 using an MTS 858 load frame with a 25 kN load cell. Composite samples manufactured with all organosheets oriented in the machine and cross directions of the nonwoven roll were tested to provide bounds on the shear properties. Spatially resolved strains were measured on one side using DIC. To validate the DIC data, strain gauge rosettes were mounted to the back surface of one sample of each set tested. Nominal sample thickness was 2.0 mm, with all other dimensions according to the standard. G-10 glass fiber tabs were adhered to the specimens using Loctite 501 to prevent local crushing of the thin samples. The full-field strain was calculated for a subsection within the notched region. The resulting shear strain measured by DIC was then correlated with the shear stress measured by the load frame to determine the shear modulus and strength.

Digital Image Correlation to Evaluate Material Variation

DIC was used to measure spatially resolved strains. After milling, composite specimens were prepared for DIC with a flat white spray paint base layer and flat black spray paint as a speckle to track local surface strain. Images were taken at a rate of 10 Hz to match the test acquisition rate. The average strain was taken in a subsection of the sample to evaluate the stress-strain behavior. Additionally, the Poisson’s ratio across the surface of the tensile specimens was calculated. A total of four organosheet laminae and four laminate samples were tested in tension using DIC. Each set of four tests consisted of samples cut in the cross and machine directions of unidirectional recycled and virgin fiber composites processed for 5 minutes. The average strain across eight subregions of each sample was

determined using a MATLAB script and compared to the global average strain, thereby providing a metric for determining inhomogeneity (see SII-1. Discussion of Inhomogeneity Metric).

Void Content Analysis

Void content can strongly influence the mechanical properties of fiber-reinforced composites. Void content was analyzed using two methods: optical microscopy and water displacement. Micrographs were obtained with an optical microscope at 200X resolution (VHX-7100, Keyence) and the voids were segmented using an open-source image analysis software (Fiji, imagej.net/Fiji). A pixel counting method similar to the author's prior work was used to determine the fraction of the image consisting of voids[13]. Water displacement density measurements were completed according to the ASTM D792 standard using an analytical balance density kit (model ML-DNY-43, Mettler Toledo) where the sample volume was 0.346 ± 0.023 cm^3. A minimum of two tests per sample were run to ensure that the samples did not absorb water during testing.

Laminate Theory Calculations

Classical lamination theory has been utilized extensively to describe the elastic behavior of transversely anisotropic materials in plane-stress loading. As such, a single lamina can be characterized by four independent constants to build the stiffness matrix, *[Q]*, along the principal axes:

$$[Q] = \begin{bmatrix} \frac{E_1}{1-\upsilon_{12}\upsilon_{21}} & \frac{\upsilon_{21}E_1}{1-\upsilon_{12}\upsilon_{21}} & 0 \\ . & \frac{E_2}{1-\upsilon_{12}\upsilon_{21}} & 0 \\ . & . & G_{12} \end{bmatrix} \quad (1)$$

The stiffness constants can be determined through three simple mechanical tests: longitudinal tension, transverse tension, and shear.

Once lamina behavior is characterized, laminate theory can be used to predict the stiffness and strength of laminated composites. For brevity, only the most important steps of laminate theory are detailed in this manuscript. Further details on classical lamination theory are detailed in the text by Daniel and Ishai[14]. The laminate compliance matrix, [a], is determined from the laminate stacking sequence and can be used to determine the elastic modulus by:

$$E_x = \frac{1}{h a_{xx}} \quad (2)$$

where *h* refers to the laminate thickness, which is 1.757 mm and 1.948 mm for the recycled and virgin carbon fiber composites respectively.

To determine the laminate strength, the Tsai-Hill failure criterion was used in a first-ply failure scheme. This failure criterion is defined as:

$$\left(\frac{\sigma_1}{F_1}\right)^2 + \left(\frac{\sigma_2}{F_2}\right)^2 + \left(\frac{\tau_{12}}{F_{12}}\right)^2 - \frac{\sigma_1\sigma_2}{F_1^2} = \left(\frac{1}{F}\right)^2 \quad (3)$$

where F_i corresponds to the tensile or shear failure stress of the lamina and σ and τ correspond to the principal stresses in a lamina.

To predict the tensile properties of the randomly-oriented laminate experiments, the laminate sequence used to predict the laminate modulus and strength was randomized. Due to high variability in the local fiber distribution and orientation of the nonwoven preforms, the mechanical properties vary significantly more than continuous fiber composites. To account for this, the mechanical properties were perturbed by an amount within the 95% percentile interval of the inhomogeneity metric. A Monte Carlo simulation written in MATLAB using these methods to capture the stochastic variation in properties was run 10,000 times to generate a distribution of modulus and strength. This approach is justified, as the mechanical properties of similar composites have been shown to be stochastic[15]. When designing with such materials, it is essential to consider the stochastic nature of the mechanical properties.

Results

Nonwoven Tensile Tests

Tensile testing of the nonwoven preforms revealed that both exhibit a level of anisotropy. The reused virgin fiber preform produced via a wet-laid process exhibited an average peak load of 67.3 N ± 6.8 N in the machine direction and 43.3 N ± 4.8 N in the cross direction, indicating that the fibers were more aligned in the machine direction. The strain-to-failure was 0.008 ± 0.002 in both the machine and cross directions. The failure mode in the machine direction was one of delamination between layers of the preform spanning the length of the sample, while the failure mode in the cross direction involved local fiber pullout (see SII-2. Discussion of Dry Nonwoven Preform Testing in Tension). The delamination between layers indicates that the virgin fiber preform exhibits a strongly planar fiber orientation.

Tensile testing of the recycled fiber preform produced via a carding process exhibited a much lower peak load. The peak load in the machine direction was 1.5 N ± 0.2 N, while in the cross direction the peak load was 5.2 N ± 0.6 N. The strain-to-failure was 0.290 ± 0.052 in the machine direction and 0.216 ± 0.064 in the cross direction. The failure mode of these samples was indistinguishable between the cross and machine directions. No delamination was evident, with all failure resulting in fiber stretching and eventual pullout. This failure mode differed from the virgin fiber preform fiber pullout in that there was significant necking of the sample, leading to significantly increased strain relative to the virgin fiber preforms.

Previous work has also shown that the machine direction of carded nonwoven preforms exhibits lower peak loads than the cross direction[12]. This may be explained by the reorientation of fibers in the machine-direction into the z-direction during the carding process. The results of these tests can be used to rapidly evaluate the anisotropy of the preforms, which can significantly reduce processing time in the early stages of material design and when producing nonwoven materials.

Tensile Testing

Tensile testing results are shown in Table II-1. As expected from nonwoven testing, the laminate orientation had a strong influence on the tensile properties. The repurposed virgin fibers were preferentially oriented in the machine-direction, resulting from alignment induced by hydrodynamic forces in the continuous processing of the preforms. The recycled fiber preforms exhibited even greater anisotropy. Recycled fibers were preferentially oriented in the cross-direction during the manufacturing of the carded preforms. As fiber bundles were opened during the carding process, the combs pulled the fibers apart along the length of the carding drum to induce cross-direction orientation.

For both composites, the Poisson's ratio measured by DIC was found to be higher in the fiber-dominant direction, as is typically found in continuous fiber composites. As expected, the recycled fiber composites with greater anisotropy exhibited a higher fiber-direction Poisson's ratio than the virgin fiber composites. Due to the increased anisotropy of the recycled fiber composites, the maximum unidirectional strength and modulus were significantly higher than obtained for the virgin fiber composites. For the recycled fiber composites, the strain-to-failure was less in the cross-direction since more fibers were oriented longitudinal to the load, as the fiber strain-to-failure is much lower than that of the matrix. However, this did not hold for the virgin fiber composites, which indicates that the virgin fiber composite may have failed to adequately translate the loading to the fibers. Likewise, the lower mechanical properties of the virgin fiber composites despite higher fiber volume fraction indicates that the binder may have inhibited stress transfer at the fiber-matrix interface. Future work will measure the interfacial shear strength to evaluate this hypothesis.

The organosheet lamina testing yielded relatively similar results to that of the composite laminate, as shown in Table II-2. As found for the laminate level testing, the recycled fiber organosheets showed higher cross-direction properties than machine direction. The inverse was found for the virgin fiber organosheets. The Poisson's ratio of the recycled fiber organosheet lamina was found to be very similar to that of the composite, while the virgin fiber organosheet Poisson's ratio was not. Further testing may yield better agreement but is beyond the scope of this paper. Overall, the strength and modulus of the organosheets were found to be less than that of the composite laminates, while the strain-to-failure increased. The variation was also larger for the organosheets than the laminates, indicating that

Table II-1. Tensile properties of carbon fiber/PPS composites

Fiber Type	Orientation	Strength (MPa)		Tensile Modulus (GPa)		Strain-to-Failure (%)		Poisson's Ratio	Number of Samples (n)
		Avg.	StDev.	Avg.	StDev.	Avg.	StDev.		
PPS films*		80	-	3.4	-	4.0	-	0.38	-
Virgin	Random	179	16.1	24	3.3	0.76	0.08	-	12
	Random**	183	10.4	24	3.0	0.82	0.10	-	11
	MD	201	12.3	26	1.8	0.81	0.10	0.34	6
	CD	139	14.7	19	2.0	0.75	0.12	0.23	6
Recycled	Random	214	30.0	23	3.5	0.93	0.06	-	8
	MD	139	12.5	16	0.7	0.90	0.08	0.19	12
	CD	268	32.3	34	2.6	0.80	0.09	0.40	15

*Values taken from manufacturer's datasheet
**Processed for 30 minutes under vacuum

Table II-2. Tensile properties of carbon fiber/PPS organosheet lamina

Fiber Type	Orientation	Strength (MPa)		Tensile Modulus (GPa)		Strain-to-Failure (%)		Poisson's Ratio	Number of Samples (n)
		Avg.	StDev.	Avg.	StDev.	Avg.	StDev.		
Virgin	MD	139	30.1	17	3.3	0.84	0.12	0.31	9
	CD	111	29.4	13	1.9	0.91	0.19	0.34	11
Recycled	MD	94	12.5	10	0.7	0.99	0.12	0.19	10
	CD	190	32.5	21	2.6	1.01	0.31	0.39	7

the organosheets were more inhomogeneous. The reduction in strength and modulus can be attributed to the void content of the organosheets, which was significantly higher than the composites. In producing the organosheet laminae, the processing time had to be limited to avoid matrix degradation. As such, only partial impregnation was achieved, with final impregnation occurring during the laminate consolidation step.

The DIC data indicates that strain is inhomogeneous across the surface. Violin plots were generated for the inhomogeneity metric from 0.25% strain until failure, as shown in Figure II-2. The average strain of each of the eight subregions in each image was used to generate a distribution of strain to calculate the inhomogeneity metric. A value a 1.0 indicates that the strain in the subregion is exactly the same as the global strain. Hence, the mean strain is very near 1.0 in all cases. A wider distribution indicates that the strain is more inhomogeneous. Likewise, a median that is significantly far away from the mean indicates greater inhomogeneity. The 95% percentile interval was calculated from the data to describe the variability in strain across the surface.

The results indicate that carded recycled fiber composites exhibited greater homogeneity than the wet-laid virgin fiber for both the organosheet lamina and composite laminate testing. The 95% percentile interval for the recycled fiber composites was {0.950, 1.045}, while the virgin fiber interval was {0.903, 1.095}. Organosheet lamina testing showed greater variability than the composite samples, where the recycled fiber organosheet interval was {0.895, 1.092} and the virgin fiber was {0.838, 1.147}. Lamina tests also showed similar strains on both sample sides for some samples, while laminate testing exhibited inhomogeneous strain through the sample thickness for all samples. As such, it is expected that thicker samples will be less likely to fail near regions of high local surface strain as the surface comprises a smaller volume of the sample. This trend was found to be true for all of the samples tested in this study. This behavior has also been observed in studies of platelet-based composites[15]. Additionally, the region of maximum local strain did not always correspond to the failure location. For example, in Figure II-3, both the organosheet lamina and laminate failure occurred in a region of relatively low strain on Side 1, but high strain on Side 2.

Shear Testing

Shear testing revealed that there was little difference in the shear properties between the two sample types. The results are found in Table I-3. The shear strength and strain-to-failure of the recycled fiber composite appear to have a dependence on the orientation, indicating mixed-mode failure as opposed to pure shear failure. For an orthotropic material with transverse isotropy, the shear strength should not be a function of orientation if tested in perpendicular principal directions. However, due to the inhomogeneity of the material, the recycled fiber organosheets appear to behave instead as general anisotropic materials. Fibers

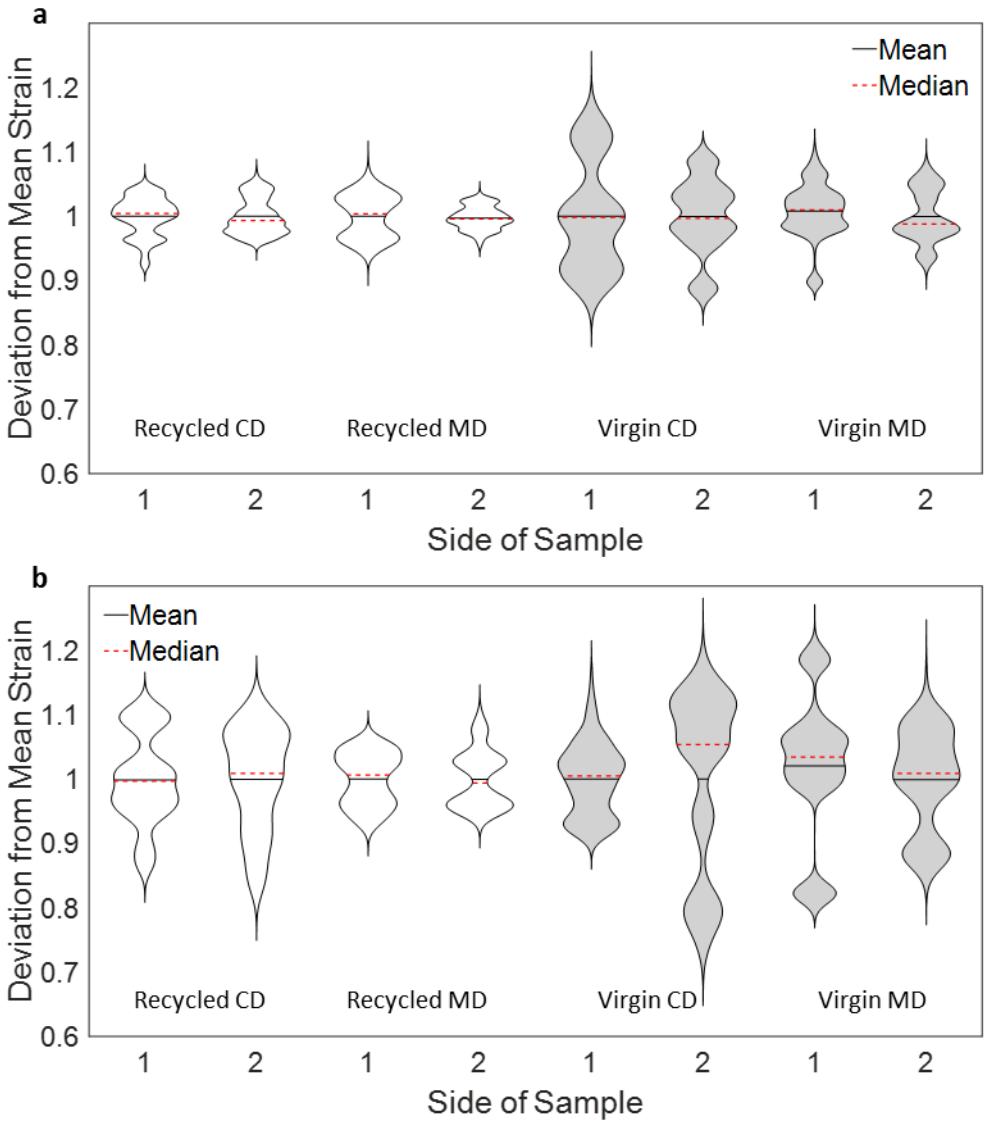

Figure II-2 a) Violin plots of composite samples; b) Violin plots of organosheet samples

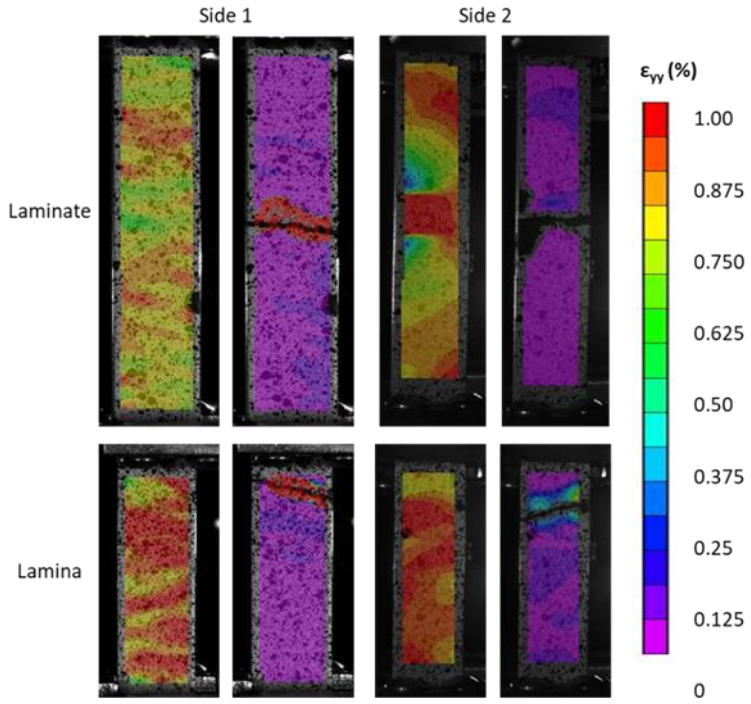

Figure II-3. Example of failure behavior of laminate and lamina under tensile loading that illustrates a case in which strain concentration that caused failure was apparent on one side of the sample, but not the other

Table II-3. Shear properties of carbon fiber/PPS composites

Fiber Type	Orientation	Shear Strength (MPa)		Shear Modulus (GPa)		Shear Strain-to-Failure (%)		Number of Samples (n)
		Avg.	StDev.	Avg.	StDev.	Avg.	StDev.	
Virgin	MD	111	8.0	7.8	0.1	1.75	0.13	4
	CD	108	4.3	7.7	0.8	1.83	0.23	4
Recycled	MD	106	7.5	7.7	0.6	1.53	0.10	4
	CD	138	14.7	8.1	0.3	1.95	0.13	4

oriented out of plane due to the carding process may also contribute to the failure mode, blunting cracks differently than in-plane fibers. This would significantly complicate any analysis and is not considered further. The relative closeness of the two shear measurements justifies the assumption of transverse isotropy. The shear strength of the organosheet material was much higher than typical for unidirectional composites, largely due to the range in fiber orientation. As such, this material could provide shear resistance when laminated with unidirectional continuous fiber organosheets for components in which the dominant loading cases are unidirectional.

Overall, strain gauge data conformed closely with the average DIC data, validating the applicability of full-field strain measurements. However, the DIC measurements on samples with strain gauges varied significantly. The strain gauge adhesive likely arrested and redirected crack growth away from the strain gauge region. As such, the variation in shear strain through the thickness was significant, leading to much higher shear strains on the DIC surface. This issue appears to have more significantly affected the thinner recycled carbon fiber samples. The effect of the strain gauge on the recycled fiber samples was also likely magnified by the lower fiber volume fraction, i.e., there were fewer fibers to arrest cracks in the matrix. Significantly thicker specimens than tested here are likely to limit the effect of the strain gauge.

Void Content Analysis

The void content of the composites characterized by both optical microscopy and density measurements is found in Table II-4. The variation between the density-based void content measurement and void content measured via optical microscopy can likely be attributed to the difference in measurement scale, i.e., the density measurement is based over a larger region of the composite, while the optical micrographs are only taken at discrete points where local inhomogeneity has a stronger influence. This effect was minimized by taking optical micrographs at different depths in the sample. Overall, good agreement is found between the void content predicted by density measurements and the void content measured in optical micrographs.

The void content of the recycled fiber composites is consistently lower than that of the virgin fiber composites. The repurposed virgin fibers exhibit much larger bundles than the recycled fibers, which are difficult to impregnate with a highly viscous thermoplastic resin, thereby yielding interbundle porosity. Additionally, the binder on the virgin fibers likely gasified at the processing temperature, thereby introducing porosity that did not escape during processing. Evidence of this behavior is shown in Figure II-4, where large fiber bundles are apparent in the virgin fiber composites alongside regions of large round porosity indicative of entrapped gas.

Table II-4 explicitly separates the machine and cross direction recycled fiber samples based on the plate from which test specimens were taken, showing that there exists a significant difference in void content between the two plates. Despite

Table II-4. Comparison of void content characterization methods

Fiber Type	Orientation	Optical void content (%)	Density Void Content (%)
Virgin	Random	12.0 ± 2.3	14.6 ± 3.0
	Random*	5.6 ± 3.0	7.3 ± 1.6
	MD	17.7 ± 6.2	18.6 ± 1.3
	CD	17.6 ± 4.9	16.8 ± 3.8
Recycled	Random	3.5 ± 2.6	5.6 ± 2.7
	MD1	1.5 ± 0.2	4.8 ± 0.1
	MD2	7.0 ± 2.2	9.6 ± 0.5
	CD1	2.9 ± 3.3	6.2 ± 4.2
	CD2	5.6 ± 5.6	7.3 ± 4.9

*Processed for 30 minutes under vacuum

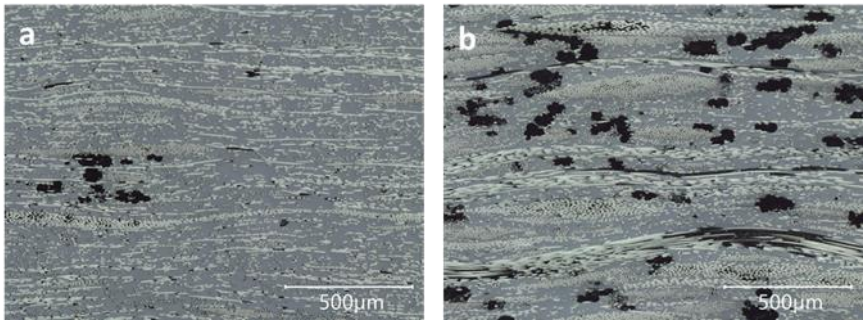

Figure II-4. a) Optical micrograph of recycled fiber composite displaying small fiber bundles and small porosity; b) Optical micrograph of virgin fiber composite displaying large fiber bundles and large round porosity indicative of entrapped gas due to the binder

the significant void difference, the average mechanical properties were similar. The moduli were identical, while the strength of plate 1 was only 7.3% higher in the cross direction and 11.5% higher in the machine direction. The strain to failure was found to slightly increase with decreased porosity. These results are in good agreement with those of the virgin fiber composites shown in Table II-1 that exhibited significantly different porosity with processing time.

Surprisingly, the similarity of the mechanical properties indicated that void content has little effect on the mechanical properties of organosheet composites. This behavior is contrary to continuous fiber-reinforced composites, in which high void content typically has extremely detrimental effects on the mechanical properties. Furthermore, void content alone cannot be used to explain why the recycled carbon fiber composites achieved higher mechanical properties than the virgin fiber composites since those processed for 30 minutes exhibited similar void content to the recycled fiber composites. Instead, the mechanical properties are likely more dependent on other parameters such as fiber orientation, fiber bundle architecture, or interfacial bonding. The latter warrants additional research beyond the scope of this manuscript.

Mechanical Property Estimates for Random Laminates

Due to the difference in measured properties between the organosheet lamina and the unidirectional-laminated composites, one must choose which mechanical properties to use to model the elastic behavior using laminate theory. We have chosen to utilize the composite properties, as these are believed to better represent the behavior of the material in a laminated composite format. However, for very thin laminates (e.g., as few as two layers), it may be necessary to measure the fully-consolidated lamina properties due to thickness effects. The resulting predicted modulus and strength are shown alongside the measured properties in Figure II-5. In general, the laminate theory calculations utilizing a first-ply failure criterion conservatively estimate the strength and modulus of randomly-oriented composites and adequately capture the variability in modulus and strength exhibited in experiments as evident from the comparably-sized error bars.

Discussion

As described earlier, there was significant variation in mechanical properties between samples, which can likely be attributed to local inhomogeneities. From the inhomogeneity metric, the virgin wet-laid preforms exhibited a less homogeneous microstructure than the recycled carded preforms. This is also evident in the failure mode of the unimpregnated fiber preform experiments: virgin fiber nonwovens exhibited either delamination or pull-out failure modes emanating from a local region while necking and increased strain-to-failure were observed in the recycled fiber nonwoven samples. The more gradual failure than the virgin fiber preforms indicated that the recycled fiber preforms exhibited greater homogeneity, as opposed to rapid failure induced by local material defects.

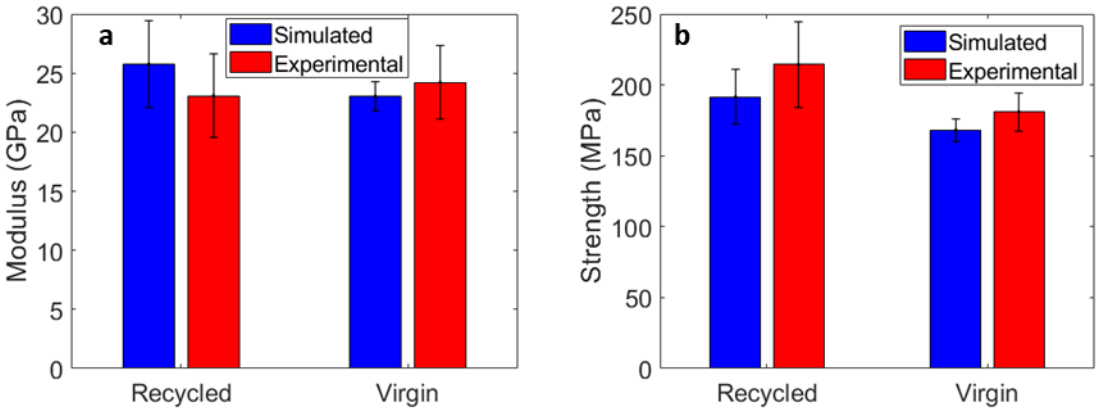

Figure II-5. a) Comparison of modulus simulation of recycled and virgin fiber composites; b) Comparison of strength simulation of recycled and virgin fiber composites

Beyond fiber orientation effects, the mechanical properties of composites are usually strongly influenced by the fiber volume fraction. Typically, an increase in fiber volume fraction leads to an increase in strength and modulus and a decrease in strain-to-failure. As expected, the strain-to-failure of the more fiber-dense virgin fiber composites was lower than the recycled fiber composites; however, the strength and modulus were higher for less fiber-dense recycled fiber composites.

One possible explanation for the increase in strength with decreasing fiber volume fraction is the existence of voids in the virgin fiber composites that reduce the mechanical properties. This behavior has been observed by other authors who claim that there exists a critical fiber volume fraction for thermoplastic composites at which the mechanical properties decrease with increasing fiber loading due to poor wetting at high fiber concentrations[16]. Voids also tend to reduce the strain-to-failure by providing crack initiation sites leading to premature failure. Another explanation for the reduced properties of the virgin fiber composites involves the fiber-matrix interface: the interface may have been compromised in the case of repurposed virgin fibers. For example, the repurposed virgin fibers may have contained a sizing that was incompatible with the PPS matrix. Similarly, incompatibility between the PPS matrix and binder would degrade the interfacial bond strength. As the recycled fiber composites contained no sizing after undergoing pyrolysis, the friction-bonded fiber surfaces likely yielded a stronger interface than one that was chemically incompatible.

The inhomogeneity strain metric can guide appropriate lamina property variations when modeling the strength and modulus values in Monte Carlo simulations. Typical variation from homogeneity was in the range of 5% to 10%, which matched well with the experimentally observed variation of the strength, modulus, and failure strain of the composites. The standard deviation of maximum load measured for the dry preforms was also in agreement with the deviation in composite properties. As a result, it is possible to screen candidate materials at the unimpregnated preform level to estimate the expected variation in composite properties. For applications requiring narrow variation in mechanical properties, this screening process can significantly reduce the time spent on initial material selection.

Conclusions

This manuscript introduced a novel new class of composite materials that utilize nonwoven preforms made of repurposed or recycled fibers. This is particularly significant to the automotive industry due to the potential to utilize low cost recycled carbon fibers as a reinforcement in a structural material that meets established strength requirements at short cycle times. By strategically integrating continuous fiber tapes in a laminating process, the modulus requirement would likely be met with ease. It is also likely that repurposed fibers can achieve the target strength when properly sized. In addition to low cost, this material offers high-temperature

stability, infinite shelf life, and rapid cycle times, making it a good candidate for automotive lightweighting. The key results of this paper are as follows:

1. Carbon fiber reinforced thermoplastic organosheets that utilize low-cost composite waste can be produced using readily-available compression molding techniques.
2. The strength of repurposed and recycled carbon fiber reinforced thermoplastic organosheets have been shown to meet some of the requirements put forth by a consortium of auto manufacturers.
3. The void content has relatively little effect on the mechanical properties of carbon fiber reinforced thermoplastic organosheets, allowing for additional lightweighting through targeted porosity.
4. Tensile testing of the nonwoven preforms before consolidation provides insight into their degree of anisotropy, which can serve as a method of screening materials before extensive processing and testing.
5. The properties of repurposed and recycled carbon fiber reinforced thermoplastic organosheet laminates are inherently stochastic but can be accurately predicted using Monte Carlo simulations based on classical lamination theory using stochastic lamina stiffness and strength chosen from load variation measured in dry preform tensile tests, the local surface strain measured via DIC, or composite testing.

Repurposed and recycled carbon fiber organosheets show great promise as a candidate for cost-effective vehicle lightweighting.

References

[1] W.J. Joost, Reducing vehicle weight and improving U.S. energy efficiency using integrated computational materials engineering, Journal of The Minerals, Metals, and Materials Society. 64 (2012) 1032–1038. doi:10.1007/s11837-012-0424-z.

[2] U.S. Driving Research and Innovation for Vehicle efficiency and Energy sustainability, Materials Technical Team Roadmap, 2017.

[3] S. Pimenta, S.T. Pinho, Recycling carbon fibre reinforced polymers for structural applications: Technology review and market outlook, Waste Management. 31 (2011) 378–392. doi:10.1016/j.wasman.2010.09.019.

[4] U.K. Vaidya, K.K. Chawla, Processing of fibre reinforced thermoplastic composites, International Materials Reviews. 53 (2008) 185–218. doi:10.1179/174328008x325223.

[5] M. Pervaiz, S. Panthapulakkal, B. KC, M. Sain, J. Tjong, Emerging Trends in Automotive Lightweighting through Novel Composite Materials, Materials Sciences and Applications. 07 (2016) 26–38. doi:10.4236/msa.2016.71004.

[6] E. Asmatulu, J. Twomey, M. Overcash, Recycling of fiber-reinforced composites and direct structural composite recycling concept, Journal of Composite Materials. 48 (2014) 593–608. doi:10.1177/0021998313476325.

[7] J.P. Snudden, C. Ward, K. Potter, Reusing automotive composites production waste, Reinforced Plastics. 58 (2014) 20–27. doi:10.1016/S0034-3617(14)70246-2.

[8] H. Wei, W. Nagatsuka, H. Lee, I. Ohsawa, K. Sumimoto, Y. Wan, J. Takahashi, Mechanical properties of carbon fiber paper reinforced thermoplastics using mixed discontinuous recycled carbon fibers, Advanced Composite Materials. 27 (2018) 19–34. doi:10.1080/09243046.2017.1334274.

[9] B. Xiao, T. Zaima, K. Shindo, T. Kohira, J. Morisawa, Y. Wan, G. Yin, I. Ohsawa, J. Takahashi, Characterization and elastic property modeling of discontinuous carbon fiber reinforced thermoplastics prepared by a carding and stretching system using treated carbon fibers, Composites Part A: Applied Science and Manufacturing. 126 (2019) 105598. doi:10.1016/j.compositesa.2019.105598.

[10] B. Vieille, J. Aucher, L. Taleb, Carbon fiber fabric reinforced PPS laminates: influence of temperature on mechanical properties and behavior, Advances in Polymer Technology. 30 (2011) 80–95. doi:10.1002/adv.

[11] K. Giannadakis, M. Szpieg, J. Varna, Mechanical Performance of a Recycled Carbon Fibre/PP Composite, Experimental Mechanics. 51 (2011) 767–777. doi:10.1007/s11340-010-9369-8.

[12] M. Amiot, M. Lewandowski, P. Leite, M. Thomas, A. Perwuelz, An evaluation of fiber orientation and organization in nonwoven fabrics by tensile, air permeability and compression measurements, Journal of Materials Science. 49 (2014) 52–61. doi:10.1007/s10853-013-7323-8.

[13] P.R.. Barnett, S.A. Young, D. Penumadu, Chopped Carbon Fiber Reinforced Thermoplastic Composites, in: American Society for Composites

32nd Annual Technical Conference, DEStech Publications, Inc., West Lafayette, IN, 2017.
[14] I.M. Daniel, O. Ishai, Engineering Mechanics of Composite Materials, 2nd ed., Oxford University Press, New York, 2006.
[15] S.G. Kravchenko, D.E. Sommer, B.R. Denos, A.J. Favaloro, C.M. Tow, W.B. Avery, R.B. Pipes, Tensile properties of a stochastic prepreg platelet molded composite, Composites Part A: Applied Science and Manufacturing. 124 (2019) 105507. doi:10.1016/j.compositesa.2019.105507.
[16] N.-J.J. Lee, J. Jang, The effect of fibre content on the mechanical properties of glass fibre mat/polypropylene composites, Composites Part A: Applied Science and Manufacturing. 30 (1999) 815–822. doi:10.1016/S1359-835X(98)00185-7.

Roles

Philip Barnett: Conceptualization, Methodology, Software, Formal analysis, Writing – Original draft, Visualization; **Colby Gilbert:** Investigation; **Dayakar Penumadu:** Supervision, Project administration, Funding acquisition, Writing – Review & editing

CHAPTER III. MULTISCALE THERMOMECHANICAL PROPERTY ANALYSIS OF CHOPPED CARBON FIBER REINFORCED THERMOPLASTIC ORGANOSHEET COMPOSITES

A version of this chapter is in preparation for publication by Philip R. Barnett, Stephen A. Young, Vivek Chawla, Darren Foster, and Dayakar Penumadu:

Abstract

The integration of repurposed and recycled carbon fibers into high-performance composites is essential to the adoption of composites for automotive structures due to their low-cost, high formability, and reduced environmental impact. When high areal density nonwovens of these fibers are infused with a semi-crystalline thermoplastic resin, organosheets offering competitive mechanical properties can be produced. This study examined the optimization of such composites through multiscale material characterization and post-process annealing. Single fiber tensile tests were used to characterize repurposed and recycled fibers. The thermomechanical properties of the polyphenylene sulfide matrix and resulting composites subjected to different post-process annealing conditions were characterized using differential scanning calorimetry, dynamic mechanical analysis, and nano-indentation. Single fiber push-in testing was conducted to evaluate the fiber-matrix interface as a function of annealing. It was shown that statistical methods based on the bootstrap principle successfully identify the effects of post-process annealing, which are otherwise masked by material inhomogeneity. Post-process annealing was shown to be an effective method of improving the resulting mechanical properties of repurposed and recycled carbon fiber organosheet composites, thereby optimizing their properties for use as a high-performance automotive structural material.

Introduction

Carbon fiber-reinforced composites offer many properties that are desirable for the automotive industry: for example, high specific strength and stiffness, corrosion resistance, and fatigue resistance. However, carbon fiber composites have struggled to gain a large share of the automotive materials market due to high material costs, slow production rate, and concerns about recyclability[1]. International trends in legislation requiring improved vehicle efficiency have led to a significant interest in light-weighting through the integration of composite materials. Previous studies have shown that a 10% reduction in passenger vehicle weight typically yields a 6-8% reduction in fuel consumption[2]. Furthermore, reduced weight improves battery electric vehicle range, thereby allowing for smaller battery packs and therefore lower unit cost. Automotive manufacturers have begun to adopt composite materials to achieve these goals through the incorporation of thermoset matrix composites such as bulk molding compounds (BMCs) and sheet molding compounds (SMCs). However, these materials exhibit substantially lower mechanical properties than continuous fiber-reinforced composites and have a limited shelf life. To make matters worse, the thermoset matrices present a problem for vehicle recycling, which plays a significant role in the European Union, where vehicle manufacturers are responsible for recycling 85% by weight of each vehicle produced after 2015 under the End of Life Vehicles

Directive[3]. As a result, thermoplastic composites appear to be the most viable option for future automotive composites.

Thermoplastic matrix composites offer enhanced impact properties, rapid cycle times, improved assembly and joining methods, and unlimited shelf life of raw materials, making them a strong alternative to thermoset matrix composites[4]. These properties have led to the adoption of thermoplastic composites in the aerospace industry. For example, the J-nose (fixed wing leading edge) of the Airbus A340-600 airliner is made of glass fiber/polyphenylene sulfide[5]. The polyphenylene sulfide (PPS) matrix provides shorter manufacturing times than traditional thermoset resins, higher service temperatures than many thermosets, and makes resin recycling feasible[6].

Furthermore, thermoplastics such as PPS have successfully utilized recycled carbon fibers as a reinforcement in high-volume processes such as injection molding[7]. However, these parts tend to be low-performance due to fiber length degradation during the compounding and extrusion processes. A similar problem plagues 3-D printed fiber-reinforced thermoplastics. In recent years, fiber recycling methods such as matrix pyrolysis, chemical solvolysis, and fluidized-bed processing have shown good mechanical property retention while retaining moderately long fibers[8]. However, common manufacturing methods for these fibers significantly degrade fiber length, thereby reducing their value. As a result, novel processing routes that do not degrade fiber length have been developed and can yield mechanical properties that are much closer to that of continuous fibers. These so-called discontinuous long fiber thermoplastic composites offer significant promise in semi-structural applications within the automotive industry.

One processing route used to produce discontinuous long fiber thermoplastic composites utilizes nonwoven fibrous mats that are infiltrated with resin. These mats can be produced using a variety of techniques such as wet deposition, air deposition, and carding, among other processes. When fibers are randomly-oriented, in-plane material isotropy can be expected, making designs with this material similar to traditional automotive metals[9], [10]. Similarly, traditional manufacturing techniques such as compression molding can be utilized for the production of complex geometries with little fiber disturbance due to the reduced stiffness of chopped fibers, as opposed to continuous fibers that require more labor-intensive processes such as vacuum infusion, autoclaving, and reaction injection molding[4], [11]. When compression molding semi-crystalline thermoplastic composites, the mold temperatures and cooling rates largely dictate the matrix morphology. For example, previous studies have shown that the semi-crystalline thermoplastic PPS experiences a change in the degree of crystallinity associated with cooling rate and molding temperature, which strongly affects mechanical properties including modulus, strength, and elongation[12], [13]. Post-processing techniques such as annealing can be further used to induce crystal growth to tune the mechanical properties of PPS as desired[14]. Therefore, studies of the processing, post-processing, and mechanical behavior of these composites are of great interest.

The present paper details the manufacturing and evaluation of a randomly-oriented, recycled and repurposed fiber thermoplastic matrix organosheet produced via a compression molding process. Organosheet laminae were subsequently compression molded to form composite parts. These parts were then annealed at various conditions to induce cold crystallization. Two types of carbon fiber reinforcement were studied: repurposed virgin and recycled via pyrolysis. The thermal transition properties were explored using dynamic mechanical thermal analysis (DMTA) and differential scanning calorimetry (DSC). The tensile properties of the composite were studied at room temperature and modulus dependence with temperature using thermo-mechanical testing. Optical microscopy was used to study the microstructure of the resulting composites. Single-fiber push-in tests were used to measure the interfacial shear strength (IFSS) to determine the effects of annealing and fiber type on the fiber-matrix bond. This work is primarily motivated by the need for a greater understanding of the effects of high-temperature annealing on organosheet composites that may be induced during automotive production. For example, automotive painting processes, which typically involve high temperatures, can influence the resulting properties of semicrystalline thermoplastic composites. Therefore, an understanding of these effects is essential to the design of automotive organosheet composite structures.

Materials and Methods

Polyphenylene Sulfide Matrix

The matrix material used in this study is polyphenylene sulfide (PPS). Films of 0.127 mm nominal thickness and 1.34 g cm^{-3} density were purchased for use in the film infusion process (Ryton AQ200P, Solvay). The enthalpy of fusion for the as-received PPS was found to be 7.53 J g^{-1} by DSC testing described later in this paper, suggesting that it is highly amorphous. This material offers many desirable properties such as high-temperature stability, inherent flame resistance, and good chemical resistance[15]. PPS is typically rated for low-stress applications up to 240 °C and when used as the matrix in a continuous carbon fiber composite shows no significant drop in tensile properties at 120 °C[16]. Furthermore, PPS can be bonded using resistance welding techniques to additively build complex structures and dramatically reduce the number of fasteners required for assembly[17]. The inclusion of fibers is known to increase the thermal transition temperatures in fiber-reinforced PPS by increasing the crystallinity of the matrix[18]. This increase in crystallinity often appears as transcrystallinity about the fiber, characterized by highly lamellar crystal nucleation in directions radial to the fiber that leads to a more brittle fiber-matrix interface and enhanced shear strength[19]–[21]. Studies have shown that increasing crystallinity in PPS-matrix composites also leads to an increase in mechanical properties[12], [14], [22].

Nonwoven Carbon Fibers

Two types of nonwoven carbon fiber preforms were considered: repurposed virgin wet-laid and recycled carded fibers. The virgin carbon fibers in this study were provided in the form of a nominal 300 g m^{-2} mat (measured 310.0 ± 6.6 g m^{-2}) produced using a modified papermaking process. In this process, fibers are mixed into a water slurry, drained, and dried [23]. During the draining process, the fibers are deposited on a filter to form a mat of in-plane random orientation. A binder was present, as evident by fiber burn off tests conducted in a furnace at 500 °C for 30 minutes (1.1 ± 0.2% mass loss). Additionally, the repurposed virgin fibers may contain a sizing for their initial intended use. The recycled carbon fibers were provided in the form of a nominal 200 g m^{-2} mat (measured 184.2 ± 11.2 g m^{-2}) produced using a carding process. The carding process involves mechanical entanglement and orienting of fibers using a series of combs. Fiber burn off tests did not reveal any appreciable mass loss, indicating that there was no binder present and sizing had been removed during the pyrolysis recycling process.

Compression Molding

Compression molding was used to process the constituent materials into organosheets. The processing time, fiber type, and atmosphere were varied, while the temperature and pressure served as controls. All molding was done at 300 °C and 1 MPa pressure using a heated press (Carver, model 3895) with pressure held throughout the processing time and cooling. The heating rate to reach the target temperature was 5 °C min^{-1} and the cooling rate was 20 °C min^{-1} based on measurements using external thermocouples. Recycled fiber organosheets were processed in air for 5 minutes, while virgin fiber organosheets were processed in air for 5 minutes or under vacuum for 30 minutes. PPS is known to cross-link when exposed to oxygen at processing temperatures, thereby reducing crystallinity and increasing resin viscosity, which in turn increases the pressure required for consolidation and reduces the recyclability of the matrix[24]. Hence, the material processed for 30 minutes was placed in a polyimide vacuum bag to prevent matrix degradation. All samples were placed between polyimide films to aid in sample removal. In general, one layer of carbon fiber mat was placed between two layers of PPS film in an aluminum mold to form a 250 mm X 250 mm organosheet. Following production of the organosheet, it was cut into 100 mm X 100 mm sheets, stacked into a 1.6 mm thick picture frame mold (chosen slightly thinner than the target composite thickness to limit void content while maintaining shape), and compression-molded following the same schedule to form a final plaque. Recycled fiber composites consisted of five stacked organosheet lamina, while virgin fiber composites consisted of four to achieve the desired thickness. The virgin composite had a nominal density of 1.563 g cm^{-3} and a nominal fiber volume fraction of 41.7%, while the recycled composite had a nominal density of 1.494 g cm^{-3} and a nominal fiber volume fraction of 30.1% based upon the constituent materials. Before manufacturing, the mass of the PPS films and carbon fiber nonwovens was measured to estimate the fiber volume fraction of each resulting

organosheet. The composite fiber volume fraction was then estimated based upon the organosheets that were used to produce it.

After processing, the plaques were cut into tensile bars and then annealed in a vacuum oven for two hours at either 140 °C or 210 °C. This annealing cycle was used to induce cold crystallization in the samples. Some samples were left unannealed to provide baseline property data. A naming convention was developed for the samples in the following format: fiber type – processing time – annealing temperature. For example, virgin fiber samples processed for 30 minutes with 140 °C annealing are labeled V-30-140. Samples were trimmed to testing size using a low-speed band saw and machined using a manual mill. Milled particles were gathered for DSC analysis.

Single Fiber Testing

Single filament testing of the carbon fibers was performed on an MTS Nano Bionix Universal Testing System (Nano UTM) affording load resolution on the order on nN and displacement resolution of the order of nm. The load is measured by the Nano UTM's Nano Mechanical Actuating Transducer (NMAT) column governed by three main components namely, the electromagnetic coil, capacitive gauge, and leaf springs enabling the system to deform the sample with a load resolution of 50 nN and a displacement resolution of 0.1 nm. Additionally, the Nano UTM contains a stepper motor with displacement position resolution steps of 35 nm to extend the deforming sample[25].

Forty virgin and forty recycled individual carbon fiber filaments were mounted on tabs based on the ASTM C 1557-03 and ISO 11566-1996 standards with modifications to account for template bending and fiber alignment described in detail elsewhere[25]–[28]. In short, prefabricated aluminum templates were positioned in precision machined alignment blocks where Nylon 6/6 strip supports were adhered to two aluminum templates using a cyanoacrylate-based adhesive forming a temporary frame for testing. The use of aluminum templates hinders bending moments and preloading of the temporary frame commonly experienced when utilizing plastic or paper disposable templates[26]. Each aluminum template consisted of an etched centerline where the filament was precisely positioned and temporarily adhered to the template using an epoxy-based resin system (West System, Gougeon Brothers, Inc.) to ensure alignment of the filament along the loading axis[26], [27]. The templates with 10 mm gauge length were then mounted onto the Nano UTM grips. The average fiber diameter was measured using a polarized optical microscope (BX53M, Olympus) before mechanical testing. To avoid the effect of noncircular cross-sections, these measurements were confirmed on similar fibers using a scanning electron microscope (1525 SEM, LEO Electron Microscopy, Inc.). The filaments were loaded in tension at a strain rate of 0.0001 s^{-1} until mechanical failure. Modulus, failure strength, and corresponding failure strain was recorded. The modulus values were calculated between 0.1% and 0.6% strain.

Differential Scanning Calorimetry

Differential scanning calorimetry was completed using a power-compensated DSC (Diamond DSC, Perkin Elmer) at 100 °C min^{-1} heating and cooling rates. The high heating rate was chosen per previous literature to prevent cold crystallization during the measurement[30]. Nitrogen was used as a purge gas set to 20 mL min^{-1}. Samples of mass 5 ± 1 mg were heated from 40 °C to 320 °C. The resulting thermogram was used to calculated the degree of crystallinity using a rule of mixtures modification[30], [31]:

$$\boldsymbol{X_C}(\%\ \boldsymbol{crystallinity}) = \frac{\Delta \boldsymbol{H_m} + \Delta \boldsymbol{H_c}}{\Delta \boldsymbol{H_f}(\mathbf{1} - \boldsymbol{W_f})} \quad (1)$$

where ΔH_m is the enthalpy of melting described by the area under the melting peak, ΔH_c is the enthalpy of crystallization described by the area under the exothermal crystallization peak, ΔH_f is the enthalpy of fusion for a 100% crystalline phase sample, and W_f is the weight fraction of the reinforcing fibers. Milled particles were used to increase the sample surface area and reduce the measurement variance. Initial testing of cut samples showed significant variation, likely attributed to variations in fiber volume fraction and poor thermal contact. The effect of milling on the mean measured crystallinity was insignificant, indicating that strain-induced crystallization was minimal.

Dynamic Mechanical Thermal Analysis

Dynamic mechanical thermal analysis was completed according to the ASTM D4065 standard in three-point flexure. The sample dimensions were nominally 50 mm x 10 mm x 2 mm with a test span of 40 mm. Results were obtained using a Perkin Elmer Pyris Diamond DMTA at a heating rate of 2 °C min^{-1} between 40 °C and 190 °C at 1 Hz in an air atmosphere with a target displacement of 20 µm. Glass transition temperatures were calculated from the peak of the loss modulus curve.

Composite Tensile Testing

Tensile testing was completed according to the ASTM D3039 standard at room temperature. Specimens were loaded to failure using an MTS 858 load frame with a 25 kN load cell, with true strain measurements taken using an extensometer having a gauge length of 25.4 mm. The sample dimensions were nominally 100 mm X 12.7 mm. Thickness varied depending on fiber type and void content but was near 2.0 mm. These modified dimensions remain within the acceptable range defined by the standard. G-10 fiberglass tabs were applied to the samples in the grip region to promote failure in the gauge length. Hydraulic grips with gripping pressure set to 5.5 MPa were used to hold the specimen during testing. Samples were tested at a displacement rate of 2 mm min^{-1}. The samples were prepared using laminae oriented at random.

Microstructure Characterization

The microstructure of the composites was characterized using optical micrographs and water displacement density measurements. Optical microscopy was used to quantify fiber and void content in the composite specimens, as well as laminate stacking sequence. More details on this procedure can be found in SIII-1. Laminate Orientation from Pixel Intensity. Samples were mounted in epoxy and polished using an automated polishing system (Buehler, MetaServ 250). After polishing, the samples were imaged at 200X resolution using an optical microscope (Keyence, VHX-7100). The resulting images were analyzed using a custom MATLAB script that utilized local thresholding to segment the fiber and void phases from the matrix[32]. The fiber volume fraction and void fraction were calculated based upon the total number of pixels corresponding to fiber, void, and matrix. These values were used compared with measurements taken using the water displacement method for density according to the ASTM D792 standard. An analytical balance density kit (Mettler Toledo, model ML-DNY-43) was used to measure the density of samples of 0.316 ± 0.031 cm^3 volume. Samples were tested a minimum of two times to ensure that they did not absorb significant amounts of water during testing.

Nano-Indentation

The effect of annealing on the matrix stiffness was determined using nano-indentation tests following the Oliver-Pharr method[33]. Indentations were performed on a nano-indentation device (Nanomechanics, iMicro) using a Berkovich tip to a depth of 1000 nm in regions that were resin-rich using a continuous stiffness measurement method with an oscillation frequency of 110 Hz and an amplitude of 2 nm. The average stiffness from 300 to 500 nm depth was reported. A minimum of 10 samples per annealing condition was tested. To ensure that hidden subsurface fibers did not play a significant role in the indentation results, a neat PPS sample was also indented. After testing, the samples were observed using a 3D laser scanning microscope (Keyence, VK-X250K) microscope to confirm that significant pile-up had not occurred.

Single fiber push-in tests were completed on samples after microscopy to measure the apparent interfacial shear strength (IFSS). The nanoindenter was equipped with a rounded conical tip of 5.0 ± 0.5 μm radius with an included angle of 90° ± 5°. SEM micrographs were obtained to ensure that this tip did not lead to indentation of the fibers, but rather breakage of the fiber-matrix interface. Tests were conducted at a rate of 50 nm/s to a maximum displacement of 1200 nm. Due to the high speed of these tests, thermal drift measurements were not taken as the thermal drift is not expected to be significant over such short timescales. Only fibers oriented in the longitudinal direction were tested. For the recycled fiber composites, only round fiber cross-sections were tested to simplify calculations. Analysis of the load-displacement data was completed using the shear lag model described by Rodriguez et al.[34]. The interface debond force was determined by observing the second derivative of the load-displacement curve as described in

SIII-2. Interfacial Shear Strength Measurement Procedure. The energy absorbed was also calculated, defined as the area under the load-displacement curve from the onset of interface loading to debonding. After indentation, optical micrographs were taken using the laser scanning microscope to study the surface topology near the indented fibers.

Statistical Analysis of Tensile Properties

Statistical methods were used to evaluate the effects of annealing on the resulting tensile properties of the composites. A MATLAB script was developed for this process. First, outliers were identified in the data, where any elements more than three scaled median absolute deviations away from the median were flagged. The outliers were not necessarily invalid data points, but rather points that would dramatically skew the results due to the relatively small number of samples. The outliers were then replaced with the median properties of all the samples from the same plate. By using the median of the samples from the same plate, potential bias in the data due to laminate stacking sequence variations between plates was avoided. For example, the five laminae used to build the recycled carbon fiber composites could be oriented [0/90/0/90/0] or [90/0/90/0/90], depending on the cutting direction, thereby yielding different mechanical properties. An even number of laminae in each laminate would have avoided this issue; however, this would lead to significantly different laminate thicknesses for the virgin and recycled fiber composites. The laminate thickness should be kept the same since the mechanical properties of discontinuous fiber composites are known to be thickness-dependent[35]. As such, the effects of annealing should only be identified for samples coming from plates with the same laminate sequence. The properties were then evaluated using hypothesis testing based on the parametric two-sample t-test and nonparametric Wilcoxon rank-sum test to a 5% significance level. Despite the removal of outliers, there still exists significant variance in sample sets due to the relatively small number of experiments that were performed. Additional testing could reduce this variance, but quickly becomes infeasible due to the number of variables tested here.

It is well-known that the variance of small data sets can be reduced through a process known as bootstrapping, a form of resampling with replacement. This is an effective way of analyzing strength and modulus data for wood/plastic composites[36]. In the current studies, confidence intervals were used to study the difference between samples as a result of annealing. A set of one-thousand bootstrap samples was generated for each sample type and the mean of each bootstrap sample was estimated. The bootstrap means were then normalized by the mean of the set, as relative changes are more meaningful for samples with different laminate sequences. Next, the difference in the means for the two normalized bootstrap samples was estimated, generating a new distribution of the mean differences. Two-tailed confidence intervals at 95% confidence-level were then calculated for the differences in bootstrap sample relative mean based on the z-score. Upper and lower bounds for the mean differences were estimated for the

strength, modulus, and strain-to-failure. If this interval contained zero, the samples were not significantly different as a result of processing conditions or annealing. This process was repeated one-thousand times to ensure that the bootstrap algorithm was sufficiently random, thereby providing a distribution of the upper and lower bounds. This process provides insight into sample sets with relatively small sample sizes and large deviations that is not apparent from simple statistical methods such as a t-test or rank-sum test.

Results

Single Fiber Tensile Testing

The recycled fiber modulus, strength, and elongation are 206 ± 14 GPa, 4426 ± 386 MPa, and 2.0 ± 0.09%, respectively, where the bounds represent the range of a 95% confidence interval. The fiber diameter based on images of the fiber taken under the optical microscope was 7.3 ± 0.23 µm. As is apparent in Figure III-1.a, many of the recycled fibers exhibited a non-circular cross-section. The virgin fiber modulus, strength, and elongation are 197 ± 10 GPa, 3302 ± 238 MPa, and 1.7 ± 0.11%, respectively. The fiber diameter was measured as 7.9 ± 0.19 µm, where circular cross-sections were identified (Figure III-1.b). The mechanical properties of the recycled carbon fibers indicate that it was likely sourced from aerospace-grade fiber (for example, the properties are quite close to AS4), while the virgin fibers appear to be standard modulus or automotive-grade fibers.

Differential Scanning Calorimetry

The 100% crystalline enthalpy of fusion for virgin PPS is not well-agreed upon, with literature values range from 50 J g^{-1} to 150.4 J g^{-1}[37]. As a result, the enthalpy of fusion for the PPS in this study was determined experimentally. First, PPS films were annealed at various temperatures or quenched from the melt in liquids of various temperatures. The samples were then analyzed using differential scanning calorimetry to determine the enthalpy of melting for each sample. Next, the density of the samples was precisely measured using a gas pycnometer (Micromeritics, AccuPyc II 1340) with ultra-high purity helium. It is well-documented in the literature that amorphous PPS has a density of 1.32 g cm^{-3} and a crystalline density of 1.43 g cm^{-3} [38], [39]. From this information, the mass fraction of the crystalline region can be determined based on the density measured using the pycnometer. The corresponding enthalpy of melting can then be plotted against mass fraction to extrapolate the 100% crystalline enthalpy of fusion using a linear fit with an intercept of (0,0). Figure III-2 displays the plot that was generated to determine the enthalpy of fusion. A linear fit in which the bisquare weighting method was used to weight the residuals to limit the effect of outliers provided the best fit to the data. The resulting enthalpy of fusion was 88.37 J g^{-1}, which is in the range reported in the literature.

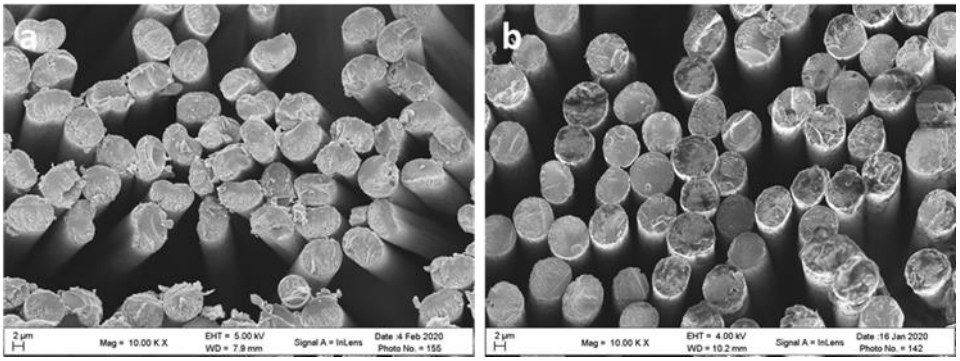

Figure III-1. Scanning electron micrographs of cross-section of (a) recycled carbon fibers and (b) virgin carbon fibers

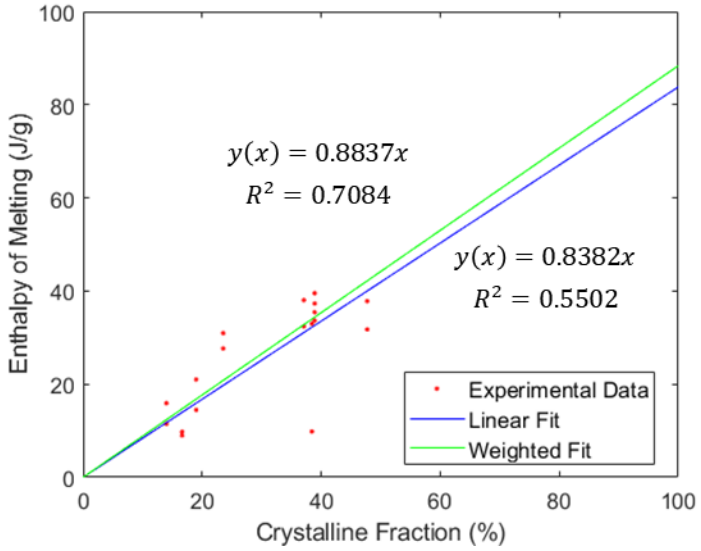

Figure III-2. Experimental data used to identify enthalpy of fusion for a 100% crystalline PPS sample

Differential scanning calorimetry results shown in Table III-1 indicate that annealing chopped carbon fiber/PPS composites at 140 °C has an appreciable effect on the total crystallinity of the composite samples. However, annealing at 210 °C has little effect beyond that of the lower temperature annealing. Overall, annealing has a fairly small effect on the total crystallinity of composite specimens, indicating that they were near full crystallization before annealing. There was a clear increase in crystallinity over the as-received PPS.

Figure III-3 displays a typical DSC thermogram from this study. There is no residual crystallization during the heating ramp, indicating that the 100 °C min^{-1} heating ramp rate was appropriate. As expected, a recrystallization peak occurs around 190 °C in the cool down[40]. Previous work has shown that neat PPS exhibits a critical quench rate near 20 °C s^{-1}, which does not account for the increased nucleation rate due to fibers[29]. The significant recrystallization apparent when cooling at 100 °C min^{-1} indicates that the critical quench rate with fibers is significantly higher than the cooling rate during compression molding. As such, the samples were likely to be nearly fully crystallized before annealing.

Dynamic Mechanical Thermal Analysis

Dynamic mechanical thermal analysis results indicated that annealing chopped carbon fiber/PPS composites improves thermal resilience. This was apparent through both the peak value of tan δ and the storage modulus loss at the tan δ peak temperature. A lower peak value indicates that the material behaves more elastically, thereby exhibiting increased thermal stability. Similarly, a smaller loss in storage modulus indicates that the material retains greater elasticity at high temperatures. This behavior is apparent in Figure II-4.a, where the storage modulus of the samples annealed at 210 °C was retained at higher temperatures than the ones annealed at 140 °C or left unannealed. This behavior has been observed previously, where it was also noted that the storage modulus retention persisted up to the annealing temperature and also yielded an increase in glass transition temperature[41]. Figure III-4.b further demonstrates the thermal resilience of annealed composites, as the tan δ peak decreases with increasing annealing temperature.

The glass transition temperature measured by the peak loss modulus (E”) can be found in Table III-2. Compared to the as-received PPS, it is apparent that the inclusion of fibers increased the glass transition temperature. Annealing further increased the glass transition temperature of the composites. This increase was less pronounced in the case of the recycled fiber composites. It has been theorized that the loss modulus is a function of the fiber/matrix interface[12]. Hence, it is expected that the glass transition temperature measured by the loss modulus peak is also a function of the fiber/matrix interface.

Tensile Testing

Tensile testing results are shown in Table III-3. The resulting tensile strength and modulus vary significantly from sample-to-sample within each set. As

Table III-1. Crystallinity of samples generated by different annealing cycles as reported by DSC (n = 5 samples)

Sample Identifier	Percent Crystallinity (%)	Average Enthalpy of Fusion (J g^{-1})
PPS Film	8.0 ± 2.8	7.03 ± 2.49
V-30-UA	36.2 ± 1.8	16.31 ± 0.83
V-30-140	39.0 ± 4.2	17.57 ± 1.88
V-30-210	38.9 ± 1.9	17.55 ± 0.84
V-5-UA	40.0 ± 7.2	17.76 ± 3.21
V-5-140	47.3 ± 6.6	20.89 ± 2.90
V-5-210	45.7 ± 3.5	20.18 ± 1.56
R-5-UA	36.0 ± 5.4	20.60 ± 3.06
R-5-140	43.2 ± 2.2	23.79 ± 1.21
R-5-210	45.2 ± 4.6	24.89 ± 2.56

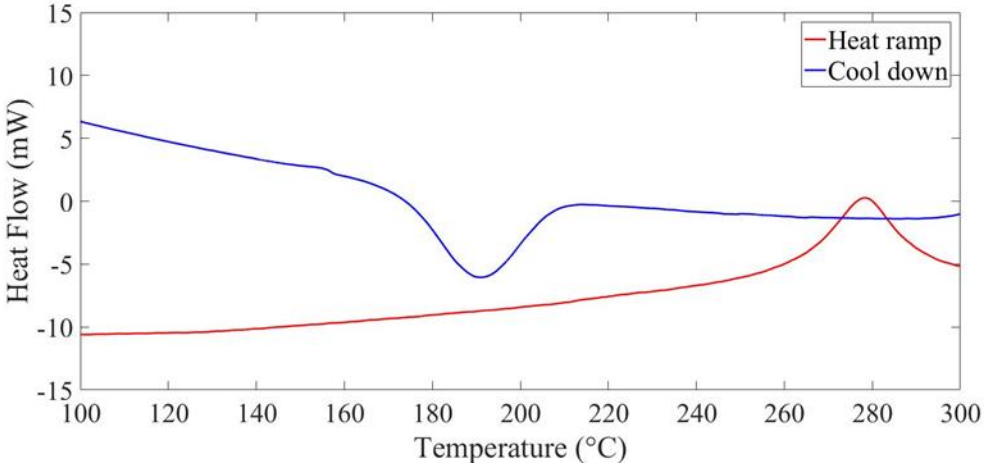

Figure III-3. Typical DSC thermogram showing clear melting and crystallization peaks near 278 °C and 190 °C respectively

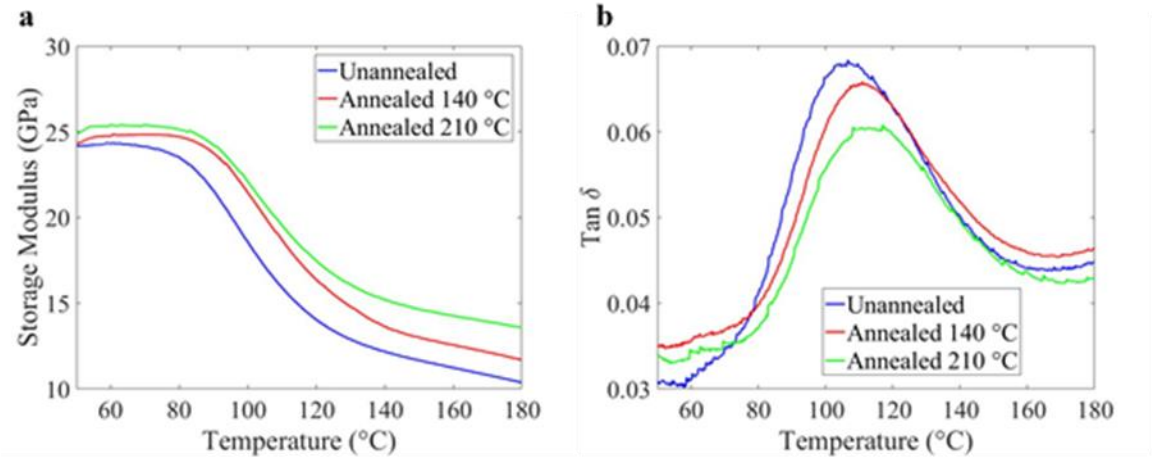

Figure III-4. (a) Storage modulus measured by DMTA; (b) tan δ measured by DMTA

Table III-2. Glass transition temperature measured by loss modulus (n = 3 to 5 samples)

Sample Identifier	T_g Average (°C)	Tan δ Peak Value	Storage Modulus Loss at Tan δ Peak (%)
PPS film	87.2 ± 0.1	3.145	98.9
V-30-UA	96.1 ± 0.4	0.067	25.9
V-30-140	102.7 ± 1.3	0.064	23.1
V-30-210	101.0 ± 2.7	0.061	23.5
V-5-UA	99.5 ± 0.3	0.074	32.1
V-5-140	102.5 ± 1.1	0.066	30.7
V-5-210	103.4 ± 1.9	0.063	30.0
R-5-UA	102.0 ± 1.8	0.071	28.8
R-5-140	103.9 ± 1.1	0.068	28.6
R-5-210	102.2 ± 0.9	0.061	26.8

Table III-3. Tensile properties of carbon fiber/PPS composites

Sample Identifier	Strength (MPa)		Modulus (GPa)		Strain-to-Failure (%)		Number of samples (n)
	Avg	StDev	Avg	StDev	Avg	StDev	
V-30-UA*	183	10.4	24	3.0	0.82	0.10	11
V-30-140**	212	20.5	29	2.6	0.77	0.09	10
V-30-210*	194	11.3	23	1.1	0.92	0.02	5
V-30-210**	218	5.3	32	2.3	0.75	0.04	5
V-5-UA	179	16.1	24	3.3	0.76	0.08	12
V-5-140	184	16.6	23	2.3	0.83	0.06	6
V-5-210	207	13.0	26	1.6	0.79	0.03	6
R-5-UA	214	30.0	23	3.5	0.93	0.06	8
R-5-140	221	31.7	25	4.7	0.88	0.07	8
R-5-210	224	37.2	24	4.3	0.93	0.09	7

*Denotes equivalent laminate sequence between V-30-UA and V-30-210
**Denotes equivalent laminate sequence between V-30-140 and V-30-210

a result, it is very difficult to analyze the effects of processing time and annealing. It appears that there is an increase in strength with annealing temperature in the samples processed for five minutes, but modulus and strain-to-failure results are inconclusive. The large variance in the data makes it difficult to discern the true effects of annealing.

Hypothesis testing results using the two-sample t-test and Wilcoxon rank-sum test are shown in Table III-4. A p-value below 0.05 indicates that the null hypothesis (the means in the case of the t-test and the medians in the rank-sum test are equal) should be rejected. In general, there are few significant differences between samples based on hypothesis testing. The results for the two test methods are generally in good agreement, indicating that the distribution of most sample properties is near normal, thereby justifying the use of the bootstrap mean in confidence interval analysis.

As described earlier, the large variance between samples makes it difficult to draw conclusions about the effects of processing time and annealing using hypothesis testing. Instead, confidence intervals of bootstrap sample relative means provide a more useful way of analyzing the differences arising from annealing. The 95% confidence interval for the difference between bootstrap sample relative means is reported in Table III-5. Negative values indicate that the property of the baseline sample was lower than that of the comparison sample, while positive values indicate the opposite. Any interval containing zero indicates that the samples are not significantly different. The results of the confidence intervals analysis indicate that each of the modulus, strength, and strain-to-failure are all significantly affected by annealing at a 95% two-tailed confidence level. It was found that the strength increased with annealing for both the virgin and recycled carbon fiber composites regardless of processing time. The modulus of the composites generally increased, but it cannot be conclusively said to increase in the case of the virgin fiber composites. The increase in tensile strength was most significant for samples annealed at 210 °C for both virgin and recycled fiber composites processed for 5 minutes. In general, strain behavior did not follow a clear trend.

Microstructure Characterization

The fiber and void volume fractions of the composites in this study are shown in Table III-6. The void content of virgin fiber composites processed under vacuum was much lower than those processed in air. Consequentially, the fiber volume fraction of the virgin fiber composites processed under vacuum was significantly higher than those processed in air. In general, it was found that the void content of the recycled carbon fiber composites was significantly lower than the virgin fiber composites. However, the void content of the virgin fiber composites processed for 30 minutes under vacuum exhibited void content much more similar to the recycled fiber composites than the virgin fiber composites processed in air.

Table III-4. Hypothesis testing results for the effect of annealing on tensile properties.

		Modulus p-value		Strength p-value		Strain-to-Failure p-value	
Sample 1	**Sample 2**	**t-test**	**Rank-sum**	**t-test**	**Rank-sum**	**t-test**	**Rank-sum**
V-30-UA	V-30-210	0.023	0.106	0.166	0.168	4.847E-07	4.579E-04
V-30-140	V-30-210	0.069	0.099	0.403	0.953	0.512	0.745
V-5-UA	V-5-140	0.090	0.102	0.608	1.000	0.022	0.032
V-5-UA	V-5-210	0.138	0.155	0.002	0.003	0.155	0.151
R-5-UA	R-5-140	0.679	0.099	0.586	0.544	0.720	0.751
R-5-UA	R-5-210	0.829	0.575	0.408	0.339	0.517	0.621

Underlined samples represent a rejection of the null hypothesis

Table III-5. Confidence intervals for the difference between samples

Sample 1	Sample 2	Strength Difference (%)	Modulus Difference (%)	Strain-to-Failure Difference (%)
V-30-UA	V-30-210	{-4.9, -4.6}	{7.8, 8.1}	{-17.2, -17.1}
V-30-140	V-30-210	{-3.0, -2.6 }	{-9.4, -8.9}	{2.7, 3.2}
V-5-UA	V-5-140	{-2.2, -1.7}	{7.7, 8.3}	{-10.9, -10.5}
V-5-UA	V-5-210	{-14.9, -14.4}	{-6.5, -6.0}	{-6.2, -5.8}
R-5-UA	R-5-140	{-3.9, -3.1}	{-4.4, -3.3}	{1.3, 1.8}
R-5-UA	R-5-210	{-6.1, -0.7}	{-2.9, -1.7}	{-3.4, -2.8}

Table III-6. Porosity measurements for carbon fiber/PPS composites (n > 4 samples)

Sample Identifier	Calculated Void Content (%)	Measured Void Content (%)	Calculated Fiber Volume Fraction (%)
V-30-UA	6.6 ± 1.6	7.3 ± 1.6	41.0 ± 2.6
V-30-140	5.6 ± 2.2	9.4 ± 0.8	36.8 ± 3.2
V-30-210	6.1 ± 0.6	8.9 ± 0.3	42.2 ± 5.9
V-5-UA	18.0 ± 10.7	13.0 ± 4.4	31.0 ± 4.6
V-5-140	14.0 ± 3.5	19.1 ± 0.7	31.7 ± 2.0
V-5-210	16.0 ± 3.3	19.7 ± 3.3	33.6 ± 1.5
R-5-UA	3.5 ± 2.6	5.6 ± 2.7	31.1 ± 3.1
R-5-140	2.7 ± 2.8	5.4 ± 2.7	30.8 ± 3.0
R-5-210	2.2 ± 0.6	5.8 ± 1.5	28.4 ± 2.7

Nano-Indentation Testing

The results of the matrix indentation testing are shown in Table III-7. The matrix stiffness is not strongly influenced by annealing, indicating that nearly full crystallization had likely been achieved before annealing. This is in good agreement with the results obtained via DSC. It is interesting to note that the virgin fiber composites processed under vacuum yielded a higher stiffness post-annealing than the samples processed in air. This indicates that some matrix structural changes may have occurred in the samples processed under vacuum, possibly in the form of chain extension or crosslinking (as evident from the lower degree of crystallinity observed by DSC). Similarly, the decrease in stiffness found in all samples annealed at 210 °C (relative to the samples annealed at 140 °C) indicates that some matrix degradation such as oxidation may occur at temperatures below the melt when exposed for long times.

The apparent interfacial shear strength of all composites decreased with annealing at 140 °C and increased (relative to the 140 °C annealing case) when annealed at 210 °C. The debonding force followed a similar trend, as did the interface energy absorption. In the samples processed for 5 minutes in air, the debonding force, apparent IFSS, and energy absorbed by the interface all significantly increased with 210 °C annealing relative to the unannealed baseline. This was not the case for samples processed for 30 minutes under vacuum, indicating that matrix degradation may have occurred at longer processing times. The modulus and strength increased with annealing at 210 °C for all composites, indicating that the IFSS should also increase if it is the primary driver of mechanical properties. Instead, the properties of the virgin fiber samples processed for 30 minutes under vacuum appears to be more sensitive to other properties such as matrix stiffness. This result indicates that the matrix of random discontinuous long fiber composites plays a strong role in their mechanical properties, which typically is not the case in continuous fiber composites.

Discussion

Annealing Influence on Thermo-Mechanical Properties

There was a clear increase in crystallinity for all annealed specimens as compared to the unannealed case. The increase was more significant in the case of the recycled fiber composites, due to their lower fiber volume fraction and larger fiber-free regions. Fibers have been shown to significantly increase the rate of crystallization in PPS, serving as nucleation sites during crystallization[42]. As such, the lower volume of fibers in the recycled fiber composites leaves larger inter-fiber spacing for bulk crystallite growth. These crystallites are likely larger than those on a fiber surface, which impinge upon the fiber and neighboring crystallites more quickly. As such, the bulk crystallites may have failed to impinge upon either other during the cooling stage of compression molding.

Table III-7. Nano-indentation results (n > 9 samples for each test case) where bounds represent a 95% confidence interval with outliers removed

Sample Identifier	Matrix Stiffness (N/m)	Apparent IFSS (MPa)	Debonding Force (mN)	Interface Energy Absorbed (nJ)
PPS	17373 ± 180	-	-	-
V-30-UA	18246 ± 148	14.29 ± 2.25	52.80 ± 3.38	22.82 ± 2.67
V-30-140	18952 ± 277	11.94 ± 1.47	50.41 ± 3.05	21.50 ± 1.49
V-30-210	18608 ± 323	12.56 ± 2.70	51.61 ± 4.02	22.03 ± 1.69
V-5-UA	18374 ± 273	12.02 ± 1.40	46.66 ± 3.12	21.01 ± 1.31
V-5-140	18559 ± 239	10.31 ± 1.87	45.37 ± 3.46	19.76 ± 2.10
V-5-210	18331 ± 143	14.37 ± 1.93	52.63 ± 2.26	22.43 ± 1.22
R-5-UA	18239 ± 255	14.16 ± 2.96	46.82 ± 5.26	20.43 ± 2.58
R-5-140	18681 ± 352	13.77 ± 2.07	49.21 ± 2.05	21.55 ± 1.16
R-5-210	18331 ± 316	18.04 ± 3.54	55.49 ± 5.77	24.96 ± 2.24

The maximum crystallinity achieved after annealing is similar between the virgin and recycled fiber composites. As compared to the virgin fiber samples processed for 5 minutes, the ones processed for 30 minutes exhibit significantly lower crystallinity. This may be due to morphological changes in the PPS matrix during the long processing time. For example, chain growth may have yielded larger crystallites that more readily impinged upon one another, thereby leaving larger regions of amorphous material. Similarly, the small decrease in crystallinity measured in the virgin fiber samples annealed at 210 °C may be due to crosslinking during the annealing process. As such, annealing at a temperature of 140 °C for 2 hours is sufficient to achieve full crystallization.

Despite minimal differences in crystallinity among the annealed specimens, there is a clear improvement in the strength and modulus of the composites with annealing at 210 °C. This behavior is typically associated with increased crystallinity[12], [14]. However, the crystallinity was largely unchanged between the two annealing conditions, indicating that other factors play a significant role. It has been reported previously that annealing relaxes thermal residual stresses in thermoplastic composites, but in doing so can decrease the fiber-matrix interfacial shear strength as compressive stresses exerted on the fiber by matrix shrinkage significantly aid in mechanical bonding[43]. Other authors have noted that annealing induces transcrystallinity about fibers that appears to improve interfacial bonding[12], [22]. These competing descriptions of the influence of annealing create significant confusion about the role of annealing on the interfacial properties of thermoplastic composites. More recent work has provided new insight, where the IFSS measured using traditional shear lag models showed a decrease with annealing, but the crack propagation energy along the interface showed a significant increase with annealing[44]. This behavior was apparent in the results for the recycled fibers shown here. As a result, the improvement in mechanical properties for these samples can be attributed to increased fiber/matrix interface energy absorption. The virgin fiber composite interface may be complicated by the binder present on the as-received fibers.

The increase in mechanical properties was evident in both the DMTA and tensile testing. The lower tan δ of the annealed specimens corresponds to improved thermal resilience, a desirable property for materials loaded in high-temperature environments such as under-the-hood automotive applications. Similarly, the increase in glass transition temperature suggests that annealed, discontinuous carbon fiber-reinforced PPS is more suitable for higher temperature applications than its neat counterpart. Higher temperature annealing may be used to further improve the thermal resilience of the composites by increasing modulus retention above the glass transition temperature.

Annealing Influence on Strain-to-Failure

The effect of annealing on the strain-to-failure deserves special consideration, as it is much less pronounced than the effect on the strength and modulus. This behavior is unexpected, as an increase in modulus typically leads

to a decrease in strain-to-failure. While the strain-to-failure did decrease in a few cases, this behavior was not evident in others. As a result, two possible explanations may be considered. First, the strain-to-failure change may be so small that the variation between measurements within a sample set masks the trends, even when studied with bootstrap statistical estimates. The strain-to-failure is expected to vary more than the modulus and strength, as the strain is a local measurement taken between the two extensometer knife-edges. A second explanation is that fiber/matrix interface changes resulting from annealing complicate the analysis. For example, increased energy absorption at the interface will result in locally greater strain-to-failure. Meanwhile, the strain-to-failure in the bulk matrix would be expected to decrease with annealing as it stiffened. Then, the resulting global strain-to-failure would be a combination of these effects that strongly depends on local inhomogeneity such as matrix-rich regions. As such, these two explanations indicate that the effect of annealing on the strain-to-failure is very complex and may not be a reliable indicator of the microstructural changes in macro-scale testing. However, strength and modulus more clearly illustrate the benefits of annealing.

Microstructure Effects

The variation in void content between the two virgin fiber composite processing methods indicates that the processing atmosphere and time have a significant effect on the consolidation process. Air trapped in the composite during the shorter processing cycle may have been unable to escape the composite during processing. By removing most of the air before processing, the vacuum process would significantly reduce this issue. However, the existence of void content in the vacuum-processed samples indicates that there may have still been significant air content that was not removed via the vacuum process or that gasification of the binder used to hold the nonwoven together occurred. Additionally, the longer processing time likely allowed infiltration into small pores that may have not been infiltrated during the short processing time, as pore wetting preferentially occurs at large pores first. As expected, the fiber volume fraction increased as the void fraction decreased due to the decrease in sample thickness.

Despite the relatively large variation in void content, the mechanical properties of the virgin fiber composites remained relatively constant. Furthermore, it appears that increasing the fiber volume fraction does not significantly improve the mechanical properties, as is typical in continuous fiber laminates. This indicates that there may exist a threshold void content, at which properties rapidly degrade and then reach a plateau value. Void content below this value would likely yield higher properties, as is the case in the recycled fiber composites. However, it cannot be definitively stated that the recycled fiber composites were below such a threshold void content as the fiber modulus and strength were significantly higher than the virgin fibers.

Despite significant void content, the mechanical properties of the randomly-oriented nonwoven composites were quite high. Table III-8 lists the properties of

Table III-8. Comparison of current results to existing literature

Matrix Material	Carbon Fiber Type	Fiber Format	Fiber Volume Fraction (%)	Strength (MPa)	Modulus (GPa)	Source
PPS	Recycled	Carded	28	224	24	Current
PPS	Virgin	Wet Lay	42	218	32	Current
Polypropylene	Recycled	Wet Lay	30	27.9	9.6	[23]
Epoxy	Virgin	Air Lay	31.1	215.5	27	[45]
Nylon 66	Recycled	Carded	30	217.1	27	[46]
Polypropylene	Virgin	Wet Lay	19.4	205	14	[47]
Epoxy	Recycled	Wet Lay	24.8	100	12	[48]
Nylon 6/Nylon 66	Virgin	Wet Lay	25	170	19	[49]
Nylon 6/Nylon 66	Recycled	Wet Lay	25	150	16	[49]
Polypropylene	Recycled	Wet Lay	25	225	24	[50]
Nylon 6	Virgin	Platelet	55.2	400	35	[11]
Epoxy	Virgin	Platelet	57	185	36	[51]
Epoxy	Virgin	Platelet	64	240	43	[52]

several similar composite materials found in the literature. In general, platelet composites exhibiting high fiber volume fraction yield the highest mechanical properties. However, platelet composites are generally made from cut prepreg, which is cost-prohibitive. As such, chopped fiber composites produced via wet lay, air lay, and carding processes are more economical. It is apparent that the matrix material has a strong influence on the properties of these composites, which is typically not the case for continuous fiber composites with tensile properties that are fiber-dominated. Thermoplastic discontinuous fiber composites also generally yield greater tensile properties than thermosets, likely due to their enhanced fracture toughness that limits crack propagation through the composite. It is also unclear from the prior studies if fiber orientation effects for the preforms were considered. The measured values may represent the strong direction, though the effect of orientation obviously cannot be ignored as shown by this study. As such, it is apparent that recycled/repurposed carbon fiber/PPS organosheet composites offer significant promise as an automotive structural material.

Conclusions

The key results of this paper are summarized as follows:

1. Annealing at 140 °C was shown to increase the crystallinity of carbon fiber/PPS discontinuous fiber composites, with annealing at 210 °C yielding similar results.
2. Despite exhibiting similar crystalline fractions, samples annealed at 210 °C exhibited improved thermal resilience.
3. The effects of annealing on the tensile properties of the composites were not immediately evident using traditional hypothesis testing due to small sample sizes and large variance, but a novel bootstrap analysis using confidence intervals elucidates the differences between samples.
4. Void content in the range of 5 to 20% has relatively little influence on the mechanical properties obtained for these composites, providing a unique opportunity for lightweighting through targeted porosity.
5. Nanoindentation can be used to study the impact of annealing on the microstructure of the composites to show that annealing locally stiffens the bulk matrix and results in increased energy absorption at the fiber/matrix interface.

Future work should seek to evaluate the influence of annealing on other properties such as shear and flexure. Typical automotive painting processes involve high temperatures that will impact the mechanical properties of organosheet composites that must be accounted for in structural designs.

References

[1] E. Ghassemieh, Materials in Automotive Application , State of the Art and Prospects, InTech, 2011. https://doi.org/10.5772/1821.

[2] W.J. Joost, Reducing vehicle weight and improving U.S. energy efficiency using integrated computational materials engineering, Journal of The Minerals, Metals, and Materials Society. 64 (2012) 1032–1038. https://doi.org/10.1007/s11837-012-0424-z.

[3] S. Pimenta, S.T. Pinho, Recycling carbon fibre reinforced polymers for structural applications: Technology review and market outlook, Waste Management. 31 (2011) 378–392. https://doi.org/10.1016/j.wasman.2010.09.019.

[4] U.K. Vaidya, K.K. Chawla, Processing of fibre reinforced thermoplastic composites, International Materials Reviews. 53 (2008) 185–218. https://doi.org/10.1179/174328008x325223.

[5] M. Favaloro, Properties and Processes of Linear Polyphenylene Sulfide (PPS) for Continuous Fiber Composites Aerospace Applications, SAE Aerotech Conference. (2009). https://doi.org/doi:10.4271/2009-01-3242.

[6] J. Diaz, L. Rubio, Developments to manufacture structural aeronautical parts in carbon fibre reinforced thermoplastic materials, Journal of Materials Processing Technology. 143–144 (2003) 342–346. https://doi.org/10.1016/S0924-0136(03)00450-3.

[7] K. Stoeffler, S. Andjelic, N. Legros, J. Roberge, S.B. Schougaard, Polyphenylene sulfide (PPS) composites reinforced with recycled carbon fiber, Composites Science and Technology. 84 (2013) 65–71. https://doi.org/10.1016/j.compscitech.2013.05.005.

[8] E. Asmatulu, J. Twomey, M. Overcash, Recycling of fiber-reinforced composites and direct structural composite recycling concept, Journal of Composite Materials. 48 (2014) 593–608. https://doi.org/10.1177/0021998313476325.

[9] S.Y. Fu, B. Lauke, The elastic modulus of misaligned short-fiber reinforced polymers, Composites Science and Technology. 58 (1998) 389–400. https://doi.org/10.1016/S0266-3538(97)00129-2.

[10] S.Y. Fu, B. Lauke, Effects of fiber length and fiber orientation distributions on the tensile strength of short-fiber-reinforced polymers, Composites Science and Technology. 56 (1996) 1179–1190. https://doi.org/10.1016/S0266-3538(96)00072-3.

[11] Y. Wan, J. Takahashi, Tensile and compressive properties of chopped carbon fiber tapes reinforced thermoplastics with different fiber lengths and molding pressures, Composites Part A: Applied Science and Manufacturing. 87 (2016) 271–281. https://doi.org/10.1016/j.compositesa.2016.05.005.

[12] N.L. Batista, P. Olivier, G. Bernhart, M.C. Rezende, E.C. Botelho, Correlation between degree of crystallinity , morphology and mechanical properties of PPS / carbon fiber laminates, Materials Research. 19 (2016) 195–201. https://doi.org/10.1590/1980-5373-MR-2015-0453.

[13] F.Y.C. Boey, T.H. Lee, C.Y. Yue, Annealing Effects on the Dynamic Mechanical-Properties of Aromatic Polyphenylene Sulfide Fiber Reinforced Composite, Polymer Testing. 10 (1991) 221–228. https://doi.org/10.1016/0142-9418(91)90034-u.
[14] J. Cao, L. Chen, Effect of thermal cycling on carbon fiber-reinforced PPS composites, Polymer Composites. 26 (2005) 713–716. https://doi.org/10.1002/pc.20148.
[15] B. Vieille, J. Aucher, L. Taleb, Carbon fiber fabric reinforced PPS laminates: influence of temperature on mechanical properties and behavior, Advances in Polymer Technology. 30 (2011) 80–95. https://doi.org/10.1002/adv.
[16] B. Vieille, J. Aucher, L. Taleb, Influence of temperature on the behavior of carbon fiber fabrics reinforced PPS laminates, Materials Science and Engineering A. 517 (2009) 51–60. https://doi.org/10.1016/j.msea.2009.03.038.
[17] P. Jaeschke, D. Herzog, H. Haferkamp, C. Peters, A.S. Herrmann, Laser transmission welding of high-performance polymers and reinforced composites - a fundamental study, Journal of Reinforced Plastics and Composites. 29 (2010) 3083–3094. https://doi.org/10.1177/0731684410365365.
[18] G.P. Desio, L. Rebenfeld, Crystallization of Fiber-Reinforced Poly (phenylene Sulfide) Composites. 1. Experimental Studies of Crystallization Rates and Morphology, Journal of Applied Polymer Science. 44 (1992) 1989–2001. https://doi.org/10.1002/app.1992.070441114.
[19] H. Quan, Z.M. Li, M.B. Yang, R. Huang, On transcrystallinity in semi-crystalline polymer composites, Composites Science and Technology. 65 (2005) 999–1021. https://doi.org/10.1016/j.compscitech.2004.11.015.
[20] B. Liu, X. Wang, S. Long, J. Yang, Interfacial micromechanics of carbon fiber-reinforced polyphenylene sulfide composites, Composite Interfaces. 21 (2014) 359–369. https://doi.org/10.1080/15685543.2014.878875.
[21] E. Schulz, G. Kalinka, W. Auersch, Effect of transcrystallization in carbon fiber reinforced poly(p-phenylene sulfide) composites on the interfacial shear strength investigated with the single fiber pull-out test, Journal of Macromolecular Science, Part B. 35 (1996) 527–546. https://doi.org/10.1080/00222349608220393.
[22] A. Arici, T. Sinmazcelik, L. Capan, I. Yilgor, E. Yilgor, Influence of Annealing on the Performance of Short Glass Fiber-reinforced Polyphenylene Sulfide (PPS) Composites, Journal of Composite Materials. 39 (2005) 21–33. https://doi.org/10.1177/0021998305046432.
[23] K. Giannadakis, M. Szpieg, J. Varna, Mechanical Performance of a Recycled Carbon Fibre/PP Composite, Experimental Mechanics. 51 (2011) 767–777. https://doi.org/10.1007/s11340-010-9369-8.
[24] L. Caramaro, B. Chabert, J. Chauchard, T. Vu-Khanh, Morphology and mechanical performance of polyphenylenesulfide carbon fiber composite, Polymer Engineering and Science. 31 (1991) 1279–1285. https://doi.org/10.1002/pen.760311708.

[25] M. Kant, D. Penumadu, Dynamic mechanical characterization for nonlinear behavior of single carbon fibers, Composites Part A: Applied Science and Manufacturing. 66 (2014) 201–208. https://doi.org/10.1016/j.compositesa.2014.07.019.
[26] International Organization for Standardization, BS ISO 11566:1996. Carbon fibre - determination of the tensile properties of single-filament specimens., (1996).
[27] M. Kant, D. Penumadu, Fracture behavior of individual carbon fibers in tension using nano-fabricated notches, Composites Science and Technology. 89 (2013) 83–88. https://doi.org/10.1016/j.compscitech.2013.09.020.
[28] American Society for Testing and Materials, ASTM C1557-20: Standard Test Method for Tensile Strength and Young's Modulus of Fibers, (2014) 1–10. https://doi.org/10.1520/C1557-14.2.
https://doi.org/10.1016/j.compositesa.2014.07.019.
[29] W.J.B. Grouve, G. Vanden Poel, L.L. Warnet, R. Akkerman, On crystallisation and fracture toughness of poly(phenylene sulphide) under tape placement conditions, Plastics, Rubber and Composites. 42 (2013) 282–288. https://doi.org/10.1179/1743289812Y.0000000039.
[30] A. Saleem, L. Frormann, A. Iqbal, High Performance Thermoplastic Composites: Study on the Mechanical, Thermal, and Electrical Resistivity Properties of Carbon Fiber-Reinforced Polyetheretherketone and Polyethersulphone, Polymer Composites. 28 (2007) 785–796. https://doi.org/10.1002/pc.
[31] G.M.K.K. Ostberg, J.C. Seferis, Annealing Effects on the Crystallinity of Polyetheretherketone (PEEK) and Its Carbon Fiber Composite, Journal of Applied Polymer Science. 33 (1987) 29–39. https://doi.org/10.1002/app.1987.070330103.
[32] P.R.. Barnett, S.A. Young, D. Penumadu, Chopped Carbon Fiber Reinforced Thermoplastic Composites, in: American Society for Composites 32nd Annual Technical Conference, DEStech Publications, Inc., West Lafayette, IN, 2017.
[33] W.C. Oliver, G.M. Pharr, An improved technique for determining hardness and elastic modulus using load and displacement sensing indentation experiments, Journal of Materials Research. 7 (1992) 1564–1583. https://doi.org/10.1557/JMR.1992.1564.
[34] M. Rodríguez, J.M. Molina-Aldareguía, C. González, J. Llorca, A methodology to measure the interface shear strength by means of the fiber push-in test, Composites Science and Technology. 72 (2012) 1924–1932. https://doi.org/10.1016/j.compscitech.2012.08.011.
[35] S.G. Kravchenko, D.E. Sommer, B.R. Denos, A.J. Favaloro, C.M. Tow, W.B. Avery, R.B. Pipes, Tensile properties of a stochastic prepreg platelet molded composite, Composites Part A: Applied Science and Manufacturing. 124 (2019) 105507. https://doi.org/10.1016/j.compositesa.2019.105507.

[36] D.J. Edwards, R. V. León, T.M. Young, F.M. Guess, K.A. Crookston, Comparison of two wood plastic composite extruders using bootstrap confidence intervals on measurements of sample failure data, Quality Engineering. 25 (2012) 23–33. https://doi.org/10.1080/08982112.2012.728496.
[37] J.E. Spruiell, C.J. Janke, S.W. Case, K.L. Reifnider, A review of the measurement and development of crystallinity and its relation to properties in neat PPS and its fiber reinforced composites, 2004. https://doi.org/10.2172/885940.
[38] P.C. Dawson, D.J. Blundell, X-ray data for poly (aryl ether ketones), Polymer. 21 (1980) 577–578.
[39] J.M. Kenny, A. Maffezzoli, Crystallization kinetics of poly(phenylene sulfide) (PPS) and PPS/carbon fiber composites, Polymer Engineering & Science. 31 (1991) 607–614. https://doi.org/10.1002/pen.760310812.
[40] J. Deporter, D.G. Baird, The Effects of Thermal History on the Structure/Property Relationship in Polyphenylenesulfide/Carbon Fiber Composites, Polymer Composites. 14 (1993) 201–213. https://doi.org/10.1002/pc.750140305.
[41] J.J. Scobbo, C.R. Hwang, Annealing effects in poly(phenylene sulfide) as observed by dynamic mechanical analysis, Polymer Engineering and Science. 34 (1994) 1744–1749. https://doi.org/10.1002/pen.760342305.
[42] G.P. Desio, L. Rebenfeld, Crystallization of fiber-reinforced poly(phenylene sulfide) composites. I. Experimental studies of crystallization rates and morphology, Journal of Applied Polymer Science. 44 (1992) 1989–2001. https://doi.org/10.1002/app.1992.070441114.
[43] P.P. Parlevliet, H.E.N. Bersee, A. Beukers, Residual stresses in thermoplastic composites - a study of the literature. Part III: Effects of thermal residual stresses, Composites Part A: Applied Science and Manufacturing. 38 (2007) 1581–1596. https://doi.org/10.1016/j.compositesa.2006.12.005.
[44] M. Greisel, J. Jäger, J. Moosburger-Will, M.G.R.R. Sause, W.M. Mueller, S. Horn, Influence of residual thermal stress in carbon fiber-reinforced thermoplastic composites on interfacial fracture toughness evaluated by cyclic single-fiber push-out tests, Composites Part A: Applied Science and Manufacturing. 66 (2014) 117–127. https://doi.org/10.1016/j.compositesa.2014.07.010.
[45] L.T. Harper, T.A. Turner, N.A. Warrior, C.D. Rudd, Characterisation of random carbon fibre composites from a directed fibre preforming process: The effect of tow filamentisation, Composites Part A: Applied Science and Manufacturing. 38 (2007) 755–770. https://doi.org/10.1016/j.compositesa.2006.09.008.
[46] M. Holmes, Recycled carbon fiber composites become a reality, Reinforced Plastics. 62 (2018) 148–153. https://doi.org/10.1016/j.repl.2017.11.012.
[47] Y. Wan, J. Takahashi, Tensile properties and aspect ratio simulation of transversely isotropic discontinuous carbon fiber reinforced thermoplastics,

Composites Science and Technology. 137 (2016) 167–176. https://doi.org/10.1016/j.compscitech.2016.10.024.
[48] D.U. Shah, P.J. Schubel, On recycled carbon fibre composites manufactured through a liquid composite moulding process, Journal of Reinforced Plastics and Composites. 35 (2015) 533–540. https://doi.org/10.1177/0731684415623652.
[49] K.H. Wong, T.A. Turner, S.J. Pickering, Challenges in Developing Nylon Composites Commingled With Discontinuous Recycled Carbon Fibre, ECCM16 - European Conference on Composite Materials. (2014) 22–26. https://doi.org/10.1007/s002030050525.
[50] J. Wölling, M. Schmieg, F. Manis, K. Drechsler, Nonwovens from Recycled Carbon Fibres - Comparison of Processing Technologies, Procedia CIRP. 66 (2017) 271–276. https://doi.org/10.1016/j.procir.2017.03.281.
[51] G. Nicoletto, E. Riva, A. Stocchi, Mechanical Characterization of Advanced Random Discontinuous Carbon/Epoxy Composites, Materials Today: Proceedings. 3 (2016) 1079–1084. https://doi.org/10.1016/j.matpr.2016.03.052.
[52] P. Feraboli, E. Peitso, T. Cleveland, P.B. Stickler, F. Deleo, T. Cleveland, P.B. Stickler, Characterization of prepreg-based discontiuous carbon fibre/epoxy systems, Journal of Reinforced Plastics and Composites. 28 (2009) 1191–1214. https://doi.org/10.1177/0731684408088883.

Roles

Philip Barnett: Conceptualization, Methodology, Software, Formal analysis, Writing – Original draft, Visualization; **Stephen Young:** Writing – Original draft, Investigation, Formal analysis; **Vivek Chawla:** Investigation, Methodology, Formal analysis; **Darren Foster:** Investigation; **Dayakar Penumadu:** Supervision, Project administration, Funding acquisition, Writing – Review & editing

CHAPTER IV. PREDICTION OF STRENGTH AND MODULUS IN DISCONTINUOUS FIBER COMPOSITES CONSIDERING STOCHASTIC MICROSTRUCTURE

A version of this chapter is in preparation for publication by Philip R. Barnett, Stephen A. Young, Neel Patel, and Dayakar Penumadu:

Abstract

Modeling the mechanical behavior of discontinuous fiber composites has long been a challenge for the composites community. Micromechanical models typically predict the stiffness accurately, but good strength models have been largely elusive due to their highly stochastic microstructure. This paper presents a novel stiffness and strength laminate analogy model for discontinuous fiber composites using stochastic fiber orientation, length, fiber volume fraction, and void volume fraction. For the first time, the master ply invariant approach has been applied to discontinuous fiber composites and shows good agreement in modeling the stiffness. A strain energy density based terminating condition was developed that successfully predicts the tensile strength of these composites. The results of this work make accurate, first-order strength and stiffness predictions possible for discontinuous fiber composites with simple constituent properties readily obtained from material datasheets.

Introduction

It is well-known that the mechanical properties of fiber-reinforced composites vary significantly with fiber orientation. As such, in continuous fiber composite laminates, it is of utmost importance that the stacking sequence is exactly as prescribed concerning both ply location and orientation to achieve the predicted properties. Unlike continuous fiber composites, discontinuous fiber composites often do not exhibit a regularly repeating microstructure. Therefore, it is much more difficult to model their mechanical properties. It is known that the mechanical properties are strongly influenced by fiber orientation, fiber volume fraction, and fiber length[1]. Due to the large number of fibers present in chopped fiber-reinforced composites, it is not feasible to measure these properties as inputs to a model at the single fiber level for large parts. Instead, fiber orientation and length distributions are commonly used to approximate the local microstructure and then normalized over the part volume[2]. Furthermore, it has been shown that the strength and modulus of discontinuous fiber composites are strongly thickness-dependent[3,4]. Thinner samples typically achieve lower mechanical properties as local inhomogeneities that span a larger portion of the thickness of the sample have a larger effect on the global properties. Thicker samples reduce the likelihood of local inhomogeneities occurring that span the entire thickness of the sample. As such, knowledge of the local microstructure is of the utmost importance when attempting to predict the mechanical properties in the presence of local inhomogeneity.

Much of the previous work on the prediction of the modulus of short fiber composites has sought to develop micro-mechanical models that assume a simple, repeating microstructure that can then be used to model local regions in a

randomly oriented composite. There exist several empirical and semi-empirical methods for predicting the modulus of short fiber composites. For example, the Halpin-Tsai equations are a semi-empirical method that can be used to calculate the modulus of aligned discontinuous fiber composites using the fiber aspect ratio and elastic properties of the constituent materials[5]. This method has often been combined with composite laminate theory to estimate the stiffness of composites with random orientation. Micro-mechanics-based shear lag methods such as that proposed by Cox provide an estimate of the modulus longitudinal to aligned discontinuous fibers by considering a representative volume element consisting of a single fiber in a sheath of matrix[6]. Other models are strictly empirical, based only on fiber and matrix modulus using a rule-of-mixtures approach[7,8]. One such simple empirical model developed by Chamis is based on the rule-of-mixtures is unique in that it accounts for the void fraction[9]. Self-consistent models use the Eshelby inclusion method to approximate the stiffness of a dilute composite containing ellipsoidal inclusions and can be used for non-dilute composites by updating the stiffness of the surrounding matrix in an iterative scheme[10]. These models can also account for void content, by considering multiple inclusion phases. Historically, each of these methods gives reasonably-accurate modulus estimates, but strength estimates have been much more elusive.

Traditionally, the prediction of the strength of discontinuous fiber composites has been approached using empirical models that account for fiber length and orientation distributions used to generate an equivalent laminate[1,11–14]. Often, these properties are measured in a specific region and then assumed to be representative of the entire part. However, strength is largely dependent on local inhomogeneity in fiber-reinforced composites. Therefore, some have focused on developing representative volume elements (RVEs) that can be adjusted based on local properties to predict the strength of discontinuous fiber composite structures[15,16]. The local volume fraction and orientation data are generally gathered by destructive processes such as cross-sectioning and matrix pyrolysis[17,18]. More recent work utilizing x-ray computed tomography shows promise as a non-destructive way of evaluating microstructure properties such as fiber length and orientation to form RVEs[19–21]. With this knowledge, the tensile modulus of platelet-based discontinuous fiber composites has been predicted, though strength predictions require additional extensive mechanical testing, thereby adding additional cost and time to generating reliable predictions of mechanical properties[21]. Furthermore, if there is significant flow during processing, the platelet morphology breaks down, thereby making the generation of appropriate RVEs much more difficult. Other problems associated with modeling platelet-based composites via x-ray computed tomography are as follows: the process is very time-intensive, only small samples can be analyzed, and variability between molded parts may be significant as input platelet orientation is unlikely to be repeatable. As such, a more ideal material format for analysis via x-ray imaging would consist of a microstructure that does not flow and shows little part-to-part variation. Such a format would also be expected to yield composites with greater

homogeneity of microstructure and mechanical properties. One such format, nonwoven carbon fiber preforms produced via carding processes, is a good candidate material, as the local microstructure is quite comparable to the global microstructure and the high level of interconnectedness between fibers is not conducive to material flow during processing.

In addition to knowledge of the local fiber properties, a failure model must be adopted to predict the strength of discontinuous fiber composites. As these composites often exhibit progressive failure modes, continuum damage mechanics (CDM) has proven to be an effective strategy for modeling the failure of discontinuous fiber composites[22–24]. In short, CDM uses a continuous damage variable to degrade the stiffness of a material subjected to stresses inducing damage as determined by a failure theory. Recent work by Shokrieh and Moshrefzadeh-Sani showed that CDM applied to an equivalent laminate whose properties were defined by the Halpin-Tsai equations and existing micro-mechanical models for the prediction of the strength of oriented short fiber composites showed good agreement with experimental results[24]. The appeal of their model is that only the properties of the constituent materials are required as an input for strength predictions, as opposed to utilizing extensive mechanical testing to characterize the failure behavior. However, this model fails to account for inhomogeneities such as local variations in fiber volume fraction and the inclusion of voids that may significantly affect the mechanical properties. Furthermore, their model was idealized for randomly oriented composites and did not include an evaluation of the actual microstructure.

The present paper describes a new micro-mechanical model combined with CDM to predict the strength and modulus of discontinuous fiber composites where the local stochastic microstructure details are gathered via x-ray computed tomography and optical microscopy. To illustrate the applicability of this model to a variety of composites, two types of nonwoven carbon fiber preform were considered: carded recycled fibers and wet-laid virgin fibers. Semicrystalline and amorphous thermoplastic matrices, as well as a thermoset epoxy, were studied. Thermoplastic organosheet laminae were produced and subsequently compression molded to form composite plates. Epoxy-matrix parts were produced in a single step using compression molding. The tensile properties of the composites were studied at both the organosheet lamina and composite laminate scale to evaluate the model. The use of three significantly-different matrix types indicates that this model provides a robust way of predicting composite performance based on the constituent properties without the need for extensive composite material characterization. The model was then used to predict the unidirectional properties of an epoxy composite for the calculation of the properties of a multi-directional laminate.

Materials and Methods

Matrix Materials (PPS, ABS, Epoxy)

Polyphenylene sulfide films of 0.127 mm nominal thickness were purchased (Ryton AQ200P, Solvay). This material is of particular interest to the automotive industry due to its high-temperature stability, inherent flame resistance, and good chemical resistance[25]. PPS is typically rated for low-stress applications up to 240 °C and when used as the matrix in a continuous carbon fiber composite shows no significant drop in tensile properties at 120 °C[26]. Furthermore, PPS can be bonded using resistance welding techniques to additively build complex structures and reduce the number of fasteners required for assembly. PPS is a semicrystalline thermoplastic, wherein the mechanical properties can be tuned through process-induced crystallization controlled by cooling rates and post-process annealing. Samples produced using PPS were compression molded per previous work by the author.

Acrylonitrile butadiene styrene films of 0.127 mm nominal thickness were purchased (Cycolac EXABS01, Sabic). This material is commonly used in the automotive industry in the form of bumper covers and other injection-molded plastic components. ABS does not offer the chemical resistance or high-temperature performance of PPS but is considerably cheaper. ABS is an amorphous thermoplastic that does not crystallize due to annealing or changes in the cooling rate. Samples produced using ABS were preheated for 5 minutes on at mold at 210 °C and then compression molded for 10 minutes under 1 MPa pressure.

A two-part structural epoxy system was also used as a matrix material (Epikote Resin 862/Epikure Curing Agent W, Resolution Performance Products). This system is typically used in the civil engineering industry, offering low-cost, high mechanical performance, and good chemical resistance. Samples were produced via a wet-compression setup, in which the fibrous preforms were first wetted with epoxy and then compressed at 1 MPa in a hydraulic press to cure at the manufacturer's recommended cure schedule. An additional sample was made using 0.1 MPa pressure and laminate sequence of [90/0/90/90/90] to validate the model against a range of fiber volume fractions and orientations.

Nonwoven Carbon Fibers

Two nonwoven carbon fiber reinforcements were studied: recycled and virgin fiber preforms. The recycled carbon fibers (rCF) were provided in the form of a nominal 200 gm^{-2} mat (measured 184.2 ± 11.2 g m^{-2}) produced using a carding process. The carding process involves mechanical entanglement and orienting of fibers using a series of combs. The virgin fibers (vCF) were provided in the form of a nominal 300 gm^{-2} mat (measured 310.0 ± 6.6 g m^{-2}) produced using a wet deposition process. The wet deposition process is similar to papermaking, in that the fibers are mixed in a water slurry, deposited on a screen, and dried. Single filament testing of the carbon fibers was performed on an MTS Nano Bionix

Universal Testing System (Nano UTM) affording load resolution of 50 nN and displacement resolution of 0.1 nm. Forty individual carbon fiber filaments of each type were mounted on tabs based on ASTM C 1557-03 and ISO 11566:1996 standards with modifications to account for template bending and fiber alignment described in detail elsewhere [1-4]. The diameter of each filament was examined using a polarized optical microscope (Olympus BX53M) and measured using a commercial image processing software (Olympus Stream Start) before mechanical testing. Additional fiber samples were coated with gold (Au) using a sputter coater (SPI Module, Structure Probe, Inc.) and the cross-section of the fibers was examined using a scanning electron microscope (Leo 1525 SEM, LEO Electron Microscopy, Inc.) with accelerating voltage of 4 kV and an in-lens detector. The templates with 10 mm gauge length were loaded in tension at a strain rate of 0.0001 s^{-1} until mechanical failure where modulus, failure strength, and corresponding failure strain were recorded. The modulus values were calculated between 0.1% and 0.6% strain.

Composite Mechanical Testing

Tensile testing was completed at room temperature according to ASTM D3039. Specimens were loaded to failure using an MTS 858 load frame with a 25 kN load cell, with true strain measurements taken using an extensometer having a gauge length of 25.4 mm. The sample dimensions were nominally 100 mm X 12.7 mm X 2.0 mm. G-10 fiberglass tabs were utilized in the grip region to promote failure in the gauge length, and the gripping pressure was set to 5.5 MPa. A constant deformation control tensile test was performed at a displacement rate of 2 mm min^{-1}. Samples prepared with all lamina oriented in the machine and cross directions of the nonwoven roll were tested. The Poisson's ratio of at least one sample from each orientation was measured using digital image correlation (DIC). An average value was calculated over the entire surface of the sample to avoid strain localization due to inhomogeneity.

Shear testing was completed according to ASTM D5379. DIC was used to measure surface strains throughout testing. G-10 fiberglass tabs were utilized in the load region to prevent end crushing. Force data gathered from the load frame was correlated with the DIC images taken at the same frequency to evaluate the stress-strain behavior. DIC images were analyzed using the VIC 3D software (Correlated Solutions).

Optical Microscopy

The microstructure of the composites was characterized using optical microscopy of cross-sections of failed specimens (Keyence, model VHX-7100). Previously tested specimens were cut near the failure region, mounted in epoxy, and polished. Images were converted to binary using a Fiji routine to segment the fibers and voids. The resulting images were imported into a custom MATLAB script for pixel counting. The pixel counts were used to identify the local fiber and void volume fractions for the composite. An example of this process is provided in

Figure IV-1. To gather data about the local volume fraction in the composite, this process was employed across 100 pixel X 100 pixel regions in the image, which corresponds to approximately 104 μm X 104 μm.

X-ray Computed Tomography

X-ray computed tomography (XCT) of the dry fiber preforms was completed using a laboratory source (Hamamatsu, model L9421-02) and detector (Varex, model 1622). Voxel resolution was 22 μm^3, which allows imaging of a 12.7 mm X 76 mm region that is the same size as the region of the tensile bars between the tabs. A minimum of two samples were scanned from each dry fiber preform. The fiber orientation of the resulting images was identified using the Directionality plugin for the ImageJ/Fiji image analysis software[27,28]. The XCT images were transformed into slices through the thickness of the composite for which the planar fiber orientation was determined. The overall orientation was identified as the average of all of the planar images, as described by Fleigner et al[19]. To confirm that the orientation of the dry fiber preform was representative of the composite, two consolidated samples of carbon fiber/PPS approximately 40 mm X 40 mm in size were mounted in epoxy and polished through the thickness. The fiber orientation was measured using the same method as for the XCT specimens. The samples were then ground at least one organosheet thickness and polished for image analysis at a second depth in the samples to confirm that the orientation was consistent from layer to layer. Figure IV-2 shows an example image of a polished sample and the corresponding orientation.

Strength and Modulus Predictions

The strength and modulus of discontinuous carbon fiber organosheet composites with a stochastically measured microstructure were predicted using an equivalent digital laminate method that failed according to a continuum damage mechanics model. The material properties necessary for evaluation of the model are found in Table IV-1. It was assumed that the matrix materials behaved as an isotropic medium, allowing the calculation of the matrix shear modulus and strength from the tensile properties. To produce a digital laminate, the properties of individual lamina representative of the local microstructure were estimated from the average fiber orientation from the XCT and microscopy images and the local fiber and void volume fractions obtained via optical microscopy. Each lamina was assumed to consist of unidirectional short fibers of length, fiber volume fraction, and orientation chosen randomly from the measured stochastic properties. Then, composite laminate theory was used to determine the stiffness and failure behavior of the composites. A MATLAB program was written to perform the following calculations.

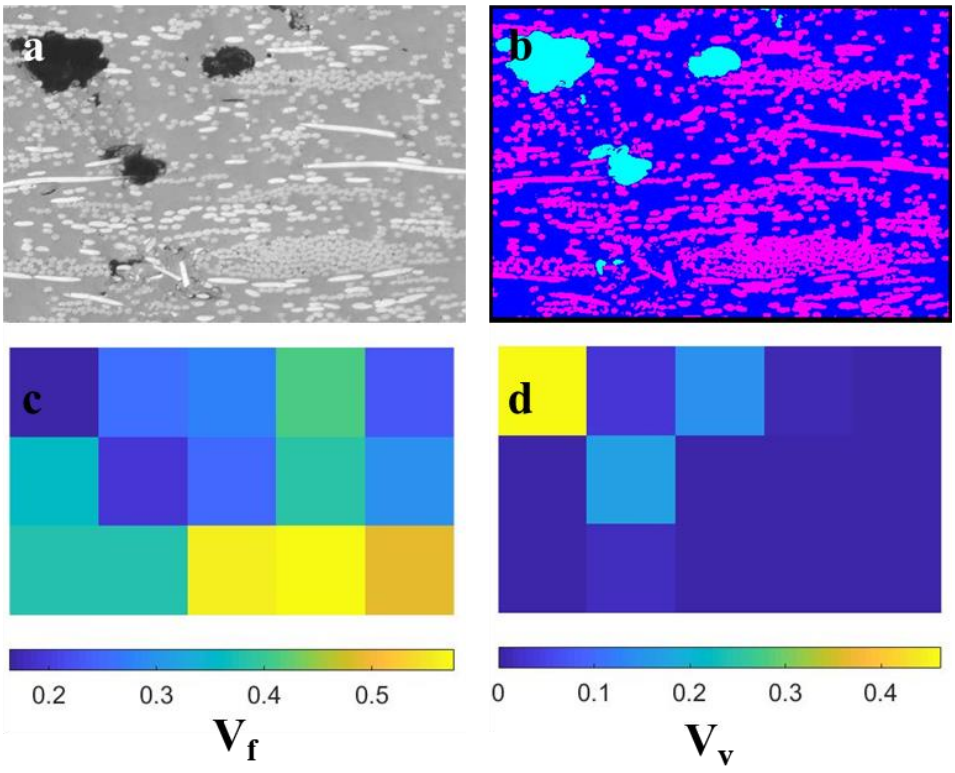

Figure IV-1. a) Raw image; b) image of segmented fibers and voids; c) local fiber volume fraction of 100 X 100 pixel subdomains; d) local void volume fraction of 100 X 100 pixel subdomains

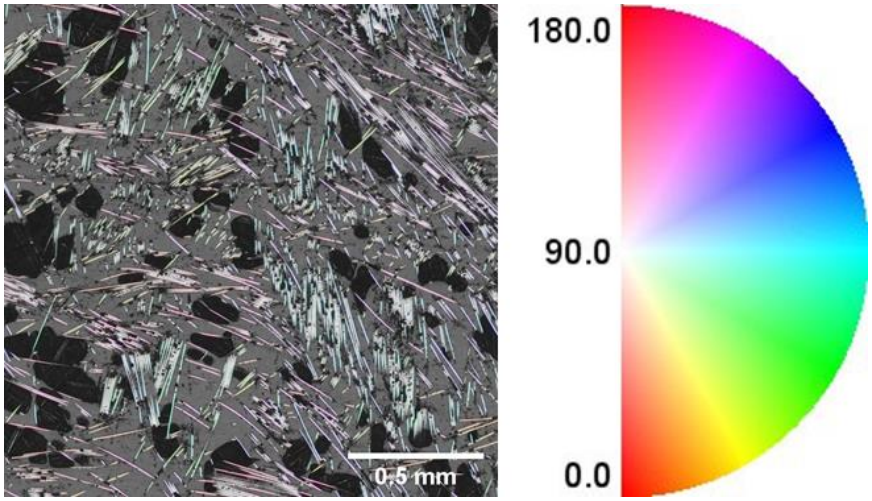

Figure IV-2. Example optical micrograph showing fiber orientation of recycled carbon fiber composites (color bar in degrees)

Table IV-1. Mechanical properties input into the model

Property	Material	Value
Longitudinal Elastic Modulus	Recycled Carbon Fiber	206 GPa
	Virgin Carbon Fiber	197 GPa
	ABS	2.0 GPa*
	PPS	3.4 GPa*
	Epoxy	2.7 GPa*
Tensile Strength	Recycled Carbon Fiber	4426 MPa
	Virgin Carbon Fiber	3302 MPa
	ABS	39 MPa*
	PPS	80 MPa*
	Epoxy	79 MPa*
Tensile Failure Strain	Recycled Carbon Fiber	0.020
	Virgin Carbon Fiber	0.017
	ABS	0.320*
	PPS	0.040*
	Epoxy	0.071*
Poisson's Ratio	Carbon Fiber	0.20**
	ABS	0.35***
	PPS	0.38***
	Epoxy	0.35***
Interfacial Shear Strength	rCF/ABS	5.74 MPa
	rCF/PPS	14.58 MPa
	vCF/PPS	12.59 MPa
	rCF/Epoxy, 1 MPa	13.87 MPa
	rCF/Epoxy, 0.1 MPa	15.88 MPa

*Value from manufacturer datasheet
**Value estimated from [29]
***Value estimated based on typical values for similar materials

Each digital lamina consisted of discontinuous aligned fibers with a thickness of the average matrix sheath. The Cox shear lag model was used to predict the stiffness in the fiber direction:

$$E_1 = E_{1f} V_f \eta_L + V_m E_M \tag{1}$$

$$\eta_L = 1 - \frac{\tanh(ns)}{ns} \tag{2}$$

$$n = \sqrt{2 \frac{G_m}{E_{1f} \log\left(\frac{r_m}{r_f}\right)}} \tag{3}$$

$$s = \frac{L_f}{2r_F} \tag{4}$$

where V_f is the fiber volume fraction, V_m is the matrix volume fraction, E_{1f} is the modulus of the fiber in the longitudinal direction, G_m is the matrix shear modulus taken as $G_m = E_m/(2(1+v_m))$, L_f is the fiber length, r_f is the fiber radius, and r_m is the radius of the sheath of matrix around the fiber in the RVE taken as $r_m = r_f/\sqrt{Vf}$. The average fiber length was measured as 38.8 mm for the recycled fibers and 28.8 mm for the virgin fibers from at least 100 measurements taken from an image taken on a flatbed scanner. The fiber length distribution is shown in Figure IV-3. The fiber length varied much more in the recycled fiber preforms due to fiber breakage that occurred during the carding process. In modeling each lamina, the fiber length was chosen from this distribution at random. Fibers that would extend beyond the tensile bar dimensions (e.g., a fiber oriented 90° from the loading axis and longer than the 12.7 mm tensile bar width) were shortened accordingly. From geometry, the fiber length in a given lamina where the length would exceed the tensile dimensions was $L_f = W/\sin\Theta$ where W is the width of the sample and Θ is the angle with respect to the loading direction. As a result, larger specimen sizes would yield longer fibers and therefore improved mechanical properties.

The stiffness of the transverse and shear directions was calculated using the master ply invariant-based approach described by Tsai and Melo[30]. This theory is particularly powerful, as it has shown that the elastic properties of unidirectional carbon fiber composites made with both thermoplastic and thermoset matrices can be described knowing only the stiffness in one direction and using a trace normalization approach to determine the remaining stiffness values. For the master ply, the ratio of $E_1/Tr(Q)$ is 0.880, the ratio of $E_2/Tr(Q)$ is 0.052, and the ratio of $G_{12}/Tr(Q)$ is 0.031, where Tr(Q) refers to the trace of the stiffness matrix. Recent work by Arteiro et al. has applied micro-mechanics to predict the stiffness of continuous fiber composites using the master ply theory with success[31]. However, to this point, the master ply concept has not been

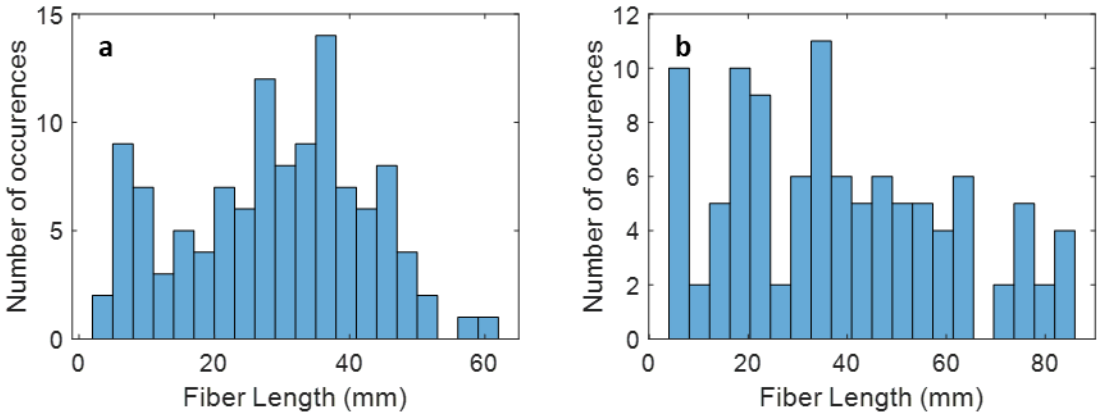

Figure IV-3. a) Fiber length distribution of virgin fiber composites; b) Fiber length distribution of recycled fiber composites

applied to discontinuous fiber composites. Here, the master ply concept is applied to determine the transverse and shear modulus using the longitudinal modulus E_1 predicted using the Cox shear lag model. The Poisson's ratio of each digital lamina was then calculated using the rule of mixtures:

$$\upsilon_{12} = \upsilon_{12f} V_f + \upsilon_m V_m \tag{5}$$

where v_{12f} is the fiber Poisson's ratio and v_m is the matrix Poisson's ratio.

The orientation of the lamina was selected at random from the measured fiber orientation distribution. This process was repeated several times until the organosheet thickness was achieved. The thickness of each lamina was chosen to be equal to the diameter of an RVE with the mean fiber volume fraction.

Once the microstructure-informed lamina properties were attained, composite laminate theory was used to predict the stiffness of the laminate. Unidirectional stress was incrementally applied and at each step, the Tsai-Hill failure criterion was used to determine if any of the microstructure-informed laminae had failed:

$$1 < \left(\frac{\sigma_1}{F_1}\right)^2 + \left(\frac{\sigma_2}{F_2}\right)^2 + \left(\frac{\tau_{12}}{F_{12}}\right)^2 - \frac{\sigma_1 \sigma_2}{F_1^2} \tag{6}$$

where the subscripts *1* and *2* denote the principal stresses in the lamina and F_i denotes the failure stresses in the *i*-direction. The failure stresses were identified as follows:

$$F_1 = \frac{E_x \sigma_f}{E_f} \frac{1}{1 - \operatorname{sech}\left(\frac{L_{fc}}{2}\sqrt{\frac{E_m}{E_f r_f (r_m - r_f)(1+\upsilon_m)}}\right)} \tag{7}$$

$$F_2 = \sigma_m \left(1 - 2\sqrt{\frac{V_f}{\pi}}\right) \tag{8}$$

$$F_{12} = \frac{\sigma_m}{\sqrt{3}} \tag{9}$$

where L_{fc} is the critical fiber length defined as $L_{fc} = r_f \sigma_f / \tau_i$ where τ_i is the interfacial shear strength. The interfacial shear strength used in determining the longitudinal failure stress was measured in accordance with the author's previous work. If the void content, V_v, in the lamina was greater than the fiber volume fraction, the following strength reductions were applied to those calculated in equations (10)-(12):

$$F_1 = \sigma_1 \left(1 - \pi \left(\frac{3}{4\pi} \right)^{\frac{2}{3}} V_v^{\frac{2}{3}} \right) \quad (10)$$

$$F_2 = \sigma_2 \left(1 - \pi \left(\frac{3}{4\pi} \right)^{\frac{2}{3}} V_v^{\frac{2}{3}} \right) \quad (11)$$

$$F_{12} = \tau_{12}(1 - V_v) \quad (12)$$

The longitudinal and transverse strength reduction factors were chosen following the work of Eudier[32], while the shear strength reduction factor was based on a simple rule of mixtures.

Once a layer was damaged, the mechanical properties of the preform were reduced to update the damage variable. This reduction was chosen based upon the failure type. Fiber failure occurred when the longitudinal term of equation (6) dominated, while matrix failure occurred when the remaining terms dominated. When fiber failure first occurred, the fibers were modeled to all break to their critical length and the Cox shear lag model was used to update the longitudinal modulus, followed by updating the transverse and shear moduli using the master ply theory. Matrix damage and subsequent fiber failure modes were modeled by the debonding of fibers in the unidirectional plies. The ply fiber volume fraction was decreased by a percentage chosen by generating a random number between 0 and 1. This is analogous to fibers debonding from the matrix and being unable to transfer load. The Cox shear lag model was then used to update the longitudinal elastic modulus and the master ply approach was applied to update the other elastic constants of the reduced-stiffness composite. The Poisson's ratio was updated as in equation (5).

After each iteration, the damage variable, D, was updated according to D = 1-√(E/E0) where E is the reduced laminate stiffness in the load direction and E0 is the undamaged laminate stiffness. In the next iteration, the effective stress was calculated as $\sigma_{eff} = \sigma/(1-D)$. The effective stress was then applied to the undamaged laminate, assuming strain energy equivalence between the damaged and undamaged laminates. This process was repeated until failure.

The composite was determined to have failed once the stain energy density of the virtual test was equal to the strain energy density calculated using a modified rule of mixtures:

$$u_c = \frac{(1 - V_f) u_{m^*}}{(1 - V_f) u_{m^*} + V_f u_f} \quad (13)$$

where u_f is the strain energy density of the fiber and u_{m^*} is the modified strain energy density of the matrix. The strain energy densities are calculated as:

$$u_{m^*} = \frac{1}{2}\frac{\sigma_m^2}{E_m} + \sigma_m\left(\varepsilon_{ult} - \frac{\sigma_m}{E_m}\right)(1-\phi) \quad (14)$$

$$u_f = \frac{1}{2}\sigma_f \varepsilon_f \quad (15)$$

where ε_{ult} is the tensile failure strain of the polymer matrix and ϕ represents the proportion of plies oriented ± 35° from the loading axis. The limit angle was chosen such that the stiffness of the average ply was half of the longitudinal value. This additional term was chosen such that the fiber dominant direction would exhibit less plasticity than the matrix dominant direction, as has been observed in experiments. The matrix was treated as an elastic, perfectly plastic material, while the fibers were treated as a perfectly elastic material for strain energy density calculations. Since the shear strain energy density is not easily found using datasheet values, the shear terminating condition was chosen to be when half of the plies had failed.

Three load cases were considered for the composites: longitudinal tension, transverse tension, and shear. These load cases were applied to virtual samples in the cross and machine-directions. Multiple simulations of each sample were run to generate an average result due to the stochastic nature of the stiffness degradation and input properties. A sensitivity study was used to determine the appropriate number of simulations. Then, to illustrate the applicability of this model, the virtual properties were generated for the plies of a multidirectional laminate, which was predicted using composite laminate theory, as has been shown to describe this type of material in the author's prior work. A first ply failure method using the Tsai-Hill failure criterion was implemented. A Monte Carlo simulation was run using the stochastically-generated properties to generate a distribution of expected tensile properties.

Results and Discussion

Single Fiber Tensile Testing

The recycled carbon fibers exhibited mechanical properties typical of aerospace-grade fibers such as AS4, indicating a high-quality feedstock for the recycling process. The single fiber properties are described in Table IV-1. The recycled fiber diameter was measured to be 7.30 ± 0.23 µm. The tests indicate that the mechanical properties of the fibers are near those of typical virgin carbon fibers. The pyrolysis-based recycling process ensures that the fibers are free of sizing, which may negatively impact interface strength for thermoplastic matrices.

The virgin carbon fibers exhibited properties typically found in standard modulus fibers. Their diameter was measured to be 7.90 ± 0.19 µm. The modulus was slightly lower than the recycled fibers, while the strength was significantly lower. The strain-to-failure of the two fiber types was quite similar. Unlike the recycled fibers, the virgin fibers were not necessarily free of sizing. Furthermore, a

binding agent was used in the wet deposition process to hold the fiber preform together, which was shown to influence the fiber-matrix interface in the composites.

Interfacial shear strength was measured by fiber push-in testing using a nanoindenter (Nanomechanics, iMicro) according to the method described by the author's prior work. At least 10 tests were completed per sample. The epoxy samples processed at different pressures were both tested, as neighboring fibers are expected to influence the interfacial shear strength in push-in tests.

Mechanical Testing

Tensile testing results are shown in Table IV-2. As expected, the organosheet orientation had a strong influence on the tensile properties, indicating that the nonwoven mats are anisotropic. The modulus is expected to be significantly affected by the fiber orientation, while the strength will have a slightly lesser effect. This can be explained by the tendency of local inhomogeneities to have a strong effect on strength, which is dominated by local flaws, as opposed to modulus, which is a global material property as measured with an extensometer. The strain-to-failure naturally decreases when more fibers are oriented longitudinal to the load, as the fiber strain-to-failure is much lower than that of the matrix. This behavior was not apparent in the rCF/ABS samples or vCF/PPS samples, indicating that the weaker fiber/matrix interface plays a significant role in strain-to-failure behavior.

Shear testing results can be found in Table IV-3. Shear modulus showed a clear dependence on the matrix elastic modulus, while shear strength correlates with both matrix and interface strength. For example, the rCF/PPS composites showed higher shear strength than vCF/PPS despite using the same matrix material.

Fiber and Void Volume Fraction

Optical micrographs reveal a variation in local fiber and void volume fraction throughout the samples studied. Figure IV-4 displays a high-resolution micrograph of an example rCF/PPS composite specimen where resin-rich regions exist that may serve as failure initiation zones. Despite these regions of local inhomogeneity, the total fiber and void volume fraction of the composite cross-section is very close to the nominal volume fractions determined by density measurements, as shown in Table IV-4. Figure IV-5 and Figure IV-6 show the histograms of the measured fiber and void volume fractions. The recycled fiber composites show a narrower range of fiber volume fraction than the virgin. Additionally, the void content of the recycled fiber composites is significantly lower than the virgin.

Fiber Orientation

The fiber orientation measured by XCT and optical micrographs was in good agreement, as shown in Figure IV-7. This indicates that the fiber orientation was not disturbed during processing into composites. In general, it is clear that the

Table IV-2. Results of experimental tensile testing

Matrix	Fiber Type	Orientation	Tensile Strength (MPa)		Tensile Modulus (GPa)		Strain-to-Failure (%)		Number of Samples
			Avg.	StDev.	Avg.	StDev.	Avg.	StDev.	
ABS	Recycled	MD	88	6.6	12	0.5	0.89	0.09	10
		CD	223	5.7	26	1.2	1.00	0.06	10
PPS	Recycled	MD	139	12.5	16	0.7	0.90	0.08	12
		CD	268	32.3	34	2.6	0.80	0.09	15
	Virgin	MD	201	12.3	26	1.8	0.81	0.10	6
		CD	139	14.7	19	2.0	0.75	0.12	6
Epoxy	Recycled	MD	150	10.3	15	0.8	1.01	0.09	10
		CD	281	14.8	32	1.1	0.88	0.05	10

Table IV-3. Results of experimental shear testing

Matrix	Fiber Type	Shear Strength (MPa)		Shear Modulus (GPa)		Strain-to-Failure (%)		Number of Samples
		Avg.	StDev.	Avg.	StDev.	Avg.	StDev.	
ABS	Recycled	68	3	5.4	0.4	1.73	0.30	8
PPS	Recycled	122	20	7.9	0.4	1.72	0.27	8
	Virgin	111	8	7.8	0.1	1.75	0.13	8
Epoxy	Recycled	143	16	6.4	0.4	2.46	0.21	9

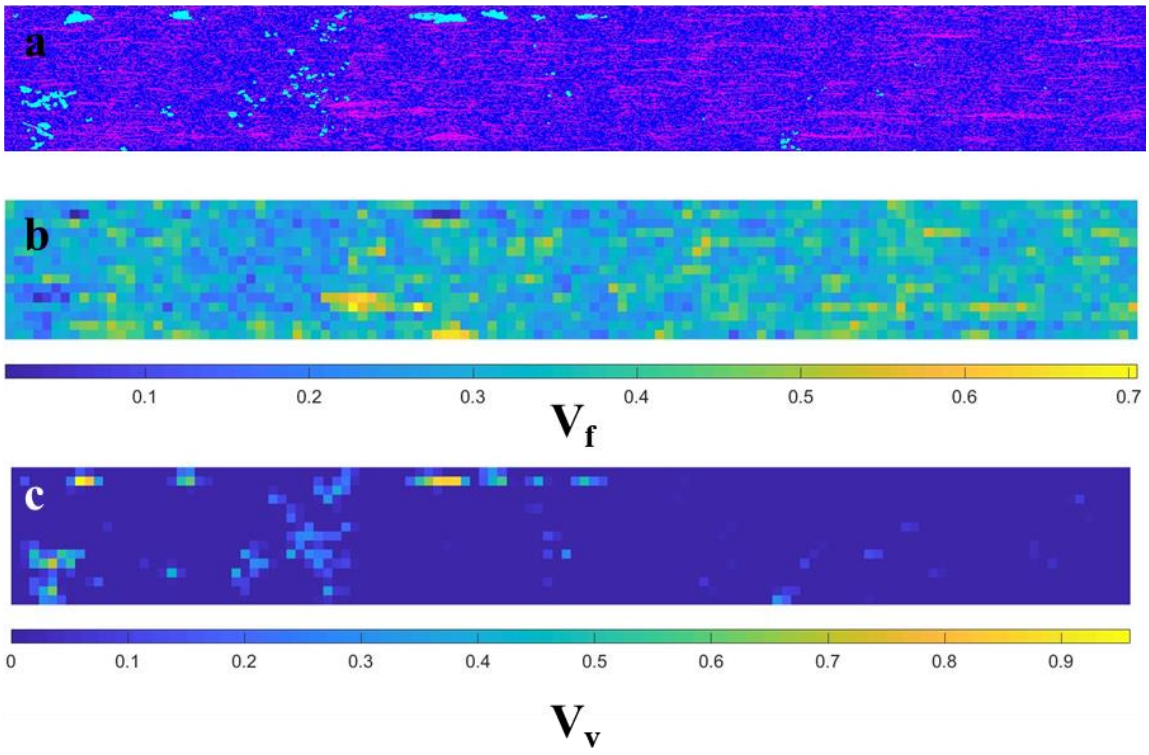

Figure IV-4. a) Segmented image show cross-section of a tensile specimen; b) Local fiber volume fraction of a tensile specimen; c) Local void volume fraction of a tensile specimen

Table IV-4. Void content analysis

Sample	Calculated Void Content (%)	Measured Void Content (%)
ABS/rCF	4.1 ± 2.6	0.7 ± 1.7
PPS/rCF	3.5 ± 2.6	5.6 ± 2.7
PPS/vCF	18.0 ± 10.7	13.0 ± 4.4
Epoxy/rCF 1 MPa	15.8 ± 2.2	15.9 ± 1.7
Epoxy/rCF 0.1 MPa	12.3 ± 2.5	13.0 ± 3.0

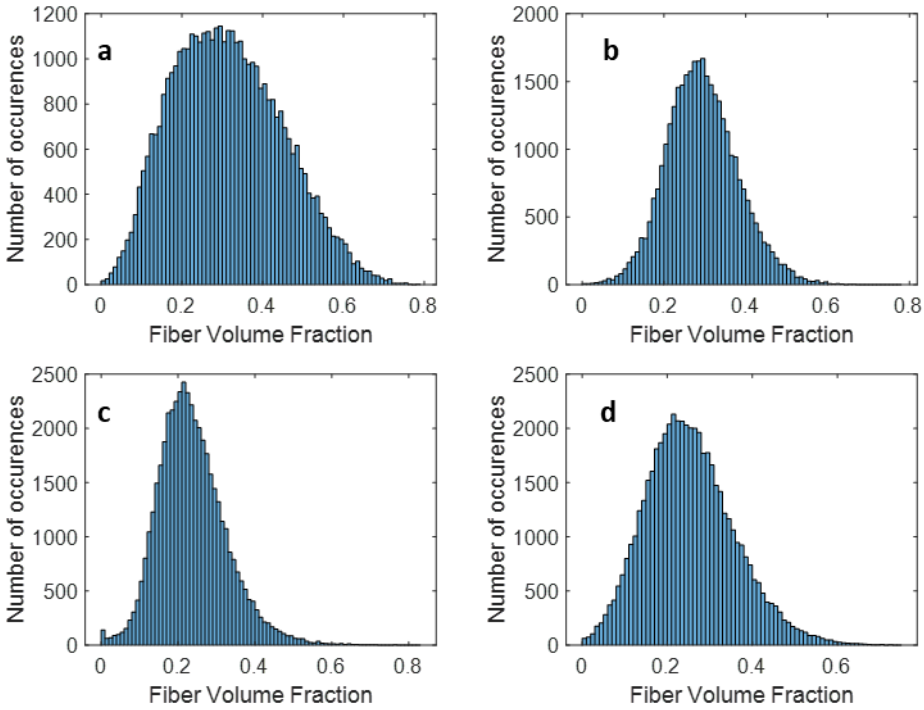

Figure IV-5. Measured fiber volume fraction distribution: a) vCF/PPS composites; b) rCF/PPS composites; c) rCF/ABS composites; d) rCF/Epoxy composites;

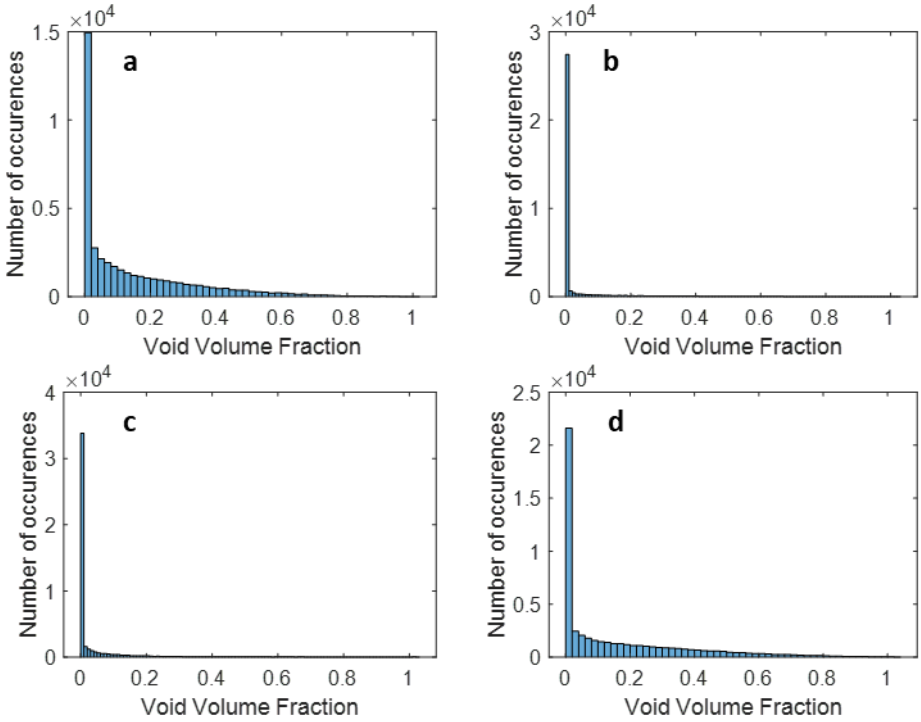

Figure IV-6. Measured void volume fraction distribution: a) vCF/PPS composites; b) rCF/PPS composites; c) rCF/ABS composites; d) rCF/Epoxy composites;

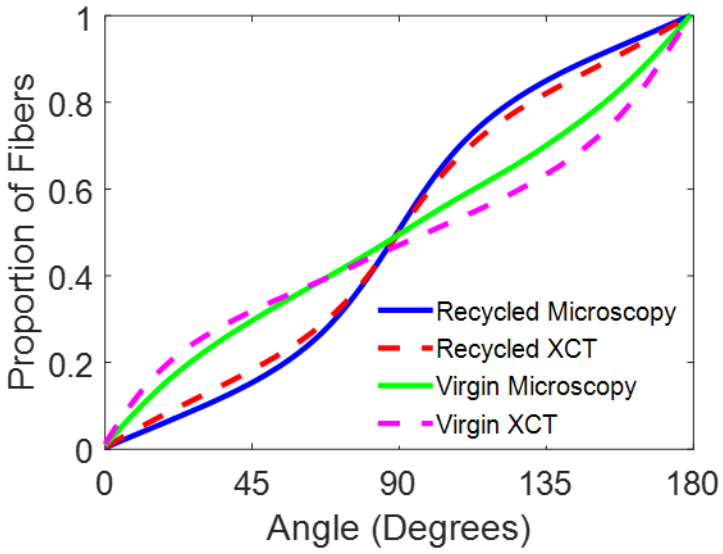

Figure IV-7. Fiber orientation distribution for recycled and virgin fiber preforms and composites

recycled fiber samples were most strongly oriented in the cross-direction, while the virgin fiber samples were oriented in the machine direction. In the calculations, the average of the microscopy and XCT behavior was used to represent the fiber orientation distribution.

Property Predictions

To determine the number of simulations required to converge to a stable solution, a sensitivity study was undertaken. The results for the normalized strength, modulus, and strain-to-failure are shown in Figure IV-8. After 100 simulations, the variation in mechanical properties indicated by the error bars representing the 95% confidence interval becomes sufficiently small that additional simulations are unnecessary. As a result, 100 simulations were run to generate the results found here.

The strength, modulus, and strain to failure of each sample type were predicted for the shear and tensile properties in both the machine and cross-directions. The results, along with the experimental results are shown in Figure IV-9. Overall agreement is very good for the tensile modulus, though a few samples were not well predicted. For example, the machine-direction vCF/PPS composite modulus was much higher in the model than was measured. This is likely explained by the high void content, which was not captured in the Cox shear lag model. Despite this limitation, the Cox model using the master ply theory provides an acceptable estimate for the modulus of organosheet composites. The tensile strength showed very good agreement with experiments. As with the modulus, the predicted vCF/PPS composite machine direction strength was higher than measured. Overall, the tensile strain behavior was less accurately predicted. However, it should be noted that experimental data was taken using an extensometer, which only captures strain data in the gauge region of the samples. As such, local inhomogeneity may yield a large variation in strain measurements.

The shear modulus of composites was generally predicted very well. However, the shear strain-to-failure and strength were generally not-well predicted. This is due to the terminating condition (i.e., 50% of the plies having failed) that was constant for all samples due to the lack of readily-available datasheet values to develop a shear strain energy density terminating condition. With additional information such as measured shear strength, shear modulus, and shear strain-to-failure for the matrix and fiber, such a condition could be developed. Despite this limitation, the predicted shear properties are reasonably close as a first estimate.

The machine and cross-direction properties of the rCF/PPS composites were also estimated using the Shokrieh model. While the modulus is in relatively good agreement with experiments, the strength and strain-to-failure are highly overestimated. This is due to their chosen terminating condition: damage to every ply. The stress-strain curves shown in *Figure **IV-10***.a show that plies oriented in the loading direction lead to large and unrealistic amounts of plasticity. As this model was originally developed for randomly oriented composites, their terminating

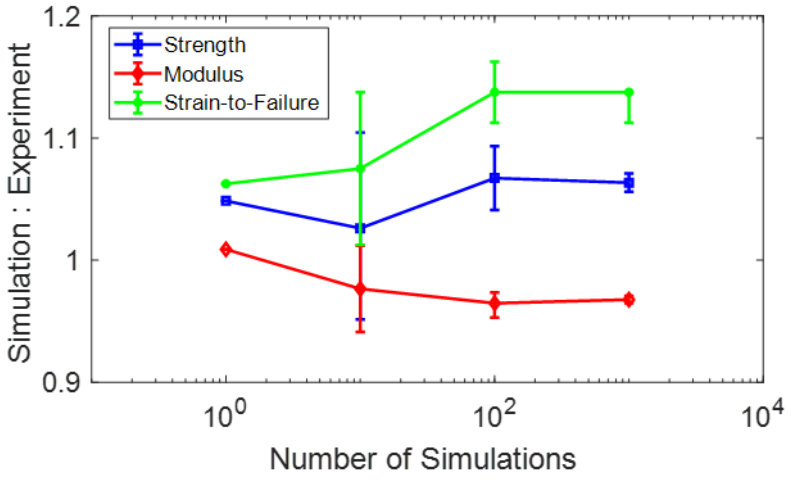

Figure IV-8. Sensitivity study for rCF/PPS cross-direction sample

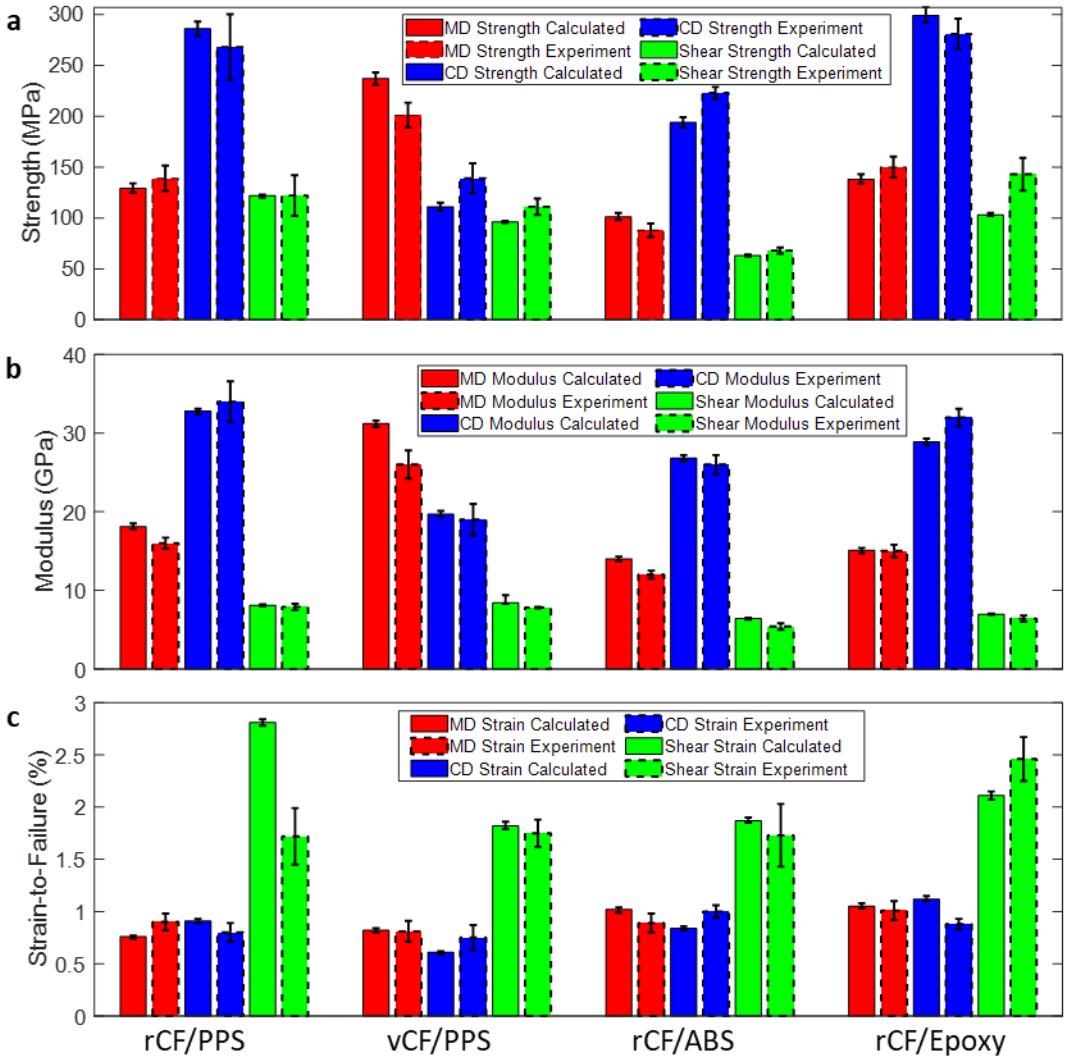

Figure IV-9. a) Strength predictions; b) Modulus predictions; c) Strain-to-Failure predictions; error bars on experiments represent one standard deviation and error bars on calculations represent the 95% confidence interval

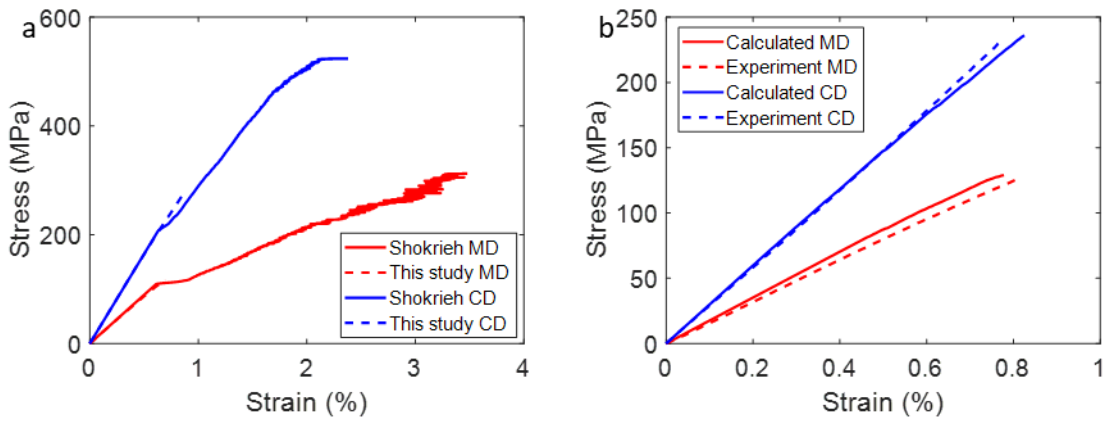

Figure IV-10. a) Comparison of Shokrieh model to proposed model for rCF/PPS; b) Comparison of rCF/PPS experiment to proposed model

condition is invalid for discontinuous fiber composites with non-random fiber orientation. Hence, this must be a primary consideration when modeling the strength of discontinuous fiber composites. Figure IV-10.b shows that the behavior shown in experiments was captured very well with the proposed model.

The modulus of the rCF/epoxy samples produced at 0.1 MPa molding pressure was well-predicted by the model proposed here, as shown in *Figure **IV-11***. The strength was less well-predicted. The unidirectional properties that were predicted exceed those found in the more fiber dense rCF/epoxy samples. This is primarily due to the increased plasticity allowed by the terminating condition at lower fiber volume fractions. As such, composites with extremely low fiber volume fractions may not be accurately predicted without additional modification. Conversely, it is expected that composites with higher fiber volume fraction will still be well-predicted, as their behavior will be more elastic. Similarly, since the terminating condition is dependent on the fiber orientation, highly aligned composite properties in the fiber dominant direction can likely be predicted using this model, though the transverse direction properties may be predicted less accurately if too much plasticity is modeled.

Conclusions

The key findings of this paper are:

1. Discontinuous fiber composite stiffness and strength properties can be modeled using constituent material properties commonly found in material datasheets, thereby reducing the need for extensive testing.
2. Fiber volume fraction should not be assumed to be homogeneous and therefore must be stochastically accounted for in simulations.
3. Quantification of the fiber orientation and length distributions is essential to accurately model the mechanical properties of discontinuous fiber composites.
4. For the first time, the master ply invariant approach has been shown to accurately model the modulus of discontinuous fiber composites.
5. Stochastic void content must be accounted for when modeling the stiffness degradation of discontinuous fiber composites.
6. A proper terminating condition based on fiber and matrix strain energy density was developed that applies to a variety of matrices and void content levels.

The results show much better agreement with experimental data than the state of the art, indicating that the terminating chosen here is more applicable to a range of composite materials. Future work should seek to improve this terminating condition to account for lower fiber volume fraction composites and develop a micromechanical model for the prediction of the longitudinal modulus in discontinuous fibers containing significant void content.

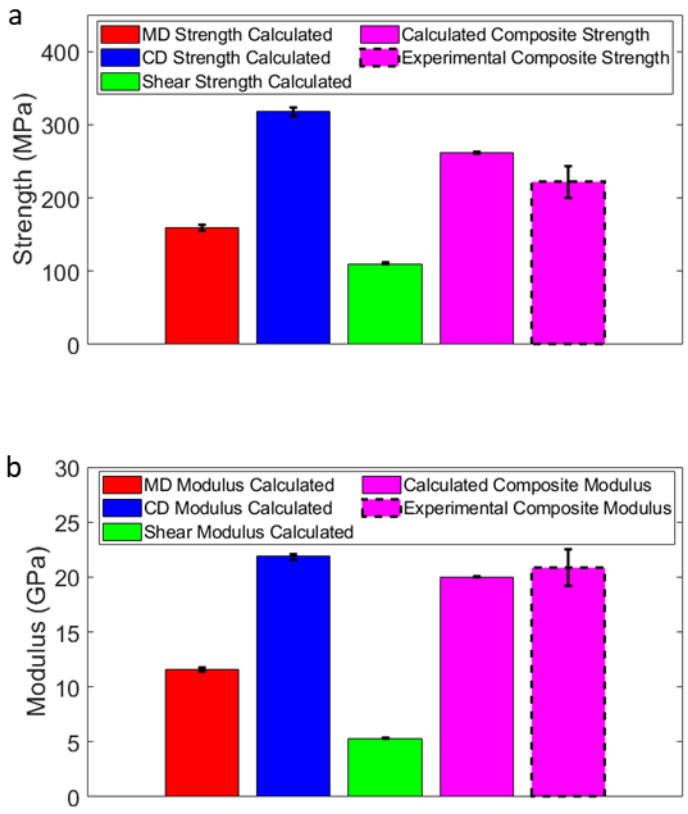

Figure IV-11. Predicted and simulated properties of rCF/Epoxy composite produced at 0.1 MPa pressure

References

[1] S.Y. Fu, B. Lauke, Effects of fiber length and fiber orientation distributions on the tensile strength of short-fiber-reinforced polymers, Composites Science and Technology. 56 (1996) 1179–1190. https://doi.org/10.1016/S0266-3538(96)00072-3.

[2] F. Garesci, S. Fliegener, Young's modulus prediction of long fiber reinforced thermoplastics, Composites Science and Technology. 85 (2013) 142–147. https://doi.org/10.1016/j.compscitech.2013.06.009.

[3] P. Feraboli, E. Peitso, T. Cleveland, P.B. Stickler, F. Deleo, T. Cleveland, P.B. Stickler, Characterization of prepreg-based ygrothermal carbon fibre/epoxy systems, Journal of Reinforced Plastics and Composites. 28 (2009) 1191–1214. https://doi.org/10.1177/0731684408088883.

[4] S. Ko, J. Davey, S. Douglass, J. Yang, M.E. Tuttle, M. Salviato, Effect of the thickness on the fracturing behavior of discontinuous fiber composite structures, Composites Part A: Applied Science and Manufacturing. 125 (2019) 105520. https://doi.org/10.1016/j.compositesa.2019.105520.

[5] J.C. Halpin, Stiffness and Expansion Estimates for Oriented Short Fiber Composites, Journal of Composite Materials. 3 (1969) 732–734. https://doi.org/10.1177/002199836900300419.

[6] H.L. Cox, The elasticity and strength of paper and other fibrous materials, British Journal of Applied Physics. 3 (1952) 72–79. https://doi.org/10.1088/0508-3443/3/3/302.

[7] R.M. Christensen, F.M. Waals, Effective stiffness of randomly oriented fibre composites, Journal of Composite Materials. 6 (1972) 518–535. https://doi.org/10.1177/002199837200600307.

[8] N. Pan, The Elastic Constants of Randomly Oriented Fiber Composites: A New Approach to Prediction, Science and Engineering of Composite Materials. 5 (1996) 63–72. https://doi.org/10.1515/SECM.1996.5.2.63.

[9] C.C. Chamis, Mechanics of composite materials: Past, present, and future, Journal of Composites Technology and Research. 11 (1989) 3–14. https://doi.org/10.1520/ctr10143j.

[10] R. Hill, Theory of mechanical properties of fibre-strengthened materials—III. Self-consistent model, Journal of the Mechanics and Physics of Solids. 13 (1965) 189–198. https://doi.org/10.1016/0022-5096(65)90008-6.

[11] J.K. Lees, A study of the tensile strength of short fiber reinforced plastics, Polymer Engineering & Science. 8 (1968) 195–201. https://doi.org/10.1002/pen.760080304.

[12] F.W.J. Van Hattum, C.A. Bernardo, Model to predict the strength of short fiber composites, Polymer Composites. 20 (1999) 524–533. https://doi.org/10.1002/pc.10376.

[13] J.C. Halpin, J.L. Karoos, Strength of discontinuous reinforced composites: I. Fiber reinforced composites, Polymer Engineering & Science. 18 (1978) 496–504. https://doi.org/10.1002/pen.760180612.

[14] S. Mortazavian, A. Fatemi, Effects of fiber orientation and anisotropy on tensile strength and elastic modulus of short fiber reinforced polymer composites, Composites Part B: Engineering. 72 (2015) 116–129. https://doi.org/10.1016/j.compositesb.2014.11.041.
[15] J. Henry, S. Pimenta, Semi-analytical simulation of aligned discontinuous composites, Composites Science and Technology. 144 (2017) 230–244. https://doi.org/10.1016/j.compscitech.2017.01.027.
[16] T. Okabe, T. Sasayama, J. Koyanagi, Micromechanical simulation of tensile failure of discontinuous fiber-reinforced polymer matrix composites using Spring Element Model, Composites Part A: Applied Science and Manufacturing. 56 (2014) 64–71. https://doi.org/10.1016/j.compositesa.2013.09.012.
[17] Y. Lee, S. Lee, J. Youn, K. Chung, T. Kang, Characterization of fiber orientation in short fiber reinforced composites with an image processing technique, Materials Research Innovations. 6 (2002) 65–72. https://doi.org/10.1007/s10019-002-0180-8.
[18] R.S. Bay, C.L. Tucker III, Stereological measurement and error estimates for three-dimensional fiber orientation, Polymer Engineering & Science. 32 (1992) 240–253. https://doi.org/10.1002/pen.760320404.
[19] S. Fliegener, M. Luke, P. Gumbsch, 3D microstructure modeling of long fiber reinforced thermoplastics, Composites Science and Technology. 104 (2014) 136–145. https://doi.org/10.1016/j.compscitech.2014.09.009.
[20] A. Bernasconi, F. Cosmi, P.J. Hine, Analysis of fibre orientation distribution in short fibre reinforced polymers: A comparison between optical and tomographic methods, Composites Science and Technology. 72 (2012) 2002–2008. https://doi.org/10.1016/j.compscitech.2012.08.018.
[21] S.G. Kravchenko, D.E. Sommer, B.R. Denos, A.J. Favaloro, C.M. Tow, W.B. Avery, R.B. Pipes, Tensile properties of a stochastic prepreg platelet molded composite, Composites Part A: Applied Science and Manufacturing. 124 (2019) 105507. https://doi.org/10.1016/j.compositesa.2019.105507.
[22] B.N. Nguyen, M.A. Khaleel, A mechanistic approach to damage in short-fiber composites based on micromechanical and continuum damage mechanics descriptions, Composites Science and Technology. 64 (2004) 607–617. https://doi.org/10.1016/S0266-3538(03)00293-8.
[23] S.G. Kravchenko, D.E. Sommer, R.B. Pipes, Uniaxial strength of a composite array of overlaid and aligned prepreg platelets, Composites Part A: Applied Science and Manufacturing. 109 (2018) 31–47. https://doi.org/10.1016/j.compositesa.2018.02.032.
[24] M.M. Shokrieh, H. Moshrefzadeh-Sani, A novel laminate analogy to calculate the strength of two-dimensional randomly oriented short-fiber composites, Composites Science and Technology. 147 (2017) 22–29. https://doi.org/10.1016/j.compscitech.2017.04.034.
[25] B. Vieille, J. Aucher, L. Taleb, Carbon fiber fabric reinforced PPS laminates: influence of temperature on mechanical properties and behavior, Advances in Polymer Technology. 30 (2011) 80–95. https://doi.org/10.1002/adv.

[26] B. Vieille, J. Aucher, L. Taleb, Influence of temperature on the behavior of carbon fiber fabrics reinforced PPS laminates, Materials Science and Engineering A. 517 (2009) 51–60. https://doi.org/10.1016/j.msea.2009.03.038.
[27] J. Schindelin, I. Arganda-Carreras, E. Frise, V. Kaynig, M. Longair, T. Pietzsch, S. Preibisch, C. Rueden, S. Saalfeld, B. Schmid, J.-Y. Tinevez, D.J. White, V. Hartenstein, K. Eliceiri, P. Tomancak, A. Cardona, Fiji: an open-source platform for biological-image analysis., Nature Methods. 9 (2012) 676–82. https://doi.org/10.1038/nmeth.2019.
[28] J.-Y. Tinevez, Directionality Plugin for ImageJ, (2017). https://imagej.net/Directionality.
[29] I.M. Daniel, O. Ishai, Engineering Mechanics of Composite Materials, 2nd ed., Oxford University Press, New York, 2006.
[30] S.W. Tsai, J.D.D. Melo, An invariant-based theory of composites, Composites Science and Technology. 100 (2014) 237–243. https://doi.org/10.1016/j.compscitech.2014.06.017.
[31] A. Arteiro, L.F. Pereira, M.A. Bessa, C. Furtado, P.P. Camanho, A micro-mechanics perspective to the invariant-based approach to stiffness, Composites Science and Technology. 176 (2019) 72–80. https://doi.org/10.1016/j.compscitech.2019.04.002.
[32] M. Eudier, The mechanical properties of sintered low-alloy steels, Powder Metallurgy. 5 (1962) 278–290. https://doi.org/10.1179/pom.1962.5.9.005.

Roles

Philip Barnett: Conceptualization, Methodology, Software, Formal analysis, Writing – Original draft, Visualization; **Stephen Young:** Writing – Original draft, Investigation, Formal analysis; **Neel Patel:** Investigation, Formal analysis; **Dayakar Penumadu:** Supervision, Project administration, Funding acquisition, Writing – Review & editing

CHAPTER V. RESIN INFILTRATION IN COMPRESSION MOLDED CARBON FIBER ORGANOSHEET COMPOSITES

A version of this chapter is in preparation for publication by Philip R. Barnett, Zachary Cook, Brett Hulett, Nalin H. Varma, and Dayakar Penumadu:

Abstract

This manuscript details an experimental study of the resin infiltration process in compression molded recycled/repurposed carbon fiber organosheet composites using a novel x-ray imaging technique. Experiments measuring the fiber preform deformation behavior and permeability were used to generate inputs to an existing infiltration model. A custom permeameter capable of measuring the permeability of fibrous preforms using a highly viscous infiltrating fluid to mimic a thermoplastic melt was developed and the results were compared to traditional porometry methods using water and air. X-ray radiographic imaging was used to view the infiltration of the fiber preforms to validate the infiltration model. In general, the model underpredicted the infiltration time due to interbundle permeability that cannot be measured using traditional techniques, elucidating the need for this novel measurement technique.

Introduction

The production of fiber-reinforced thermoplastics is often hindered by the difficulty of fully infiltrating fibrous preforms with a highly viscous thermoplastic resin. Typical fibrous preforms such as woven fabric, unidirectional fabrics, and unidirectional tows exhibit relatively low porosity during processing. As such, their permeability is low, thereby making impregnation with highly viscous thermoplastics difficult. To avoid this issue, several technologies have been developed for the production of fiber-reinforced thermoplastics[1], [2]. For example, solution impregnation processes have been developed in which the thermoplastic is dissolved in a solvent that is evaporated off once the preform is infiltrated. By reducing the viscosity of the thermoplastic, the solution can more readily impregnate the preform. However, this often leaves significant voids in the composite and can be quite expensive. Similarly, in powder-based systems, fine thermoplastic powders are mixed into an evaporative medium (typically water), which coats the fibers. Once the evaporative medium is removed, the powder is left and then melted to finalize impregnation. The cost of granulating the thermoplastic resin tends to be significant, as the powder must be very fine. Others have used intermingled fibers to achieved consolidation. In this method, thermoplastic fibers are intertwined with reinforcing fibers and then melted to impregnate the composite, thereby reducing the infiltration length. Similar to powder impregnation, the cost of processing thermoplastic fibers tends to make this option less attractive. Another typical thermoplastic composite production method involves in-situ polymerization. In this process, a low viscosity liquid monomer and catalyst infiltrate the preform and then react to polymerize the resin. This process tends to be time-consuming and cost-prohibitive for high production volume industries. One process that shows promise is film stacking, which involves sandwiching the preform between polymer films and then consolidating the

composite through a melt impregnation process. This process is low-cost, as the production of thermoplastic films is much cheaper than that of fibers or powders. However, the low transverse permeability of fibrous preforms combined with the high melt viscosity of the thermoplastic resin makes this process relatively time-consuming and good consolidation is often difficult to achieve for high-density preforms. Furthermore, the kinetics of thermoplastic infiltration are not well-understood, as many models of transverse resin infiltration rely on basic assumptions about the preform and resin behavior that may not be valid given the extreme viscosity of thermoplastic melts and multi-scale porosity in the fibrous preforms. The focus of this work was to characterize the transverse permeability of chopped fiber preforms using different candidate fluids and model the melt impregnation process. An existing model was evaluated to describe impregnation in a film stacking process and then compared to in-situ experiments.

Theory and Modeling

The basis of most composite infiltration models relies on Darcy's Law, which is stated as:

$$\frac{Q}{A} = -\frac{k}{\mu}\frac{\Delta P}{L} \tag{1}$$

where Q is the volumetric flow rate, A is the cross-section area, k is the permeability, μ is the fluid dynamic viscosity, and ΔP is the pressure drop over length L. Darcy's Law is valid for fluid flow through a porous medium at low flow rates, such that the fluid inertial effects are negligible. The criterion for such behavior has been established as Reynold's number below 1, though Darcy-Forchheimer flow can occur up to Re near 10[3]. Furthermore, when using a gas as the testing fluid, the Knudsen number must remain below 0.01[4]. The Reynold's number is the ratio of the inertial to viscous forces, which in the case of fiber-reinforced composites is defined as:

$$Re = \frac{\rho U_D d}{\mu} \tag{2}$$

where ρ is the fluid density, U_D is the superficial velocity (defined as $U_D = Q/A$), and d is the fiber diameter. Keeping the Reynolds number below 10 ensures that the flow is laminar and remains Darcian. The Knudsen number is the ratio of the mean molecular free path length to a representative physical length scale. Maintaining a low Knudsen number is essential to ensuring that the fluid does not slip at the surface. The Knudsen number is defined as:

$$Kn = \frac{Ma}{Re}\sqrt{\frac{\gamma\pi}{2}} \tag{3}$$

where *Ma* is the Mach number (defined as $Ma = U_D / c$, where *c* is the speed of sound) and *γ* is the heat capacity ratio of the fluid (1.4 for air).

Several authors have proposed models for infiltration using the definition of Darcy's Law prescribed above. The most simple models involve integration of Darcy's Law to determine the infiltration processing time[5], [6]. Many authors have proposed various models describing the viscosity and pressure evolution as a function of time, temperature, and resin-fiber interfacial behavior[7], [8]. In Darcian flow models, the time required for infiltration is a linear relation to the pressure applied, permeability, and viscosity, and a nonlinear (squared) relation to the infiltration length. As such, decreasing the infiltration length will significantly reduce the infiltration time. However, in the case of highly compressible preforms, many of these variables are closely connected; therefore, decreasing the infiltration length may not necessarily be the best way to reduce infiltration time. For example, in the case of compressible preforms, the infiltration length can be reduced by increasing the pressure applied. However, this may also lead to a decrease in permeability due to the rearrangement of the porous microstructure. If the effect of the decrease in permeability is more significant than the combined effects of the increased pressure and reduced infiltration length, the time to impregnation will increase. As a result, several models that describe the infiltration of compressible preforms have been developed[9]–[12].

A model proposed by Steggall-Murphy et al. was adapted for this work[13]. This model was originally developed to describe the one-dimensional flow of a thermoplastic resin into fiber tows in a continuous fiber laminate, where the permeability and tow volume were held constant. A unit cell was developed, which is shown in **Error! Reference source not found.**. The model describes two stages f infiltration: in the first stage, the pressure is gradually increased. The second stage occurs at isobaric conditions. For brevity, the derivation of the equations describing the infiltration kinetics is not included here. The resulting balance equations must be solved using an iterative time-stepping method to a suitable tolerance to determine the infiltration time:

Ramp Stage
$$\frac{H_{g0}\left(H_{g0}+d\right)}{\phi^2}\ln\left(\frac{H_{g0}+d}{H_{g0}+d-L\phi}\right)-\frac{H_{g0}}{\phi}L=\frac{KB}{\mu\phi}\frac{t^2}{2} \tag{4}$$

Isobaric Stage
$$\frac{H_{g0}\left(H_{g0}+d\right)}{\phi^2}\ln\left(\frac{H_{g0}+d-L_r\phi}{H_{g0}+d-L\phi}\right)+\frac{H_{g0}}{\phi}\left(L_r-L\right)=\frac{PK}{\mu\phi}\left(t-t_r\right) \tag{5}$$

where H_{g0} is the resin film thickness, *d* is the preform thickness, *L* is the infiltration length, ϕ is the porosity of the preform, and *B* is the pressure ramp rate. The subscript *r* refers to the infiltration length and time at the end of the ramp. Equations

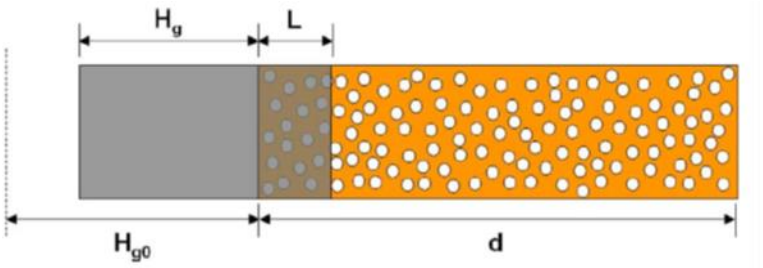

Figure V-1. Illustration of Stegall-Murphy model unit cell from [17]

(4) and (5) were solved using an iterative finite difference method since they have no closed-form solution. First, the time was updated by a small increment. Then, an iterative solution was used to find the infiltration length at that time (ranging from the prior infiltration length to d) that minimized the difference between the left and right-hand sides of the equation.

As an extension of this work, the compression of the fiber preform could be considered. At each time step, the current pressure would be calculated ($P = Bt$). The permeability, preform thickness, and porosity would all be updated before solving equation (4). This process would then be repeated until the ramp time was reached. Once at the isobaric stage, the permeability, preform thickness, and porosity would all be held constant and the previously described solution method would be implemented.

The effects of various material properties on this model were explored. Three properties that can typically be controlled were considered: applied pressure, permeability, and permeant viscosity. The permeability is directly linked to the compressive stiffness and applied pressure through changes in fiber volume fraction. Meanwhile, the permeant viscosity is independent of all other properties. The results are shown in Figure V-2. Decreasing the viscosity of the fluid is a very effective way of reducing infiltration times. Similarly, increasing the permeability of the preform also has a very significant effect, though this may not be feasible for high fiber volume fraction composites. An increase in applied pressure also leads to a decrease in processing time; however, increasing pressure also results in decreased permeability, as the fibrous preform densifies. Therefore, a time-optimized organosheet composite would utilize a highly permeable, stiff fiber preform with a low viscosity resin. The applied pressure would be chosen such that preform deformation is minimized while providing sufficient force to drive the flow of resin into the fibers.

Experimental Methods

Materials

These studies considered two types of nonwoven carbon fiber preforms: virgin wet-laid and recycled carded fibers. The wet-laid process is a modified papermaking process in which fibers are dispersed in water to induce random orientation, the water is drained, and then the preform is dried to remove any residual moisture. Nonrandom orientation can be achieved through controls of process variables such as line speed and drain location. This method leads to good fiber length retention, relative to many other chopped fiber processing methods such as compounding and pelletizing[14]. Furthermore, wet-laid nonwovens typically exhibit 2D mechanical isotropy. A binder is often applied to the fibers to enhance handleability. This was true in the case of the 310.0 gm^{-2} virgin fiber nonwoven used in these studies. Recycled carbon fiber preforms were provided in the form of a 184.2 gm^{-2} carded mat. Carding processes involve mechanical

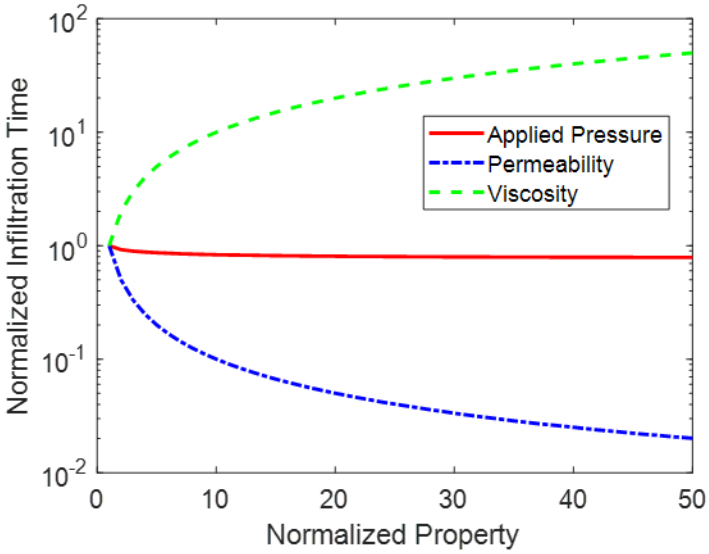

Figure V-2. Effects of common parameters on the infiltration time

entanglement and orienting of fibers using a series of combs. As such, this process leads to mechanical anisotropy, as well as greater 3D fiber orientation.

The matrix used in these studies is in the form of a polyphenylene sulfide (PPS) film (Ryton AQ200P, Solvay) of 0.127 mm thickness. PPS is a semicrystalline polymer exhibiting low melt viscosity, high-temperature stability, and excellent chemical resistance[15]. PPS offers shorter manufacturing times than traditional thermoset resins, higher service temperatures than many thermosets, and makes resin recycling feasible, leading to adoption within the aerospace industry[16]. These properties make PPS a good candidate material film stacking processes. For room temperature permeability measurements, polydimethylsiloxane (PDMS) fluid was used to simulate the PPS melt. PDMS fluids of varying viscosity were mixed to produce a fluid exhibiting a shear viscosity similar to the PPS melt (PSF-100000 and PSF-1000000, Clearco Products Co., Inc).

Infiltrating Fluid Rheology

To effectively model the infiltration process of the materials studied in this proposal, accurate rheological characterization of the resin viscosity must be completed. All rheological characterization was completed on a rotational rheometer (AR-G2, TA Instruments). The temperature was set to 300 °C for all samples unless otherwise noted. The viscosity was studied in air and an inert Argon atmosphere to determine the effects of cross-linking and other oxidative processes. PPS tests were completed using parallel plates with a 25 mm diameter. Stress corrections were applied to account for the non-constant shear rate along the radius of the plate. Additionally, the Cox-Merz rule was used to convert frequency data gathered during oscillatory testing to the corresponding shear rates that would be obtained using a flow procedure. The shear rates applicable to compression molding according to the model proposed by Gebart[8] are:

$$\dot{\gamma} = \frac{1 - V_f}{\left(\sqrt{\frac{V_{f\,max}}{V_f} - 1}\right)} \frac{3U_D}{R} \tag{6}$$

where R is the fiber radius and V_{fmax} is the maximum fiber volume fraction (assumed to be $\pi/4$ for square packing). This model describes the shear rate experienced by fluid in the pores of fibrous composites during processing, with a focus on continuous fiber resin transfer molding. For a 0.5 mm thick composite with 30% fiber volume fraction processed with a flow rate range of 0.1 mm min^{-1} to 5 mm min^{-1} (infiltration time of 6 seconds to 5 minutes), the shear rate should be on the order of 0.7 to 35 s^{-1}. The actual flow rate is likely near the lower end of this estimate, as typical shear rates in continuous unidirectional fiber preforms have been estimated to be on the order of 0.2 to 3.5 s^{-1}[17]. This estimate is in the

Newtonian range of PPS, which ensures that Darcy's law will remain valid at sufficiently low flow rates.

Single-frequency tests were used to study the effects of atmosphere-induced degradation, as well as temperature, on the melt viscosity. In single-frequency tests, the appropriate frequency was chosen as where the material exhibits Newtonian behavior; this was found to be 1 Hz. Isothermal time sweeps were used to determine appropriate processing conditions and provide inputs for the infiltration models. Rotational rheometry was also used to study the PDMS fluid used to simulate the PPS melt during permeability measurements. Since the PDMS does not require high-temperature processing, a cone and plate geometry (40 mm diameter, 1° angle) was used to study the viscosity as a function of shear rate at room temperature.

Permeability Testing

A custom permeameter was developed to measure the permeability of the carbon fiber nonwoven preforms. Relevant details regarding the design and operational principles of this apparatus can be found in SV-1. Custom Permeameter. An Instron 5567 load frame equipped with a 500 N load cell was used to measure the force required to maintain a set flow rate through the sample. The 500 N load cell was chosen because it was very close to the maximum force the fixture was capable of withstanding and would provide a relatively small load measurement error (0.025% full scale). The flow rate was controlled by the crosshead displacement rate, which was set to either 0.10, 0.15, or 0.20 mm min^{-1}. The frame was screw-driven, making it highly capable of monotonic, displacement-based tests (as opposed to hydraulic frames, which excel in force-based testing). During the test, the pressure rose until it reached a steady state. Occasionally, there was noise in the test data caused by entrapped air bubbles. These points were excluded from the steady-state calculations described later. Once steady-state had been reached, the next testing rate was used. Each sample was tested for at least the three rates, with many tested at the same rate more than once. After testing, the fixture was checked for leaks, at which point the sample would be excluded if one were found. None of the samples were excluded, as the fixture remained leak-free.

The resulting data was analyzed using a custom MATLAB script. This script utilized a series flow model to exclude fixture effects on the steady-state pressure. The permeability of the fixture was determined by running tests without a sample, resulting in an average permeability of 2.22e-8 m^2. This permeability is between 3 and 4 orders of magnitude greater than the permeability of the preforms, thereby limiting the effects of the fixture on the measurements. To determine the steady-state pressure, the force-displacement curves generated during the test were plotted, revealing a sigmoidal response. As such, the curves were fit with a logistic function of the form:

$$F(\delta) = \frac{A}{1 + e^{-B*(\delta - C)}} \tag{7}$$

This function fits the data very well, typically exhibiting an R^2 value greater than 0.99. The steady-state response of this function is determined by the asymptote as δ grows large, which is the fitting variable A. This force was used to determine the pressure imparted on the PDMS fluid, which was used to calculate the ΔP term in Darcy's Law. At least three steady-state measurements were taken per sample to generate an average permeability. It was found that the measurement repeatability was aligned with that found in existing literature[18], [19].

The permeability of the preforms was also measured using a commercially available capillary flow porometer (Porous Materials, Inc.). This device measures the air and water permeability of preforms using highly accurate flow controllers and pressure transducers. However, to ensure that the Reynold's number requirement for Darcian flow was met, a special fixture had to be developed for the air and water permeability tests. This fixture was very similar to the one developed for the PDMS permeability tests. It consisted of two perforated plates that are clamped together to compress the sample. O-rings are used to prevent in-plane flow through the fibrous preform. The permeability of the plate was considered in the calculation of the final permeability, using the simple series model described earlier. The air permeability tested was completed by holding constant air pressure to measure the output flow rate. It has been previously reported that inertial pressure losses are significant for compressible fluids such as air at even low Reynold's numbers[20]. This effect has been reported to be significant in the flow regime tested here, where the Reynolds number and Knudsen numbers averaged 1.62 and 0.0084 respectively. As a result, a modified version of Darcy's Law, termed the Forchheimer equation, is used:

$$\frac{\Delta P}{L} = -\frac{\mu}{K}\frac{Q}{A} - \rho\beta\left(\frac{Q}{A}\right)^2 \tag{8}$$

The Darcy permeability found from equation (1) is calculated as usual without accounting for inertial effects. The inverse of permeability is then plotted against the volumetric flow rate and a linear fit is determined. The y-intercept of the fit represents the permeability at which inertial effects are negligible. This procedure yields an effective permeability higher than the measured permeability due to the exclusion of inertial pressure losses that occur in the Darcy-Forchheimer regime. For the water fixture, the permeability measurement was taken using a falling head method. In this method, the head pressure of the water due to gravity and the output flow rate were measured. Samples were tested three times each to ensure repeatability of the measurement and ensure that the sample was fully wetted. The permeability of each test was calculated, with the average permeability reported.

The permeability measurements were then fit to a curve to determine the permeability as a function of fiber volume fraction. This data exhibited power-law behavior. As such, a custom power-law curve was fit to the permeability data:

$$K(V_f) = A(V_f^{-B} - 1) \tag{9}$$

This equation represents the physical phenomena of permeability, which reaches zero for a fully dense fiber bed (i.e., a solid fiber) and approaches infinity as the fiber volume fraction approaches zero. For the form of this function, the permeability, *K*, is in units of Darcys and the power-law exponent, *B*, must be positive. This fit was determined for each fluid and fiber preform type.

Preform Compressibility

Carbon fiber nonwoven preforms cut into circular specimens of 50.8 mm diameter were compressed between flat platens on an MTS Criterion Model 45 load frame using a 100 kN load cell. Platen separation was measured using an MTS model LX500 laser extensometer. The monotonic compression rate was set at 1 mm min^{-1} and reversed once 10 MPa compressive stress had been reached until the initial thickness was reached. Previous work on the compression of fibrous preforms has shown that the stress-strain behavior follows a power-law function[21]. Toll defined the compression behavior of the form[22]:

$$\sigma = kE(V_f^n - V_{f0}^n) \tag{10}$$

where *k* is a constant, *E* is the elastic modulus of the fiber, V_f is the fiber volume fraction, and V_{f0} is the minimum fiber volume fraction. Furthermore, the power-law exponent can be used to describe the state of material isotropy, with 3D isotropic materials having an exponent of 3 and 2D isotropic materials having an exponent of 5. Aligned planar materials such as unidirectional fabrics typically exhibit an exponent of greater than 5. This power-law equation describes the behavior in a physically meaningful way, as the minimum fiber volume fraction information is retained, as opposed to other curve fitting forms such as an exponential that may also provide a good fit to the data.

The resulting stress-strain data was converted to stress-fiber volume fraction using a simple relation between the strain and fiber volume fraction:

$$V_f = \frac{A_w}{h\rho} = \frac{A_w}{(1-\varepsilon)h_0\rho} \tag{11}$$

where A_w is the preform areal weight, *h* is the height, ρ is the fiber density, h_0 is the initial preform thickness, and ε is the strain. It was found that the stress-fiber volume fraction curves varied much more from sample to sample than the stress-strain curves. This observation is likely the result of variability in the h_0 values that were recorded at the 5 N pre-load using the load frame. Due to the random nature

of the fiber preforms, the pre-load did not compress all samples to the same level. A higher pre-load would not be appropriate, as nonwoven carbon fiber is known to exhibit a stress-induced hysteresis[23]. As a result, an average stress-fiber volume fraction curve would not be meaningful. Instead, an average stress-strain curve was generated and then used to generate a stress-fiber volume fraction curve. When calculating the fiber volume fraction, the average h_0 value was used.

For accuracy in modeling, the infiltration behavior curve fit must accurately capture the uncompressed fiber volume fraction. As such, to generate a highly accurate fit, a modification must be made to the power-law equation as follows:

$$\sigma = A * V_f^{(B+C*V_f)} \tag{12}$$

In this form, the uncompressed fiber volume fraction is not considered, as the only zero of the function occurs at zero fiber volume fraction. To overcome this problem, a fourth parameter, *D*, was added to the equation above:

$$\sigma = A * V_f^{(B+C*V_f)} + D \tag{13}$$

This parameter was equal to the negative of the stress calculated by the curve fit at the minimum fiber volume fraction, which was experimentally determined by the 5 N pre-load. This ensured that the fiber volume fraction could be non-zero when the stress was zero. By enforcing that the fiber volume fraction at zero stress is exactly equal to the measured uncompressed fiber volume fraction, the model is much more accurate than a curve fit of the form proposed by Toll, but still provides a physically meaningful description of the compression behavior. To ensure that the addition of the third term did not severely impact the goodness of fit of the model, the R^2 values of both functions were compared and found to be negligibly different. As a result, the stress-fiber volume fraction behavior could be modeled accurately using established power-law functions.

In-Situ X-ray Monitoring of Infiltration Flow Front

A custom compression molding apparatus was designed and built to mold samples while gathering x-ray images. Details of this apparatus are found in SV-2. Permeability Measurement Results. Images were taken from x-rays generated at 70 kV and 500 μA by a cone beam source (Hamamatsu, L8121-03) and detected by a flat panel detector (Varex, 1207N). The magnification was 8.2, such that each pixel had a height of 9 μm. Images were acquired at 30 Hz for at least one minute to identify any changes in thickness that appeared after infiltration. Samples were tested at pressures ranging from 0.5 to 4.0 MPa, discretized in 0.5 MPa increments at 300 °C. The thickness and infiltration time were compared to the estimates provided by the aforementioned model. Samples of both virgin and recycled carbon fiber were tested.

After testing, the samples were embedded in a mounting epoxy and polished for optical microscopy. Before, the samples were cut in half in the flow region to reduce edge effects. The microscopy images were segmented to show the fiber and void phases, which were then used to calculate the fiber and void volume fraction in the samples following the author's previous work.

Results and Discussion

Infiltrating Fluid Rheology

It is known that PPS undergoes significant degradation when processed at high temperatures[24]. This is expected to have a significant impact on the viscosity of the PPS melt. The degradation at a given temperature can often be reduced by reducing processing time or processing in an inert atmosphere, as the degradation of PPS is dominated by kinetic oxidation processes. Oscillatory tests were completed in both an inert atmosphere (Argon) and in a standard air atmosphere. The data shown in Figure V-3 illustrates that the maximum allowable processing time increases considerably in an inert atmosphere. The viscosity is shown to continually decrease in an inert atmosphere throughout a 30-minute processing time. This is likely due to the melting of residual crystallites, which may persist in the bulk polymer melt, as the equilibrium melting point of PPS has been estimated to be as high as 348.5 °C[25]. The results of the time sweep at 300 °C indicate that in a standard air atmosphere, processing times greater than 10 minutes will lead to significant degradation and therefore an increase in viscosity.

Additionally, increasing the temperature reduces the melt viscosity of polymers. However, increased temperature will also increase the rate of degradation, thereby decreasing the allowable processing time. This is illustrated by the viscosity increase apparent in the samples tested at 325 °C in air after approximately 5 minutes. It is also noteworthy that the viscosity in an inert atmosphere at 325 °C continues to decrease, but much more slowly than in the 300 °C temperature case. Likely, many of the crystallites that were melting in the latter times of the lower temperature time sweep were melted at the start of the higher temperature test. This is supported by the initially lower melt viscosity.

Darcy's Law assumes that fluid behavior is Newtonian. Therefore, it is important to check that the melt exhibits Newtonian behavior for the range of shear rates experienced during processing. Figure IV-4.a displays the viscosity as a function of shear rate at 300 °C in a standard air atmosphere. It is apparent that at high shear rates, the data becomes noisy. Therefore, an oscillatory mode was used to study the behavior at higher shear rates via the Cox Merz transformation (Figure V-4.b). The behavior of the PPS melt is Newtonian in the range of shear rates experienced during compression molding. Therefore, models based on Darcy's Law should be representative of the system.

The viscosity of the PDMS fluid was found to be in good agreement with the melt viscosity of the PPS at 300 °C as shown in Figure V-4. In the shear

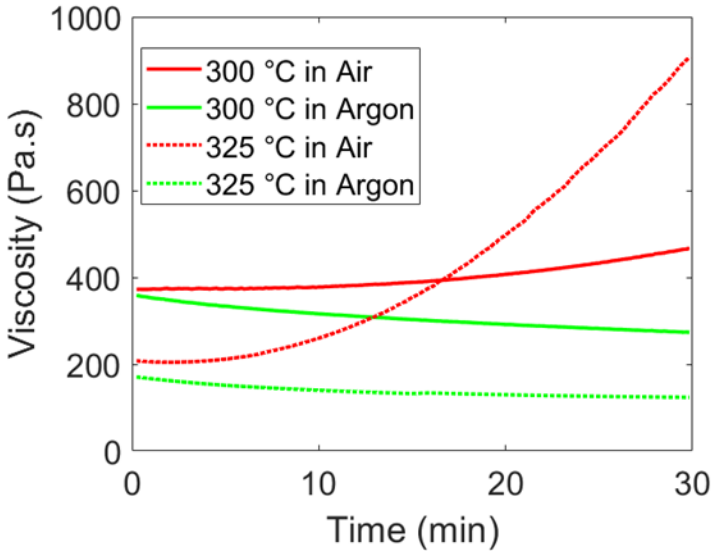

Figure V-3. Time-dependent behavior of PPS melt with 225 Pa oscillatory stress at 1 Hz; solid lines represent 300 °C melt temperature and dashed lines represent 325 °C melt temperature

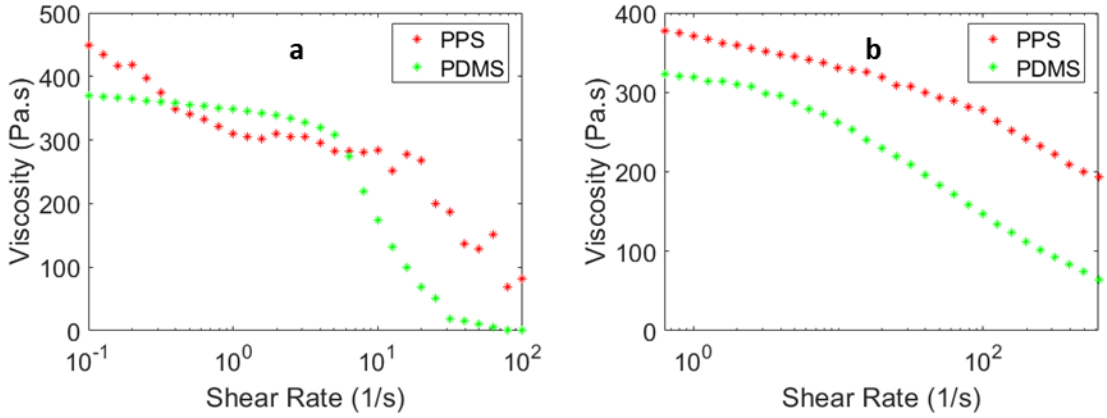

Figure V-4. a) Shear deformation mode test at 300 °C; b) Oscillatory deformation mode test at 300 °C with 225 Pa oscillatory stress

deformation mode, the PPS melt viscosity is initially higher than the PDMS, though it soon drops below the PDMS melt at shear rates in the range of 1 to 10 s^{-1}. It is possible that shear thinning was more significant in the shear deformation mode than the oscillatory mode. This was not found to be the case for the PDMS melt, which showed Newtonian behavior in the shear deformation mode from 1 s^{-1} until nearly 10 s^{-1}. When tested in an oscillatory mode, the PPS melt viscosity remains slightly higher than the PDMS throughout the range of frequencies studied. The PDMS shear deformation data and PPS melt oscillatory deformation data agree reasonably well, indicating that the PDMS fluid is a good analog for modeling the behavior of a PPS melt for permeability testing at room temperature.

Permeability Testing

The permeability of the two fiber preforms appears to be dependent upon the infiltrating fluid. Figure V-5 displays the permeability of the wet-laid preforms. The permeability decreases with increased fiber volume fraction (i.e., decreased porosity). This behavior is expected, as larger pore sizes will enable greater flow at a given fluid pressure. Furthermore, the behavior is asymptotic, much like the preform compression curves. This can be explained by shrinking pore spaces, which change size more rapidly at low compression levels, but then reach a critical size at higher compression levels.

In general, the measured permeability decreases with a decrease in permeant viscosity. This effect is much more pronounced at low fiber volume fractions. It is interesting to note that the permeability measured using water was less than that of the permeability measured using air. In general, the pressure imparted on the preform in the water permeability tests (typically less than 4.3 kPa) was lower than that of the air and PDMS tests (typically less than 41.4 kPa and 380 kPa, respectively). It is possible that the microstructure was less disturbed in the water tests, thereby yielding lower permeability. In the case of the air and PDMS, the high pressures could cause significant fiber deformation that enlarged some pore spaces and shrunk others. This would lead to preferential flow through the larger pores, increasing the measured permeability. It is therefore expected that significant dry spots may exist in regions where pore size is small enough that the pressure required for flow into the pore space exceeded the pressure applied to the preform. This is supported by the significant void content that was apparent in thermoplastic composites in the author's previous work. The variation in permeability measurement methods was reduced at higher fiber volume fractions, indicating that the more dense fiber beds may have been less prone to fluid-induced deformation. As such, a general rule can be established: permeability measurements should be made with fluids most representative of the fluid that is being used in processing as close as possible to the pressures experienced during processing.

In this work, an accurate measurement of the permeability of fiber preforms is especially significant, as the processing time exhibits a linear dependence with

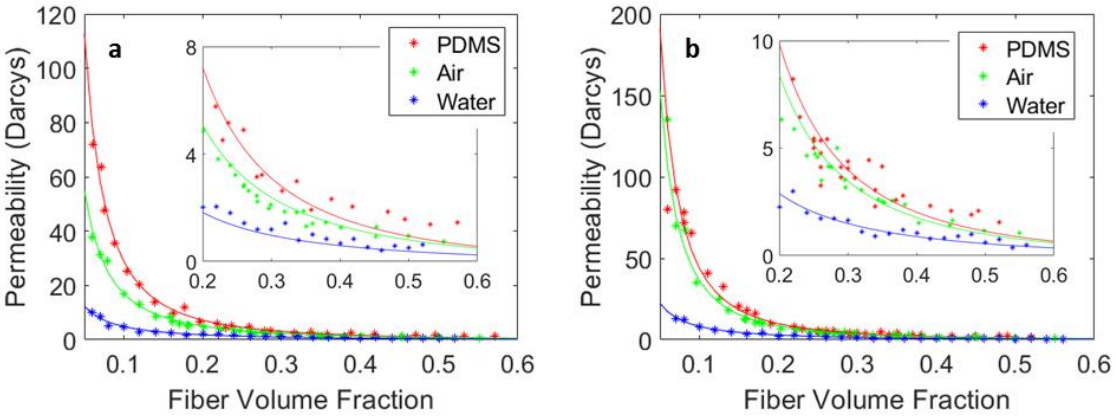

Figure V-5. a) Carded fiber permeability as a function of fiber volume fraction; b) Wet-laid fiber permeability as a function of fiber volume fraction; Solid lines represent fit according to equation (9)

permeability. The fit parameters for the permeability measurements are found in Table V-1. Parameter *A* has little influence on the overall results. However, the parameter *B* has a strong influence on the rate of decay of the permeability as a function of fiber volume fraction. A larger value of *B* indicates that the permeability is more fiber volume fraction-dependent.

The permeability of the carded preforms was found to be less than that of the wet-laid ones. This behavior indicates that the wet-laid preforms may be a more ideal choice for the production of organosheets. The difference between the two preforms was found to be nonlinear, as shown in Figure V-6, which shows that as the fiber volume fraction is increased, the permeability of the two preforms becomes more alike. It is possible that as the fiber volume fraction increases in the preforms, any out-of-plane fiber orientation is reduced, thereby yielding a more similar in-plane microstructure.

Preform Compression

The compression and relaxation of the carbon fiber preforms show asymptotic behavior, as expected from prior work. The average stress-fiber volume fraction behavior is shown in Figure V-7. The fiber volume fraction of the wet-laid carbon fiber nonwovens converged to a maximum much more quickly than the carded fiber nonwovens. Additionally, the maximum fiber volume fraction for the carded fiber nonwovens is significantly higher than the wet-laid nonwovens. Both fiber preform types exhibited an unloaded hysteresis, where the preform thickness post-loading was significantly reduced (yielding increased stress-free fiber volume fraction). The constants in the model describing the compression behavior are found in Table V-2. Recall, *D* is a parameter that serves as a correction to the model to ensure that the minimum fiber volume fraction is achieved at zero stress. As such, the very small scale of this correction factor, relative to the parameter, *A*, indicates that this term has very little effect on the fit.

Toll's model was used to generalize the behavior of the preform compression. The exponent from a fit to the stress-fiber volume fraction data based on equation (10) can be found in Table V-2. The wet-laid preforms exhibit an exponent value of 2.833, which according to Toll, represents 3D isotropic behavior. The carded preforms have an exponent value of 2.468 which indicates that there are more fibers oriented out-of-plane, as a linear elastic, isotropic preform would exhibit an exponent value of unity. In the unidirectional case, the fibers would not undergo rearrangement, but instead only axial compression. As such, the wet-laid preforms exhibit more planar fiber orientation than carded preforms. Furthermore, it is well-documented the permeability along a fiber array is significantly greater than the transverse permeability[26], [27]. However, the measured permeability is not in agreement with this; instead, the permeability of the carded nonwoven is less than that of the wet-laid one.

This seemingly contradictory phenomenon can be explained instead by the microstructure of the preforms. Optical micrographs (Figure V-8) of composite specimens reveal that the wet-laid preforms exhibit a bundle architecture, while

Table V-1. Permeability curve-fitting parameters

Nonwoven Type	Permeant	A	B
Wet-Laid	PDMS	0.3388	2.115
	Air	0.3129	2.068
	Water	0.3366	1.404
Carded	PDMS	0.3276	1.950
	Air	0.3655	1.676
	Water	0.2578	1.298

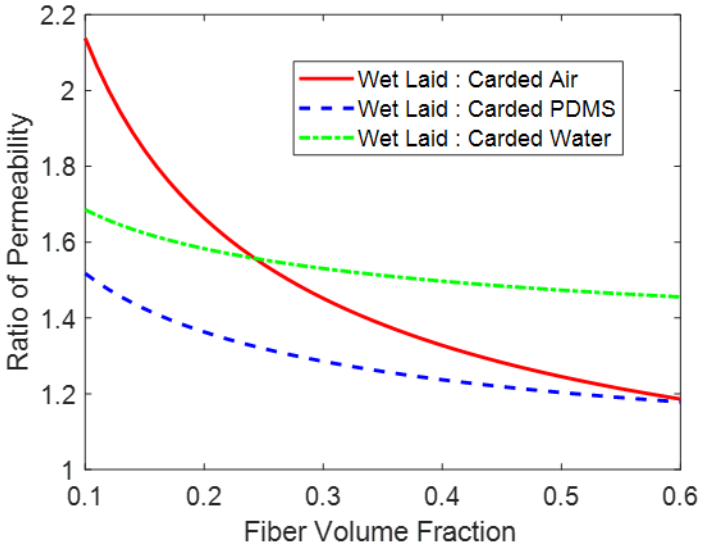

Figure V-6. Ratio of permeability for nonwovens using different fluids

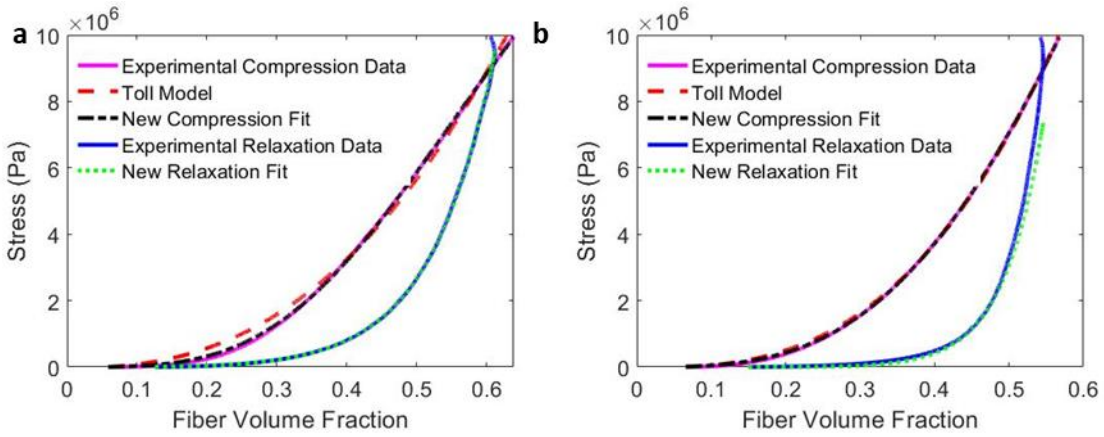

Figure V-7. Carded fiber compression-relaxation behavior and best fit; b) Wet laid fiber compression-relaxation behavior and best fit

Table V-2. Compression behavior curve-fitting parameters

Nonwoven Type	Behavior	A	B	C	D	Toll Model n
Wet-laid	Compression	3.329e7	3.006	-1.535	-1.202e4	2.833
	Relaxation	3.736e10	7.956	11.24	-419.97	-
Carded	Compression	1.343e7	3.052	-3.743	-4.379e3	2.468
	Relaxation	7.342e8	4.777	6.644	-6.408e3	-

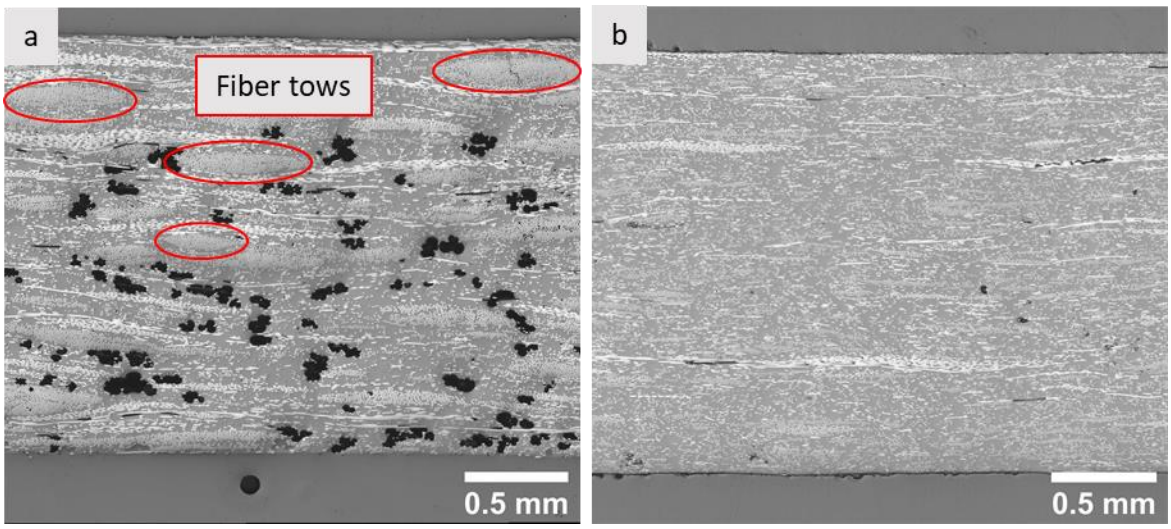

Figure V-8. a) Wet-laid composite micrograph; b) Carded composite micrograph

the carded preforms exhibit more individual filaments. As such, the pore space between bundles is much larger than the pore space between filaments, thereby increasing the permeability of the wet-laid preform. The carding process is especially good at producing preforms with high surface area by opening fiber bundles. However, this comes at the cost of reducing the bulk permeability. For the infiltration of nonwoven preforms with a thermoplastic resin, this yields a significant cost in terms of increased manufacturing time. However, it is also likely that the fiber bundles in the wet-laid preforms are much less permeable at a micro-scale due to the high fiber volume fraction within bundles, thereby leading to incomplete consolidation. It is expected that this incomplete consolidation would lead to reduced mechanical properties, though this may not necessarily render such an organosheet composite useless. If the not fully-realized mechanical properties are sufficient and the manufacturing time is reduced significantly enough, such these composites may be of interest in applications where manufacturing time dominates the decision to use composite materials.

Infiltration Modeling

The infiltration of the fibrous preforms was modeled using the Steggall-Murphy model. The preform compressibility and permeability were chosen following equations (9) and (13) respectively. The viscosity of the infiltrating fluid was fixed at 350 Pa s. The model was solved assuming instantaneous compression. The in-situ experiments revealed that the compression was near-instantaneous, typically captured in less than 0.1 seconds. A time step of 1.0e-4 s was used to solve to a tolerance of 1.0e-12. Figure V-9 shows the infiltration time and thickness predictions based on the model and from in-situ experiments. As expected, the infiltration time and thickness both decrease with increasing molding pressure. The measured thickness from in-situ molding experiments reveals that a plateau in thickness is reached for molding pressures above 1.2 MPa for the recycled fiber preforms and above 3.7 MPa for the virgin fiber preforms. At higher pressures, the thickness is constant, as the minimum composite thickness is that of the two films and the fully-dense carbon fiber preform. The rate of change in infiltration time with pressure begins to decrease at higher pressures as the change in permeability with additional pressure becomes small. At pressures before the thickness plateau, the permeability remains high, but the volume of resin is insufficient to fully consolidate the preform, resulting in relatively small changes in infiltration time.

The Stegall-Murphy model predicted the void content in the carded fiber composites reasonably well. As shown in Figure V-10, the wet-laid composites exhibited a higher void content than the carded. It should be noted that the void fraction reported here refers to the final composite laminate, as opposed to the organosheets that were shown to exhibit much higher void content in previous work. The model indicates that there was insufficient resin volume to fully impregnate the organosheet at 1 MPa molding pressure for both preforms. Additional pressure was shown to lower the void content of the carded composites,

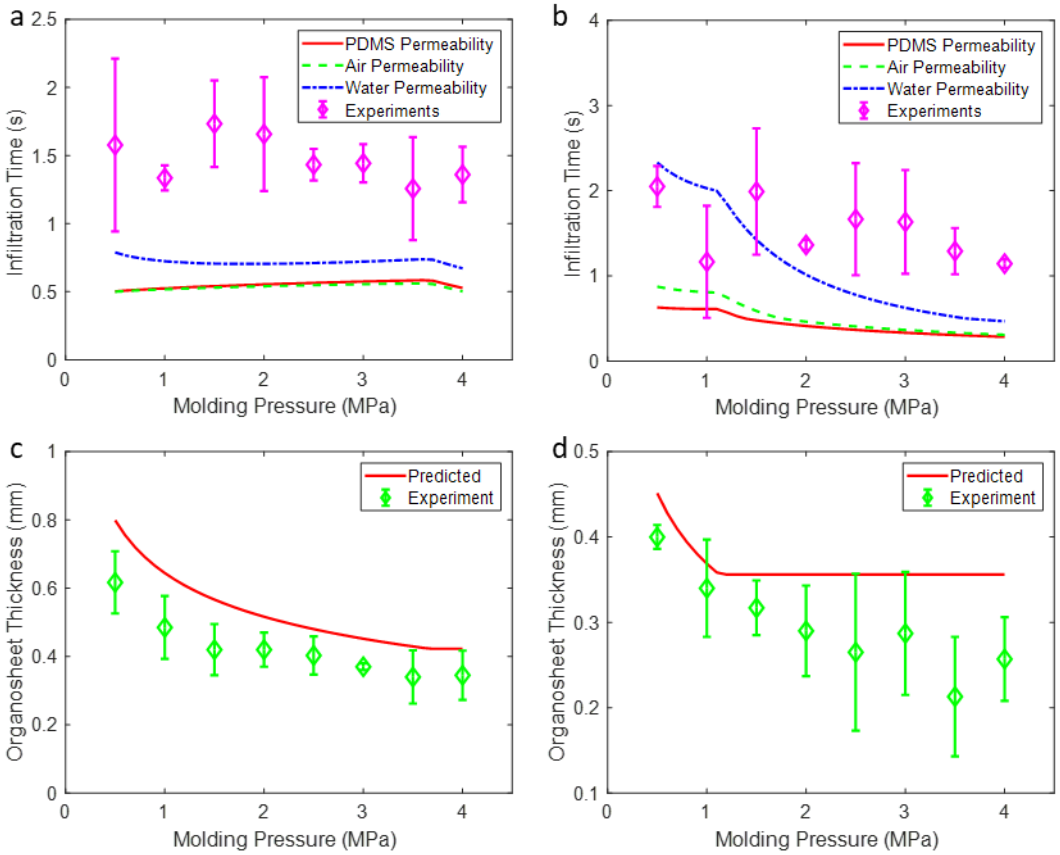

Figure V-9. a) Infiltration time estimates for wet-laid organosheets; b) infiltration time estimates for carded organosheets; c) thickness estimates for wet-laid organosheets; d) thickness estimates for carded organosheets; error bars represent standard deviation

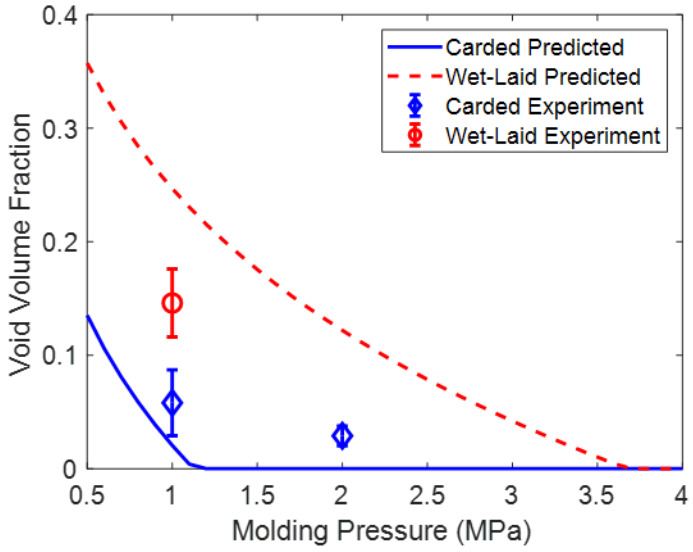

Figure V-10. Stegall-Murphy model for void volume fraction in organosheet composites; error bars represent standard deviation

though the predicted zero void content was not achieved. Increasing the molding pressure can lead to other problems such as fiber flow, so an acceptable level of void content should be chosen such that molding pressure is minimized. Prior work has shown that discontinuous fiber organosheet composites are largely insensitive to void content, indicating that low molding pressure provides equivalent mechanical properties.

In-Situ X-ray Monitoring of Infiltration Flow Front

The infiltration time and organosheet thickness measured in experiments are shown alongside the calculations in Figure V-9, where the error bars represent one standard deviation. In general, the in-situ monitoring showed that the model overestimated the infiltration time required for the wet-laid preforms, but was reasonably accurate for the carded preforms. This is likely due to the fiber bundle architecture described earlier. The interbundle permeability is expected to be significantly less than the intrabundle permeability. Hence, the radiographs identified flow into the bundles resulting in an intensity change that could not be found using traditional optical methods.

An example series of x-ray images is shown in Figure V-11. Initially, the PPS films remain on the surface of the fiber preform, but then begin to infiltrate once the pressure is applied. As time continues to increase, the films infiltrate further into the sample until the infiltration limit is reached. This limit may correspond to full consolidation if the compressive force is enough such that the void space in the fiber preform is equal to the resin volume or partial consolidation such that the resin fills what void space it can. More details about the image processing techniques employed to determine the infiltration time can be found in SV-3. Analysis of Infiltration.

Imaging for times beyond the infiltration time revealed that at high pressures, fiber flow occurs in-plane. Figure V-12 shows the thickness behavior as a function of time for a few samples, where there is a clear continually decreasing thickness for samples at higher loads. This behavior is not desirable for organosheet composites, as a disturbance in the fiber orientation leads to inhomogeneous properties that are not easily modeled. Additionally, fiber flow results in significantly varying fiber and void content. Figure V-13 shows box plots of the fiber and void content shown in optical micrographs. The results indicate that the carded fiber preforms produce composites with similar fiber volume fraction, but generally lower void content than the wet-laid preforms. At high molding pressures, the wet-laid preforms exhibited significant fiber flow, as the fiber tow architecture led to resin and void-rich regions. Local fiber and void content across the samples was calculated and is reported in SV-8. Optical Micrograph Analysis. As such, molding pressures should be limited to around 2.0 MPa to prevent significant fiber realignment.

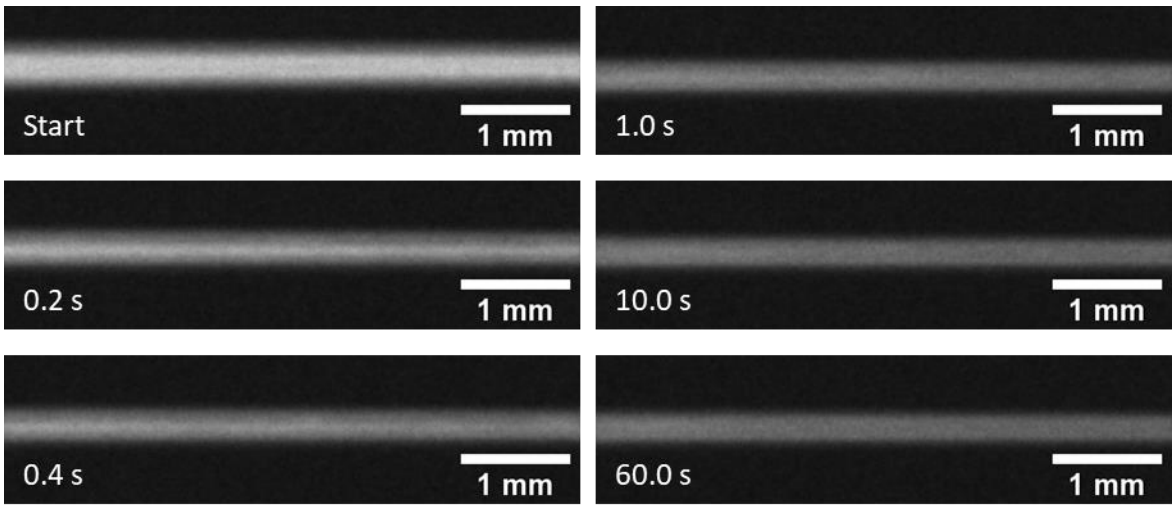

Figure V-11. Images of infiltration behavior in a carded recycled fiber preform at 3.0 MPa molding pressure

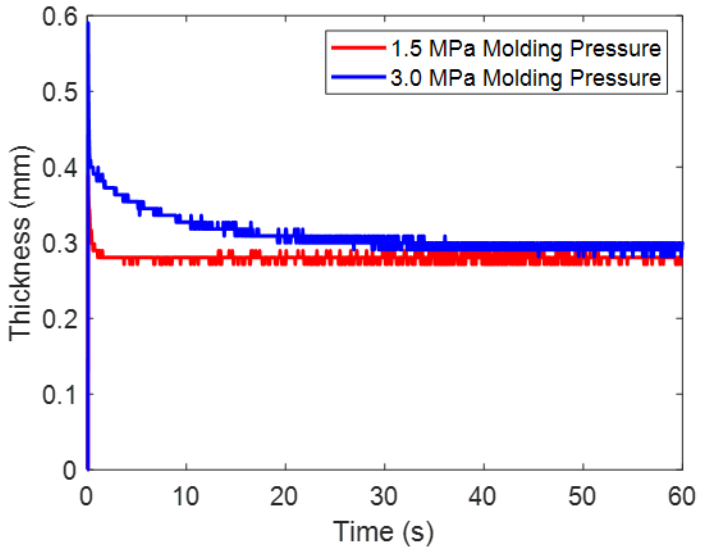

Figure V-12. Thickness change with time for carded recycled fiber samples

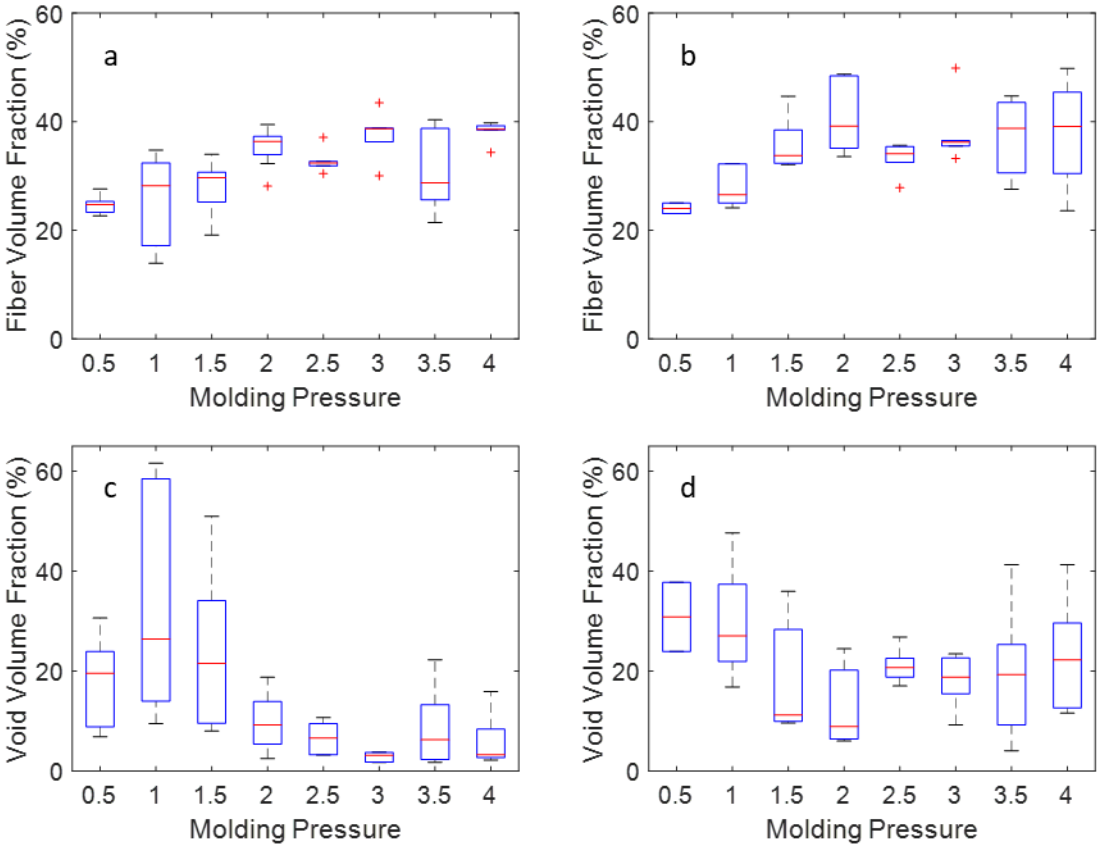

Figure V-13. Box plots of fiber and void content: a) Carded fiber volume fraction; b) Wet-laid fiber volume fraction; c) Carded void volume fraction; d) Wet-laid void volume fraction

Conclusions

The key results of this study can be summarized as:

1. The choice of permeant and method of testing has a strong influence on the measured permeability for fibrous preforms. Constant pressure tests using air and PDMS yielded a relatively good agreement in measured permeability, but falling head tests using water were found to yield much lower permeability.
2. Nonwoven preforms containing well-dispersed and smaller fiber bundles yield lower global permeability than is achieved from preforms maintaining a tow architecture. Despite this, the porosity of their composites is significantly lower due to the avoidance of dense fiber bundles with locally low permeability.
3. The infiltration model proposed by Stegall-Murphy predicts the thickness of organosheets reasonably well, but it consistently underpredicts the infiltration time as macro-scale permeability measurements do not account for interbundle permeability.
4. Radiographic imaging can be used to measure the flow of molten thermoplastic into a fibrous preform to determine the infiltration time required for consolidation. Unlike traditional surface-based infiltration time measurement methods, interbundle infiltration can be measured.
5. Fully consolidated composites yielded significantly lower void content than was predicted by the model, though the organosheet void content was in reasonable agreement.
6. Molding pressure should be kept relatively low to prevent fiber flow that will disturb the preform architecture.

Future work on the topic of discontinuous fiber preform permeability should consider evaluating permeability using radiographic imaging, as it was shown to capture interbundle permeability in a way that is not measured using traditional porometry techniques. Additionally, the lower void content observed in laminated composites relative to the organosheets despite the same quantity of matrix should be studied in further detail. The low infiltration times measured in these experiments show that recycled/repurposed carbon fiber organosheet composites offer promise as an automotive composite material.

References

[1] U.K. Vaidya, K.K. Chawla, Processing of fibre reinforced thermoplastic composites, International Materials Reviews. 53 (2008) 185–218. https://doi.org/10.1179/174328008x325223.

[2] J.B. Cattanach, G. Guff, F.N. Cogswell, The processing of thermoplastics containing high loadings of long and continuous reinforcing fibers, Journal of Polymer Engineering. 6 (1986) 345–362.

[3] O.H. Andersen, H.F. Burcharth, On the One-Dimensional Steady and Unsteady Porous Flow Equations, Coastal Engineering. 24 (1995) 233–257.

[4] G.W. Jackson, D.F. James, The permeability of fibrous porous media, The Canadian Journal of Chemical Engineering. 64 (1986) 364–374. https://doi.org/10.1002/cjce.5450640302.

[5] C. Mayer, X. Wang, M. Neitzel, Macro- and micro-impregnation phenomena in continuous manufacturing of fabric reinforced thermoplastic composites, Composites Part A: Applied Science and Manufacturing. 29 (1998) 783–793. https://doi.org/10.1016/S1359-835X(98)00056-6.

[6] P. Ouagne, L. Bizet, C. Baley, J. Bréard, Analysis of the film-stacking processing parameters for PLLA/flax fiber biocomposites, Journal of Composite Materials. 44 (2010) 1201–1215. https://doi.org/10.1177/0021998309349019.

[7] R. Phillips, D.A. Akyüz, J.A.E. Månson, D.A. Akyiiz, J.A.E. Manson, Prediction of the consolidation of woven fibre-reinforced thermoplastic composites. Part I. Isothermal case, Composites Part A: Applied Science and Manufacturing. 29 (1998) 395–402. https://doi.org/10.1016/S1359-835X(97)00099-7.

[8] B.R. Gebart, Permeability of unidirectional reinforcements for RTM, Journal of Composite Materials. 26 (1992) 1100–1133. https://doi.org/10.1177/002199839202600802.

[9] J. Park, M.K. Kang, A numerical simulation of the resin film infusion process, Composite Structures. 60 (2003) 431–437. https://doi.org/10.1016/S0263-8223(03)00021-7.

[10] S.T. Jespersen, M.D. Wakeman, D. Cramer, V. Michaud, J.-A.E. Månson, Film Stacking Impregnation Model for Thermoplastic Composites Applied To a Novel Net-Shape Preforming Process, in: The 8th International Conference on Flow Processes in Composite Materials, Douai, France, 2006: pp. 165–172.

[11] J.L. Sommer, A. Mortensen, Forced unidirectional infiltration of deformable porous media, Journal of Fluid Mechanics. 311 (1996) 193–217. https://doi.org/10.1017/S002211209600256X.

[12] V. Michaud, R. Törnqvist, J.A.E. Månson, Impregnation of compressible fiber mats with a thermoplastic resin. Part II: Experiments, Journal of Composite Materials. 35 (2001) 1174–1200. https://doi.org/10.1106/MLLN-4EF9-4KFU-XCWL.

[13] C. Steggall-Murphy, P. Simacek, S.G. Advani, S. Yarlagadda, S. Walsh, A model for thermoplastic melt impregnation of fiber bundles during consolidation of powder-impregnated continuous fiber composites, Composites Part A: Applied

Science and Manufacturing. 41 (2010) 93–100. https://doi.org/10.1016/j.compositesa.2009.09.026.
[14] A. Endres, S. Schramm, C. Lutke, S. Nendel, C. Lütke, S. Nendel, Prospects of wet-laid nonwovens for organosheet-products, Reinforced Plastics. 00 (2017) 2–5. https://doi.org/10.1016/j.repl.2017.07.002.
[15] A.S. Rahate, K.R. Nemade, S.A. Waghuley, Polyphenylene sulfide (PPS): State of the art and applications, Reviews in Chemical Engineering. 29 (2013) 471–489. https://doi.org/10.1515/revce-2012-0021.
[16] J. Diaz, L. Rubio, J. D??az, L. Rubio, J. Diaz, L. Rubio, J. Díaz, L. Rubio, Developments to manufacture structural aeronautical parts in carbon fibre reinforced thermoplastic materials, Journal of Materials Processing Technology. 143–144 (2003) 342–346. https://doi.org/10.1016/S0924-0136(03)00450-3.
[17] S.T. Jespersen, M.D. Wakeman, V. Michaud, D. Cramer, J.A.E. Månson, Film stacking impregnation model for a novel net shape thermoplastic composite preforming process, Composites Science and Technology. 68 (2008) 1822–1830. https://doi.org/10.1016/j.compscitech.2008.01.019.
[18] R. Arbter, J.M. Beraud, C. Binetruy, L. Bizet, J. Bréard, S. Comas-Cardona, C. Demaria, A. Endruweit, P. Ermanni, F. Gommer, S. Hasanovic, P. Henrat, F. Klunker, B. Laine, S. Lavanchy, S. V. Lomov, A. Long, V. Michaud, G. Morren, E. Ruiz, H. Sol, F. Trochu, B. Verleye, M. Wietgrefe, W. Wu, G. Ziegmann, Experimental determination of the permeability of textiles: A benchmark exercise, Composites Part A: Applied Science and Manufacturing. 42 (2011) 1157–1168. https://doi.org/10.1016/j.compositesa.2011.04.021.
[19] N. Vernet, E. Ruiz, S. Advani, J.B. Alms, M. Aubert, M. Barburski, B. Barari, J.M. Beraud, D.C. Berg, N. Correia, M. Danzi, T. Delavière, M. Dickert, C. Di Fratta, A. Endruweit, P. Ermanni, G. Francucci, J.A. Garcia, A. George, C. Hahn, F. Klunker, S. V. Lomov, A. Long, B. Louis, J. Maldonado, R. Meier, V. Michaud, H. Perrin, K. Pillai, E. Rodriguez, F. Trochu, S. Verheyden, M. Weitgrefe, W. Xiong, S. Zaremba, G. Ziegmann, Experimental determination of the permeability of engineering textiles: Benchmark II, Composites Part A: Applied Science and Manufacturing. 61 (2014) 172–184. https://doi.org/10.1016/j.compositesa.2014.02.010.
[20] J.T. Gostick, M.W. Fowler, M.D. Pritzker, M.A. Ioannidis, L.M. Behra, In-plane and through-plane gas permeability of carbon fiber electrode backing layers, Journal of Power Sources. 162 (2006) 228–238. https://doi.org/10.1016/j.jpowsour.2006.06.096.
[21] M. Amiot, M. Lewandowski, P. Leite, M. Thomas, A. Perwuelz, An evaluation of fiber orientation and organization in nonwoven fabrics by tensile, air permeability and compression measurements, Journal of Materials Science. 49 (2014) 52–61. https://doi.org/10.1007/s10853-013-7323-8.
[22] S. Toll, Packing mechanics of fiber reinforcements, Polymer Engineering and Science. 38 (1998) 1337–1350. https://doi.org/10.1002/pen.10304.

[23] D. Poquillon, B. Viguier, E. Andrieu, Experimental data about mechanical ygrothe during compression tests for various matted fibres, Journal of Materials Science. 40 (2005) 5963–5970. https://doi.org/10.1007/s10853-005-5070-1.
[24] D.R. Fagerburg, J.J. Watkins, P.B. Lawrence, Melt viscosity increase during rheological testing of poly(phenylene sulfide), Journal of Applied Polymer Science. 50 (1993) 1903–1907. https://doi.org/10.1002/app.1993.070501106.
[25] J.D. Menczel, G.L. Collins, Thermal analysis of poly(phenylene sulfide) polymers. I: Thermal characterization of PPS polymers of different molecular weights, Polymer Engineering & Science. 32 (1992) 1264–1269. https://doi.org/10.1002/pen.760321713.
[26] M.M. Tomadakis, T.J. Robertson, Viscous permeability of random fiber structures: Comparison of electrical and diffusional estimates with experimental and analytical results, Journal of Composite Materials. 39 (2005) 163–188. https://doi.org/10.1177/0021998305046438.
[27] R.C. Lam, J.L. Kardos, The permeability and compressibility of aligned and cross-plied carbon fiber beds during processing of composites, Polymer Engineering & Science. 31 (1991) 1064–1070. https://doi.org/10.1002/pen.760311411.

Roles

Philip Barnett: Conceptualization, Methodology, Software, Formal analysis, Writing – Original draft, Visualization; **Zachary Cook:** Methodology, Investigation; **Brett Hulett:** Methodology, Investigation; **Nalin Varma:** Methodlogy, Investigation; **Dayakar Penumadu:** Supervision, Project administration, Funding acquisition, Writing – Review & editing

CHAPTER VI. CRASHWORTHINESS OF RECYCLED CARBON FIBER ORGANOSHEET COMPOSITES

A version of this chapter is in preparation for publication by Philip R. Barnett, Brett Hulett, and Dayakar Penumadu:

Abstract

The crashworthiness of discontinuous fiber organosheet composites using recycled carbon fiber as reinforcement was studied. Sinusoidal crush specimens were manufactured of acrylonitrile butadiene styrene, polyphenylene sulfide, and a common structural epoxy reinforced with recycled carbon fibers. Samples were tested at a range of strain rates and temperatures representative of automotive conditions. Crush debris size was quantified using sieving to correlate with energy absorption. The effect of manufacturing flaws such as embedded foreign objects, porosity, and ductile tearing was studied by comparing x-ray computed tomography images with crush test data gathered using digital image correlation. The results show great promise for organosheet composites as a novel material for automotive crash structures, exceeding the energy absorption capabilities of many continuous fiber thermosets.

Introduction

Fiber-reinforced composites offer many advantages over traditional automotive metals such as corrosion resistance, high strength and stiffness, and reduced weight. These materials typically exhibit highly elastic deformation behavior, which benefits designs requiring rigidity and dimensional stability, but leads to explosive failure mechanisms in which little energy is absorbed. When energy is not absorbed in the structure of a vehicle, it is instead imparted upon the passengers and can lead to fatality. This failure behavior would obviously be non-ideal for vehicles that are involved in traffic accidents at a rate of nearly 6.5 million per year in the United States in 2017[1]. However, when properly initiated, progressive crushing in composite materials can lead to significantly more energy absorption than occurs in the progressive folding of metal structures.

Typical coupon-level crashworthiness testing involves the compression of an extruded section between flat platens. Traditionally, square or circular tubular samples are compressed while the load and displacement are measured. To initiate failure, a defect must be present in the sample. In metal tubes, this is often found in the form of a crimp that initiates progressive folding, while a bevel is typically applied to composites to initiate progressive crushing[2]. The structure dissipates energy as it is deformed, which is identified by the area under the load-displacement curve. On a per-mass basis, this is termed the specific energy absorbed (SEA). The SEA of common automotive metals such as steel and aluminum is in the range of 15 to 30 kJ kg^{-1}, while fiber-reinforced composites typically absorb between 40 and 80 kJ kg^{-1}[3]. SEA has even been shown to exceed 150 kJ kg^{-1} when fiber orientation and the choice of matrix material are favorable for energy absorption[4]. As a result, composite materials offer an opportunity for superior crashworthiness relative to metals.

Several factors influence the SEA of composite materials. Much of the prior work has focused on circular tubes, which are discussed here unless otherwise noted. It has been found that the SEA is maximized for $\pm\theta$ tubes when the angle is around 10° from the load direction[5], and an increase in SEA is realized when increasing the number of plies oriented in the loading direction for $[90/0_n/90]$ laminates[6]. It has also been determined that purely unidirectional composites exhibit unstable failure modes due to the lack of a hoop constraint[7]. As such, some non-axial fibers must be present to constrain delamination growth. Large delaminations in axial plies result in large fronds of material that splay outward and absorb relatively little energy due to limited fiber fracture. In general, plies oriented in the loading direction fail by splaying, while transverse plies fail by fragmentation. By constraining the length of the fronds developed during splaying, greater energy absorption can be achieved through increased fragmentation in the load-bearing axial plies.

SEA is also influenced by fiber type, with glass fiber composites typically achieving a lower value than carbon fiber largely due to the difference in density[2]. The matrix properties also play a significant role in the SEA of composites. For example, carbon fiber/polyether ether ketone (PEEK) composites have been shown to exhibit significantly higher SEA than carbon fiber/epoxy composites[4], largely due in part to their significantly improved mode I fracture toughness. This result was also apparent for a variety of thermoplastic matrices, in which the composites exhibiting higher mode I fracture toughness yielded higher SEA[5]. In the case of fiberglass-reinforced vinyl ester composites, a linear relationship was found between matrix compressive strength and energy absorption[8]. It has been noted that the matrix strength and modulus have a stronger influence on the SEA of glass fiber thermosets composites than the fracture toughness[2].

The fiber format has also been found to influence the SEA. For glass fiber composites, randomly oriented strand composites exhibit higher SEA than non-crimped fabrics[9]. It was also determined that the randomly oriented composites exhibited higher mode I fracture toughness, though improving the interlaminar fracture toughness through the use of inter-leaf urethane films, stitching, and powdered thermoplastic additives played a much smaller role than the matrix modulus and strength. Similarly, continuous filament random mat glass fiber composites were shown to exhibit much higher SEA with a vinyl ester matrix as opposed to polyester[10]. The SEA of chopped fiber composites has also been studied on flat coupon samples for a variety of fiber lengths, tow sizes, and volume fractions[11,12]. It was found that fiber volume fraction played the most significant role in determining the SEA of the composites, as the interlaminar fracture toughness increased with decreasing fiber volume fraction. In these studies, it was also found that the SEA of chopped fiber composites exceeded that of cross-ply continuous fiber composites[13]. Another study of chopped carbon fiber/epoxy composites found that the tow size significantly impacts the SEA, where shorter tows resulted in higher SEA[14]. It was believed that increased homogeneity in composites made with smaller tows was responsible for the increase in energy

absorption, which was also validated by an increase in SEA for thicker specimens. These results bode well for the use of discontinuous fiber-reinforced composites as crashworthy structures in the automotive industry, as their low cost and high formability are conducive to mass production.

When performing crush tests, three variables have been shown to consistently influence the results: testing rate, testing temperature, and geometry. In terms of the testing rate, it has been established that continuous strand mat glass fiber/polyurethane composite plates show reduced SEA with increased loading rate[15], carbon fiber/PEEK composite tubes show increased SEA with increased loading rate[16], glass fiber/vinyl ester composite rods show increased SEA with increased loading rate[8], and glass fiber/epoxy and carbon/fiber epoxy show increased SEA with increased loading rate, while polyesters show decreased SEA with loading rate[2]. Clearly, the testing rate affects the measured SEA, which is strongly dependent on the matrix properties.

Similarly, the testing temperature has been shown to influence the SEA of both epoxy and PEEK composites[17]. It was reported that the SEA gradually increases in temperature up to a point at which it remains largely constant until the glass transition temperature of the matrix is reached, followed by a rapid decrease in energy absorption thereafter. The maximum specific energy absorbed was found to be below room temperature for both glass fiber/epoxy and carbon fiber/PEEK composites, indicating that the increased matrix elasticity at low temperatures plays a significant role.

The effect of geometry on the SEA of composites is quite complicated. It has been noted that rectangular and square tubes typically yield lower SEA values than circular tubes[2]. Furthermore, it has been found that truncated cone specimens exhibit non-uniform SEA through the crush depth[18]. The ratio of the diameter to the thickness of circular tube specimens has been found to influence SEA, with smaller D:t yielding higher SEA[7]. Furthermore, the crush fixture geometry influences SEA. It was found that the SEA of glass fiber rods was lower when crushed against a flat plate as opposed to a radial depression[8]. Similarly, the SEA of flat plate samples constrained by frictionless rollers and crushed against a rounded surface was found to vary with roller pressure and crush plate radius of curvature[15]. In all of these cases, the primary effect of sample and fixture geometry was on the failure mode of the composite. In general, composite crush specimens fail in either fragmentation or splaying modes. The fragmentation mode involves local crushing of the material as a debris wedge moves along the crush length. The splaying mode involves significant friction between the composite plies and the test fixture, as well as significant energy absorption from fiber breakage as the splayed plies bend. As such, test fixtures that suppress fiber breakage in the splaying mode will decrease the SEA[15], and fixtures that increase the contact area of the splayed plies and reduce their radius of curvature will result in higher SEA[8]. For samples in which the cross-section is too narrow, instabilities and local buckling lead to reduced SEA[7]. Additionally, the damage initiation trigger has been shown to affect the failure behavior, though the effect is

largely limited to the peak load instead of the SEA provided that stable crushing ensues.

All of these results indicate that SEA should not be treated as a material value, but rather a structure value. Fortunately, it has been found that self-supporting structures generally exhibit very similar SEA. For example, it has been shown that sinusoidal samples crushed against a flat plate exhibit SEA equivalent to circular tubes[19]. Recent finite element simulations validating experiments on different geometries have also shown good agreement for circular tubes, semi-circular corrugated, and hat-shaped specimens[20]. The semi-circular corrugated specimen geometry was proposed by Feraboli and has seen extensive use in recent work[21–29]. As such, significant data exists for this geometry to make comparisons between experiments.

The study detailed in this manuscript seeks to evaluate the crashworthiness of discontinuous carbon fiber composites using the Feraboli geometry. Recycled carbon fibers are used to reinforce polyphenylene sulfide (PPS), acrylonitrile butadiene styrene (ABS), and epoxy matrices. Crush tests are conducted at multiple temperatures and rates to further understand the impact of these parameters on the crashworthiness of these composites. Digital image correlation is used to measure the local strain to identify the impact of manufacturing defects identified from x-ray computed tomography images. The results are compared to the existing literature.

Materials and Methods

Recycled Carbon Fibers

Recycled carbon fibers were provided in the form of carded nonwoven preforms of nominal 200 g m^{-2} areal density (measured 184.2 ± 11.2 g m^{-2}). The preforms were produced using a carding process, in which the fibers were mechanically entangled using a series of combs. As described in the author's earlier work, the preforms were anisotropic. Fibers were found to be primarily oriented in the cross direction of the as-received rolls of material. Since it is known from the literature that energy absorption is maximized when a greater number of fibers are oriented in the load direction, all test specimens for temperature and rate testing were produced with fibers oriented in the cross direction. To validate this, testing of machine direction specimens was completed at 50.8 mm min^{-1} to illustrate the effect of fiber orientation.

Polymer Matrix

Three polymer matrices were considered: polyphenylene sulfide (PPS), acrylonitrile butadiene styrene (ABS), and epoxy. The PPS was purchased as films of nominal 0.127 mm thickness (Ryton QC160P, Solvay). Organosheet samples were produced by compressing a fiber preform between two films for five minutes at 300 °C and 1 MPa pressure. The organosheets were then cut to size and placed in the semi-circular corrugated mold for processing at the same time and

temperature, with increased molding pressure of 2 MPa. Two additional PPS films were placed at the mold surfaces to ensure good surface quality for the samples. The resulting Feraboli crush geometry is shown in Figure VI-1[21]. The tensile and shear properties of the PPS/recycled carbon fiber composites are shown in Table VI-1, along with their glass transition temperature determined by dynamic mechanical analysis, storage modulus retention at the glass transition temperature, and IZOD impact resistance. Three samples each were used to measure the dynamic mechanical properties and ten samples each were used to determine the IZOD impact resistance. The 1-direction is defined as the machine direction of the as-received fiber roll. PPS is a semi-crystalline thermoplastic, thereby exhibiting properties that are largely dictated by its thermal history.

The ABS was purchased as films of nominal 0.127 mm thickness (Cycolac EXABS01, Sabic). Organosheet samples were produced by compressing a single fiber preform between two films for 10 minutes at 210 °C and 1 MPa pressure. The samples were pre-heated on the press for 5 minutes before molding. Crush specimens were produced using the same temperature and time at 2 MPa molding pressure. The thermal and mechanical properties are also found in Table VI-1. Oddly, the impact resistance of the ABS composites was lower than that of the neat ABS, indicating that the fibers failed to absorb energy. Prior work by the author has shown that these composites have very poor interfacial shear strength. ABS is an amorphous thermoplastic, thereby exhibiting properties that are not dictated by thermal history.

The epoxy was a two-part system typically used in the civil engineering industry (Epikote Resin 862/Epikure Curing Agent W, Resolution Performance Products). Samples were produced in the corrugated mold using a wet-compression setup. The cure temperature and time followed the manufacturer's recommendation (2.5 hours at 177 °C) at 1 MPa pressure imparted by a heated hydraulic pressure. The thermal and mechanical properties can be found in Table VI-1. Epoxy is a thermoset material that undergoes an irreversible curing process that is strongly influenced by the cure cycle.

Quasi-Static Testing

Quasi-static testing was completed between flat steel plates at a constant displacement rate. The sample dimensions are found in Figure VI-1. A 45° chamfer was cut along one side of the sample to initiate crushing. Displacement was limited to 25.4 mm to prevent interference between the crushed debris and bottom platen. Force was recorded using a calibrated load cell, while displacement was measured at the crosshead. Three decades of quasi-static rates were considered: 5.08, 50.8, and 500.8 mm min^{-1}. These tests were completed at room temperature. The lower 12.7 mm of samples tested at the highest rate was clamped in a fixture to prevent the sample from falling over or leaning due to imperfections in the geometry. Preliminary testing found no difference in the crush behavior of clamped and unclamped samples. Additional tests at the 50.8 mm min^{-1} test rate were completed in a temperature chamber, where the temperature was set to -40 °C,

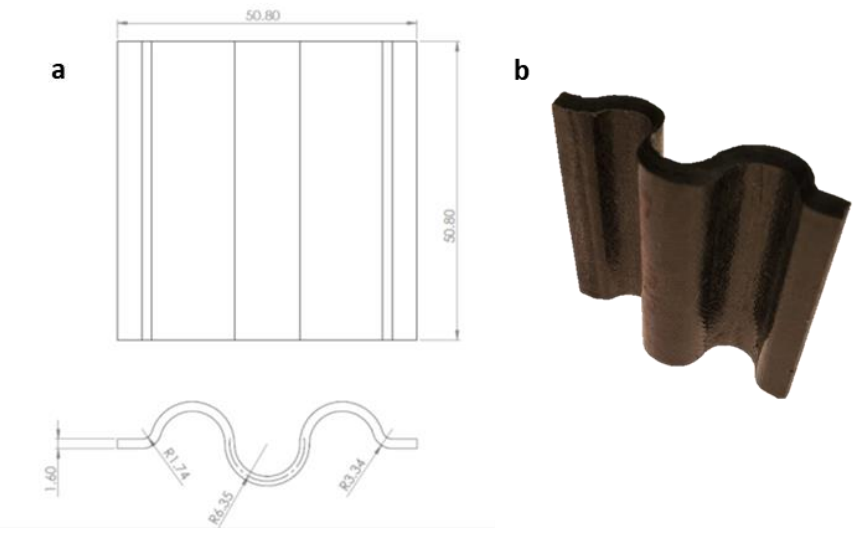

Figure VI-1. a) Feraboli crush geometry (sample dimensions in mm); b) ABS crush sample

Table VI-1. Thermal and mechanical properties of composites (resin properties in parenthesis)

Matrix	**T_g (°C)**	**Storage Modulus Retention (%)**	**IZOD Impact Resistance (J m^{-1})**	**E_1 (GPa)**	**E_2 (GPa)**	**G_{12} (GPa)**	**σ_1 (MPa)**	**σ_2 (MPa)**	**τ_6 (MPa)**
PPS	109	80.6	156 (53*)	16 (3.4*)	34 (3.4*)	7.9 (1.2*)	139 (75*)	268 (75*)	122 (43*)
ABS	109	66.3	366 (411*)	12 (2.0*)	26 (2.0*)	5.4 (0.7*)	88 (39*)	223 (39*)	68 (23*)
Epoxy	150	53.5	84 (28)	15 (2.7*)	32 (2.7*)	6.4 (1.0*)	150 (79*)	281 (79*)	143 (46*)

*Values taken from datasheets

room temperature, 80 °C, and the glass transition temperature. The lower three temperatures represent the typical range of temperatures that automotive materials must withstand as specified by automotive manufacturers[30]. The glass transition temperature behavior is of interest as it provides an even more aggressive upper bound for crashworthy structures. The lower clamping fixture was used in all non-room temperature tests.

Particle Size Distribution

The distribution of the particle sizes of the crushed debris was quantified using sieves and a shaker (Gilson Company, SS-12R). Crushed samples and debris were placed in a 25 mm sieve and allowed to fall through progressively smaller sieves of sizes 12.5 mm, 4 mm, 2 mm, 0.85 mm, and 0.5 mm. Shaking time was limited to 1 minute to limit damage induced during the sieving process. The sieves were cleaned before each test. After testing, the material was carefully placed in a clean ceramic weighing boat and the mass of the debris at each size was recorded to the tenth of a milligram. Two samples were run per test condition. A correlation of debris size to energy absorption is explored using this data.

X-ray Computed Tomography

X-ray computed tomography (XCT) was used to identify local manufacturing defects such as void content in the samples. A total of six samples of each type were scanned together at 40 keV and 89 µA to a resolution of approximately 40 μm^3. Scans were completed on a laboratory source (Hamamatsu, model L9421-02) and detector (Varex, model 1622).

Digital Image Correlation

Digital image correlation (DIC) was used to evaluate the strain behavior encountered during testing of the samples imaged using XCT. The image acquisition rate was chosen for each crosshead displacement rate such that a minimum of 10 images was captured per 1 mm displacement. The images were correlated and the local behavior was measured using the commercially-available software, Vic-3D (Correlated Solutions). Two samples for each room temperature test condition were analyzed using DIC. The regions of manufacturing defects were observed to determine their impact on the crush behavior of organosheet composites. If local microstructural flaws strongly impact the crashworthiness of organosheet composites, the digital image correlation data would show strain irregularities.

Results

Crush Testing

The results of the crush tests can be found in Table VI-2. In addition to the SEA, the steady-state crush force and mean crush stress were reported. The

Table VI-2. Crush test results

Matrix Material	Rate (mm min^{-1})	Temperature (°C)	Number of Samples	Steady State Crush Stress (MPa)	SEA (kJ kg^{-1})
PPS	50.8	-40	5	140.4 ± 16.3	115.1 ± 8.6
	50.8	RT	7	122.0 ± 13.8	95.2 ± 4.8
	50.8	80	5	99.3 ± 10.2	72.9 ± 4.6
	50.8	109	5	65.7 ± 4.3	51.8 ± 3.5
	5.08	RT	5	110.6 ± 18.7	88.4 ± 5.4
	508	RT	5	140.0 ± 33.7	109.7 ± 13.9
MD	50.8	RT	6	106.5 ± 7.1	77.8 ± 4.8
ABS	50.8	-40	5	74.7 ± 10.0	69.9 ± 5.6
	50.8	RT	6	46.7 ± 7.1	47.3 ± 6.5
	50.8	80	5	31.5 ± 2.1	30.2 ± 1.9
	50.8	109	4	13.3 ± 1.9	13.0 ± 2.0
	5.08	RT	5	45.6 ± 10.1	44.9 ± 10.8
	508	RT	4	58.0 ± 11.0	52.2 ± 5.2
MD	50.8	RT	6	35.3 ± 5.4	33.2 ± 3.9
Epoxy	50.8	-40	5	110.8 ± 12.4	99.3 ± 8.3
	50.8	RT	6	132.3 ± 7.1	109.8 ± 7.8
	50.8	80	5	99.3 ± 5.6	95.9 ± 3.2
	50.8	150	5	65.7 ± 5.3	31.4 ± 4.7
	5.08	RT	5	131.4 ± 5.3	109.5 ± 8.4
	508	RT	7	138.1 ± 11.8	118.6 ± 10.6
MD	50.8	RT	6	105.2 ± 5.2	89.2 ± 4.4

steady-state crush force occurs after the chamfer has been consumed and the crush behavior stabilizes. In this study, the steady-state crush force was typically in the range of 5 to 20 mm of crosshead displacement. The mean crush stress is defined as the steady-state crush force divided by the cross-sectional area of the sample. While not a true measurement of the stress state within the sample, it provides an estimate of the compressive stresses experienced by the material immediately ahead of the crush front.

General trends revealed that thermoplastic samples exhibited an increase in SEA and mean crush stress with the loading rate in the quasi-static regime. This behavior is likely due to increased matrix elasticity with increasing loading rate. Epoxy samples were shown to be strain rate insensitive in the quasi-static regime. The machine direction crush properties were found to be lower than the cross-direction for all samples, indicating that the crush behavior of the material is dependent upon material anisotropy.

The effect of temperature on the SEA and the mean crush stress of thermoplastic composites was one of decreasing energy absorption with increasing temperature. For both ABS and PPS, the maximum SEA was realized at -40 °C. This behavior is likely due to increased elasticity, as in the case of increasing loading rates. Conversely, the epoxy samples exhibited a decreased SEA at low temperatures due to embrittlement.

Increased temperatures were found to decrease the SEA and mean crush stress in all samples. The thermoplastic samples showed a stronger decrease at 80 °C, with ABS losing 36% and PPS losing 23% of their initial SEA, while the epoxy samples saw only a 13% decrease. However, this trend changed at the glass transition temperature. The ABS samples showed a 73% decrease and the epoxy samples showed a 71% decrease, while the PPS samples showed only a 46% decrease. These results agree with the storage modulus retention values obtained via DMA, where PPS composites were shown to retain the greatest elasticity at their glass transition temperature.

Particle Size Distribution

The particle sizes measured by sieving the samples can be found in Figure VI-2. A few trends are obvious. In general, the epoxy composites produced finer particles than the thermoplastic composites. The ABS composites produced the largest particles, indicating that particle size is likely a function of matrix elasticity and fracture toughness. Similarly, the particle size tended to increase with temperature. ABS samples exhibited no crush debris when tested at their glass transition temperature. For small sieve sizes, the trends were less clear, likely the result of small amounts of error in gathering crush debris from the samples. In the case of the epoxy samples tested at -40 °C, the particle sizes were very small, with no particles found in the range of 4 mm to 25 mm. Only the uncrushed sample portion and a significant amount of fine dust remained, indicating that high matrix elasticity and low toughness at low temperatures led to a pulverization failure mode. As shown in Figure VI-3, these samples exhibited no frond formation, which

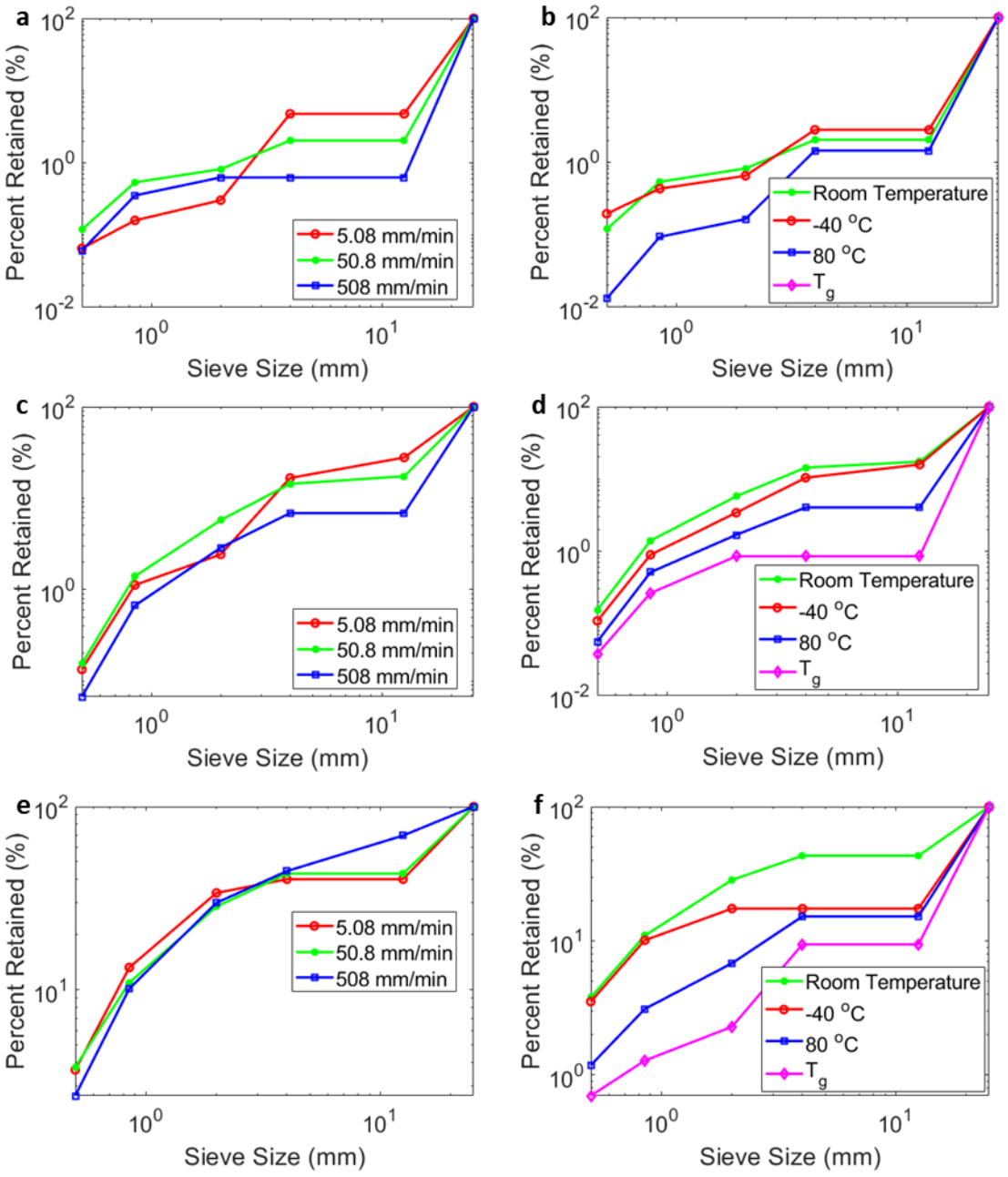

Figure VI-2. Particle size distribution results for: a) ABS rate testing; b) ABS temperature testing; c) PPS rate testing; d) PPS temperature testing; e) Epoxy rate testing; f) Epoxy temperature testing

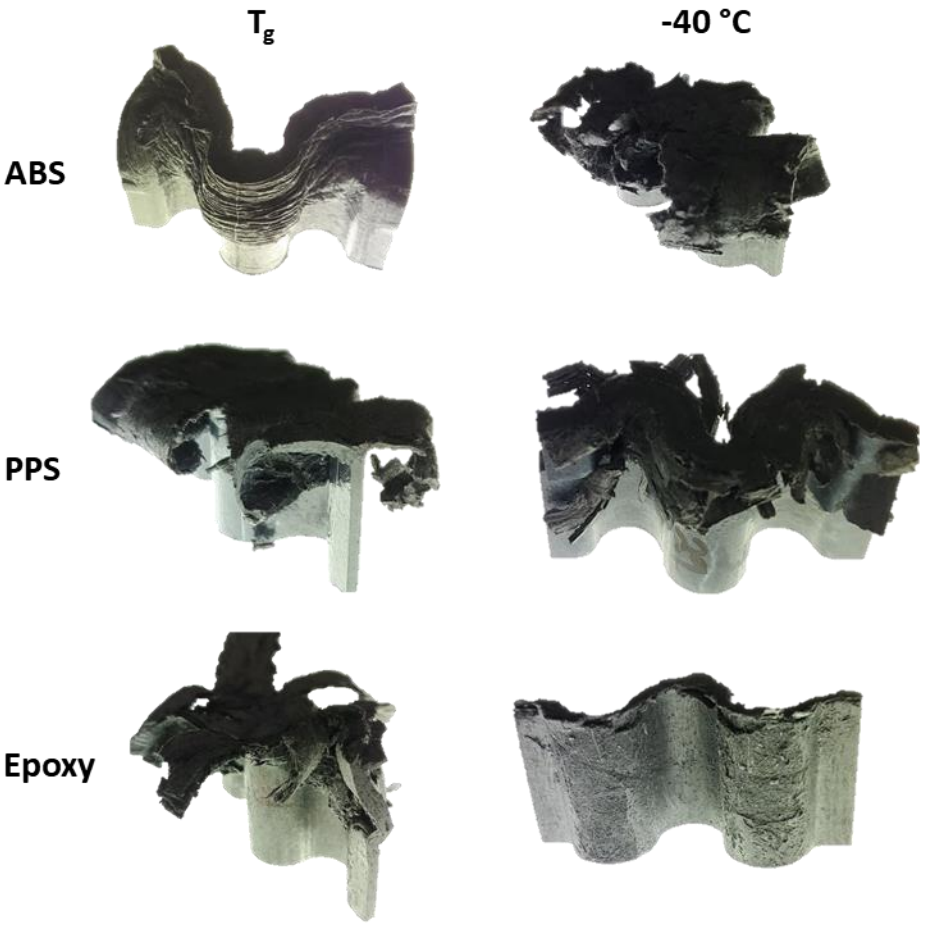

Figure VI-3. Crush morphology of samples tested at high and low-temperature limits

explains their decrease in energy absorption. Conversely, larger fronds formed at higher temperatures for all matrix materials, indicating an improvement in fracture toughness. However, the decrease in mechanical properties associated with an increase in temperature led to lower energy absorption. The ABS composites tested at their glass transition temperature yielded no fronds and instead failed in a progressive folding mode typical of metal crush tubes. In general, larger particle sizes indicate less energy absorption, though very small particle size may indicate embrittlement and therefore decreased energy absorption.

Impact of Defects on Crush Behavior

Manufacturing defects identified in the composites were primarily in the form of porosity. Figure VI-4 shows a cross-section taken from the XCT imaging for each sample type with common flaw types associated with each sample. The ABS sample shows poor interlayer adhesion, with void content near the peaks of the sinusoidal curve. This type of defect was commonly found in many ABS samples. The PPS sample shows ductile tearing at the steepest portion of the sinusoidal curve, as the organosheet may have not sufficiently softened before pressure was applied during molding. This defect was not apparent in all samples, though it also was apparent in some ABS samples. The epoxy samples show micro-porosity throughout the sample, which was apparent in all samples. This is in agreement with porosity found in flat plate samples made in the author's prior work.

It was found that ductile tearing in the thermoplastic composites always had a strong impact on their stability during testing, while the micro-porosity of the epoxy samples did not cause unstable failure. Ductile tearing was apparent in both the ABS and PPS samples, though more prevalent in the PPS. It was likely caused by the relative stiffness of the organosheets that did not always conform well to the heated mold. When present, this flaw always led to a reduction in the relevant crash properties due to unstable crushing. Interestingly, the failure location was not always at the tear. In many cases, failure initiated on the side opposite the tear, indicating that the load was primarily borne by that side until failure. An example of this is shown in Figure VI-5.a. Another manufacturing defect that can occur in composites is foreign object damage. One epoxy sample showed a foreign object, apparent as a bright spot in the XCT scan, which caused local buckling. The buckling did not affect the overall crush behavior of the sample though. However, large foreign objects could have a more severe effect and therefore care should be taken to avoid embedding debris in these composites. In general, the poor interlayer adhesion in some ABS composites did not have a significant effect on their crush behavior.

Discussion

The results of this study indicate that discontinuous fiber composites offer enhanced crashworthiness relative to most continuous fiber composites. Table VI-3 provides a comparison of the results of this study with the existing literature

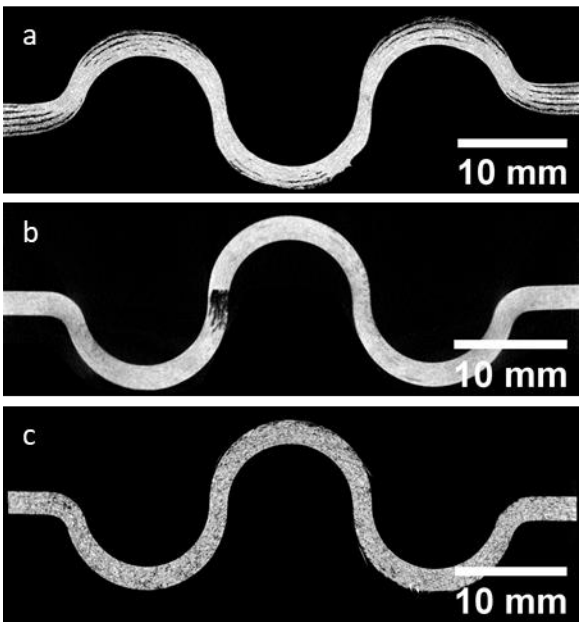

Figure VI-4. Defects captured in XCT scans: a) ABS sample containing interlayer voids; b) PPS sample exhibiting ductile tearing; c) Epoxy sample exhibiting micro-porosity

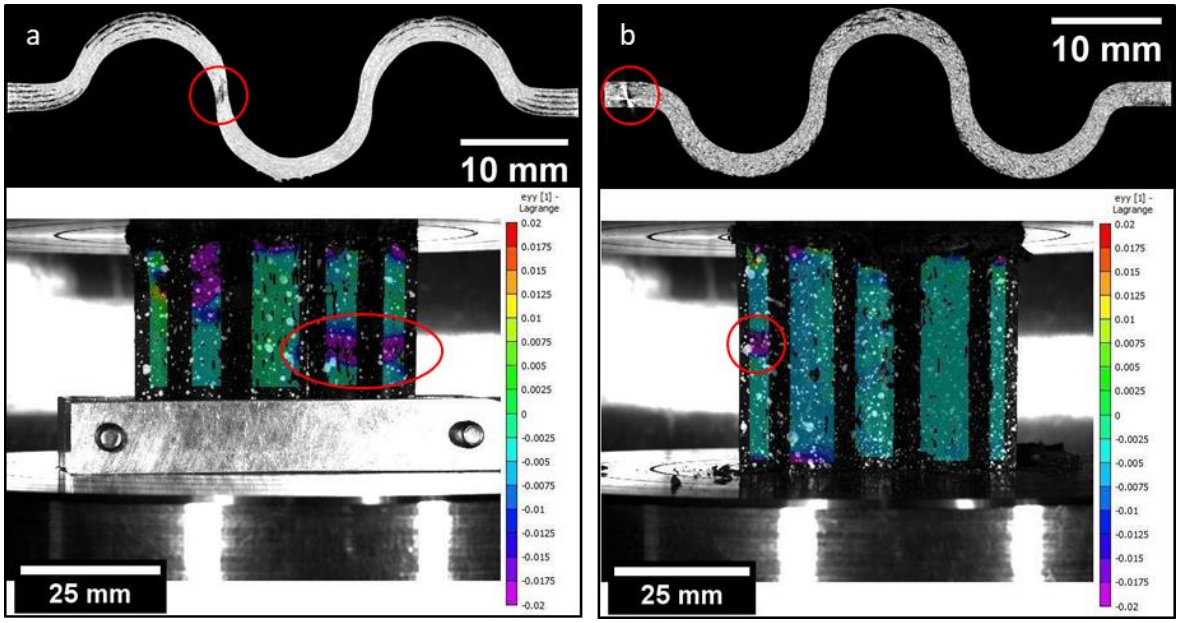

Figure VI-5. Correlation between XCT and DIC data: a) Example ductile tearing flaw and corresponding strain concentration on opposite sides of an ABS sample; b) Foreign object flaw and corresponding local buckling in an epoxy sample

on semi-circular corrugated specimens. The SEA and mean crush stress are reported for samples tested between 2.5 and 50.8 mm min^{-1}. The literature indicates that typical continuous carbon fiber epoxy composites in a $[0/90]_{ns}$ layup yield a SEA of about 70 kJ kg^{-1} that is independent of the thickness between 1.6 and 3.0 mm and testing rate between 2.5 and 50.8 mm min^{-1}. For high toughness epoxy resins tested, the SEA of the same laminate is typically about 98 kJ kg^{-1}, indicating that matrix toughness may play a significant role in the energy absorption of continuous fiber composites. Unidirectional fiber composites made with a high toughness thermoplastic PEKK matrix tested at 5 mm min^{-1} have a SEA of about 110 kJ kg^{-1}, the highest measured result found in the existing literature for the Feraboli geometry, further validating that matrix toughness plays a significant role. The experiments here show that comparable energy absorption to PEKK is possible with an epoxy matrix reinforced with discontinuous recycled carbon fibers. A PPS matrix offers energy absorption near toughened epoxy continuous fiber composites and exceeding that of standard epoxies.

The effect of laminate orientation is also apparent from the literature. Fewer 0° plies lead to reduced energy absorption, as described in the literature for circular tube specimens[6]. The lowest measured SEA value was found to occur for an angle-ply laminate, though adding a small number of 0° plies significantly improved the SEA. In fact, a $[0/\pm45]_{2s}$ laminate was found to have greater energy absorption capability than a cross-ply laminate, indicating that ±45° plies are more favorable than 90° plies for constraining delamination, despite the reduction in the number of 0° plies. Similarly, a toughened epoxy with 75% of the plies oriented in the 90° direction exhibited low energy absorption capabilities. A similar trend was found for the samples manufactured with the machine direction along the crush axis. Prior work by the author has shown that nearly twice as many fibers are oriented in the cross direction than the machine direction in the recycled carbon fiber preforms used in this study.

Laminates consisting of woven fabrics yielded a greater range of properties with some interesting results. Plain weave fabrics made with a toughened epoxy achieve SEA values near 70 kJ kg^{-1} for both $[0/90]_{2s}$ and $[\pm45]_{2s}$ laminate sequences, while standard epoxies yield near 90 kJ kg^{-1} for $[0/90]_{2s}$ laminates. This result is unexpected, as toughened epoxy systems yield greater SEA than standard epoxies in unidirectional fiber laminates. Further studies will be necessary to establish this trend. It is possible that the crush failure mechanism of woven composites is significantly different than that of unidirectional composites due to fiber crimp, thereby negating the effects of improved matrix toughness. For the composites studied here, splaying failure modes were typically suppressed in favor of fragmentation due to strong interlaminar bonding, unlike in typical unidirectional continuous fiber laminates.

Overall, the PPS composites exhibited the most stable crush properties across a range of temperatures and loading rates. At its glass transition temperature, the PPS composites yielded 39% higher SEA than the epoxy

Table VI-3. Comparison to crashworthiness of continuous fiber composites found in literature utilizing the semi-circular corrugated geometry and tested at quasi-static rates

Matrix Type	**Matrix Notes**	**Laminate Orientation**	**Steady State Crush Force (kN)**	**Steady State Crush Stress (MPa)**	**SEA (kJ kg^{-1})**	**Reference**
PPS	Thermoplastic	Quasi-Random	18.2	119	93.8	This study
ABS	Thermoplastic	Quasi-Random	7.8	49	49.5	This study
Epoxy	Standard	Quasi-Random	18.6	135	112.1	This study
PEKK	Thermoplastic	$[0/90]_{3s}$	22.4	176	110.1	[23]
Epoxy	Toughened	$[90/0/90_2]_s$	17.7	90	56.4	[24]
Epoxy	Standard	$[0/90]_{3s}$	34.6	129	73.9	[26]
Epoxy	Standard	$[0/90]_{3s}$	15.5	109	70.0	[21]
Epoxy	Toughened	$[0/90]_{3s}$	21.0	147	93.0	[21]
Epoxy	Standard	$[0/\pm45]_{2s}$	17.9	126	81.0	[21]
Epoxy	Standard	$[\pm45]_{3s}$	12.4	87	56.0	[21]
Epoxy	Standard	$[0/90]_{4s}$	15.7	111	72.5	[31]
Epoxy	Standard	$[0/90]_{3s}$	14.6	102	67.1	[22]
Epoxy	Standard	Plain Weave Fabric $[0/90]_{2s}$	19.3	135	89.0	[29]
Epoxy	Toughened	Plain Weave Fabric $[0/90]_{2s}$	16.6	116	70.3	[28]
Epoxy	Toughened	Plain Weave Fabric $[\pm45]_{2s}$	17.2	120	73.0	[28]
Epoxy	Toughened	$[0/90]_{3s}$	22.2	156	102.4	[28]

composites at their glass transition temperature. As such, recycled carbon fiber/PPS organosheet composites are a strong candidate as a crashworthy automotive material. Beyond the crashworthiness of the material, thermoplastic composites offer reduced cycle time, reduced material storage requirements, and improved recyclability relative to epoxy composites. These traits are each of great importance to the automotive industry, as each lowers the cost of adoption of composite materials. In cases where the cost of PPS resin may be prohibitive, lower-cost thermoplastics such as ABS may still be a viable option, as the SEA exceeds that of common automotive metals such as steel and aluminum.

Conclusions

The key results of this paper can be summarized as follows:

1. Organosheet composites offer energy absorption that meets or exceeds continuous fiber composites at a significantly reduced cost due to the use of recycled carbon fibers.
2. The orientation of the organosheet lamina influences energy absorption, but not as severely as in the case of continuous fiber composites.
3. Thermoplastic composites exhibit better energy absorption capabilities at low temperatures due to matrix stiffening, whereas epoxy composites become overly brittle and exhibit reduced energy absorption relative to room temperature testing.
4. Thermoplastic composites exhibit a clear rate-dependence with increasing energy absorption with increased strain rate, while epoxy composites are rate-independent.
5. Of the composites tested here, PPS exhibits the most stable energy absorption capabilities across a range of temperatures and rates expected in automotive applications.
6. Crush debris particle size correlates well with energy absorption, where larger particle sizes indicate less energy absorption.
7. Local flaws such as micro-porosity do not impact energy absorption significantly, but larger flaws such as ductile tearing of thermoplastic organosheets during molding can lead to premature failure in crush testing.

Future work will seek to test these composites at higher strain rates that are indicative of automotive crash scenarios. Other suggested future work include improving the molding capabilities to reduce ductile tearing, further study of the crashworthiness of woven fabrics, and studying other matrix materials that are relevant to the automotive industry.

References

[1] N.H.T.S. Administration, Traffic Safety Facts 2017: A Compilation of Motor Vehicle Crash Data, 2019. https://crashstats.nhtsa.dot.gov/Api/Public/ViewPublication/812806.

[2] P.H. Thornton, J.J. Harwood, P. Beardmore, Fiber-reinforced plastic composites for energy absorption purposes, Composites Science and Technology. 24 (1985) 275–298. Doi:10.1016/0266-3538(85)90026-0.

[3] H. Dirk, J.A. Lukaszewicz, Automotive composite structures for crashworthiness, in: Advanced Composite Materials for Automotive Applications: Structural Integrity and Crashworthiness, 2013: pp. 99–127. Doi:10.1002/9781118535288.

[4] H. Hamada, J.C. Coppola, D. Hull, Z. Maekawa, H. Sato, Comparison of energy absorption of carbon/epoxy and carbon/PEEK composite tubes, Composites. 23 (1992) 245–252. Doi:10.1016/0010-4361(92)90184-V.

[5] S. Ramakrishna, H. Hamada, Z. Maekawa, H. Sato, Energy Absorption Behavior of Carbon-Fiber-Reinforced Thermoplastic Composite Tubes, Journal of Thermoplastic Composite Materials. 8 (1995) 323–344. Doi:10.1177/089270579500800307.

[6] D. Hull, A unified approach to progressive crushing of fibre-reinforced composite tubes, Composites Science and Technology. 40 (1991) 377–421. Doi:10.1016/0266-3538(91)90031-J.

[7] S. Ramakrishna, H. Hamada, Energy absorption characteristics of crash worthy structural composite materials, Key Engineering Materials. (1998) 585–620. Doi:10.4028/www.scientific.net/kem.141-143.585.

[8] W.H. Tao, R.E. Robertson, P.H. Thornton, Effects of material properties and crush conditions on the crush energy absorption of fiber composite rods, Composites Science and Technology. 47 (1993) 405–418. Doi:10.1016/0266-3538(93)90009-6.

[9] N.A. Warrior, T.A. Turner, F. Robitaille, C.D. Rudd, The effect of interlaminar toughening strategies on the energy absorption of composite tubes, Composites Part A: Applied Science and Manufacturing. 35 (2004) 431–437. Doi:10.1016/j.compositesa.2003.11.001.

[10] T.A. Turner, F. Robitaille, N.A. Warrior, C.D. Rudd, E.J. Cooper, Effect of resin formulation on crash energy absorbing composite structures made by RTM, Plastics, Rubber and Composites. 31 (2002) 49–57. Doi:10.1179/146580102225001436.

[11] G.C. Jacob, J.M. Starbuck, J.F. Fellers, S. Simunovic, Effect of fiber volume fraction, fiber length and fiber tow size on the energy absorption of chopped carbon fiber-polymer composites, Polymer Composites. 26 (2005) 293–305. Doi:10.1002/pc.20100.

[12] G.C. Jacob, J.M. Starbuck, J.F. Fellers, S. Simunovic, R.G. Boeman, Crashworthiness of various random chopped carbon fiber reinforced epoxy composite materials and their strain rate dependence, Journal of Applied Polymer Science. 101 (2006) 1477–1486. Doi:10.1002/app.24224.

[13] G.C. Jacob, J.F. Fellers, J.M. Starbuck, S. Simunovic, Crashworthiness of Automotive Composite Material Systems, Jounal of Applied Polymer Science. 92 (2004) 3218–3225. Doi:10.1002/app.20336.
[14] T. Turner, L. Harper, N. Warrior, A. Caliskan, Energy absorption performance of meso-scale discontinuous carbon fibre composites, International Journal of Vehicle Structures and Systems. 3 (2011) 80–86. Doi:10.4273/ijvss.3.2.02.
[15] G.C. Jacob, J. Michael Starbuck, S. Simunovic, J.F. Fellers, Energy Absorption in Glass-Reinforced Continuous Strand Mat Composites, Journal of Applied Polymer Science. 90 (2003) 3222–3232. Doi:10.1002/app.12999.
[16] H. Hamada, S. Ramakrishna, Comparison of Static and Impact Energy Absorption of Carbon Fiber/PEEK Composite Tubes, in: Composite Materials: Testing and Design: Twelfth Volume, ASTM International, 100 Barr Harbor Drive, PO Box C700, West Conshohocken, PA 19428-2959, 1996: pp. 182-182–16. Doi:10.1520/STP16545S.
[17] H. Hamada, S. Ramakrishna, H. Sato, Effect of testing temperature on the energy absorption behavior of carbon fiber/PEEK composite tubes, Journal of Reinforced Plastics and Composites. 15 (1996) 30–47. Doi:10.1177/073168449601500103.
[18] J.N. Price, D. Hull, Axial crushing of glass fibre-polyester composite cones, Composites Science and Technology. 28 (1987) 211–230. Doi:10.1016/0266-3538(87)90003-0.
[19] S. Hanagud, J.I. Craig, P. Sriram, W. Zhou, Energy Absorption Behavior of Graphite Epoxy Composite Sine Webs, Journal of Composite Materials. 23 (1989) 448–459. Doi:10.1177/002199838902300502.
[20] L.N.S. Chiu, B.G. Falzon, B. Chen, W. Yan, Validation of a 3D damage model for predicting the response of composite structures under crushing loads, Composite Structures. 147 (2016) 65–73. Doi:10.1016/j.compstruct.2016.03.028.
[21] P. Feraboli, Development of a Corrugated Test Specimen for Composite Materials Energy Absorption, Journal of Composite Materials. 42 (2008) 229–256. Doi:10.1177/0021998307086202.
[22] P. Feraboli, B. Wade, F. Deleo, M. Rassaian, M. Higgins, A. Byar, LS-DYNA MAT54 modeling of the axial crushing of a composite tape sinusoidal specimen, Composites Part A: Applied Science and Manufacturing. 42 (2011) 1809–1825. Doi:10.1016/j.compositesa.2011.08.004.
[23] W. Tan, B.G. Falzon, Modelling the crush 148ygrothe of thermoplastic composites, Composites Science and Technology. 134 (2016) 57–71. Doi:10.1016/j.compscitech.2016.07.015.
[24] S.J. Pety, J.E. Aw, A.C. Gendusa, P.R. Barnett, Q.A. Calvert, N.R. Sottos, S.R. White, S. Pety, S; En Aw, J; Gendusa, A.; Barnett, P; Calvert, Q; Sottos, N; White, Effect of microchannels on the crashworthiness of fiber-reinforced composites, Composite Structures. 184 (2018) 428–436. Doi:https://doi.org/10.1016/j.compstruct.2017.09.105.

[25] S. Duan, Y. Tao, X. Han, X. Yang, S. Hou, Z. Hu, Investigation on structure optimization of crashworthiness of fiber reinforced polymers materials, Composites Part B: Engineering. 60 (2014) 471–478. Doi:10.1016/j.compositesb.2013.12.062.
[26] L. Grauers, R. Olsson, R. Gutkin, Energy absorption and damage mechanisms in progressive crushing of corrugated NCF laminates: Fractographic analysis, Composite Structures. 110 (2014) 110–117. Doi:10.1016/j.compstruct.2013.11.001.
[27] Y. Ren, H. Jiang, W. Ji, H. Zhang, J. Xiang, F.G. Yuan, Improvement of Progressive Damage Model to Predicting Crashworthy Composite Corrugated Plate, Applied Composite Materials. 25 (2018) 45–66. Doi:10.1007/s10443-017-9610-z.
[28] E. Troiani, L. Donati, G. Molinari, R. Di Sante, Influence of plying strategies and trigger type on crashworthiness properties of carbon fiber laminates cured through autoclave processing, Strojniski Vestnik/Journal of Mechanical Engineering. 60 (2014) 375–381. Doi:10.5545/sv-jme.2013.1506.
[29] F. Deleo, P. Feraboli, Crashworthiness energy absorption of carbon fiber composites: Experiment and simulation, in: Society of Plastics Engineers – 11th-Annual Automotive Composites Conference and Exhibition, ACCE 2011, 2011.
[30] M. Kardos, O. Täger, E. Körner, New class-A sheet molding compounds for automotive exterior components using a single-step surface hybridization: Co-compression molding of high-quality surfaces, in: International Congress PIAE Europe 2020, VDI Verlag GmBbH, Mannheim, Germany, 2020: pp. 249–264.
[31] H.L. Mou, X. Su, J. Xie, Z.Y. Feng, Parametric analysis of composite sinusoidal specimens under quasi-static crushing, The Aeronautical Journal. (2018) 1–19. Doi:10.1017/aer.2018.64.

Roles

Philip Barnett: Conceptualization, Methodology, Software, Formal analysis, Writing – Original draft, Visualization; **Brett Hulett:** Methodology, Investigation, Formal analysis; **Dayakar Penumadu:** Supervision, Project administration, Funding acquisition, Writing – Review & editing

CHAPTER VII. CONCLUSIONS

Future Outlook for Recycled/Repurposed Organosheet Composites

These studies have shown that recycled and repurposed carbon fiber organosheet composites offer immense opportunities for the automotive industry. The mechanical properties exceed existing composite technologies used by the industry such as sheet molding compounds, injection-compression molding, and bulk molding compounds. While not truly competitive with continuous fiber composites in stiffness and strength driven-designs, the superior crashworthiness and reduced material cost make these composites attractive for some applications. Furthermore, relative to traditional thermoset matrices, the simpler storage requirements, infinite shelf life, and reduced environment and health hazards of thermoplastics make these composites more attractive. Other important characteristics of recycled/repurposed organosheet composites include improved fracture toughness, faster cycle time, and the opportunity for end-of-life recycling. These properties, in combination with the current push towards the integration of composite materials in automotive applications, make the impact of this work immediately applicable to solving industry-relevant problems.

Impact of the Current Work

The current work has made the following key contributions to advance the science of recycled/repurposed organosheet composites:

1. The basic mechanical properties were characterized to show that traditional composite laminate theory can be applied to predict their behavior.
2. Void content was found to have relatively little effect on the tensile properties of organosheet composites, allowing opportunities for targeted porosity to meet weight, thermal, or other requirements.
3. The thermo-mechanical properties at a micro and macro level were studied to explain the impact of annealing on composite behavior.
4. The Master Ply invariant approach to predicting continuous fiber composite properties was shown to apply to discontinuous fiber composites.
5. The stochastic behavior of the composites was accurately captured in a novel, highly adaptable micromechanical model to predict the strength of discontinuous fiber composites.
6. A new method of observing the dual-scale permeability effects of composite materials using x-ray imaging was developed and showed that existing permeability measurement techniques do not sufficiently capture the infiltration behavior of film-infused composites.
7. Recycled/repurposed organosheet composites were shown to exhibit superior crashworthiness to continuous fiber composites.

Future Work

Much remains to be understood about recycled/repurposed organosheet composites. Additional thermal and mechanical characterization must be completed to more fully understand their behavior. For example, their compressive properties have not yet been studied. Similarly, a better understanding of their fracture behavior could inform improved modeling. Testing of fatigue and 152ygrothermal effects also presents a unique opportunity that is especially pertinent to the automotive industry. The development of sizings that can be applied to recycled fibers to improve fiber/matrix bonding is of importance for maximizing the mechanical properties of discontinuous fiber composites.

Additional work in modeling the strength of discontinuous fiber composites must be pursued. For example, the model proposed here works well for carbon fiber composites but has not been validated on glass fiber composites. Likewise, modeling of the crush behavior of organosheet composites deserves special consideration. The fiber orientation and volume fraction distributions may yield locally inhomogeneous properties that make such modeling more difficult than for continuous fiber composites.

Inevitably, scrap material will be generated from the production of any composite. Organosheet composites present a unique opportunity to reuse scrap material that should also be explored. For example, the trimmings may be easily cut into platelets to be molded in parts with complex geometries that are not conducive to organosheet molding. There is no shortage of opportunities to study this new and novel class of composite material.

APPENDICES

Supplementary Information for Chapter II

SII-1. Discussion of Inhomogeneity Metric

The inhomogeneity metric was developed by taking the average strain across eight sample regions as shown in Figure S1.a. The variation from the global strain was defined as the ratio of the strain in each region to the strain across all regions. Figure S1.b shows that the inhomogeneity was greater in the virgin fiber wet-laid samples than the carded recycled fiber samples. Figure S2 illustrates the variation in strain through the thickness of a cross direction composite sample made of virgin fiber. In particular, the strain in Region 8 varies significantly across the thickness. Conversely, Figure S3 shows that the strain variation is small in the recycled fiber organosheet samples, as is expected for thin samples in which the surfaces are a larger portion of the total volume.

SII-2. Discussion of Dry Nonwoven Preform Testing in Tension

Dry nonwoven tensile testing illustrated the anisotropy of preform materials. In the case of the carded recycled fibers, the cross direction exhibited much higher peak force and reduced strain-to-failure, indicating that more fibers were aligned in the cross direction. Wet-laid virgin fiber nonwovens showed similar strain-to-failure, but a significant load increase in the machine direction, indicting anisotropy in that direction. The failure mode of the machine direction virgin fiber samples was primarily delamination along the sample length, as indicated at the arrows in Figure S5.a. The cross direction failure was primarily local fiber pull-out (Figure S5.b). Necking was observed in the carded recycled fiber preforms in both the machine and cross directions (Figure S5.c). Necking indicates that a more homogeneous failure occurred, as local flaws did not cause catastrophic failure as in the case of the virgin fiber nonwovens.

SII-3. Mechanical Testing Results

The results of the mechanical testing completed for this chapter are found in Tables S1-S4.

SII-4. Void Content Analysis Results

The results of the void content analysis are found in Tables S5 and S6.

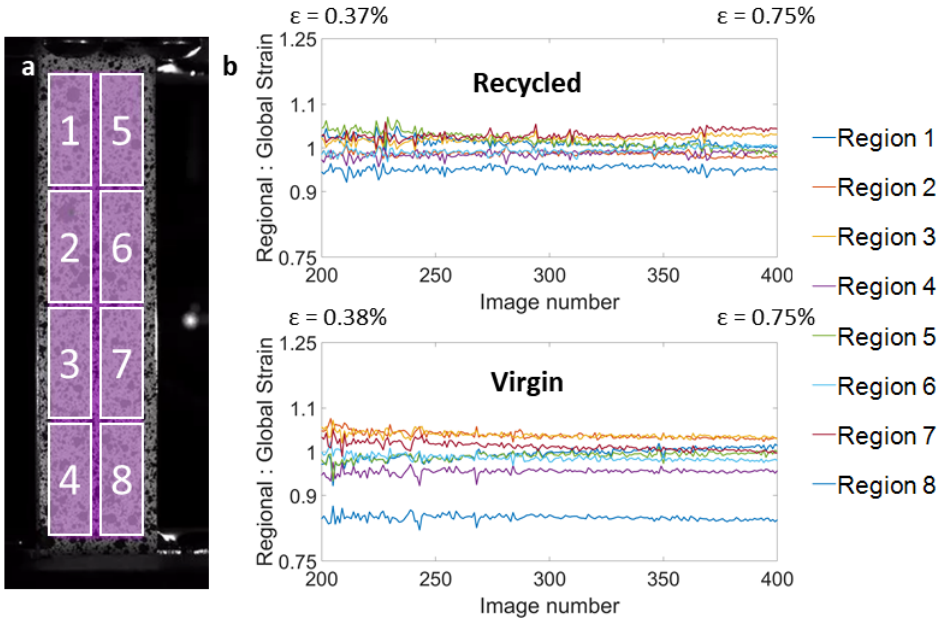

Figure S1. A) Illustration of local strain regions used to determine inhomogeneity metric; b) Example of strain variation in machine direction composite samples

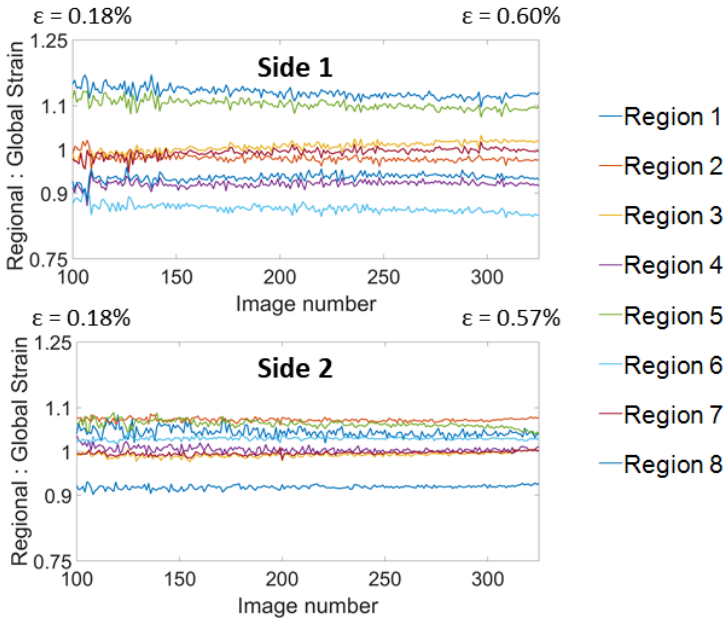

Figure S2. Illustration of large local strain variation through the thickness of the virgin fiber cross direction composite sample

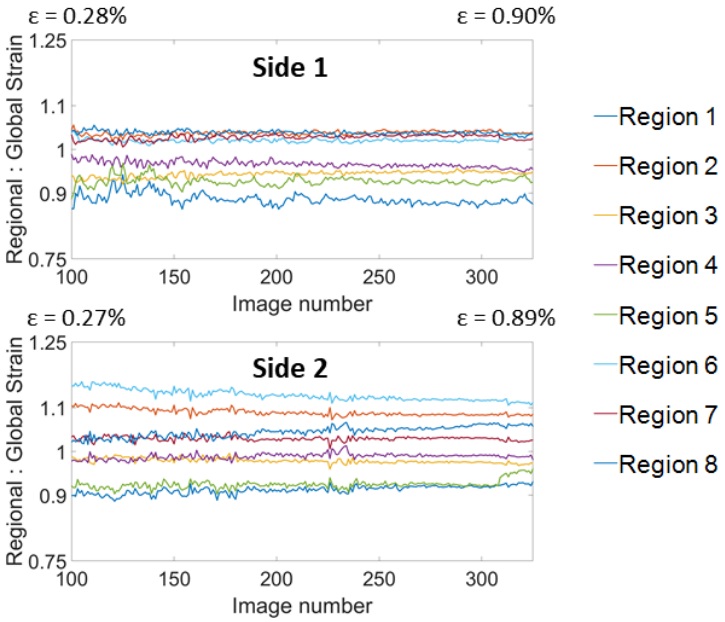

Figure S3. Illustration of small local strain variation through the thickness of the recycled fiber machine direction organosheet sample

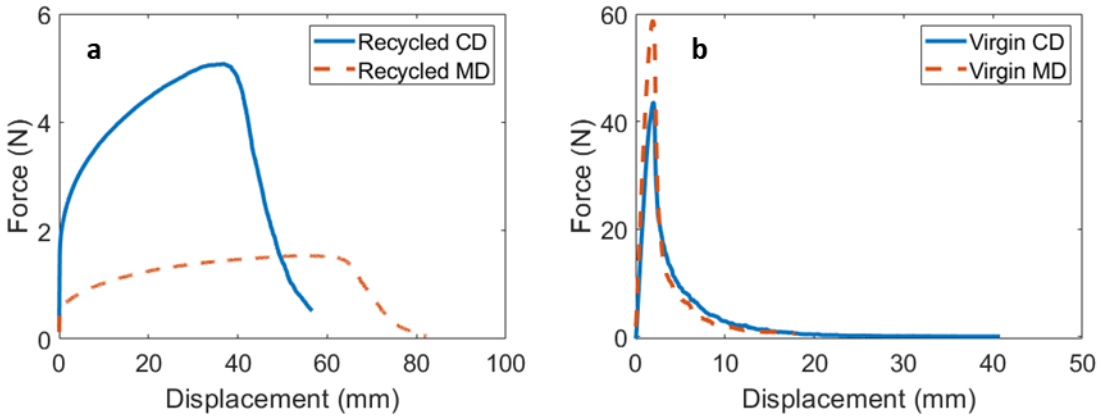

Figure S4. Typical load-displacement curves for dry preform testing

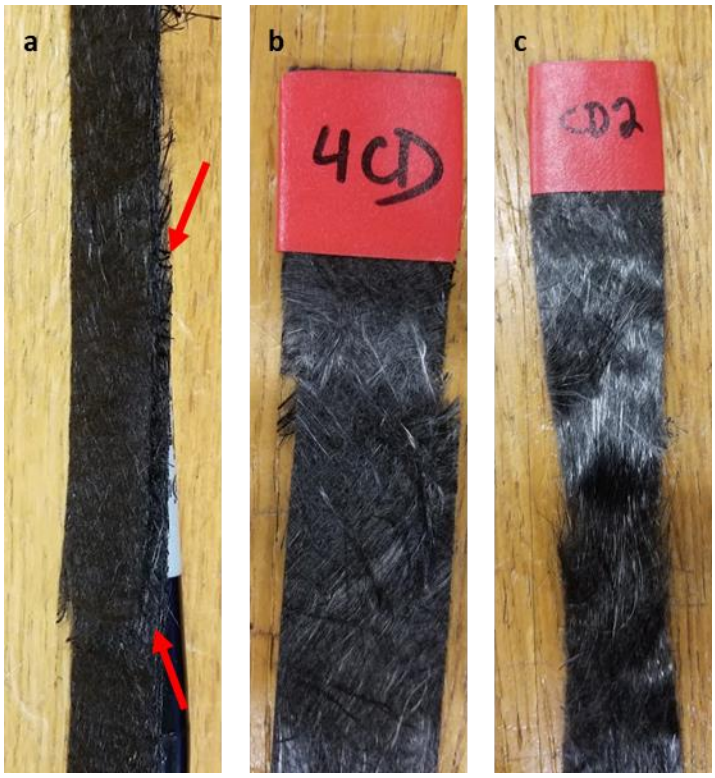

Figure S5. A) Delamination failure mode in machine direction virgin fiber composites; b) Local fiber pull-out failure mode in cross direction virgin fiber composites; c) Necking failure mode in recycled fiber composites

Table S1. Tensile test results for virgin fiber composites

Orientation	Strength (MPa)	Tensile Modulus (GPa)	Strain-to-Failure (%)
[90/0/90/0]	175.97	25.1	0.723
[90/0/90/0]	164.65	26.0	0.634
[90/0/90/0]	165.63	19.7	0.845
[90/0/90/0]	158.29	17.0	0.934
[90/0/90/0]	177.49	23.2	0.769
[90/0/90/0]	176.53	24.9	0.711
[0/0/90/0]	205.34	28.7	0.719
[0/0/90/0]	196.59	23.9	0.823
[0/0/90/0]	209.19	28.0	0.840
[0/0/90/0]	176.54	25.4	0.691
[0/0/90/0]	178.41	24.2	0.712
[0/0/90/0]	168.54	21.8	0.767
[90/90/0/0]*	163.75	23.5	0.790
[90/90/0/0]*	184.92	23.1	0.800
[90/90/0/0]*	189.25	22.8	0.930
[90/90/0/0]*	167.48	17.4	1.080
[90/90/0/0]*	181.35	23.9	0.760
[90/90/0/0]*	180.67	25.7	0.780
[90/90/0/0]*	200.11	26.3	0.840
[90/90/0/0]*	184.54	28.6	0.740
[90/90/0/0]*	186.15	25.4	0.770
[90/90/0/0]*	193.67	27.6	0.760
[90/90/0/0]*	180.00	24.7	0.750
MD	190.31	24.9	0.799
MD	194.13	28.0	0.698
MD	190.82	26.8	0.731
MD	213.87	26.4	0.816
MD	199.62	24.7	0.815
MD	218.99	22.8	0.980
CD	139.49	17.1	0.858
CD	133.63	16.5	0.815
CD	140.06	18.8	0.748
CD	113.36	21.8	0.516
CD	156.12	19.1	0.827
CD	148.95	20.8	0.726

*Processed for 30 minutes under vacuum

Table S2. Tensile test results for recycled fiber composites

Orientation	Strength (MPa)	Tensile Modulus (GPa)	Strain-to-Failure (%)
[0/90/90/90/90]	203.18	22.5	0.875
[0/90/90/90/90]	223.11	25.6	0.881
[90/90/0/0/90]	231.61	25.9	0.896
[90/90/0/0/90]	242.17	26.1	0.932
[0/90/90/0/90]	255.44	24.8	1.035
[0/90/90/0/90]	211.82	24.5	0.868
[0/90/0/0/0]	174.03	18.1	0.964
[0/90/0/0/0]	173.00	17.3	1.011
MD	140.78	15.9	0.890
MD	149.95	16.1	0.930
MD	142.10	16.2	0.876
MD	145.61	15.3	0.949
MD	156.36	15.9	0.982
MD	152.66	15.9	0.961
MD	124.30	14.4	0.867
MD	149.03	14.4	1.033
MD	126.06	14.5	0.871
MD	126.13	15.7	0.806
MD	139.90	15.6	0.899
MD	118.79	16.1	0.740
CD	226.63	30.3	0.749
CD	212.11	33.0	0.643
CD	289.44	33.4	0.866
CD	316.55	31.1	1.001
CD	308.53	31.9	0.923
CD	321.64	39.9	0.808
CD	233.31	30.0	0.764
CD	255.52	34.5	0.743
CD	252.76	32.2	0.789
CD	275.92	35.2	0.785
CD	282.90	34.5	0.822
CD	269.28	34.2	0.787
CD	243.67	37.4	0.657
CD	268.08	33.5	0.801
CD	270.38	34.5	0.787

Table S3. Tensile results for organosheet samples

Fiber Type	Orientation	Strength (MPa)	Tensile Modulus (GPa)	Strain-to-Failure (%)
Virgin	MD	172.96	18.9	0.907
	MD	138.21	16.1	0.855
	MD	130.76	18	0.747
	MD	178.63	19.5	0.907
	MD	103.06	11.5	0.894
	MD	102.21	12	0.847
	MD	114.37	20.6	0.564
	MD	142	15.6	0.969
	MD	173.22	19.2	0.904
	CD	92.17	10	0.948
	CD	86.16	12.8	0.74
	CD	136.81	12.1	1.144
	CD	109.69	13.7	0.83
	CD	150.17	14.1	1.148
	CD	141.02	15.4	1.008
	CD	145.08	16.4	1.108
	CD	70	11	0.642
	CD	94.03	11.3	0.817
	CD	125.11	12.6	1.011
	CD	75.55	11.7	0.644
Recycled	MD	108.48	9.4	1.174
	MD	91.32	8.9	1.018
	MD	96.37	10.2	0.938
	MD	99.44	9.5	1.053
	MD	91.07	9.7	0.923
	MD	89.66	9.4	0.927
	MD	109.83	9.6	1.16
	MD	92.58	9.4	0.992
	MD	98.27	11.3	0.915
	MD	64.58	8.81	0.764
	CD	168.96	18.4	0.904
	CD	231.32	22.9	1.001
	CD	202.9	18.7	1.558
	CD	165.41	18.8	0.906
	CD	234.54	22.3	1.28
	CD	156.55	25.2	0.626
	CD	172.05	21.3	0.816

Table S4. Shear results for composite samples

Fiber Type	Orientation	Strength (MPa)	Shear Modulus (GPa)	Strain-to-Failure
Virgin	MD	114.77	7.80	1.874
	MD	112.20	7.77	1.568
	MD	99.24	7.65	1.783
	MD	116.99	7.90	1.782
	CD	103.43	7.26	2.145
	CD	109.02	7.13	1.812
	CD	113.76	7.60	1.613
	CD	107.26	8.92	1.755
Recycled	MD	107.89	7.11	1.498
	MD	116.46	7.59	1.641
	MD	100.71	8.39	1.461
	MD	100.79	7.81	1.369
	CD	118.43	7.88	1.808
	CD	136.21	7.88	1.995
	CD	153.22	8.19	2.093
	CD	143.41	8.40	1.882

Table S5. Void content results for virgin fiber composites

Orientation	Optical Void Content (%)	Density Void Content (%)
Random	9.24	9.95
Random	28.92	16.12
Random	7.08	
Random	26.89	
Random	16.34	
Random	15.51	
Random	9.74	
Random	12.29	
Random	8.12	15.93
Random	12.40	15.67
Random	13.87	
Random	15.07	
Random	9.89	
Random	10.70	
Random	12.75	
Random	13.32	
Random*	6.25	6.17
Random*	7.93	8.45
Random*	4.56	
Random*	7.73	
Random*	0.83	
Random*	1.44	
Random*	7.70	
Random*	8.40	
MD	15.98	17.56
MD	24.91	19.43
MD	10.13	
MD	19.61	
CD	20.17	19.36
CD	12.28	14.04
CD	22.97	
CD	14.88	

*Processed for 30 minutes under vacuum

Table S6. Void content results for recycled fiber composites

Orientation	Optical Void Content (%)	Density Void Content (%)
Random	3.63	3.14
Random	9.83	9.44
Random	1.75	
Random	3.20	
Random	5.61	4.33
Random	5.08	5.56
Random	0.78	
Random	1.56	
Random	3.85	
Random	4.10	
Random	0.88	
Random	1.51	
MD	1.29	4.79
MD	1.44	4.89
MD	1.38	
MD	1.83	
MD	6.91	9.24
MD	10.02	9.91
MD	6.39	
MD	4.79	
CD	4.98	9.12
CD	6.47	
CD	0.02	3.25
CD	0.02	
CD	8.98	10.76
CD	11.77	
CD	0.36	3.87
CD	1.40	

SII-5. MATLAB Script for Laminate Theory Calculation

```
%Philip Barnett
%Calculator for the first ply failure criterion to determine strength
of
%ELG recycled carbon fiber/PPS laminates

clear all
close all
clc

numiters = 10000;
variation = mean([1-0.950, 1.045-1]);

for i = 1:numiters
    %Laminate orientation must be representative of experimental data
    ran = randi([1 8],1);
    if ran > 6
        angles = [90 90 90 90 0];
    elseif ran > 4 && ran < 7
        angles = [90 90 0 0 90];
    elseif ran > 2 && ran < 5
        angles = [0 90 0 90 90];
    else
        angles = [0 0 0 90 0];
    end
    [Ex(i), Fx(i)] = laminate(angles,variation);
    fprintf('Current iteration = %i \n',i)
end

Ex = Ex./1e9;
Fx = Fx./1e6;

%% Function for laminate calculation
function [Ex, Fx] = laminate(angles,var)
    %Lamina Properties
    t = 1.761/5*1e-3;
    E1 = 16e9;
    E2 = 34e9;
    G12 = 7.9e9;
    v12 = 0.19;
    v21 = E2/E1*v12;
    h = 5*t;
    zbar = [2*t t 0 -t -2*t];
    t = [t t t t t];
    F1t = 139e6;
    F2t = 268e6;
    F6 = 124e6;

    %Random number sequence to determine if reduced or enhanced
    properties are used
    ran = (rand(1)-0.5)*2;
    E1 = E1 + ran*var*E1;
```

```
F1t = F1t + ran*var*F1t;

ran = (rand(1)-0.5)*2;
E2 = E2 + ran*var*E2;
F2t = F2t + ran*var*F2t;

ran = (rand(1)-0.5)*2;
G12 = G12 + ran*var*G12;
F6 = F6 + ran*var*F6;

F1c = 139e6;
F2c = 268e6;

%Calculate Q matrix
Q11 = E1/(1-v12*v21);
Q22 = E2/(1-v12*v21);
Q12 = v21*E1/(1-v12*v21);
Q66 = G12;

%% Transform the Q matrix, CTEs, hygrothermal strains, and
hygrothermal forces

for i = 1:length(angles)
    m = cosd(angles(i));
    n = sind(angles(i));
    Qxx(i) = m^4*Q11 + n^4*Q22 + 2*m^2*n^2*Q12 + 4*m^2*n^2*Q66;
    Qyy(i) = n^4*Q11 + m^4*Q22 + 2*m^2*n^2*Q12 + 4*m^2*n^2*Q66;
    Qxy(i) = m^2*n^2*Q11 + m^2*n^2*Q22 + (m^4 + n^4)*Q12 -
    4*m^2*n^2*Q66;
    Qxs(i) = m^3*n*Q11 - m*n^3*Q22 - m*n*(m^2-n^2)*Q12 -
    2*m*n*(m^2-n^2)*Q66;
    Qys(i) = m*n^3*Q11 - m^3*n*Q22 + m*n*(m^2-n^2)*Q12 +
    2*m*n*(m^2-n^2)*Q66;
    Qss(i) = m^2*n^2*Q11 + m^2*n^2*Q22 - 2*m^2*n^2*Q12 + (m^2-
    n^2)^2*Q66;
end

sigx = 1;
sigy = 0;
taus = 0;

Nx = sigx*h;
Ny = sigy*h;
Ns = taus*h;

Nbar = [Nx; Ny; Ns];

Mbar = [0; 0; 0];

%% Calculate the A, B, and D matrices
for i = 1:length(angles)
   Axx(i) = Qxx(i)*t(i);
```

```
    Ayy(i) = Qyy(i)*t(i);
    Axy(i) = Qxy(i)*t(i);
    Axs(i) = Qxs(i)*t(i);
    Ays(i) = Qys(i)*t(i);
    Ass(i) = Qss(i)*t(i);

    Bxx(i) = Qxx(i)*zbar(i)*t(i);
    Byy(i) = Qyy(i)*zbar(i)*t(i);
    Bxy(i) = Qxy(i)*zbar(i)*t(i);
    Bxs(i) = Qxs(i)*zbar(i)*t(i);
    Bys(i) = Qys(i)*zbar(i)*t(i);
    Bss(i) = Qss(i)*zbar(i)*t(i);

    Dxx(i) = Qxx(i)*(t(i)*zbar(i)^2 + t(i)^3/12);
    Dyy(i) = Qyy(i)*(t(i)*zbar(i)^2 + t(i)^3/12);
    Dxy(i) = Qxy(i)*(t(i)*zbar(i)^2 + t(i)^3/12);
    Dxs(i) = Qxs(i)*(t(i)*zbar(i)^2 + t(i)^3/12);
    Dys(i) = Qys(i)*(t(i)*zbar(i)^2 + t(i)^3/12);
    Dss(i) = Qss(i)*(t(i)*zbar(i)^2 + t(i)^3/12);
end

Axx = sum(Axx);
Ayy = sum(Ayy);
Axy = sum(Axy);
Axs = sum(Axs);
Ays = sum(Ays);
Ass = sum(Ass);

Bxx = sum(Bxx);
Byy = sum(Byy);
Bxy = sum(Bxy);
Bxs = sum(Bxs);
Bys = sum(Bys);
Bss = sum(Bss);

Dxx = sum(Dxx);
Dyy = sum(Dyy);
Dxy = sum(Dxy);
Dxs = sum(Dxs);
Dys = sum(Dys);
Dss = sum(Dss);

A = [Axx Axy Axs; Axy Ayy Ays; Axs Ays Ass];
B = [Bxx Bxy Bxs; Bxy Byy Bys; Bxs Bys Bss];
D = [Dxx Dxy Dxs; Dxy Dyy Dys; Dxs Dys Dss];
%Floating point errors cause incorrect values
tol = 1e-8;
for i = 1:length(A)
    for j = 1:length(A)
        if A(i,j) < tol
            A(i,j) = 0;
        end
        if B(i,j) < tol
```

```
            B(i,j) = 0;
        end
        if D(i,j) < tol
            D(i,j) = 0;
        end
    end
end

full = [A B; B D];
invfull = inv(full);
a = invfull(1:3,1:3);
b = invfull(1:3,4:6);
c = invfull(4:6,1:3);
d = invfull(4:6,4:6);

%% Determine the reference plane strains
epsilon0 = a*Nbar + b*Mbar;
kappa = c*Nbar + d*Mbar;

%% Determine layer strains
for i = 1:length(angles)
    epsilonlam(:,i) = epsilon0 + zbar(i)*kappa;
end

%% Determine the layer strains relative to principal axis
for i = 1:length(angles)
    m = cosd(angles(i));
    n = sind(angles(i));
    epsilon1(i) = m^2*epsilonlam(1,i) + n^2*epsilonlam(2,i) +
    2*m*n*0.5*epsilonlam(3,i);
    epsilon2(i) = n^2*epsilonlam(1,i) + m^2*epsilonlam(2,i) -
    2*m*n*0.5*epsilonlam(3,i);
    halfgamma6(i) = -m*n*epsilonlam(1,i) + m*n*epsilonlam(2,i) +
    (m^2-n^2)*0.5*epsilonlam(3,i);
    gamma6(i) = 2*halfgamma6(i);
end

epsilon = [epsilon1; epsilon2; gamma6];

%% Determine layer stresses
for i = 1:length(angles)
   sig1(i) = Q11*epsilon1(i) + Q12*epsilon2(i);
   sig2(i) = Q12*epsilon1(i) + Q22*epsilon2(i);
   tau6(i) = Q66*gamma6(i);
end

sigma = [sig1; sig2; tau6];

%% Failure Criteria and lamiante strength calculations
    for i = 1:length(angles)
       if sig1(i) > 0
           F1 = F1t;
       else
```

```
            F1 = F1c;
        end
        if sig2(i) > 0
            F2 = F2t;
        else
            F2 = F2c;
        end
        val(i) = sig1(i)^2/F1^2 + sig2(i)^2/F2^2 + tau6(i)^2/F6^2 -
        sig1(i)*sig2(i)/F1^2;
        if sigx > 0 || sigy > 0
            Fxt(i) = sqrt(1/val(i));
        elseif sigx < 0 || sigy < 0
            Fxc(i) = sqrt(1/val(i));
        elseif sigx == 0 && sigy == 0
            Fxs(i) = sqrt(1/val(i));
        end
    end


    if sigx > 0 || sigy > 0
        Fx = min(Fxt);
%         fprintf('The FPF strength is %0.1f MPa \n',Fxt./1e6)
    elseif sigx < 0 || sigy < 0
        Fx = min(Fxc);
%         fprintf('The FPF strength is %0.1f MPa \n',Fxc./1e6)
    elseif sigx == 0 && sigy == 0
        Fx = min(Fxs);
%         fprintf('The FPF strength is %0.1f MPa \n',Fxs./1e6)
    end

    %% Laminate Modulus
    Ex = 1/(h*a(1,1));
%     fprintf('The laminate modulus is %0.1f GPa \n',Ex./1e9)
end
```

Supplementary Information for Chapter III

SIII-1. Laminate Orientation from Pixel Intensity

For laminates in which the orientation is unknown, the intensity of the pixels corresponding to fibers can be used to determine the orientation of each lamina. First, the histogram of the pixel intensity in an image is displayed, as shown in Figure S6. From this histogram, there exist four regions corresponding to voids and the mounting epoxy matrix, the PPS matrix, fibers in the axis of imaging, and fibers transverse to the axis of imaging. Thresholding can be used to segment each of the features into binary images, which can then be used for calculations such as the ratio of axial to transverse fibers. The ratio has been calculated for unidirectional composites, as shown in Table S7. From this table, it is apparent that this analysis also captures the greater anisotropy of the recycled fiber composites. For multidirectional laminates, the image can be subdivided into

horizontal regions corresponding to the lamina. Then, the ratio of axial to transverse fibers can be calculated for each region to determine the laminate orientation. These thresholding methods can also be applied to calculate fiber and void volume fractions of the laminates.

SIII-2. Interfacial Shear Strength Measurement Procedure

Interfacial shear strength (IFSS) was measured using a fiber push-in method. In this method, a rounded tip indenter (which can be approximated as a flat tip given the large radius of curvature) is pushed onto the fiber surface until the fiber/matrix interface fractures. According to this method, the shear strength is equal to:

$$\tau_s = \frac{S_0 P_c}{2\pi^2 r_f^3 E_{1f}}$$

where S_0 is the stiffness of the linear portion of the load-displacement curve, P_c is the debonding load, r_f is the fiber radius, and E_{1f} is the longitudinal modulus of the fiber. An example of the force-displacement curve generated is shown in Figure S7. The curve consists of an initial loading portion, which is nonlinear. The curve then becomes linear as the fiber/matrix interface is stressed. Once the fiber debonds at load Pc, the curve once again becomes nonlinear.

In the samples here, the linear portion of the curve was chosen to be between 15 and 25 mN for the epoxy and PPS samples and between 10 and 15 mN for the ABS samples, which exhibited much lower IFSS. A linear fit was applied to this region, to determine the stiffness. Then, the second derivative of the curve was used to identify the contact and debonding points. The contact point is defined as the point at which fiber elasticity becomes less dominant than matrix elasticity as the full area of the rounded tip comes into contact with the fiber surface (Figure S8). Before this point, the fiber elastically deforms at the small contact area. As discrete derivatives are too noisy to show the trends, the data was first smoothed using a moving average method via the MATLAB function smoothdata(). Then, the discrete first and second derivatives of the smoothed data were calculated. The point of full contact and debonding point were apparent as large jumps in the second derivative. The force measured in the original, unsmoothed data at the displacement identified in the smoothed data was chosen as the debonding load. Figure S9 provides an example of this process. The total energy of the debonding process was then calculated by integrating under the load-displacement curve from the full contact point to the debonding point.

To ensure that the fiber behavior was entirely elastic, three-dimensional topographic images were taken of some of the tested samples. Examples are shown in Figure S10. There was no apparent indent on the fiber after testing, indicating that the shear lag model is valid for this test.

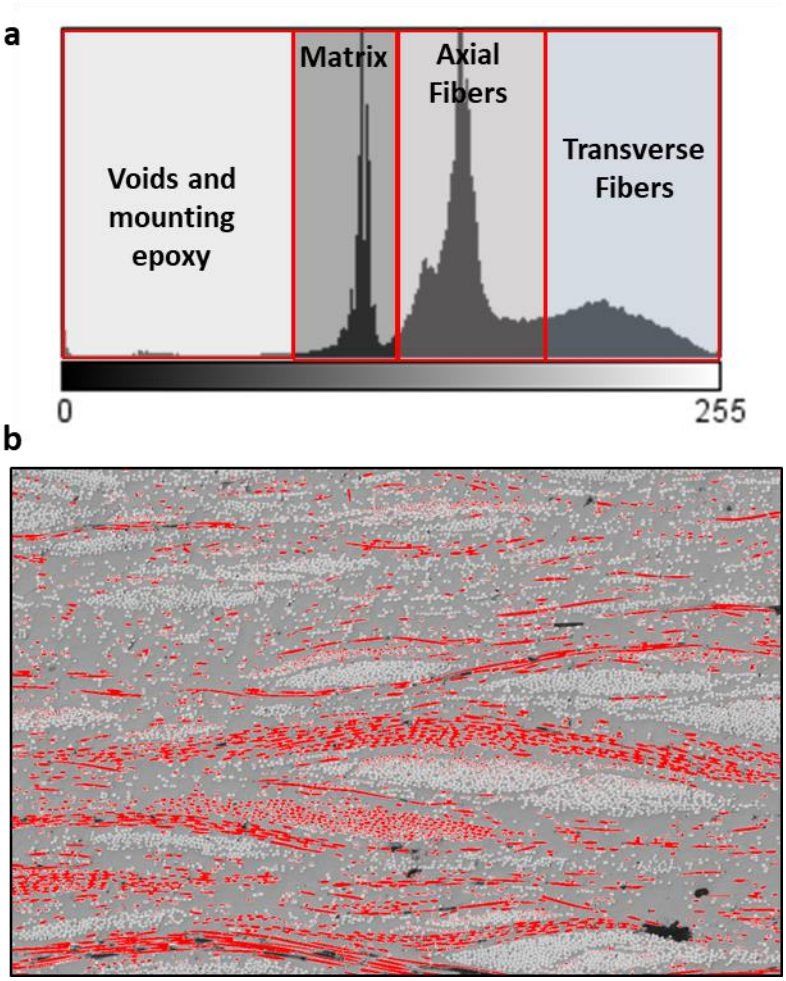

Figure S6. A) Histogram of pixel intensity and corresponding composite regions; b) Example of transverse fibers (red) in an image of a composite sample

Table S7. Transverse to axial ratio for recycled and virgin fiber composite images

Fiber Type	Direction	Transverse:Axial Ratio
Virgin	MD	0.15 ± 0.03
	CD	0.28 ± 0.06
Recycled	MD	0.49 ± 0.10
	CD	0.18 ± 0.05

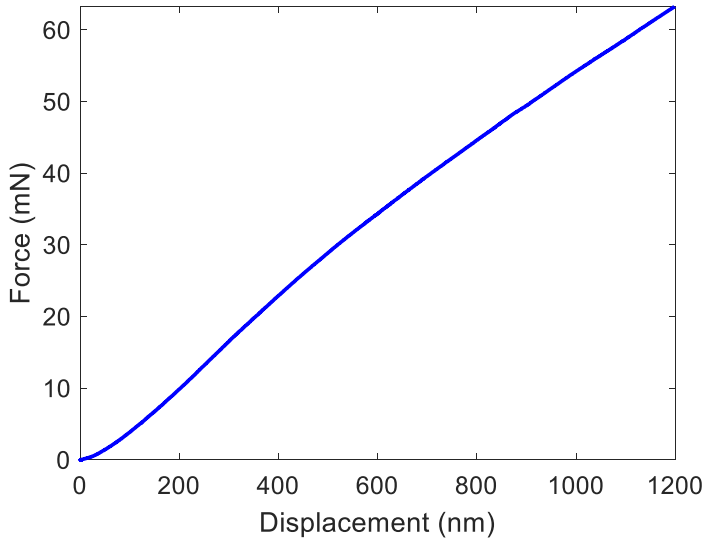

Figure S7. Typical force-displacement curve for indentation tests

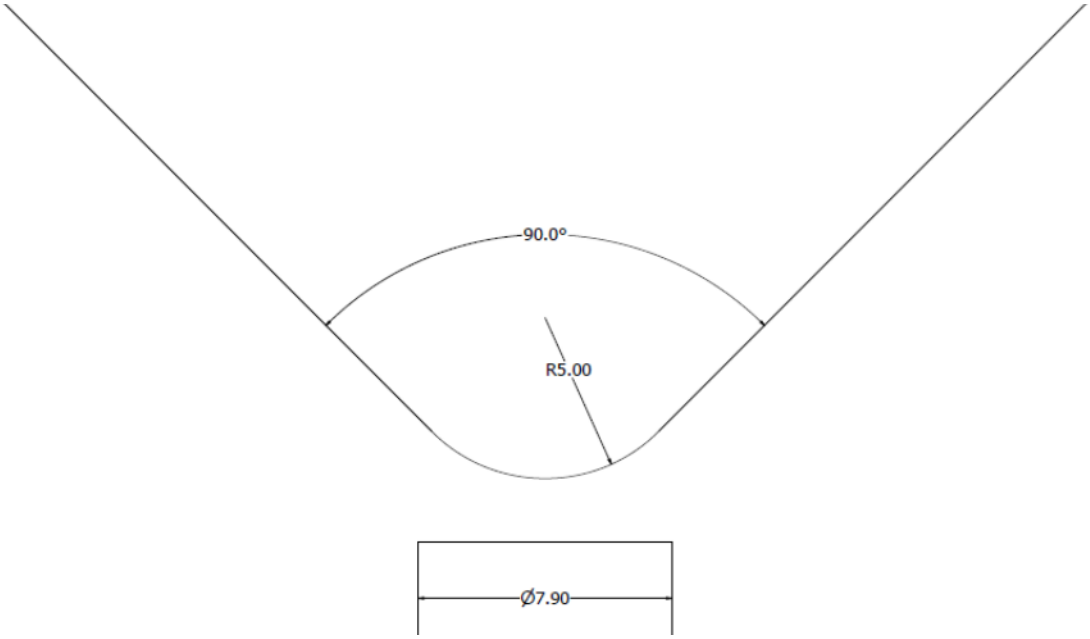

Figure S8. Illustration of tip geometry and fiber during indentation

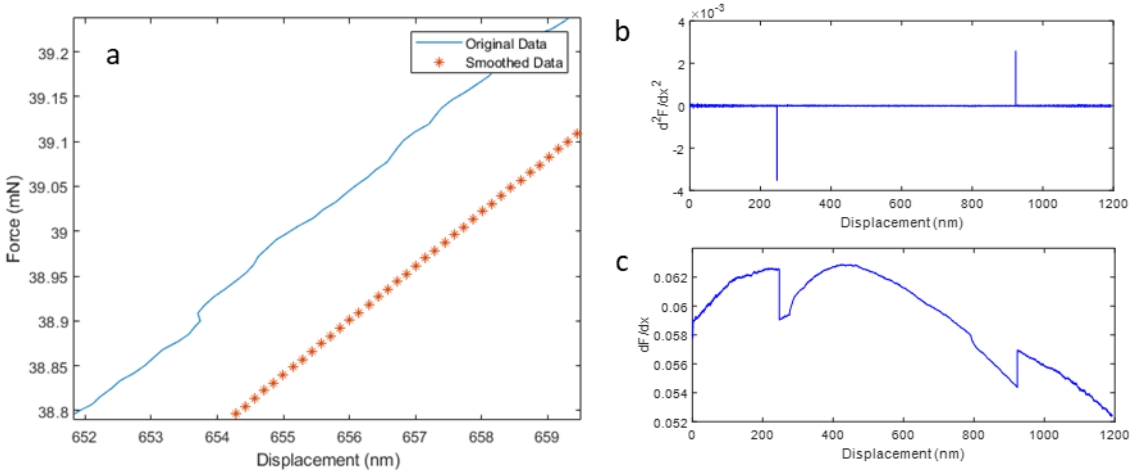

Figure S9. A) Comparison of smoothed and unsmoothed data; b) First derivative of smoothed force-displacement curve; c) Second derivative of smoothed force-displacement curve

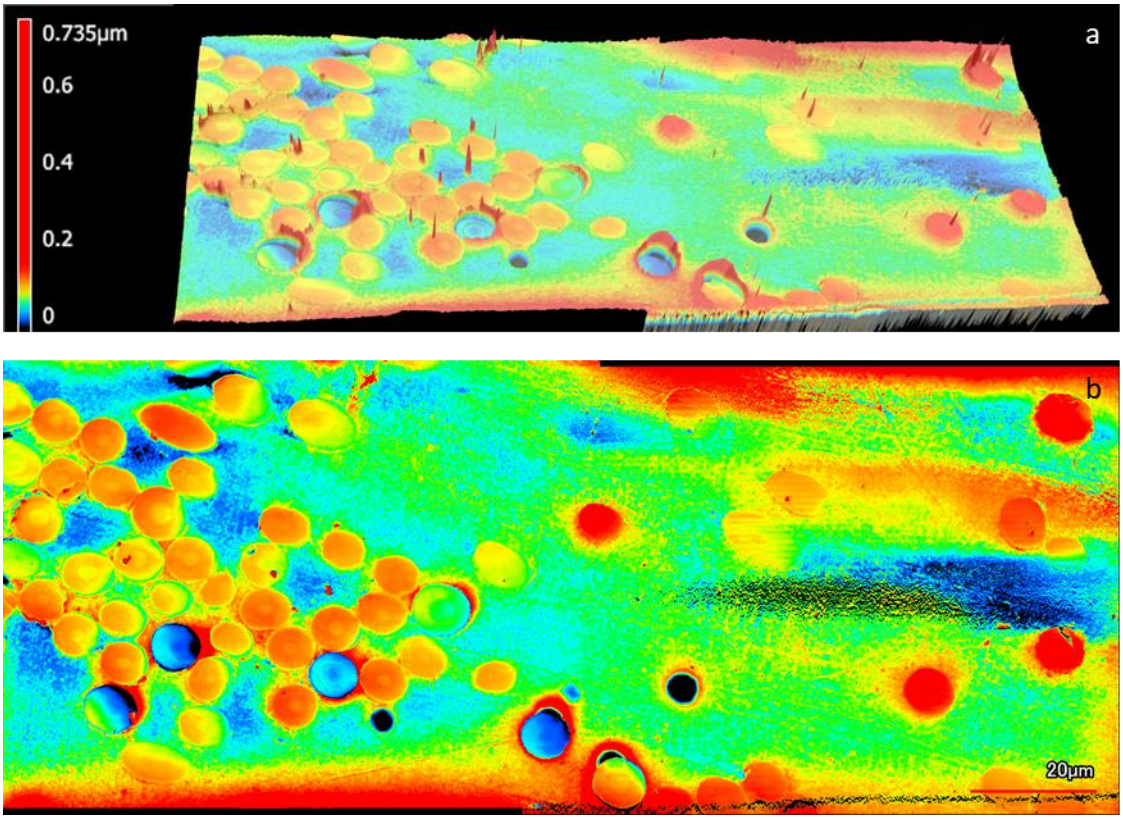

Figure S10. A) 3D laser scanning microscope image of sample topography showing pushed in fibers; b) 2D image showing pushed-in fibers

SIII-3. MATLAB Script for Push-In Analysis

```
%Philip Barnett
%Identification of critical load and slope for fiber push-in tests

clear all
close all hidden
clc

%% Input the data
[file, path] = uigetfile('*.csv', 'Select the indentation data');
pathname = strcat(path,file);
data = readmatrix(pathname);

time = data(:,21);
disp = data(:,4);
force = data(:,16);

plot(disp,force)
xlabel('Displacement (nm)')
ylabel('Force (mN)')

%% Select cutoff point if there is noisy data at the end
[x,y] = ginput(1);
if x < disp(end)
    finish = find(disp >= x,1);
else
    finish = length(disp);
end
force = force(1:finish);
disp = disp(1:finish);
plot(disp,force)
xlabel('Displacement (nm)')
ylabel('Force (mN)')
hold on

%% Determine initial slope
startval = 15;
finishval = 25; %force in mN
start = find(abs(force-startval) == min(abs(force-startval)));
finish = find(abs(force-finishval) == min(abs(force-finishval)));
S0 = polyfit(disp(start:finish),force(start:finish),1);
plot(disp(start:finish),force(start:finish))
legend('All Data', 'Initial Slope', 'Location', 'best')

%% Differentiate to find point where slope changes
force2 = smoothdata(force);
disp2 = smoothdata(disp);
dx = diff(disp2);
dF = diff(force2);
x = disp(1:end-1);
x2 = x(1:end-1);
dFdx = dF./dx;
```

```
d2Fdx2 = diff(dFdx);
absd2Fdx2 = abs(d2Fdx2);
%Find the second peak which corresponds to debonding after the initial
%linear region
postload = absd2Fdx2(finish:end);
[M,I] = max(postload);
Pc = force(I + finish);
preload = absd2Fdx2(1:finish);
[M2,I2] = max(preload);
Pstart = force(I2);

%Calculate the energy absorbed from contact to failure
E = trapz(disp(I2:I+finish),force(I2:I+finish));
```

SIII-4. MATLAB Script for Statistical Analysis

```
%Philip Barnett
%Code to identify differences between two samples using bootstrapping

%% Notes
%The samples that can be compared are dependent upon the laminate
%orientation.
%The following virgin fiber samples processed for 30 minutes can be
compared:
%PP3 & PP2 (unannealed) to PP9 (210)
%PP5 & PP6 (140) to PP7 (210)
%This means that unannealed to 140 cannot be compared directly
(differences
%may be possible)
%The following virgin fiber samples processed for 5 minutes can be
%compared:
%PP12 & PP18 (unannealed) to PP23 & PP29 (140 & 210)
%All rCF samples can be compared because they all equally came from the
%same plates
%All changes will be treated as a percent to reduce the effect of
laminate
%orientation
%Percent will be based on a percent change relative to the lower
annealing
%temperature

clear all
close all
clc

%% Import Data
[filename,path] = uigetfile('.xlsx');
pathname = strcat(path,filename);
data = readtable(pathname);

%% Restructure Data
% Separate into individual sample sets
numsamples = size(data);
```

```
for i = 1:numsamples(1)
    sample = char(data{i,1});
    sample = strrep(sample,'/','');
    letters = isletter(sample);
    sample(letters) = [];
    samples(i) = str2num(sample);
end

samples = array2table(samples');
data = [samples data];
data = removevars(data,'Plate');

for i = 1:numsamples(1)
    if data{i,6} == 1 && data{i,7} == 5
        switch data{i,8}
            case 1
                for j = 1:numsamples(2)
                   virun5(i,j) = data{i,j};
                end
            case 2
                for j = 1:numsamples(2)
                   recun5(i,j) = data{i,j};
                end
        end
    elseif data{i,6} == 1 && data{i,7} == 30
        for j = 1:numsamples(2)
            virun30(i,j) = data{i,j};
        end
    elseif data{i,6} == 140 && data{i,7} == 5
        switch data{i,8}
            case 1
                for j = 1:numsamples(2)
                   vir1405(i,j) = data{i,j};
                end
            case 2
                for j = 1:numsamples(2)
                   rec1405(i,j) = data{i,j};
                end
        end
    elseif data{i,6} == 140 && data{i,7} == 30
        for j = 1:numsamples(2)
            vir14030(i,j) = data{i,j};
        end
    elseif data{i,6} == 210 && data{i,7} == 5
        switch data{i,8}
            case 1
                for j = 1:numsamples(2)
                   vir2105(i,j) = data{i,j};
                end
            case 2
                for j = 1:numsamples(2)
                   rec2105(i,j) = data{i,j};
                end
        end
```

```
    elseif data{i,6} == 210 && data{i,7} == 30
        for j = 1:numsamples(2)
            vir21030(i,j) = data{i,j};
        end
    end
end
virun5(all(~virun5,2),:) = [];
virun5(:, all(~virun5,1)) = [];
virun30(all(~virun30,2),:) = [];
virun30(:, all(~virun30,1)) = [];
recun5(all(~recun5,2),:) = [];
recun5(:, all(~recun5,1)) = [];
vir1405(all(~vir1405,2),:) = [];
vir1405(:, all(~vir1405,1)) = [];
vir2105(all(~vir2105,2),:) = [];
vir2105(:, all(~vir2105,1)) = [];
vir14030(all(~vir14030,2),:) = [];
vir14030(:, all(~vir14030,1)) = [];
vir21030(all(~vir21030,2),:) = [];
vir21030(:, all(~vir21030,1)) = [];
rec1405(all(~rec1405,2),:) = [];
rec1405(:, all(~rec1405,1)) = [];
rec2105(all(~rec2105,2),:) = [];
rec2105(:, all(~rec2105,1)) = [];

%% Remove outliers and replace with the median

for i = 1:3
   TF(:,i) = isoutlier(virun5(:,i+2));
end
virun5 = repoutlier(virun5, TF);
clear TF

for i = 1:3
   TF(:,i) = isoutlier(virun30(:,i+2));
end
virun30 = repoutlier(virun30, TF);
clear TF

for i = 1:3
   TF(:,i) = isoutlier(vir1405(:,i+2));
end
vir1405 = repoutlier(vir1405, TF);
clear TF

for i = 1:3
   TF(:,i) = isoutlier(vir14030(:,i+2));
end
vir14030 = repoutlier(vir14030, TF);
clear TF

for i = 1:3
   TF(:,i) = isoutlier(vir2105(:,i+2));
```

```
end
vir2105 = repoutlier(vir2105, TF);
clear TF

for i = 1:3
   TF(:,i) = isoutlier(vir21030(:,i+2));
end
vir21030 = repoutlier(vir21030, TF);
clear TF

for i = 1:3
   TF(:,i) = isoutlier(recun5(:,i+2));
end
recun5 = repoutlier(recun5, TF);
clear TF

for i = 1:3
   TF(:,i) = isoutlier(rec1405(:,i+2));
end
rec1405 = repoutlier(rec1405, TF);
clear TF

for i = 1:3
   TF(:,i) = isoutlier(rec2105(:,i+2));
end
rec2105 = repoutlier(rec2105, TF);
clear TF

%% Analyze the data
%Select which samples to analyze
list = {'Virgin Unannealed 30 min', 'Virgin Unannealed 5 min', 'Virgin
Annealed 140 C 30 min', 'Virgin Annealed 140 C 5 min', ...
'Virgin Annealed 210 C 30 min', 'Virgin Annealed 210 C 5 min',
'Recycled Unannealed', 'Recycled Annealed 140 C', 'Recycled Annealed
210 C'};
[indx, tf] = listdlg('PromptString', 'Select two samples for
comparison:', 'ListString', list, 'SelectionMode', 'Multiple');
for i = 1:2
    switch indx(i)
        case 1
            data = virun30;
        case 2
            data = virun5;
        case 3
            data = vir14030;
        case 4
            data = vir1405;
        case 5
            data = vir21030;
        case 6
            data = vir2105;
        case 7
            data = recun5;
```

```
        case 8
            data = rec1405;
        case 9
            data = rec2105;
    end
    if i == 1
        data1 = data;
    elseif i == 2
        data2 = data;
    end
end

%Percent difference between samples
moddifference = [];
strdifference = [];
straindifference = [];

%Nonunique sets are specified here
if any(ismember(indx,1)) && any(ismember(indx,5)) %V-30-UA and V-30-210
    set2match = find(data2(:,1) == 9);
    mod1 = data1(:,4);
    mod2 = data2(set2match,4);
    str1 = data1(:,3);
    str2 = data2(set2match,3);
    strain1 = data1(:,5);
    strain2 = data2(set2match,5);
    moddifference = [moddifference; samplediff(mod1,mod2)];
    strdifference = [strdifference; samplediff(str1,str2)];
    straindifference = [straindifference; samplediff(strain1,strain2)];

elseif any(ismember(indx,3)) && any(ismember(indx,5)) %V-30-140 and V-
30-210
    set2match = find(data2(:,1) == 7);
    mod1 = data1(:,4);
    mod2 = data2(set2match,4);
    str1 = data1(:,3);
    str2 = data2(set2match,3);
    strain1 = data1(:,5);
    strain2 = data2(set2match,5);
    moddifference = [moddifference; samplediff(mod1,mod2)];
    strdifference = [strdifference; samplediff(str1,str2)];
    straindifference = [straindifference; samplediff(strain1,strain2)];

elseif any(ismember(indx,2)) && any(ismember(indx,4)) %V-5-UA and V-5-
140
    set2match = find(data2(:,1) == 23);
    set1match = find(data1(:,1) == 18);
    %must compare sample 12 to 29 and sample 18 to 23
    mod1 = data1(set1match,4);
    mod2 = data2(set2match,4);
    str1 = data1(set1match,3);
    str2 = data2(set2match,3);
    strain1 = data1(set1match,5);
```

```
    strain2 = data2(set2match,5);
    moddifference = [moddifference;
    samplediff(data1(set1match,4),data2(set2match,4))];
    strdifference = [strdifference;
    samplediff(data1(set1match,3),data2(set2match,3))];
    straindifference = [straindifference;
    samplediff(data1(set1match,5),data2(set2match,5))];
    set2match = find(data2(:,1) == 29);
    set1match = find(data1(:,1) == 12);
    mod1 = [mod1; data1(set1match,4)];
    mod2 = [mod2; data2(set2match,4)];
    str1 = [str1; data1(set1match,3)];
    str2 = [str2; data2(set2match,3)];
    strain1 = [strain1; data1(set1match,5)];
    strain2 = [strain2; data2(set2match,5)];
    moddifference = [moddifference;
    samplediff(data1(set1match,4),data2(set2match,4))];
    strdifference = [strdifference;
    samplediff(data1(set1match,3),data2(set2match,3))];
    straindifference = [straindifference;
    samplediff(data1(set1match,5),data2(set2match,5))];

elseif any(ismember(indx,2)) && any(ismember(indx,6)) %V-5-UA and V-5-
210
    set2match = find(data2(:,1) == 23);
    set1match = find(data1(:,1) == 18);
    %must compare sample 12 to 29 and sample 18 to 23
    mod1 = data1(set1match,4);
    mod2 = data2(set2match,4);
    str1 = data1(set1match,3);
    str2 = data2(set2match,3);
    strain1 = data1(set1match,5);
    strain2 = data2(set2match,5);
    moddifference = [moddifference;
    samplediff(data1(set1match,4),data2(set2match,4))];
    strdifference = [strdifference;
    samplediff(data1(set1match,3),data2(set2match,3))];
    straindifference = [straindifference;
    samplediff(data1(set1match,5),data2(set2match,5))];
    set2match = find(data2(:,1) == 29);
    set1match = find(data1(:,1) == 12);
    mod1 = [mod1; data1(set1match,4)];
    mod2 = [mod2; data2(set2match,4)];
    str1 = [str1; data1(set1match,3)];
    str2 = [str2; data2(set2match,3)];
    strain1 = [strain1; data1(set1match,5)];
    strain2 = [strain2; data2(set2match,5)];
    moddifference = [moddifference;
    samplediff(data1(set1match,4),data2(set2match,4))];
    strdifference = [strdifference;
    samplediff(data1(set1match,3),data2(set2match,3))];
    straindifference = [straindifference;
    samplediff(data1(set1match,5),data2(set2match,5))];
```

```
else
    %Find difference between unique samples if they exist
    uniqueset1 = unique(data1(:,1));
    mod1 = [];
    mod2 = [];
    str1 = [];
    str2 = [];
    strain1 = [];
    strain2 = [];
    for i = 1:length(uniqueset1)
        set2match = find(data2(:,1) == uniqueset1(i));
        set1match = find(data1(:,1) == uniqueset1(i));
        mod1 = [mod1; data1(set1match,4)];
        mod2 = [mod2; data2(set2match,4)];
        str1 = [str1; data1(set1match,3)];
        str2 = [str2; data2(set2match,3)];
        strain1 = [strain1; data1(set1match,5)];
        strain2 = [strain2; data2(set2match,5)];
        moddifference = [moddifference;
        samplediff(data1(set1match,4),data2(set2match,4))];
        strdifference = [strdifference;
        samplediff(data1(set1match,3),data2(set2match,3))];
        straindifference = [straindifference;
        samplediff(data1(set1match,5),data2(set2match,5))];
    end
end

%% Select what to run
list = {'T-test', 'Wilcoxon Rank Sum Test', 'Bootstrap Confidence
Interval'};
[indx, tf] = listdlg('PromptString','Select what you would like to do:
' , 'ListString', list);
for i = 1:length(indx)
    switch indx(i)
        case 1
            customttest(mod1, mod2, str1, str2, strain1, strain2)
        case 2
            wilcoxon(mod1,mod2,str1,str2,strain1,strain2)
        case 3
            numiters = 1;
            plots = true;
            if numiters > 1
                plots = false;
            end
            for j = 1:numiters
                %Bootstrap the data
                numbootstraps = 1000;
                bootstatmod1 = bootstrp(numbootstraps,@(x)[mean(x)
                std(x)],mod1);
                bootstatstr1 = bootstrp(numbootstraps,@(x)[mean(x)
                std(x)],str1);
                bootstatstrain1 = bootstrp(numbootstraps,@(x)[mean(x)
                std(x)],strain1);
```

```
            bootstatmod2 = bootstrp(numbootstraps,@(x)[mean(x)
            std(x)],mod2);
            bootstatstr2 = bootstrp(numbootstraps,@(x)[mean(x)
            std(x)],str2);
            bootstatstrain2 = bootstrp(numbootstraps,@(x)[mean(x)
            std(x)],strain2);

            %Normalize the bootstrap data by the bootstrap mean
            mod1mean = mean(bootstatmod1(:,1));
            str1mean = mean(bootstatstr1(:,1));
            strain1mean = mean(bootstatstrain1(:,1));
            moduluscomp = [bootstatmod1(:,1)./mod1mean
            bootstatmod2(:,1)./mod1mean];
            strengthcomp = [bootstatstr1(:,1)./str1mean
            bootstatstr2(:,1)./str1mean];
            straincomp = [bootstatstrain1(:,1)./strain1mean
            bootstatstrain2(:,1)./strain1mean];

            t = 1.96;
            [strengthhigh(j), strengthlow(j), modulushigh(j),
            moduluslow(j), strainhigh(j), strainlow(j)] = citest(t,
            moduluscomp, strengthcomp, straincomp, plots);
        end
        strengthhigh = mean(strengthhigh);
        strengthlow = mean(strengthlow);
        modulushigh = mean(modulushigh);
        moduluslow = mean(moduluslow);
        strainhigh = mean(strainhigh);
        strainlow = mean(strainlow);
        fprintf('The difference in strength between the two samples
        is between %0.1f and %0.1f %% \n', strengthlow*100,
        strengthhigh*100)
        if strengthlow < 0 && strengthhigh > 0
           fprintf('There is no significant difference between the
           two samples')
        end
        fprintf('The difference in modulus between the two samples
        is between %0.1f and %0.1f %% \n', moduluslow*100,
        modulushigh*100);
        if moduluslow < 0 && modulushigh > 0
           fprintf('There is no significant difference between the
           two samples')
        end
        fprintf('The difference in strain-to-failure between the
        two samples is between %0.1f and %0.1f %% \n\n',
        strainlow*100, strainhigh*100);
        if strainlow < 0 && strainhigh > 0
           fprintf('There is no significant difference between the
           two samples')
        end
    end
end

%% Function to run a confidence interval test using z-score
```

```
%Samples assumed to be normally distributed
%If the data is assumed to be normal, the confidence interval of the
difference
%between two samples can be calculated using z-scores using the
%method outlined here: stat.yale.edu/Courses/1997-98/101/meancomp.htm
%In this case, computed sample mean and standard deviation of each
bootstrap
%sample are used to estimate the difference in population means
%It is important that the same number of samples are compared in the
%confidence intervals, or else the data will could be skewed
function [strengthhigh, strengthlow, modulushigh, moduluslow,
strainhigh, strainlow] = citest(t, moduluscomp, strengthcomp,
straincomp, plots)
    if plots
        histogram(strengthcomp(:,1),25)
        hold on
        histogram(strengthcomp(:,2),25)
        xlabel('Mean Strength (MPa)')
        ylabel('Number of Occurences')

        figure
        histogram(moduluscomp(:,1),25)
        hold on
        histogram(moduluscomp(:,2),25)
        xlabel('Mean Modulus (GPa)')
        ylabel('Number of Occurences')

        figure
        histogram(straincomp(:,1),25)
        hold on
        histogram(straincomp(:,2),25)
        xlabel('Mean Strain-to-Failure (%)')
        ylabel('Number of Occurences')
    end
    strengthmean = [mean(strengthcomp(:,1)) mean(strengthcomp(:,2))];
    modulusmean = [mean(moduluscomp(:,1)) mean(moduluscomp(:,2))];
    strainmean = [mean(straincomp(:,1)) mean(straincomp(:,2))];
    strengthstd = [std(strengthcomp(:,1)) std(strengthcomp(:,2))];
    modulusstd = [std(moduluscomp(:,1)) std(moduluscomp(:,2))];
    strainstd = [std(straincomp(:,1)) std(straincomp(:,2))];
    n = length(strengthcomp);
    strengthhigh = strengthmean(1) - strengthmean(2) +
    t*sqrt(strengthstd(1)^2/n + strengthstd(2)^2/n);
    strengthlow = strengthmean(1) - strengthmean(2) -
    t*sqrt(strengthstd(1)^2/n + strengthstd(2)^2/n);
    modulushigh = modulusmean(1) - modulusmean(2) +
    t*sqrt(modulusstd(1)^2/n + modulusstd(2)^2/n);
    moduluslow = modulusmean(1) - modulusmean(2) -
    t*sqrt(modulusstd(1)^2/n + modulusstd(2)^2/n);
    strainhigh = strainmean(1) - strainmean(2) +
    t*sqrt(strainstd(1)^2/n + strainstd(2)^2/n);
    strainlow = strainmean(1) - strainmean(2) - t*sqrt(strainstd(1)^2/n
    + strainstd(2)^2/n);
end
```

```
%% Function to run the Wilcoxon Rank Sum Test
%Wilcoxon rank sum test run on the original data only
%Useful as a nonparametric test
function [] = wilcoxon(mod1,mod2,str1,str2,strain1,strain2)
    [p(1), h(1)] = ranksum(mod1,mod2);
    [p(2), h(2)] = ranksum(str1,str2);
    [p(3), h(3)] = ranksum(strain1,strain2);
    ranksumtestTable{1,1} = 'Modulus';
    ranksumtestTable{2,1} = 'Strength';
    ranksumtestTable{3,1} = 'Strain-to-failure';
    ranksumtestTable{1,2} = h(1);
    ranksumtestTable{2,2} = h(2);
    ranksumtestTable{3,2} = h(3);
    ranksumtestTable{1,3} = p(1);
    ranksumtestTable{2,3} = p(2);
    ranksumtestTable{3,3} = p(3);
    ranksumtestTable = cell2table(ranksumtestTable);
    ranksumtestTable.Properties.VariableNames = {'Dependent_Variable',
    'Reject_the_Null_Hypothesis', 'P_value'}
end

%% Function to run the two-sample t-test
%T-test run on original data only
%Assumes samples come from a normal distribution
function [] = customttest(mod1, mod2, str1, str2, strain1, strain2)
    [h(1), p(1)] = ttest2(mod1,mod2,'Vartype','unequal');
    [h(2), p(2)] = ttest2(str1,str2,'Vartype','unequal');
    [h(3), p(3)] = ttest2(strain1,strain2,'Vartype','unequal');
    %Create a table to print
    TtestTable{1,1} = 'Modulus';
    TtestTable{2,1} = 'Strength';
    TtestTable{3,1} = 'Strain-to-failure';
    TtestTable{1,2} = h(1);
    TtestTable{2,2} = h(2);
    TtestTable{3,2} = h(3);
    TtestTable{1,3} = p(1);
    TtestTable{2,3} = p(2);
    TtestTable{3,3} = p(3);
    TtestTable = cell2table(TtestTable);
    TtestTable.Properties.VariableNames = {'Dependent_Variable',
    'Reject_the_Null_Hypothesis', 'P_value'}
end

%% Function to determine percent differences between samples
function [difference] = samplediff(set1, set2)
    for i = 1:length(set1)
        for j = 1:length(set2)
            difference(i,j) = (set2(j) - set1(i))/set1(i);
        end
    end
    difference = difference(:);
end
```

```
%% Function to replace outliers with median values
function initial = repoutlier(initial, TF)
    %Determine the median values prior to removing outliers
    samples = unique(initial(:,1));
    for i = 1:length(samples)
       a = find(initial(:,1) == samples(i));
       for j = 1:length(a)
          strengthmedian(i) = nanmedian(initial(a,3));
          modulusmedian(i) = nanmedian(initial(a,4));
          strainmedian(i) = nanmedian(initial(a,5));
       end
    end

    TF = sum(TF,2);

    %Look for outliers and replace them with the median
    for i = 1:length(TF)
       if TF(i)
          b = find(samples(:) == initial(i,1));
          initial(i,3) =  strengthmedian(b);
          initial(i,4) = modulusmedian(b);
          initial(i,5) = strainmedian(b);
       end
    end
end
```

SIII-5. Mechanical Testing Results

The mechanical testing results can be found in Tables S8-S10.

SIII-6. Single-Fiber Testing Results

The single-fiber testing results can be found in Tables S11 and S12.

SIII-7. Differential Scanning Calorimetry Results

The DSC results can be found in Tables S13-S15.

SIII-8. Dynamic Mechanical Analysis Results

The DMA results can be found in Table S16.

SIII-9. Fiber and Void Content Analysis

The fiber and void content results can be found in Tables S17 and S18.

SIII-10. Nano-Indentation Results

The nanoindentation results can be found in Tables S19-S24.

Table S8. Tensile testing results for virgin fiber composites processed for 30 minutes

Sample Identifier	Strength (MPa)	Modulus (GPa)	Strain to Failure (%)
V-30-UA*	163.75	23.5	0.790
	184.92	23.1	0.800
	189.25	22.8	0.930
	167.48	17.4	1.080
	181.35	23.9	0.760
	180.67	25.7	0.780
	200.11	26.3	0.840
	184.54	28.6	0.740
	186.15	25.4	0.770
	193.67	27.6	0.760
	180.00	24.7	0.750
V-30-140**	192.20	29.0	0.660
	228.06	30.6	0.740
	186.13	28.9	0.640
	227.16	31.1	0.730
	247.70	32.6	0.830
	190.94	27.4	0.740
	218.97	28.2	0.860
	192.07	25.9	0.780
	214.26	25.3	0.930
	219.57	32.6	0.780
V-30-210*	225.06	30.6	0.790
	219.48	30.5	0.780
	213.28	33.7	0.710
	218.71	34.8	0.690
	211.96	29.5	0.760
V-30-210**	198.82	21.9	0.920
	199.74	23.8	0.890
	176.35	21.8	0.900
	188.98	23.2	0.930
	205.01	24.2	0.940

*Denotes equivalent laminate sequence between V-30-UA and V-30-210
**Denotes equivalent laminate sequence between V-30-140 and V-30-210

Table S9. Tensile testing results for virgin fiber composites processed for 5 minutes

Sample Identifier	Strength (MPa)	Modulus (GPa)	Strain to Failure (%)
V-5-UA	175.97	25.1	0.723
	164.65	26.0	0.634
	165.63	19.7	0.845
	158.29	17.0	0.934
	177.49	23.2	0.769
	176.53	24.9	0.711
	205.34	28.7	0.719
	196.59	23.9	0.823
	209.19	28.0	0.840
	176.54	25.4	0.691
	178.41	24.2	0.712
	168.54	21.8	0.767
V-5-140	202.09	25.6	0.795
	196.04	23.8	0.839
	197.88	22.4	0.895
	176.01	21.7	0.830
	167.98	19.8	0.878
	164.05	22.6	0.734
V-5-210	212.43	28.6	0.742
	220.03	26.5	0.834
	217.53	26.7	0.813
	209.73	26.2	0.799
	191.22	24.6	0.777
	190.42	24.0	0.794

Table S10. Tensile testing results for recycled fiber composites processed for 5 minutes

Sample Identifier	Strength (MPa)	Modulus (GPa)	Strain to Failure (%)
R-5-UA	203.18	22.5	0.875
	223.11	25.6	0.881
	231.61	25.9	0.896
	242.17	26.1	0.932
	255.44	24.8	1.035
	211.82	24.5	0.868
	174.03	18.1	0.964
	173.00	17.3	1.011
R-5-140	243.81	30.9	0.781
	219.33	27.7	0.791
	245.52	28.2	0.877
	248.83	27.6	0.902
	221.04	24.9	0.885
	243.55	26.3	0.927
	171.76	18.4	0.939
	174.09	18.1	0.967
R-5-210	239.35	29.7	0.804
	231.95	24.8	1.024
	269.94	27.3	0.984
	272.02	26.8	1.015
	199.12	21.8	0.915
	214.56	26.5	0.808
	182.84	18.3	1.005
	188.73	19.8	0.960

Table S11. Virgin carbon fiber single-fiber testing results

Diameter (μm)	Modulus (GPa)	Strength (MPa)	Strain-to-Failure
7.94	171.7	3899.73	0.0217
8.053	193.4	4134.97	0.0204
7.88	176.9	2564.46	0.0139
7.467	186.1	3045.25	0.0156
7.757	178.4	4060.56	0.0209
7.347	188.4	3974.62	0.0198
7.52	191.0	3059.20	0.0153
7.587	161.2	2947.72	0.0177
7.587	192.9	3561.60	0.0173
7.88	174.7	3276.80	0.0177
7.877	144.4	3230.62	0.0213
8.17	165.6	3974.37	0.0222
8.417	152.9	2205.91	0.0139
7.587	188.2	3942.53	0.0196
7.407	198.2	4243.80	0.0199
7.757	190.5	3517.18	0.0174
9.813	123.0	2814.12	0.0216
8.467	159.7	3162.23	0.0199
7.7	176.9	4003.46	0.0211
7.527	192.2	4233.12	0.0208
7.877	203.8	1475.34	0.0077
6.937	268.8	2580.39	0.0149
9.05	189.6	3459.83	0.0170
7.937	220.6	1737.08	0.0078
6.88	234.9	3393.27	0.0169
8.23	214.9	2658.22	0.0151
7.64	224.0	4321.32	0.0179
8.11	192.0	2462.88	0.0142
7.173	262.1	4722.18	0.0190
8.05	189.0	3751.59	0.0183
9.463	186.2	2293.74	0.0133
8.523	189.0	3218.04	0.0186
8.29	196.5	2375.37	0.0131
6.76	253.3	3481.02	0.0149
7.287	229.9	2906.49	0.0136
7.873	214.4	3333.27	0.0169
8.177	218.2	4041.23	0.0200
8.343	187.3	2254.54	0.0132
7.357	255.2	3483.87	0.0148
7.823	248.4	4256.33	0.0188

Table S12. Recycled carbon fiber single-fiber testing results

Diameter (μm)	Modulus (GPa)	Strength (MPa)	Strain-to-Failure
7.47	216.4	3878.18	0.0168
6.937	216.1	4497.92	0.0192
7.583	222.6	3509.03	0.0150
6.643	266.4	4929.20	0.0174
7.527	219.5	4078.34	0.0174
7.843	183.2	4197.37	0.0209
7.467	204.4	3196.81	0.0149
7.407	212.1	4331.22	0.0188
8.82	160.8	3213.60	0.0187
7.82	178.4	4698.12	0.0240
7.697	165.8	3521.75	0.0196
7.463	207.7	5409.01	0.0241
6.293	250.2	5052.76	0.0188
7.11	166.1	2672.43	0.0153
6.82	217.6	3269.25	0.0143
7.18	193.8	3872.55	0.0184
7.583	209.3	3725.94	0.0168
7.64	183.8	4039.12	0.0203
5.76	306.1	7170.85	0.0213
6.357	230.8	5642.06	0.0225
7.057	213.1	5397.99	0.0234
8.11	149.3	3649.49	0.0229
5.877	261.6	5417.45	0.0197
7.407	171.4	4011.07	0.0222
6.817	370.6	9315.89	0.0239
6.82	204.0	4665.65	0.0213
6.993	167.1	3875.75	0.0217
7.35	196.1	4448.43	0.0214
7.763	193.9	4339.04	0.0214
6.82	238.6	3829.62	0.0153
7.817	173.0	4174.08	0.0227
7.12	217.4	5200.69	0.0223
5.643	283.8	6817.80	0.0222
6.76	196.2	5267.94	0.0251
7.83	154.9	3538.98	0.0214
8.27	144.2	2948.72	0.0192
6.993	183.1	4192.40	0.0211
7.88	172.5	3725.76	0.0201
9.23	151.0	3329.82	0.0205
7.58	189.0	4003.07	0.0199

Table S13. DSC results for PPS films

Sample Identifier	Melt Temperature	Total Enthalpy of Melting	% Crystallinity
PPS Film	271.08	5.2954	6.0%
	269.84	4.8593	5.5%
	272.56	6.2622	7.1%
	273.06	7.7028	8.7%
	272.91	11.0348	12.5%

Table S14. DSC results for virgin fiber composites

Sample Identifier	Melt Temperature	Total Enthalpy of Melting	Fiber Weight Fraction	% Crystallinity
V-30-UA	275.91	17.2579	49.0%	38.3%
	276.84	15.0889	49.0%	33.5%
	275.25	15.9373	49.0%	35.4%
	274.01	16.6579	49.0%	37.0%
	273.49	16.5964	49.0%	36.8%
V-30-140	273.93	16.2752	49.0%	36.1%
	274.23	20.3463	49.0%	45.1%
	274.26	18.51	49.0%	41.1%
	275.4	15.6466	49.0%	34.7%
	276.03	17.0873	49.0%	37.9%
V-30-210	278.28	17.8544	49.0%	39.6%
	274.67	16.628	49.0%	36.9%
	272.66	17.6615	49.0%	39.2%
	277.92	16.8773	49.0%	37.4%
	273.68	18.7294	49.0%	41.6%
V-5-UA	275.77	22.0929	49.8%	49.8%
	275.03	19.1922	49.8%	43.3%
	277.04	18.3132	49.8%	41.3%
	276.84	14.9678	49.8%	33.7%
	277.07	14.2508	49.8%	32.1%
V-5-140	276.35	21.4729	50.0%	48.6%
	275.07	23.5667	50.0%	53.3%
	277.02	17.2248	50.0%	39.0%
	275.85	23.5912	50.0%	53.4%
	275.19	18.5895	50.0%	42.1%
V-5-210	276.37	21.0085	50.0%	47.5%
	277.15	22.2542	50.0%	50.4%
	276.52	20.2033	50.0%	45.7%
	277.79	18.2371	50.0%	41.3%
	275.76	19.1848	50.0%	43.4%

Table S15. DSC results for recycled fiber composites

Sample Identifier	Melt Temperature	Total Enthalpy of Melting	Fiber Weight Fraction	% Crystallinity
R-5-UA	277.04	23.1783	35.2%	40.5%
	275.4	20.5972	35.2%	36.0%
	275.8	17.307	35.2%	30.2%
	275.39	17.8214	35.2%	31.1%
	275.79	24.1155	35.2%	42.1%
R-5-140	275.15	22.4687	37.7%	40.8%
	275.42	25.6478	37.7%	46.6%
	275.73	23.0048	37.7%	41.8%
	274.91	24.0584	37.7%	43.7%
	277	23.7551	37.7%	43.1%
R-5-210	276.16	21.594	37.7%	39.2%
	274.08	25.4784	37.7%	46.3%
	275.31	27.9138	37.7%	50.7%
	278.65	23.0449	37.7%	41.9%
	275.29	26.437	37.7%	48.0%

Table S16. DMA results for composite samples

Sample Identifier	E'' Peak Temperature (°C)	Tan δ Peak Temperature (°C)	Tan δ Peak Value	Storage Modulus Loss at Tan δ Peak (%)
V-30-UA	96.5	105.5	0.068	28.6%
	95.6	101.9	0.065	18.5%
	96.1	106.6	0.068	30.4%
V-30-140	103.4	113.5	0.063	21.0%
	101.3	110.9	0.066	22.9%
	103.4	112.2	0.063	25.3%
V-30-210	101.4	110.7	0.065	21.9%
	98.1	117.0	0.061	26.4%
	103.4	110.4	0.056	22.2%
V-5-UA	99.6	110.4	0.074	33.3%
	99.7	111.2	0.072	33.9%
	99.1	111.4	0.075	29.1%
V-5-140	102.0	111.7	0.066	29.6%
	101.9	113.9	0.067	31.0%
	103.8	114.4	0.065	31.5%
V-5-210	103.9	115.4	0.062	32.1%
	101.4	110.4	0.065	29.7%
	105.0	112.5	0.062	28.2%
R-5-UA	102.8	111.7	0.073	28.1%
	103.3	112.0	0.071	30.3%
	100.0	110.8	0.069	28.0%
R-5-140	103.5	111.8	0.073	27.4%
	103.1	113.8	0.068	30.0%
	105.1	113.3	0.064	28.6%
R-5-210	101.2	111.7	0.062	27.5%
	102.8	113.3	0.060	24.0%
	102.7	114.3	0.061	28.9%
PPS Film	87.3	93.0	3.186	99.0%
	87.3	93.0	3.137	99.0%
	87.2	92.9	3.170	99.1%
	87.1	92.9	3.117	98.4%
	87.0	92.8	3.112	98.9%

Table S17. Fiber and void content of virgin fiber composites

Sample Identifier	Calculated Void Content (%)	Measured Void Content (%)	Calculated Fiber Volume Fraction (%)
V-30-UA	6.25	6.17	41.11
	7.93	8.45	39.03
	4.56		44.70
	7.73		39.19
V-30-140	3.00	9.93	39.34
	5.65	8.87	39.61
	5.33		32.91
	8.41		35.35
V-30-210	6.64	9.16	49.91
	6.42	8.68	40.31
	5.39		42.64
	5.95		35.78
V-5-UA	9.24	9.95	36.61
	28.92	16.14	21.21
	7.08		34.03
	26.89		23.29
V-5-140	17.21	19.6	33.14
	16.37	18.68	31.38
	9.71		33.19
	12.77		28.90
V-5-210	20.64	22.06	32.83
	16.11	17.4	34.42
	13.96		35.26
	13.27		31.94

Table S18. Fiber and void content of recycled fiber composites

Sample Identifier	Calculated Void Content (%)	Measured Void Content (%)	Calculated Fiber Volume Fraction (%)
R-5-UA	5.61	4.33	30.92
	5.08	5.56	28.88
	0.78		36.01
	1.56		32.56
	3.85		31.56
	4.10		31.18
	0.88		33.75
	1.51		30.36
	3.63	3.14	34.55
	9.83	9.44	24.27
	1.75		30.59
	3.20		28.28
R-5-140	5.70	7.34	31.02
	0.32	3.51	34.31
	4.63		26.91
	0.26		31.02
R-5-210	2.67	4.72	24.72
	1.44	6.84	28.05
	2.76		30.48
	1.96		30.54

Table S19. Push-in test data for virgin fiber samples processed for 30 minutes

Sample Identifier	r_f (μm)	S_0 (mN/nm)	P_c (mN)	τ_s (MPa)	Interface Energy Absorbed (nJ)
V-30-UA	8.73	0.067	50.65	12.81	19.90
	7.30	0.074	49.89	16.67	20.31
	7.73	0.067	71.08	20.31	41.05
	9.53	0.063	49.53	10.79	19.97
	8.51	0.076	61.82	18.20	26.99
	7.85	0.068	54.53	15.57	23.14
	8.28	0.060	49.28	11.77	20.51
	8.33	0.057	45.68	10.30	18.85
	9.09	0.052	55.49	10.46	30.57
	8.56	0.071	57.47	15.71	24.80
	7.98	0.066	53.68	14.64	23.11
V-30-140	8.14	0.059	49.02	11.71	21.57
	8.86	0.060	52.16	11.64	21.56
	8.54	0.053	46.38	9.49	20.25
	7.79	0.044	41.14	7.66	18.90
	8.00	0.069	57.73	16.41	24.51
	8.18	0.062	50.54	12.63	21.92
	10.45	0.067	54.82	11.59	23.88
	8.72	0.064	50.99	12.34	23.48
	8.63	0.055	45.90	9.65	19.50
	8.71	0.069	54.95	14.35	22.62
	8.03	0.070	46.73	13.43	16.52
	9.46	0.065	54.62	12.37	23.30
V-30-210	8.42	0.056	45.57	8.79	18.97
	8.01	0.064	52.42	13.43	22.53
	8.57	0.050	43.80	7.16	18.70
	7.67	0.055	46.30	11.61	20.51
	7.82	0.073	56.44	17.72	23.36
	8.24	0.067	54.62	13.44	23.83
	7.72	0.068	52.36	15.92	22.52
	8.32	0.072	58.97	15.17	25.17
	9.00	0.064	54.02	9.76	22.72

Table S20. Push-in test data for virgin fiber samples processed for 5 minutes

Sample Identifier	r_f (μm)	S_0 (mN/nm)	P_c (mN)	τ_s (MPa)	Interface Energy Absorbed (nJ)
V-5-UA	7.56	0.052	34.76	7.88	10.79
	7.72	0.058	43.87	10.86	18.09
	7.52	0.059	46.19	11.95	18.10
	8.05	0.062	50.79	12.90	22.57
	7.65	0.066	51.91	14.76	23.21
	7.43	0.061	48.82	13.21	21.47
	7.94	0.058	45.31	10.91	21.37
	7.26	0.058	44.42	11.70	20.72
	8.59	0.061	49.37	11.56	20.96
	7.21	0.065	48.25	14.34	21.89
	7.71	0.067	52.89	15.15	23.86
	7.90	0.050	43.37	9.05	18.87
V-5-140	7.85	0.057	42.20	10.10	16.65
	7.58	0.064	50.83	14.15	22.56
	7.65	0.065	51.68	14.47	22.92
	7.90	0.049	41.57	8.50	18.29
	8.31	0.062	50.88	12.51	22.07
	7.90	0.048	41.79	8.37	19.60
	7.90	0.045	44.10	8.28	19.26
	7.90	0.054	30.53	6.88	8.52
	7.90	0.054	40.56	9.14	15.12
	7.90	0.057	44.76	10.65	21.39
V-5-210	7.41	0.072	57.67	18.47	24.92
	7.70	0.067	53.85	15.45	23.11
	8.99	0.063	53.20	12.29	21.83
	9.17	0.060	49.50	10.68	20.99
	7.32	0.071	56.02	17.91	24.33
	7.33	0.070	51.20	16.12	20.72
	7.89	0.072	56.19	16.90	24.89
	8.13	0.059	50.07	11.98	21.33
	7.87	0.069	53.11	15.35	23.15
	8.04	0.057	46.07	10.77	19.33
	8.60	0.061	52.01	12.16	22.14

Table S21. Push-in test data for recycled fiber composites processed for 5 minutes

Sample Identifier	r_f (μm)	S_0 (mN/nm)	P_c (mN)	τ_s (MPa)	Interface Energy Absorbed (nJ)
R-5-UA	7.34	0.070	47.20	16.62	22.18
	7.34	0.056	38.80	10.93	14.61
	7.57	0.053	45.59	11.78	20.36
	5.93	0.055	46.61	15.96	20.47
	7.56	0.072	57.16	20.10	25.66
	7.72	0.066	51.09	16.13	21.89
	7.65	0.068	55.77	18.30	24.29
	7.40	0.055	49.15	13.49	20.70
	6.85	0.052	44.21	12.39	19.72
	7.18	0.035	32.57	5.86	14.46
R-5-140	7.54	0.071	49.54	16.14	20.55
	7.54	0.067	52.37	16.10	23.42
	7.63	0.061	48.76	13.17	20.37
	7.48	0.060	47.72	13.46	20.90
	7.69	0.055	45.09	10.73	19.69
	7.65	0.056	45.92	11.30	20.70
	7.71	0.054	37.48	8.69	12.93
	7.54	0.064	50.07	14.71	21.60
	7.36	0.061	50.42	15.18	22.70
	7.26	0.067	53.00	18.26	24.05
R-5-210	7.30	0.076	60.43	23.23	27.00
	7.40	0.064	51.23	15.92	23.43
	7.67	0.079	62.14	21.40	27.63
	7.51	0.082	66.17	25.20	29.29
	7.37	0.069	56.38	19.12	25.24
	7.58	0.079	53.36	19.02	19.93
	7.58	0.051	35.62	8.19	12.17
	7.90	0.072	60.49	17.38	26.04
	7.35	0.075	62.63	23.27	27.52
	7.83	0.059	47.86	11.57	20.70
	7.92	0.066	54.07	14.13	22.81

Table S22. Stiffness results for virgin fiber samples processed for 30 minutes

Sample Identifier	Stiffness (N/m)
V-30-UA	18282
	18316
	18172
	18293
	17913
	17940
	18612
	18097
	18445
	18665
	18682
	18090
	18302
	17905
	17978
V-30-140	18551
	19496
	19611
	18918
	18531
	18760
	18733
	19159
	19144
	18618
V-30-210	18378
	18761
	18247
	18356
	18929
	18530
	19239
	18821
	17622
	18117
	19850
	19281
	18223
	18153

Table S23. Stiffness results for virgin fiber samples processed for 5 minutes

Sample Identifier	Stiffness (N/m)
V-5-UA	17912
	18898
	18691
	18098
	17688
	18671
	18243
	18546
	18552
	18439
V-5-140	18803
	18561
	18891
	18068
	18126
	17934
	18957
	18533
	18789
	18990
	18498
V-5-210	18658
	18509
	17805
	18045
	18356
	18386
	18348
	18492
	18496
	18617
	18137
	17881
	18082
	18021
	18294
	18647
	17703
	18393
	18471
	18603
	19004

Table S24. Stiffness results for recycled fiber samples processed for 5 minutes

Sample Identifier	Stiffness (N/m)
R-5-UA	18196
	17898
	18225
	18170
	18124
	18450
	18955
	18467
	18271
	17429
	18440
R-5-140	18065
	18541
	19939
	18445
	18739
	18363
	18718
	18443
	18514
	18517
	18879
	18654
	17744
	19971
R-5-210	17652
	19146
	18010
	18532
	18976
	17989
	18733
	18147
	18389
	18155
	17914

Supplementary Information for Chapter IV

SIV-1. Mechanical Testing Results

The mechanical testing results for the ABS and epoxy samples are found in Tables S25 and S26.The PPS composite results are found in Tables S1, S2, and S4.

SIV-2. Void Content Analysis Results

The void content of the ABS and epoxy samples is reported in Table S27. The PPS composite results are in Tables S17 and S18.

SIV-3. Nano-Indentation Results

The nano-indentation results for the ABS and epoxy composites can be found in Table S28. The PPS results can be fond in Tables S20 and S21.

Table S25. Tensile results for recycled fiber composites

Sample	Orientation	Strength (MPa)	Modulus (GPa)	Strain-to-Failure (%)
ABS	MD	88.21	10.5	0.852
		88.50	10.3	0.865
		84.90	9.3	0.949
		88.85	10.7	0.833
		88.33	10.4	1.017
		90.25	10.7	0.846
		88.51	9.9	0.891
		95.38	9.9	0.991
		94.09	9.7	0.969
		71.11	10.6	0.700
	CD	220.55	22.7	0.986
		222.46	21.6	1.048
		228.41	21.4	1.070
		228.38	24.4	0.970
		225.88	24.0	0.949
		221.06	22.7	0.973
		229.59	22.5	1.032
		221.54	24.3	0.914
		210.64	21.8	0.971
		218.61	21.7	1.097
Epoxy	MD	132.45	16.2	0.817
		163.38	14.4	1.139
		152.15	14.2	1.079
		147.80	13.9	1.065
		154.88	15.9	0.975
		150.93	14.9	1.020
		141.84	14.5	0.987
		161.55	15.1	1.072
		135.44	14.4	0.942
		155.04	15.8	0.976
Epoxy	CD	274.57	30.7	0.898
		308.54	31.6	0.978
		293.17	33.2	0.884
		279.14	32.7	0.852
		290.67	32.7	0.891
		258.87	31.1	0.831
		281.88	31.0	0.919
		268.64	32.2	0.843
		265.04	32.2	0.826
		286.04	34.4	0.836
Epoxy 0.1 MPa	[90/0/90/90/90]	247.44	22.6	1.099
		243.65	21.8	1.122
		194.94	19.7	0.992
		201.20	21.6	0.932
		203.04	21.7	0.935
		245.76	22.0	1.119
		216.66	17.7	1.230
		223.89	19.7	1.137

Table S26. Shear results for recycled fiber composites

Sample	Strength (MPa)	Modulus (GPa)	Strain-to-Failure (%)
ABS	64.28	5.3	1.783
	64.87	4.9	1.562
	68.78	5.1	1.874
	73.32	5.5	1.607
	64.90	6.1	1.318
	68.76	5.5	2.196
	68.91	5.2	2.031
	71.15	5.4	1.437
Epoxy	143.57	6.5	2.230
	136.60	6.1	2.430
	124.17	6.3	2.076
	142.49	6.1	2.383
	126.05	5.6	2.673
	161.88	6.9	2.587
	165.97	6.4	2.735
	150.79	6.7	2.578
	134.80	6.8	2.415

Table S27. Calculated and measured void content in recycled fiber composites

Sample	Calculated Void Content (%)	Measured Void Content (%)
ABS	8.01	1.02
	7.26	2.65
	0.35	4.19
	2.70	3.25
	7.79	-0.10
	2.90	3.35
	5.81	-0.17
	5.74	0.94
	0.40	2.41
	1.12	1.51
	6.61	-0.96
	3.75	0.86
	6.15	0.23
	2.09	0.50
	1.94	-0.87
	6.93	-2.51
	3.15	0.09
	1.09	0.90
	4.78	-1.58
	3.57	1.87
	1.61	-0.17
	2.91	-0.62
	2.96	0.24
	9.43	-0.95
Epoxy	18.72	18.44
	18.58	17.05
	17.08	18.26
	15.60	17.59
	18.67	16.80
	17.82	16.84
	13.53	18.62
	12.35	18.50
	12.06	15.92
	16.32	14.88
	13.36	14.43
	17.75	14.74
	15.14	13.83
	15.66	14.82
	14.60	13.85
	16.92	13.97
	15.08	14.86
	15.58	14.87
	13.29	15.47
	18.75	13.60
Epoxy 0.1 MPa	15.68	13.44
	10.40	14.12
	13.97	15.29
	8.61	6.45
	14.69	13.41
	11.77	13.34
	11.26	14.90

Table S28. Nano-indentation results for ABS and epoxy composites

Sample	r_f (μm)	S_0 (mN/nm)	P_c (mN)	τ_s (MPa)
ABS	7.17	0.051	20.14	5.48
	7.26	0.045	22.10	5.11
	7.92	0.047	26.32	4.90
	7.37	0.052	24.07	6.15
	7.21	0.044	25.04	5.78
	7.39	0.047	26.92	6.17
	8.04	0.055	23.95	4.99
	7.10	0.041	26.56	5.99
	7.49	0.051	26.45	6.32
	6.94	0.055	20.23	6.55
Epoxy	7.12	0.081	54.91	24.24
	8.30	0.069	49.83	11.83
	7.72	0.078	50.14	16.72
	7.39	0.066	42.64	13.72
	8.13	0.070	50.94	13.05
	7.24	0.066	56.09	19.19
	8.13	0.062	48.29	10.96
	8.13	0.062	34.27	7.77
	7.51	0.062	53.60	15.43
Epoxy 0.1 MPa	7.60	0.074	52.72	17.47
	7.15	0.083	68.39	30.55
	7.60	0.073	58.83	19.23
	7.44	0.075	60.97	21.85
	8.03	0.074	65.01	18.28
	7.34	0.061	37.75	11.46
	6.84	0.054	30.39	10.09
	8.12	0.032	25.12	2.95
	7.90	0.067	52.14	13.94
	8.01	0.072	46.30	12.76
	7.59	0.064	55.78	16.06

SIV-4. MATLAB Script for Property Predictions

```
%Model for predicting mechanical properties of organosheet composites
%Philip Barnett

clear all
% close all
clc
tic
%% Run the calculation multiple times to generate a distribution of
results (due to inherent randomness)
iter = 1;

%input local fiber volume fraction and fiber bundle size
[file1, path1] = uigetfile('*.mat', 'Select the microscopy fiber and
void fraction data');
pathname1 = strcat(path1,file1);
load(pathname1);
vflocalsize = size(Vflocal);
%Make sure vflocal doesn't contain any 0% Vf for numerical stability
for i = 1:vflocalsize(1)
    for j = 1:vflocalsize(2)
        if Vflocal(i,j) == 0
           Vflocal(i,j) = 1e-6;
        end
    end
end

[file3, path3] = uigetfile('*.xlsx', 'Select the fiber data');
pathname3 = strcat(path3,file3);
table = readtable(pathname3);
%Determine if the data is for vCF or rCF
answer = questdlg('Is this recycled or virgin carbon fiber?','Fiber
type','Virgin','Recycled','Recycled');
if strcmp('Recycled',answer)
    Efvals = table2array(table(:,2)).*1e9;
    sigfuvals = table2array(table(:,3)).*1e6;
    strainfvals = table2array(table(:,4));
    rf = 7.3/2*1e-6;
elseif strcmp('Virgin',answer)
    Efvals = table2array(table(:,7)).*1e9;
    sigfuvals = table2array(table(:,8)).*1e6;
    strainfvals = table2array(table(:,9));
    rf = 7.9/2*1e-6;
end

[file4, path4] = uigetfile('*.mat', 'Select the orientation data');
pathname4 = strcat(path4,file4);
percenttotal = load(pathname4);
angleprobability = percenttotal.percenttotal;
Lf0 = [];

[file5, path5] = uigetfile('*.mat', 'Select the fiber length data');
pathname5 = strcat(path5,file5);
```

```
len = load(pathname5);
len = len.len*1e-3;

for i = 1:iter

    [sigma, e, Ec0, sigmaeff, percentmatrix, percentfiber, Lf] =
    strengthcalc(Vflocal, Vvlocal, angleprobability, Efvals, sigfuvals,
    strainfvals, rf, len);

    tensilemodulus(i) = Ec0;
    tensilestrength(i) = sigma(end);
    tensilestrain(i) = e(end);
    effectivestrength(i) = sigmaeff(end);
    percentmatrixdamage(i) = percentmatrix;
    percentfiberdamage(i) = percentfiber;
    Lf0 = [Lf0; Lf];
    clc
    fprintf('Current iteration: %d \n',i)
end

%Analyze the data - remove outliers and report the mean and stdev
adjustedmodulus = rmoutliers(tensilemodulus, 'quartiles');
adjustedstrength = rmoutliers(tensilestrength, 'quartiles');
adjustedstrain = rmoutliers(tensilestrain, 'quartiles');
[meanmodulus, stdmodulus, meanmodulusCI, stdmodulusCI] =
normfit(adjustedmodulus);
[meanstrength, stdstrength, meanstrengthCI, stdstrengthCI] =
normfit(adjustedstrength);
[meanstrain, stdstrain, meanstrainCI, stdstrainCI] =
normfit(adjustedstrain);
toc
%% Constants
function [sigma, e, Ec0, sigmaeff, percentmatrix, percentfiber, Lf] =
strengthcalc(fiber, void, angleprobability, Efvals, sigfuvals,
strainfvals, rf, len)

    W = 0.5*25.4e-3; %sample width
    matrix = 'Epoxy';

    switch matrix
        case 'PPS'
            Em = 3.4e9; %Matrix modulus
            sigm = 80e6; %Matrix strength
            vm = 0.38; %Matrix Poisson's ratio
            IFSS = 14.58e6; %rCF
%             IFSS = 12.59e6; %vCF
            h = 1.92e-3; %1 MPa pressure ELG
%             h = 0.48e-3; %1 MPa pressure organosheet ELG
%             h = 0.61e-3; %1 MPa pressure organosheet Neenah
%             h = 1.97e-3; %1 MPa pressure Neenah
            strainmax = 0.04;
        case 'ABS'
            Em = 2.0e9;
```

```
            IFSS = 5.74e6;
            sigm = 39e6;
            vm = 0.35;
            h = 1.56e-3; %1 MPa pressure
            strainmax = 0.32;
        case 'Epoxy'
            Em = 2.7e9;
%             IFSS = 13.87e6; %1 MPa pressure
            IFSS = 15.88e6; %0.1 MPa pressure
            sigm = 79e6;
            vm = 0.35;
%             h = 1.96e-3; %1 MPa pressure
            h = 2.87e-3; %0.1 MPa pressure
            strainmax = 0.071;
    end


    vf = 0.2; %Fiber Poisson's ratio
    Gm = Em/(2*(1+vm)); %Shear modulus
    rm = rf/sqrt(nanmean(fiber(:)));
    numangles = floor(h/(2*rm));

    %% Calculate the initial stiffnesses
    rf = rf*ones(1,numangles);
    V = zeros(numangles,2);
    for i = 1:numangles %randomize each layer
        %generate a random number to determine the angle
        randomindex = rand;
        possibleangles = 0:1:179;
        angles(i) = possibleangles(find(angleprobability > randomindex,
        1, 'first'));
        %Determine fiber length for this iteration
        randomindex1 = randi(length(len));
        Lf(i) = len(randomindex1);
        Lfmax = abs(W/sind(angles(i)));
        if Lf(i) > Lfmax
           Lf(i) = Lfmax;
        end
        vflocalsize = size(fiber);
        Vf(i) = NaN; %used to make sure that NaN values in the datasets
        aren't included
        while isnan(Vf(i))
            randomindex2 = randi(vflocalsize(1),1);
            randomindex3 = randi(vflocalsize(2),1);
            Vf(i) = fiber(randomindex2,randomindex3);
            Vv(i) = void(randomindex2,randomindex3);
        end

        if Vf(i) > Vv(i)
            Isvoid(i) = false;
        else
            Isvoid(i) = true;
        end
```

```
    V(i,1) = Vf(i);
    V(i,2) = Vv(i);

    Ef(i) = mean(Efvals);
    sigfu(i) = mean(sigfuvals);


    %Calculate the longitudinal stiffness
    nsq = 2*Gm/(Ef(i)*log(1/sqrt(Vf(i))));
    s = Lf(i)/(2*rf(i));
    etaL = 1 - tanh(sqrt(nsq)*s)/(sqrt(nsq)*s);
    Ex(i) = etaL*Vf(i)*Ef(i) + (1-Vf(i))*Em;
    %Calculate the off-axis stiffnesses
    Tr(i) = Ex(i)/0.880;
    Ey(i) = Tr(i)*0.052;
    Gxy(i) = Tr(i)*0.031;
    vxy(i) = vf*Vf(i) + vm*(1-Vf(i));
    vyx(i) = vxy(i)*Ey(i)/Ex(i);
end


%Initial, undamaged laminate
[a0, Q110, Q220, Q120, Q160, Q260, Q660] =
engconsts(Ex,Ey,vxy,vyx,Gxy,angles,h);
%% Calculations
%This loop incrementally increases the stress and decreases the
effective stiffness of the layers

damagetype = zeros(1,length(angles)); %initialize the damage matrix
sigma = 0; %initialize the stress
sigmaeff = 0; %initialize the effective stress
e = 0; %initialize the strain
D = 0; %initialize the damage variable
i = 1;
ratio = 0;
maxiters = 1000;
sigstep = 0.5e6;
percentdamaged = 0;
%Determine angles in fiber dominant and matrix dominant directions
%chosen based on half stiffness of an average ply
theta90 = (angleprobability(145) - angleprobability(35));
theta0 = (1 - (angleprobability(145) - angleprobability(35)));
property = 'Longitudinal';
switch property
    case 'Longitudinal'
        Ec0 = 1/(h*a0(1,1)); %original stiffness
        %Calculate the strain energy density of the matrix and
        fiber at failure based on datasheet values
        strainelastic = sigm/Em;
        deltastrain = strainmax - strainelastic;
        umatrixe = 0.5*strainelastic*sigm; %energy stored as
        elastic deformation
```

```
            umatrixp = sigm*deltastrain; %energy put into plastic
            deformation
            strainf = nanmean(strainfvals);
            sigf = nanmean(sigfuvals);
            ufiber = 0.5*strainf*sigf;
            %Weight the limit based on the fiber dominant diretion
            (i.e., the fiber dominant direction is less dependent on
            the matrix and should have less plasticity
            umatrix = umatrixp*(1-theta0) + umatrixe;
            limit = (1-nanmean(Vf))*umatrix/(nanmean(Vf)*ufiber + (1-
            nanmean(Vf))*umatrix);
        case 'Transverse'
            Ec0 = 1/(h*a0(2,2));
            %Calculate the strain energy density of the matrix and
            fiber at failure based on datasheet values
            strainelastic = sigm/Em;
            deltastrain = strainmax - strainelastic;
            umatrixp = sigm*deltastrain;
            umatrixe = 0.5*strainelastic*sigm;
            strainf = nanmean(strainfvals);
            sigf = nanmean(sigfuvals);
            ufiber = 0.5*strainf*sigf;
            umatrix = umatrixp*(1-theta90) + umatrixe;
            limit = (1-nanmean(Vf))*umatrix/(nanmean(Vf)*ufiber + (1-
            nanmean(Vf))*umatrix);
        case 'Shear'
            Ec0 = 1/(h*a0(3,3));
            limit = 0.5;
    end


    while ratio(i) < limit && i < maxiters
        i = i+1;
        [a, Q11, Q22, Q12, Q16, Q26, Q66] =
        engconsts(Ex,Ey,vxy,vyx,Gxy,angles,h);
        if any(isnan(a))
            sprintf('There is a problem')
            break
        end
        percentdamaged(i) = nnz(damagetype)/numel(damagetype);
        switch property
            case 'Longitudinal'
                Ecl(i) = 1/(h*a(1,1));
                if Ecl(i)-Ecl(i-1) > 10 && i > 2
                    sprintf('There is a problem')
                end
                D(i) = 1 - sqrt(Ecl(i) / Ec0); %strain energy
                equivalence
%               D(i) = 1 - (Ec1(i)/Ec0); %strain equivalence
                sigma(i) = sigma(i-1) + sigstep;
                sig = [sigma(i); 0; 0];
                sigmaeff(i) = sigma(i) / (1-D(i-1));
                sigeff = [sigmaeff(i); 0; 0];
            case 'Transverse'
```

```
                Ect(i) = 1/(h*a(2,2));
                if Ect(i)-Ect(i-1) > 10 && i > 2
                    sprintf('There is a problem')
                end
                D(i) = 1 - sqrt(Ect(i)/Ec0);
%                 D(i) = 1 - (Ect(i)/Ec0); %strain equivalence
                sigma(i) = sigma(i-1) + sigstep;
                sig = [0; sigma(i); 0];
                sigmaeff(i) = sigma(i) / (1-D(i-1));
                sigeff = [0; sigmaeff(i); 0];
            case 'Shear'
                Ecs(i) = 1/(h*a(3,3));
                if Ecs(i)-Ecs(i-1) > 10 && i > 2
                   sprintf('There is a problem')
                end
                D(i) = 1 - sqrt(Ecs(i)/Ec0);
%                 D(i) = 1 - (Ecs(i)/Ec0); %strain equivalence
                sigma(i) = sigma(i-1) + sigstep;
                sig = [0; 0; sigma(i)];
                sigmaeff(i) = sigma(i) / (1-D(i-1));
                sigeff = [0; 0; sigmaeff(i)];
        end

        % Calculate the stress in each lamina
        [eeff, sigx, sigy, tauxy] =
        stresscalc(sigeff,h,a0,Q110,Q220,Q120,Q160,Q260,Q660,angles);
        % Determine if failure has occurred and output reduced
        stiffness
        [damagetype, Ex, Ey, Gxy, vxy, vyx, V, Isvoid] = failure(Ex,
        Ey, Gxy, vxy, vyx, sigfu, Ef, Lf, Em, Gm, rf, vm, vf, sigx,
        sigy, tauxy, V, sigm, angles, damagetype, Isvoid, IFSS);
        switch property
            case 'Longitudinal'
                e(i) = eeff(1)/(1-D(i-1)); %calculate the strain from
                the effective strain
            case 'Transverse'
                e(i) = eeff(2)/(1-D(i-1));
            case 'Shear'
                e(i) = eeff(3)/(1-D(i-1));
                if nnz(damagetype)/length(damagetype) > limit
                    break %stop once half of the plies are damaged
                end
        end
        %Calculuate the strain energy density
        Utot(i) = trapz(e,sigma); %total strain energy density
        ep(i) = e(i) - sigma(i)/Ec0; %plastic strain
        Uel(i) = 0.5*Ec0*(e(i)-ep(i))^2; %elastic strain energy density
        %Calculate the ratio of the plastic to total strain energy
        ratio(i) = (Utot(i)-Uel(i))/Utot(i);
    end
    plot(e*100,sigma./1e6)
    hold on
    xlabel('Strain (%)')
    ylabel('Stress (MPa)')
```

```
    percentmatrix = sum(damagetype(:) == 2) / length(damagetype)*100;
    percentfiber = sum(damagetype(:) == 1) / length(damagetype)*100;
end
%% Determine Engineering Constants
function [a, Q11, Q22, Q12, Q16, Q26, Q66] =
engconsts(Ex,Ey,vxy,vyx,Gxy,angles,h)

    for i = 1:length(angles)
       %principal stiffness matrix
       Qxx(i) = Ex(i) / (1 - vxy(i)*vyx(i));
       Qyy(i) = Ey(i) / (1 - vxy(i)*vyx(i));
       Qxy(i) = vxy(i)*Ey(i) / (1 - vxy(i)*vyx(i));
       Qss(i) = Gxy(i);
       m = cosd(angles(i));
       n = sind(angles(i));
       %transformed stiffness matrix
       Q11(i) = m^4*Qxx(i) + n^4*Qyy(i) + 2*m^2*n^2*Qxy(i) +
       4*m^2*n^2*Qss(i);
       Q22(i) = n^4*Qxx(i) + m^4*Qyy(i) + 2*m^2*n^2*Qxy(i) +
       4*m^2*n^2*Qss(i);
       Q12(i) = m^2*n^2*Qxx(i) + m^2*n^2*Qyy(i) + (m^4+n^4)*Qxy(i) -
       4*m^2*n^2*Qss(i);
       Q16(i) = m^3*n*Qxx(i) - m*n^3*Qyy(i) - m*n*(m^2-n^2)*Qxy(i) -
       2*m*n*(m^2-n^2)*Qss(i);
       Q26(i) = m*n^3*Qxx(i) - m^3*n*Qyy(i) + m*n*(m^2-n^2)*Qxy(i) +
       2*m*n*(m^2 - n^2)*Qss(i);
       Q66(i) = m^2*n^2*Qxx(i) + m^2*n^2*Qyy(i) - 2*m^2*n^2*Qxy(i) +
       (m^2-n^2)^2*Qss(i);
    end

    dz = h/length(angles);

    for i = 1:length(angles)
       A11(i) = Q11(i)*dz;
       A12(i) = Q12(i)*dz;
       A22(i) = Q22(i)*dz;
       A16(i) = Q16(i)*dz;
       A26(i) = Q26(i)*dz;
       A66(i) = Q66(i)*dz;
    end

    A11 = sum(A11);
    A12 = sum(A12);
    A22 = sum(A22);
    A16 = sum(A16);
    A26 = sum(A26);
    A66 = sum(A66);

    A = [A11 A12 A16; A12 A22 A26; A16 A26 A66];
    if any(isnan(A(:)))
        sprintf('We have a problem')
        a = NaN;
        return
```

```
    end
    a = inv(A);
end

%% Apply incremental stress
function [e, sigx, sigy, tauxy] =
stresscalc(sigma,h,a,Q11,Q22,Q12,Q16,Q26,Q66,angles)
    %Strain in the transformed axis
    e = a*h*sigma;

    %inverted transformation matrix
    for i = 1:length(angles)
       m = cosd(angles(i));
       n = sind(angles(i));
       T11(i) =  m^2;
       T12(i) = n^2;
       T16(i) = 2*m*n;
       T21(i) = n^2;
       T22(i) = m^2;
       T26(i) = -2*m*n;
       T61(i) = -m*n;
       T62(i) = m*n;
       T66(i) = m^2 - n^2;
    end

    %stress in the principal axis
    for i = 1:length(angles)
       T = [T11(i) T12(i) T16(i); T21(i) T22(i) T26(i); T61(i) T62(i)
       T66(i)];
       Q = [Q11(i) Q12(i) Q16(i); Q12(i) Q22(i) Q26(i); Q16(i) Q26(i)
       Q66(i)];
       sig = T*Q*e;
       sigx(i) = sig(1);
       sigy(i) = sig(2);
       tauxy(i) = sig(3);
    end
end

%% Tsai-Hill Criteria
function [damagetype, Ex, Ey, Gxy, vxy, vyx, V, Isvoid] = failure(Ex,
Ey, Gxy, vxy, vyx, sigfu, Ef, Lf, Em, Gm, rf, vm, vf, sigx, sigy,
tauxy, V, sigm, angles,damagetype,Isvoid,IFSS)
    Vf = V(:,1);
    Vv = V(:,2);

    %Determine the critical length for each ply
    for i = 1:length(rf)
        rm(i) = rf(i)/sqrt(nanmean(Vf(:)));
        Lfc(i) = rf(i)*sigfu(i)/IFSS;
    end

    for i = 1:length(angles)
        %Shokrieh paper
```

```
    sigL(i) = Ex(i)*sigfu(i)/(Ef(i)*(1-
    sech(Lfc(i)/2*sqrt(Em/(Ef(i)*rf(i)*(rm(i)-rf(i))*(1+vm))))));
    %Shear lag
    sigT(i) = sigm*(1-2*sqrt(Vf(i)/pi)); %transverse tensile
    strength
    tauLT(i) = sigm/sqrt(3);

    if Isvoid(i) %treat as an isotropic solid with voids following
    Eudier
       sigL(i) = sigL(i)*(1-pi*(3/(4*pi))^(2/3)*Vv(i)^2/3);
       sigT(i) = sigT(i)*(1-pi*(3/(4*pi))^(2/3)*Vv(i)^2/3);
       tauLT(i) = tauLT(i)*(1-Vv(i));
    end
end

%check if layer has failed using Tsai-Hill failure theory
for i = 1:length(angles)
    Exold = Ex(i);
    Eyold = Ey(i);
    Gxyold = Gxy(i);
    esq1(i) = (sigx(i)/sigL(i))^2;
    esq2(i) = (sigy(i)/sigT(i))^2 + (tauxy(i)/tauLT(i))^2 -
    sigx(i)*sigy(i)/(sigL(i)^2);
    esq(i) = esq1(i) + esq2(i);
    if esq(i) > 1
        if esq1(i) > esq2(i)
            if damagetype(i) < 1
                damagetype(i) = 1; %fiber damage
                Lf(i) = Lfc(i);
                [Ex(i),Ey(i),Gxy(i)] =
                fiberdamage(Vf(i),Ef(i),Em,Lf(i),Gm,rf(i),Exold);
            else
                damagetype(i) = 2; %matrix damage
                Lf(i) = Lfc(i);
                [Vf(i),Vv(i),Ex(i),Ey(i),Gxy(i),vxy(i),vyx(i),

                Isvoid(i)] = matrixdamage(Vf(i),Vv(i),Ef(i),
                Em,Lf(i),Gm,rf(i),Isvoid(i),vf,vm,Exold,Eyold,
                Gxyold);
            end
        else
            damagetype(i) = 2;
            [Vf(i),Vv(i),Ex(i),Ey(i),Gxy(i),vxy(i),vyx(i),
            Isvoid(i)] = matrixdamage(Vf(i),Vv(i),Ef(i),
            Em,Lf(i),Gm,rf(i),Isvoid(i),vf,vm,Exold,Eyold,Gxyold);
        end
    end
    if Vf(i)<Vv(i)
        Isvoid(i) = true;
        damagetype(i) = 2;
    end
end
if any(isnan(vxy)) || any(isnan(vyx))
   sprintf('We have a problem');
```

```
    end
    V = [Vf Vv];
end

%% Cox Function
function [Ex] = Cox(Vf,Ef,Em,Lf,Gm,rf)
    nsq = 2*Gm/(Ef*log(1/sqrt(Vf)));
    s = Lf/(2*rf);
    etaL = 1 - tanh(sqrt(nsq)*s)/(sqrt(nsq)*s);
    if isnan(etaL)
      etaL = 0;
    end
    Ex = Ef*Vf*etaL + (1-Vf)*Em; %Cox method
end

%% Matrix damage function
function [Vf,Vv,Ex,Ey,Gxy,vxy,vyx, Isvoid] =
matrixdamage(Vf,Vv,Ef,Em,Lf,Gm,rf,Isvoid,vf,vm,Exold,Eyold,Gxyold)

    Vvnew = Vf*rand;
    Vf = Vf - Vvnew;
    Vv = Vv + Vvnew;
    if Vv > Vf
        Isvoid = true;
    end

    Ex = Cox(Vf,Ef,Em,Lf,Gm,rf); %Cox
    Tr = Ex/0.88;
    Ey = Tr*0.052;
    Gxy = Tr*0.031;
    vxy = Vf*vf + (1-Vf)*vm;
    vyx = Ey/Ex*vxy;
    if Ex > Exold
        Ex = Exold;
    end
    if Gxy > Gxyold
        Gxy = Gxyold;
    end
    if Ey > Eyold
       Ey = Eyold;
    end
end

%% Fiber Damage Function
function [Ex,Ey,Gxy] = fiberdamage(Vf,Ef,Em,Lf,Gm,rf,Exold)
    Ex = Cox(Vf,Ef,Em,Lf,Gm,rf);
    if Ex > Exold
        Ex = Exold;
    end
    Tr = Ex/0.88;
    Ey = Tr*0.052;
    Gxy = Tr*0.031;
end
```

SIV-5. MATLAB Script for Local Fiber and Void Content Analysis

```
%Philip Barnett
%Local Volume Fraction and Void Calculation

clear all
close all hidden
close all force
clc

%% Get the original file
[file,path] = uigetfile('*.jpg', 'Select the original file');
orig = imread(strcat(path,file));
if size(orig,3) == 3
    orig = rgb2gray(orig);
end

%% Name the figures
name = inputdlg('Enter the sample name: ');

%% Get the mask
[file,path] = uigetfile([path '*.jpg'], 'Select the mask');
mask = imread(strcat(path,file));
if size(mask,3) == 3
    mask = rgb2gray(mask);
end
mask = imcomplement(imbinarize(mask));

%% Rotate the mask
figure
imshow(mask)

%Call to the corners function to determine the corners of the mask
[C, topleftx, toplefty, botrightx, botrighty, toprightx, toprighty,
botleftx, botlefty] = corners(mask);
hold on
plot(C(:,1),C(:,2),'*','MarkerSize',10,'Linewidth',10)

done = false;
while done == false
    answer = questdlg('Were the corners properly identified?', 'Yes',
    'No');
    switch answer
        case 'Yes'
            done = true;
        case 'No'
            [topleftx,toplefty,toprightx,toprighty,botleftx,
            botlefty,botrightx,botrighty] =
            cornersmanual(topleftx,toplefty,toprightx,
            toprighty,botleftx,botlefty,botrightx,botrighty);
            plot([topleftx,botrightx,botleftx,toprightx],
            [toplefty,botrighty,botlefty,toprighty],
            '*','MarkerSize',10,'Linewidth',10);
```

```
    end
end

close

%Determine the angle of rotation
angle = atand((toprighty - toplefty)/(toprightx - topleftx));
mask = imrotate(mask,angle);
imshow(mask)

%Call to the corners function to determine the new corners
[C, topleftx, toplefty, botrightx, botrighty, toprightx, toprighty,
botleftx, botlefty] = corners(mask);
hold on
plot(C(:,1),C(:,2),'*','MarkerSize',10,'Linewidth',10)

done = false;
while done == false
    answer = questdlg('Were the corners properly identified?', 'Yes',
    'No');
    switch answer
        case 'Yes'
            done = true;
        case 'No'
            [topleftx,toplefty,toprightx,toprighty,botleftx,botlefty,
            botrightx,botrighty] = cornersmanual(topleftx,toplefty,
            toprightx,toprighty,botleftx,botlefty,botrightx,
            botrighty);
            plot([topleftx,botrightx,botleftx,toprightx],
            [toplefty,botrighty,botlefty,toprighty],'*',
            'MarkerSize',10,'Linewidth',10);
    end
end

close

%Determine the smallest width
topwidth = abs(toprightx - topleftx);
botwidth = abs(botrightx - botleftx);
diagdownwidth = abs(botrightx - topleftx);
diagupwidth = abs(botleftx - toprightx);
width = [topwidth, botwidth, diagdownwidth, diagupwidth];
width = min(width);

%Determine shortest height
rightheight = abs(toprighty - botrighty);
leftheight = abs(toplefty - botlefty);
diagdownheight = abs(toplefty - botrighty);
diagupheight = abs(botlefty - toprighty);
height = [leftheight, rightheight, diagdownheight, diagupheight];
height = min(height);

%Determine if plotting needs to start from the top or bottom for width
```

```
if botleftx < topleftx
    xstart = round(topleftx);
else
    xstart = round(botleftx);
end

%Determine if plotting needs to start from the top or bottom for height
if toplefty < toprighty
    ystart = round(toprighty);
else
    ystart = round(toplefty);
end

%Create a new mask from this region
newmask = zeros(size(mask));
for i = round(xstart):round(xstart+width)
    for j = round(ystart):round(ystart+height)
        newmask(j,i) = 1;
    end
end
mask = newmask;
close

%% Rotate the original image and overlay the mask to show ROI
orig = imrotate(orig,angle);
figure
imshowpair(orig,mask)
saveas(gcf,char(fullfile(path,strcat(name,' Mask'))),'jpeg');

%% Get the fiber phase
[file,path] = uigetfile([path '*.jpg'], 'Select the fiber phase
image');
fiber = imread(strcat(path,file));
if size(fiber,3) == 3
    fiber = rgb2gray(fiber);
end
fiber = imbinarize(fiber);
fiber = imrotate(fiber,angle);

%% Get the void phase
[file,path] = uigetfile([path '*.jpg'], 'Select the void phase image');
void = imread(strcat(path,file));
if size(void,3) == 3
    void = rgb2gray(void);
end
void = imcomplement(imbinarize(void));
void = imrotate(void,angle);
imagelist = {orig, mask, fiber, void};

%% Create an image of each step
figure
montage(imagelist)
saveas(gcf,char(fullfile(path,strcat(name,' Steps'))),'jpeg');
```

```
%% Image calculations
mask = im2double(mask);
fiber = im2double(fiber);
void = im2double(void);
masksize = sum(mask,'all');
mask(mask == 0) = NaN;
[length2, width2] = size(mask);

for i = 1:length2
    for j = 1:width2
        if isnan(mask(i,j))
           fiber(i,j) = 0;
           void(i,j) = 0;
        end
    end
end

fibersize = sum(fiber,'all');
voidsize = sum(void,'all');
fibervol = fibersize/masksize*100;
voidvol = voidsize/masksize*100;

image = zeros(length2,width2,3);
for i = 1:length2
    for j = 1:width2
        image(i,j,1) = image(i,j,1) + fiber(i,j)*255;
        image(i,j,2) = image(i,j,2) + void(i,j)*255;
        image(i,j,3) = image(i,j,3) + mask(i,j)*255;
    end
end

figure
imshow(image)
saveas(gcf,char(fullfile(path,strcat(name,' Global'))),'jpeg');

line1 = sprintf('The total fiber volume fraction is: %.2f%% \n',
fibervol);
line2 = sprintf('The total void volume fraction is: %.2f%% \n',
voidvol);
f = msgbox({line1, line2});

Vflocal = localvf(xstart, ystart, width, height, fiber, name, path);
Vvlocal = localvv(xstart, ystart, width, height, void, name, path);

save(fullfile(path,char(name)),'Vflocal','Vvlocal')
%% Function to find the corners on the mask automatically
function [C, topleftx, toplefty, botrightx, botrighty, toprightx,
toprighty, botleftx, botlefty] = corners(im)

    %Automatically select the four corners of the mask image
    C = corner(im,'MinimumEigenvalue',4);
```

```
    for i = 1:4
       Csum(i) = C(i,1) + C(i,2);
    end
    [val,topleft] = min(Csum);
    topleftx = C(topleft,1);
    toplefty = C(topleft,2);
    [val,botright] = max(Csum);
    botrightx = C(botright,1);
    botrighty = C(botright,2);
    %Leave only the remaining values in C
    for i = 1:4
        if C(i,1) == topleftx && C(i,2) == toplefty
            C(i,1) = NaN;
            C(i,2) = NaN;
        elseif C(i,1) == botrightx && C(i,2) == botrighty
            C(i,1) = NaN;
            C(i,2) = NaN;
        end
    end
    [val,topright] = min(C(:,2));
    toprightx = C(topright,1);
    toprighty = C(topright,2);
    C(topright,1) = NaN;
    C(topright,2) = NaN;
    for i = 1:4
        if ~isnan(C(i,1))
           botleftx = C(i,1);
           botlefty = C(i,2);
        end
    end
    C = corner(im,'MinimumEigenvalue',4);
end

%% Function to determine if the corners need to be found manually

function [topleftx,toplefty,toprightx,toprighty,botleftx,botlefty,
botrightx,botrighty] = cornersmanual(topleftx,toplefty,toprightx,
toprighty,botleftx,botlefty,botrightx,botrighty)
    % Manually select the four corners of the image
    for i = 1:4
        switch i
            case 1
                uiwait(msgbox('Select the top left of the mask'))
                [topleftx, toplefty] = ginput(1);
            case 2
                uiwait(msgbox('Select the top right of the mask'))
                [toprightx, toprighty] = ginput(1);
            case 3
                uiwait(msgbox('Select the bottom left of the mask'))
                [botleftx, botlefty] = ginput(1);
            case 4
                uiwait(msgbox('Select the bottom right of the mask'))
                [botrightx, botrighty] = ginput(1);
         end
```

```
    end

    round([topleftx,toplefty,toprightx,toprighty,
    botleftx,botlefty,botrightx,botrighty]);
end

%% Function to determine local fiber volume fraction
function Vflocal = localvf(xstart, ystart, width, height, fiber, name,
path)
regionsize = 100;
heightround = floor(height/regionsize)*regionsize;
widthround = floor(width/regionsize)*regionsize;
numregionsheight = heightround/regionsize;
numregionswidth = widthround/regionsize;
startheight = ystart;

for i = 1:numregionsheight
    startwidth = xstart;
    for j = 1:numregionswidth
        Vflocal(i,j) =
        sum(sum(fiber(startheight:startheight+regionsize,
        startwidth:startwidth+regionsize)))/regionsize^2;
        startwidth = startwidth + regionsize;
    end
    startheight = startheight + regionsize;
end

figure
imagesc(Vflocal);
colorbar
axis image
axis off
set(gcf,'Position',[0 400 1920 400])
saveas(gcf,char(fullfile(path,strcat(name,' Vflocal'))),'jpeg');
end

%% Function to determine local void volume fraction
function Vvlocal = localvv(xstart, ystart, width, height, void,
name,path)
regionsize = 100;
heightround = floor(height/regionsize)*regionsize;
widthround = floor(width/regionsize)*regionsize;
numregionsheight = heightround/regionsize;
numregionswidth = widthround/regionsize;
startheight = ystart;

for i = 1:numregionsheight
    startwidth = xstart;
    for j = 1:numregionswidth
        Vvlocal(i,j) =
        sum(sum(void(startheight:startheight+regionsize,
        startwidth:startwidth+regionsize)))/regionsize^2;
        startwidth = startwidth + regionsize;
```

```
    end
    startheight = startheight + regionsize;
end

figure
imagesc(Vvlocal);
colorbar
axis image
axis off
set(gcf,'Position',[0 400 1920 400])
saveas(gcf,char(fullfile(path,strcat(name,' Vvlocal'))),'jpeg');
end
```

Supplementary Information for Chapter V

SV-1. Custom Permeameter

A custom permeameter was fabricated to measure the permeability of the carbon fiber preforms using PDMS as the infiltration fluid. The permeameter, shown in Figure S11, consisted of a graphite piston that was actuated using an Instron testing machine to push PDMS fluid throughout a sample chamber. The sample chamber housed compression plates made of stainless steel that were clamped together to compress the fiber preforms to a target fiber volume fraction. The compression level was measured using a digital micrometer. O-rings were used to ensure that flow through the sample occurred through the thickness, as opposed to in-plane. The fixture was then placed in a sample chamber with a silicone seal around the edges to prevent in-plane flow that could seep past the O-rings at low fiber volume fraction. The graphite piston assembly was placed atop the sample chamber, where a gasket was used to ensure that PDMS did not leak around the chamber. An acrylic plate was bolted to the top of the piston to compress the gasket against the sample chamber. The graphite piston and glass cylinder were precisely ground to ensure no PDMS leaked past the piston. However, entrapped gas was able to escape the PDMS around the graphite piston. Due to the self-lubricating nature of the graphite piston and smooth bore of the glass cylinder, the frictional resistance to movement was less than 1 N and considered negligible. The load cell capacity was 500 N with an accuracy of 0.25% of the indicated load or 0.025% of the maximum, whichever is greater. A nylon rod connected the graphite piston to the Instron crosshead via a ball joint to ensure that only axial forces were transmitted to the piston. Therefore, the permeameter provides accurate and precise measurements.

The permeability of the fixture was measured before experiments at rates of 2 and 5 mm min^{-1} and found to be 22487 ± 2469 Darcys. As the permeability of the fiber preforms is much less than that of the fixture, the impact of the fixture on the measured permeability is small, but it has been accounted for in the calculations using a series model of the flow (i.e., the pressure loss through the

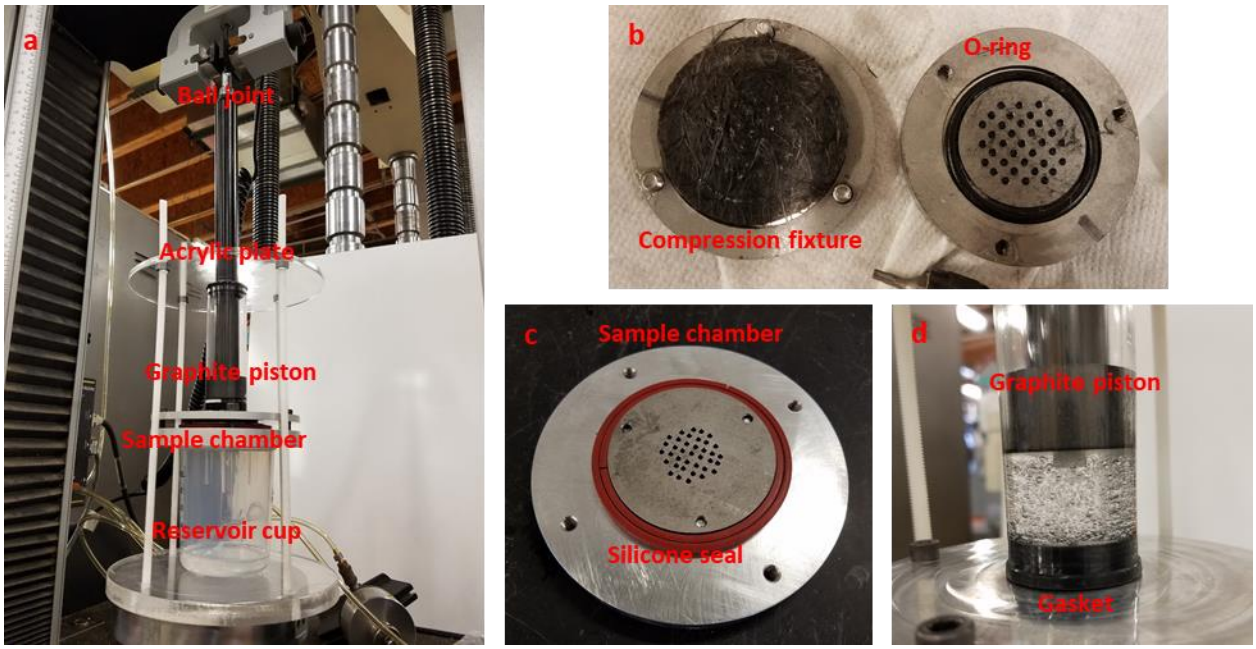

Figure S11. a) Permeameter assembly; b) compression fixture; c) sample chamber; d) piston assembly

fixture is subtracted from the total pressure). Flow rates of 0.83, 0.125, and 0.166 mL min^{-1} were used in experiments, where each sample was tested at each rate. Once a steady-state force was achieved for a given rate, the data was saved. Then, the rate was increased and the force was allowed to stabilize. An example of the force-displacement response is shown in Figure S12. The steady-state force value was then used to determine the fluid pressure as it flowed through the sample, while the flow rate was controlled by the crosshead displacement. The permeability was calculated and the average value was reported.

SV-2. Permeability Measurement Results

The results of the permeability measurements can be found in Tables S29-S34.

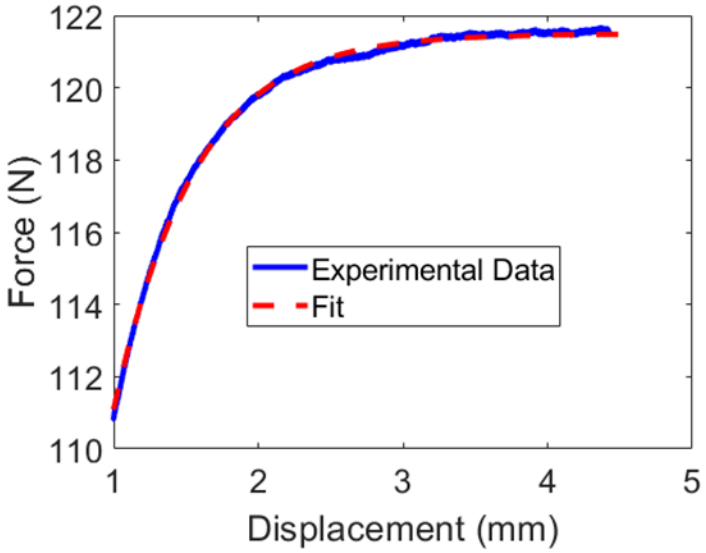

Figure S12. Example of force-displacement data for a recycled carbon fiber preform compressed to 0.609 mm and tested at 0.083 mL min^{-1}

Table S29. Water permeability measurement results for virgin fiber preforms

Fluid	Fiber Type	Fiber Volume Fraction (%)	Permeability (Darcys)
Water	Virgin	6.0	17.53
		7.0	13.13
		8.0	12.46
		10.0	7.89
		12.0	6.19
		14.0	4.80
		16.0	3.61
		18.0	4.03
		20.0	2.27
		22.0	2.99
		24.0	1.98
		26.0	1.72
		28.0	1.73
		30.0	1.65
		32.0	1.10
		34.0	0.90
		36.0	1.01
		38.0	1.19
		40.0	1.04
		42.0	0.78
		44.0	0.81
		46.0	0.90
		48.0	0.99
		50.0	0.59
		52.0	0.76
		54.0	0.37
		56.0	0.49

Table 30. Water permeability measurement results for recycled fiber preforms

Fluid	Fiber Type	Fiber Volume Fraction (%)	Permeability (Darcys)
Water	Recycled	6.0	10.09
		7.0	8.59
		8.0	5.22
		10.0	4.89
		12.0	2.81
		14.0	2.91
		16.0	2.55
		18.0	1.88
		20.0	2.01
		22.0	2.04
		24.0	1.80
		26.0	1.44
		28.0	1.20
		30.0	1.20
		32.0	1.42
		34.0	0.79
		36.0	0.99
		38.0	0.83
		40.0	0.67
		42.0	0.83
		44.0	0.54
		46.0	0.42
		48.0	0.58
		50.0	0.50
		52.0	0.62

Table S31. Air permeability measurement results for virgin fiber preforms

Fluid	Fiber Type	Fiber Volume Fraction (%)	Permeability (Darcys)
Air	Virgin	8.2	67.57
		17.5	11.34
		28.4	5.00
		9.6	35.09
		20.3	6.33
		29.5	3.53
		12.4	25.13
		22.2	5.87
		31.9	3.04
		13.7	17.89
		24.0	4.65
		34.5	2.62
		15.7	13.19
		25.6	4.60
		36.5	2.54
		17.9	10.06
		27.6	4.10
		38.3	2.38
		25.2	4.74
		35.4	2.47
		45.2	1.62
		29.7	3.19
		40.3	1.52
		49.8	1.15
		35.0	2.51
		44.8	1.39
		55.0	1.05
		6.0	135.14
		15.9	12.06
		26.2	3.51
		7.0	69.93
		17.1	10.24
		27.2	4.16

Table S32. Air permeability measurement results for recycled fiber preforms

Fluid	Fiber Type	Fiber Volume Fraction (%)	Permeability (Darcys)
Air	Recycled	8.0	29.24
		18.2	5.12
		27.9	2.43
		10.0	16.84
		20.2	4.88
		29.9	2.12
		12.0	13.04
		22.3	3.82
		32.0	1.84
		14.0	8.73
		24.0	3.58
		33.7	1.83
		16.1	6.51
		26.0	2.80
		36.0	1.40
		18.0	5.68
		27.9	2.24
		37.9	1.45
		24.7	3.23
		34.7	1.88
		45.3	1.28
		29.6	1.98
		40.1	1.27
		49.9	0.96
		35.1	1.32
		45.2	0.93
		55.1	0.74
		6.0	37.88
		15.9	8.67
		26.0	2.83
		7.0	31.45
		17.1	5.75
		26.7	2.62

Table 33. PDMS permeability measurement results for virgin fiber preforms

Fluid	Fiber Type	Fiber Volume Fraction (%)	Permeability (Darcys)	Goodness of Fit R^2
PDMS	Virgin	51.7	1.54	0.994
		48.3	1.91	0.987
		49.0	2.08	0.999
		45.0	2.09	0.999
		34.0	2.28	0.996
		42.1	2.33	0.995
		36.6	2.57	0.991
		38.0	2.79	0.999
		34.5	3.05	0.988
		26.4	3.25	0.996
		30.9	3.61	0.997
		29.1	3.65	0.985
		29.5	4.07	0.997
		29.3	4.12	0.998
		25.6	4.12	0.979
		35.1	4.14	0.990
		29.8	4.37	0.998
		32.6	4.43	0.983
		25.7	4.78	0.994
		25.0	4.99	0.973
		25.3	5.33	0.992
		25.7	5.36	0.995
		26.6	5.42	0.955
		25.4	5.45	0.994
		23.4	6.45	0.994
		21.8	8.23	0.986
		19.0	9.94	0.991
		16.8	16.18	0.995
		16.5	18.01	0.999
		14.5	20.44	0.997
		12.8	40.55	0.992
		11.4	58.36	0.984
		9.4	65.73	0.977
		7.9	72.03	0.989
		7.8	78.30	0.989
		6.4	79.86	0.990
		7.0	92.19	0.979

Table 34. PDMS permeability measurement results for recycled fiber preforms

Fluid	Fiber Type	Fiber Volume Fraction (%)	Permeability (Darcys)	Goodness of Fit R^2
PDMS	Recycled	6.1	72.12	0.958
		7.6	47.76	0.997
		7.2	63.53	0.980
		8.8	35.52	0.997
		10.5	25.44	0.997
		38.8	2.33	0.999
		12.0	20.43	0.996
		16.3	9.67	0.997
		13.9	13.72	0.992
		17.7	11.79	0.984
		19.7	6.46	0.995
		21.9	5.76	0.993
		53.2	1.37	0.997
		23.7	5.15	0.991
		22.9	4.53	0.996
		27.9	3.14	0.997
		28.6	3.22	0.997
		31.6	2.62	0.990
		35.8	1.92	0.998
		49.5	1.56	0.998
		57.1	1.45	0.998
		41.8	2.03	0.998
		47.0	1.86	0.997
		25.9	4.90	0.995
		33.7	2.98	0.997

SV-3. MATLAB Script for Permeability Calculation

```
%Script for calculation of permeability of the samples from Instron
5567 load frame
%Philip Barnett

clear all
close all hidden
close all force
clc

%% Import Data
[filename,path] = uigetfile('.csv');
pathname = strcat(path,filename);
data = readtable(pathname);
force = str2double(table2array(data(2:end,3)));
disp = str2double(table2array(data(2:end,4)));

%% Remove first 1 mm of data
newstart = find(disp >= 0, 1);
disp = disp(newstart:end);
force = force(newstart:end);

%% Plot Data
a = plot(disp,force);
xlabel('Displacement (mm)')
ylabel('Force (N)')
hold on

%% User identified region of bad data
done = false;
while done == false
    answer = questdlg('Are there regions of data that need to be
    removed?', 'Yes', 'No');
    switch answer
        case 'Yes'
            [x,y] = ginput(2);
            x = round(x,4);
            start = find(disp > x(1), 1, 'first');
            finish = find(disp < x(2), 1, 'last');
            disp(start:finish) = NaN;
            force(start:finish) = NaN;
        case 'No'
            done = true;
    end
end
b = plot(disp,force,'-g','LineWidth',5);

%% Curve Fitting
idx = isnan(force);
[curvefit, gof, output] = fit(disp(~idx),force(~idx),'a / (1 + exp(-
b*(x-c)))');
c = plot(curvefit);
legend('Data', 'Useful Data', 'Fit', 'Location', 'best')
```

```
xlabel('Displacement (mm)')
ylabel('Force (N)')
uistack(b,'bottom')
coeffs = coeffvalues(curvefit);
avgforce = coeffs(1);
rsquare = gof.rsquare;

%% Calculate permeability
L = str2double(inputdlg('Enter the sample thickness in mm: '));
dPdx = avgforce / (pi*(0.64*25.4)^2) * 1e6; %Pa
Q = ((disp(3002) - disp(2)) * pi*(0.64*25.4)^2)/1000; %mL/min
mu = 325; %Pa*s
A = pi*(0.875/2*25.4)^2; %mm^2
Kfixture = 2.22e-8; %m^2
Lfixture = 0.5; %in
dPdxfixture = (Q*1e-6/60)*mu*(Lfixture*25.4/1000) / (Kfixture*(A*1e-
6));
K = (Q*1e-6/60)*mu*(L/1000) / ((A*1e-6)*(dPdx-dPdxfixture));
Kd = K/9.869e-13;

%% Print the results
line1 = sprintf('The average force is %.2f N \n', avgforce);
line2 = sprintf('The permeability is %.2d m^2 \n', K);
line3 = sprintf('The permeability is %.2f Darcys \n', Kd);
line4 = sprintf('The R^2 of the fit is: %.4f \n', rsquare);
f = msgbox({line1, line2, line3, line4});
```

SV-4. In-Situ Compression Molding Apparatus

In-situ compression molding was conducted using a custom-built apparatus shown in Figure S13. The apparatus consists of two heated aluminum platens, both of which have a molding surface of 12.7 mm by 25.4 mm (0.5 in by 1 in). Each platen contains a cartridge heater and thermocouple for control via an individual PID controller (Automation Direct Solo 4848).

The bottom platen is seated on a 200 kg load cell (Model TAS501 from HT Sensor Technology Co., Ltd.) to measure the compression force applied on the platens. The platen and the load cell are separated by a block of Calcium Silicate insulation (Super Firetemp S, Johns Manville), which protects the load cell from the heat generated by the cartridge heaters. The CaS block has a thickness of 38.1 mm (1.5 in) and a cross-section of 76.2 mm by 88.9 mm (3 in by 3.5 in) and is secured to the bottom platen with two self-tapping screws. A small aluminum plate connects the load cell to the bottom CaS block via a piece of threaded rod.

The top platen is actuated by a pneumatic cylinder (Airpot MP44S-NX). The platen is secured rigidly to a movable horizontal plate connected to the pneumatic cylinder rod. This movable plate sides freely along the vertical alignment rods via two bronze/graphite bearings. The top platen and the plate are separated by a block of Calcium Silicate insulation (the “top CaS block”), which was included to prevent heat transfer to the cylinder. The top CaS block is dimensionally identical to the bottom block but is rotated 90° clockwise along the vertical axis. The

movable plate is directly attached to the top CaS block with self-tapping screws, which are placed along an axis aligned with the alignment rods. The top platen is attached to an intermediate aluminum plate, which translates the application plane of the screws that attach it to the top CaS block by 90°. This axis is perpendicular, rather than colinear, to the one along which the screws between the movable plate and the top CaS block are attached. Making these axes perpendicular, rather than colinear, was found to be a more promising way of preventing the brittle CaS blocks from cracking while manufacturing the apparatus.

It was found that Calcium Silicate blocks crack at relatively low applied tensile and shear stresses—on the order of those that might be achieved by applying a screw to a block. This posed a significant challenge during the manufacture of this apparatus. Several attempts to manufacture this apparatus failed due to cracking of CaS blocks, which made the manufacturing process time-consuming and expensive. We suggest several factors that might reduce the chance of failure/cracking. First, we suggest using relatively small screws, both in terms of length and diameter. During initial (failed) attempts, #12 screws were used, while the final design incorporates mostly #8 and #10 screws. X-ray images of a cracked block revealed that serious cracking started while applying the second set of screws, once the tips of the second set of screws crossed the plane of the tips of the first set of screws. This suggests that a design in which any horizontal plane contains both sets of screws makes failure more likely, although further testing is needed to confirm this conclusively.

The motion of the top platen is controlled by a pneumatic cylinder attached to a horizontal aluminum plate, which is held stationary. The stationary plate includes two non-threaded holes near the edges, through which threaded portions of the vertical rods pass. Four nuts that are placed on the rod hold the plate stationary and ensure that the alignment rods are straight. Pressurized air passes through a desiccant air dryer (Wilkerson X06-02-000) and a 250-psi standard oil removal filter (Speedaire 4ZL53) before reaching the pneumatic cylinder to ensure that it is not damaged by contaminants. A pneumatic precision regulator (Fairchild 10262) is used to control the pressure. The load cell provides a method of verifying the pressure exerted by the cylinder. The signal from the load cell was read by an Arduino-compatible Load Cell Amplifier (HX711, Avia Semiconductor) to provide accuracy to 40 grams. The signal from this Amplifier was passed through the Arduino to a laptop and converted to a force reading.

The apparatus is housed inside a custom-built X-ray cabinet containing an X-ray source (Hamamatsu, L8121-03), detector (Varex 1207N), and a motorized stage (shown in Figure S14). The apparatus is bolted to the movable stage that provides three degrees of freedom (X, Y, and Z). A digital inclinometer (Klein, 935DAG) was used to ensure that the source, detector, and apparatus were aligned in the pitch and yaw axes. As the x-ray source is a cone beam, only the detector and object had to be aligned in the roll axis. Various sizes of aluminum shim stock (ranging from 0.05 to 0.76 mm) were used to validate that the platens

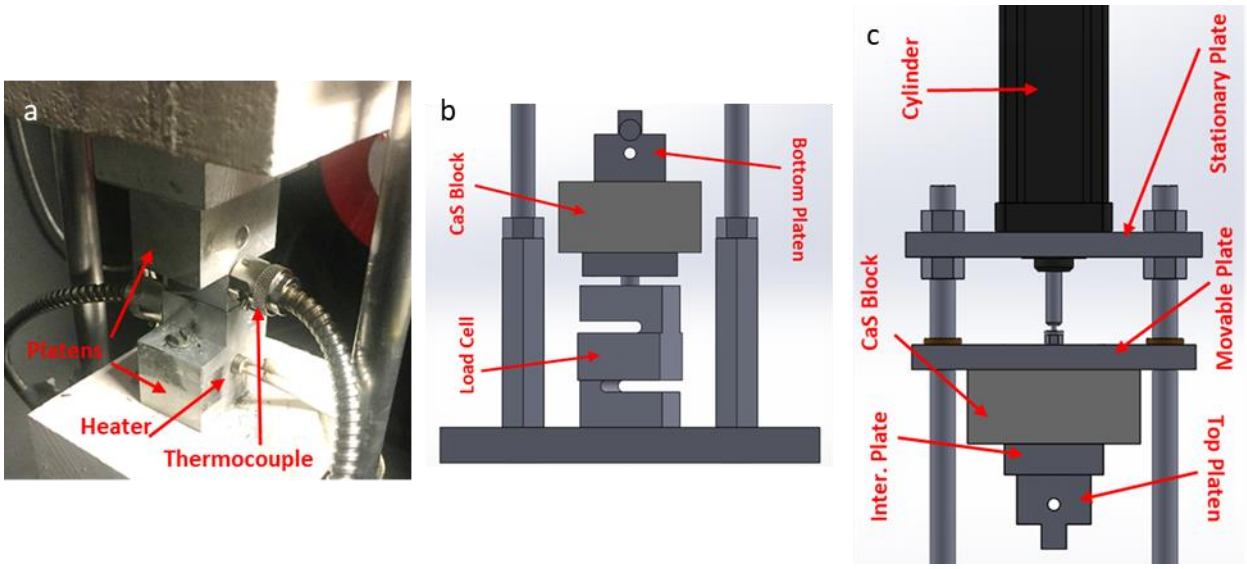

Figure S13. a) Photograph of compression platens; b) Drawing of low half of the apparatus; c) Drawing of upper half of the apparatus

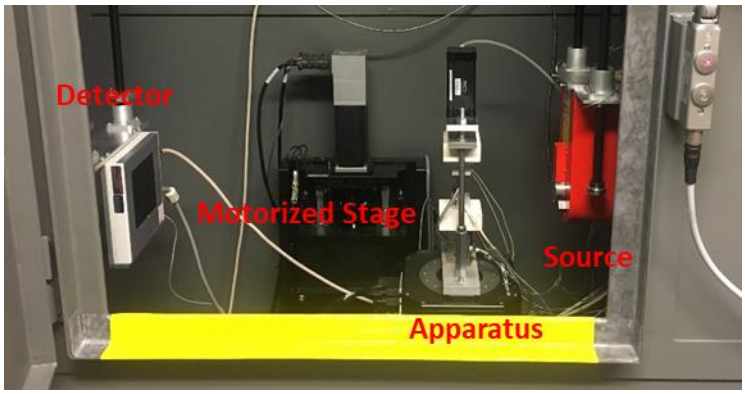

Figure S14. X-ray cabinet containing apparatus

were well aligned by placing them between the platens and measuring their thickness in a radiograph. The scale of the image was calibrated using a 6.35 mm gauge block.

SV-3. Analysis of Infiltration

A custom MATLAB script was written to analyze the radiographs of the infiltration process. In general, the script works as follows:

1. A region of interest in the image is chosen.
2. The platen edges are detected and treated as a moving boundary.
3. The fiber phase pixel intensity is determined from the first image to serve as a reference.
4. The matrix/composite phase is identified by the intensity of pixels three rows from the top and bottom platens in the first image.
5. The current height of the sample is identified as the distance between platen edges in each image
6. The current infiltration level is identified as the proportion of rows exhibiting an intensity below the midpoint intensity of the fiber and matrix/composite phases identified in steps 3 and 4
7. The infiltration time has been reached once the average intensity in the sample varies by less than 0.1% for three images

The region of interest that is chosen must be large enough to represent the sample behavior, but not so large that sample edge effects play a dominant role in the measurement. For example, the PPS films may not be well-aligned near the edges, resulting in spurious infiltration results.

The platen edges are found using a binarization and edge detection algorithm. First, the image is binarized such that the platens and sample can be separated. Then, the horizontal edges are detected using a Sobel filter. An example is shown in Figure S15. Next, the average grayscale intensity is calculated across rows of pixels. For the first image, the average intensity in the five middle rows is calculated to serve as the fiber phase reference. The matrix/composite phase reference intensity value is then identified as the average of the three rows adjacent to the upper and lower platens. Unfortunately, the contrast between matrix and composite is not sufficient to distinguish the two phases. The height is then calculated by measuring the pixel distance between the top and bottom platens surfaces and multiplying by the pixel resolution. The current infiltration level is identified by counting the number of rows with intensity below the midpoint of the fiber and matrix reference intensity values. Subsequently, the average pixel intensity of the rows between the platens is calculated and compared to the previous image. Once the image-to-image difference becomes less than 0.1% of the average intensity for three consecutive images, the infiltration time is assumed to have been reached. Figure S16 illustrates the convergence of this method as infiltration is achieved.

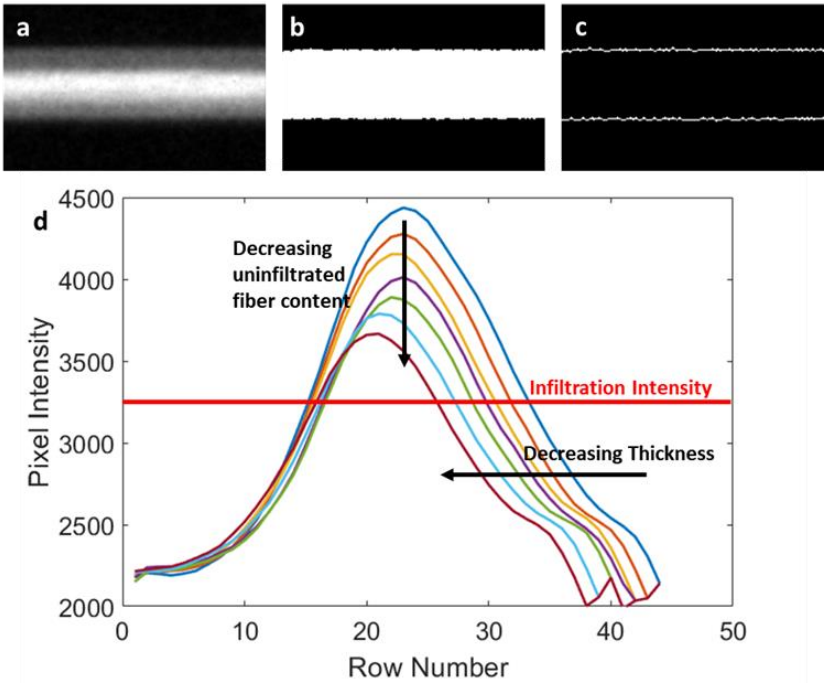

Figure S15. a) Initial image; b) Threshold image; c) Edge detection; d) Histogram of infiltration behavior

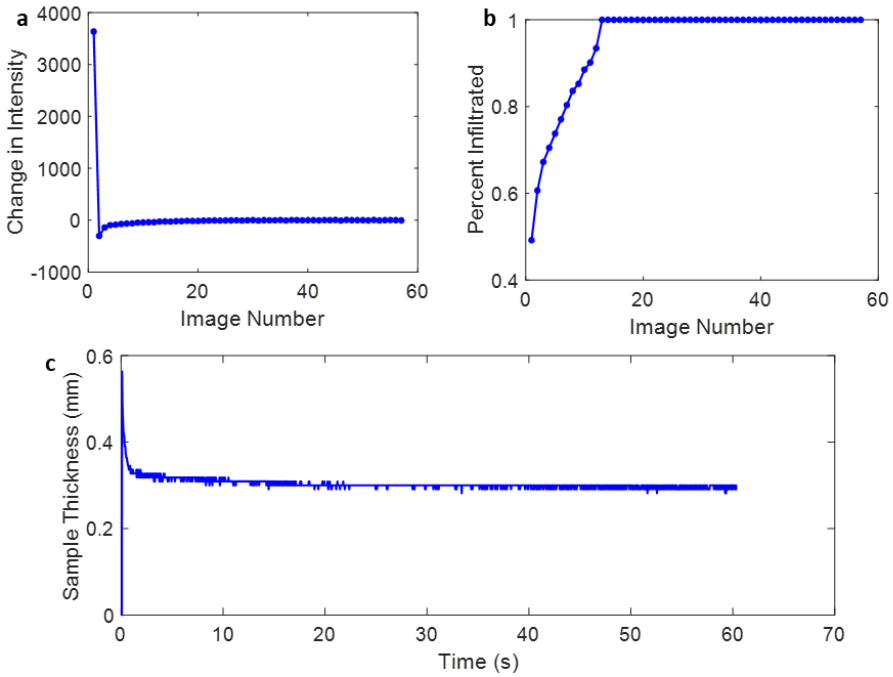

Figure S16. a) Convergence of intensity changes; b) Infiltration convergence; c) Sample thickness versus time (variation indicates measurement resolution)

SV-4. MATLAB Script for Infiltration Analysis

```
%Philip Barnett
%Script to analyze infiltration time for organosheet composites

clear all
close all hidden
clc

%% Define the file directory
path = uigetdir;

%% Identify the platen threshold
%Open an image at the middle of the stack to define the platen values
files = dir(path);
fnames = {files.name};
mid = fullfile(path,fnames{2+round(length(fnames)/2)});
immid = imread(mid);
im = imshow(imadjust(immid));
[x,y] = ginput(1);
threshregion = immid((y-10):(y+10),(x-10):(x+10));
threshold = int16(mean(threshregion(:)));

%% Request the resolution
prompt = 'Enter the resolution in pixels/mm:';
dlgtitle = 'Input resolution';
answer = str2double(inputdlg(prompt,dlgtitle));
res = 1/answer; %number of mm per pixel

%% Analyze the data in the cropped region
%First, find the edges of the platens in each image. Next, average the
grayscale across a
%row starting just below the top edge and ending just above the bottom
%edge. Then, check the average of the analysis region. Once it is no
longer
%changing, the infiltration is complete.

finished = false;

for i = 3:length(fnames)
    curpath = fullfile(path,fnames{i});
    current = imread(curpath);
    BW = imbinarize(current,2*double(threshold)/(2^16));
    %Debugging
%     figure
%     imshow(BW)
    edges = edge(BW,'Sobel',threshold+threshold*0.25,'horizontal');
    %Debugging
%     figure
%     imshow(edges)
%     figure
%     imshowpair(current,BW)
%     figure
```

```
%     imshowpair(current,edges)
    %find edges
    %Select the midpoint of the sample in the first image
    if i == 3
       imshow(imadjust(current));
       [x,y] = ginput(1);
       midpt = uint16(y);
    end
    rowvals = sum(edges,2);
    top = find(rowvals(1:midpt),1,'last');
    bot = find(rowvals(midpt:end),1)+midpt;

    %Record current height
    height(i) = res*double(bot - top);

    %take average grayscale across the rows
    for j = top+1:bot-1
       intensity(j-top) = mean(current(j,:));
    end

    %Determine fiber phase intensity
    if i == 3
        midsample = (bot-1 - top+1)/2 + top;
        fiberint = mean(current(midsample-2:midsample+2),'all');
    end

    %Determine matrix phase intensity
    if i == 3
       matrixint = mean([current(top+1:top+3) current(bot-3:bot-
       1)],'all');
    end

    %Determine point of fiber infiltration cutoff
    if i == 3
       fibercutoff = (fiberint - matrixint)/2 + matrixint;
    end

    %Determine relative infiltration distance
    %The composite and matrix phases are indistinguishable, so only
    %infiltration can be measured (not remaining matrix).
    for j = 1:length(intensity)
       if intensity(j) < fibercutoff
           infiltrated(j) = 1;
       else
           infiltrated(j) = 0;
       end
    end

    percentinf(i) = sum(infiltrated)/length(intensity);

    %Check the average intensity of the sample
    avgintensity(i) = mean(intensity);
```

```
    %Check if average intensity is not changing
    diffintensity = diff(avgintensity);
    tol = 0.001;
    if i > 5 && abs(diffintensity(i-2)) < tol*avgintensity(i) &&
    abs(diffintensity(i-3)) < tol*avgintensity(i) &&
    abs(diffintensity(i-4)) < tol*avgintensity(i) && ~finished
       finished = true;
       intconst = i;
       fprintf('The intensity in the sample is no longer changing.
       \n\n')
    end

    if i == length(fnames) && ~finished
       fprintf('Completed all frames, but the data never converged!
       \n\n')
    end
end

%% Record the time
framerate = 30; %frames per second
infiltrationtime = intconst/framerate; %seconds
fprintf('The infiltration time is: %.2f seconds \n\n',
infiltrationtime)

%% Record the final thickness and thickness at infiltration time
fprintf('The thickness at infiltration is: %.2f mm \n\n',
height(intconst));
fprintf('The thickness at the end of the test is: %.2f mm \n\n',
height(end));
```

SV-5. Load Validation

To validate that the load applied to the samples was correct, the Ardunio-connected load cell was tested both at room temperature and under thermal load at each load level applied to the specimens. Table S35 shows the results and average error for three tests. Overall, it can be seen that as the pressure increases, the error decreases as variations in the pressure provided by the pressure regulator become a smaller portion of the total. It should be noted that when heated, expansion from the platens causes an increase in load; likewise, the load decreases when the heaters turn off. An example is shown in Figure S17. The effect was found to be minimal.

SV-7. Infiltration Analysis Results

The infiltration analysis results can be found in Tables S36 and S37. The thickness at the end of the measurement was typically one minute after the beginning of the molding process.

SV-8. Optical Micrograph Analysis

The polished organosheet micrographs revealed a range of fiber volume fractions and void contents. To quantify this variation, the local fiber and void content were calculated across a micrograph. Example micrographs and corresponding local properties are found in Figure S18 and S19. The image immediately below the micrograph is the local fiber content and below that is the void content image. The local properties vary much more significantly in the wet-laid preform sample, where fiber flow occurred toward the left side of the micrograph. Both samples show incomplete infiltration at 0.5 MPa pressure, as evident by the void content in the center of the sample.

Figures S20 through S23 show the distribution of fiber and void volume fraction for all samples. The number to the left of each image indicates the pressure at which the samples were processed. In general, the best balance of fiber and void content occurs around 2 MPa pressure, as evident by the peak location and height in the fiber volume fraction distributions and the peak height near-zero void volume fraction.

Table S35. Compression force measured by the load-cell

Pressure on Sample (MPa)	Expected Reading (kg)	Average Load at Room Temperature (kg)	Average Error	Average Load at 300 °C (kg)	Average Error
0.5	8.226	8.1849	-0.50%	9.1140	10.80%
1.0	16.451	16.8149	2.21%	17.2765	5.01%
1.5	24.677	25.0628	1.56%	25.6278	3.85%
2.0	32.903	33.2310	1.00%	33.6318	2.22%
2.5	41.129	40.9994	-0.31%	41.9644	2.03%
3.0	49.354	49.3998	0.09%	50.5258	2.37%
3.5	57.580	56.8590	-1.25%	58.2469	1.16%
4.0	65.806	64.4314	-2.09%	66.5409	1.12%

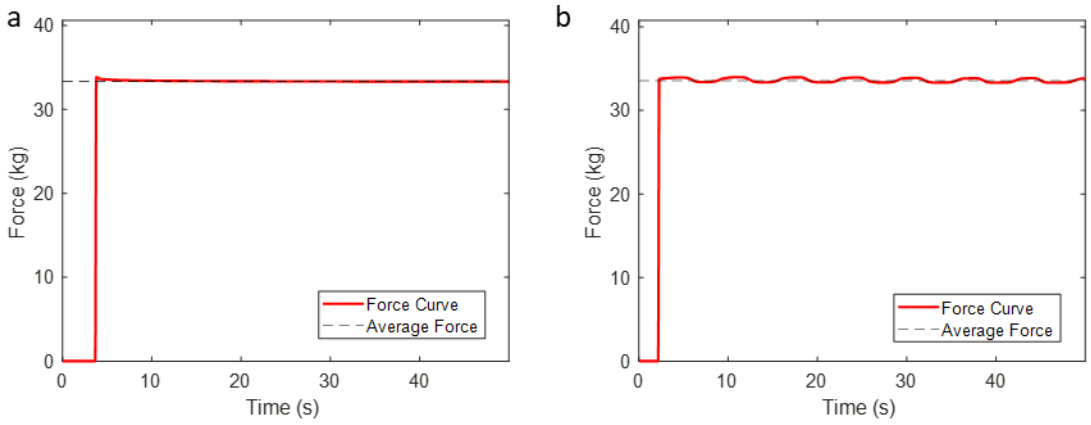

Figure S17. a) Force at room temperature for 2.0 MPa pressure; b) Force at 300 °C for 2.0 MPa pressure

Table S36. Infiltration results for recycled fiber composites

Pressure (MPa)	Infiltration Time (s)	Thickness at Infiltration (mm)	Thickness at End of Measurement (mm)
0.5	1.88	0.41	0.41
0.5	2.22	0.39	0.35
1.0	1.63	0.30	0.29
1.0	0.70	0.38	0.37
1.5	2.10	0.28	0.28
1.5	2.67	0.33	0.33
1.5	1.20	0.34	0.31
2.0	1.33	0.35	0.28*
2.0	1.43	0.25	0.24
2.0	1.33	0.27	0.24
2.5	2.13	0.33	0.26*
2.5	1.20	0.20	0.16
3.0	2.33	0.37	0.29*
3.0	1.20	0.24	0.21
3.0	1.37	0.25	0.24
3.5	1.27	0.22	0.20*
3.5	1.57	0.14	0.14
3.5	1.03	0.28	0.27
4.0	1.10	0.28	0.21*
4.0	1.13	0.29	0.29
4.0	1.20	0.20	0.15

*Final thickness measured 5 minutes after the molding process

Table S37. Infiltration results for virgin fiber composites

Pressure (MPa)	Infiltration Time (s)	Thickness at Infiltration (mm)	Thickness at End of Measurement (mm)
0.5	1.23	0.72	0.72*
0.5	2.31	0.55	0.54
0.5	1.19	0.58	0.56
1.0	1.40	0.42	0.42*
1.0	1.27	0.55	0.54
1.5	1.57	0.35	0.35*
1.5	2.10	0.50	0.51
1.5	1.53	0.41	0.42
2.0	1.27	0.37	0.35
2.0	2.10	0.47	0.42
2.0	1.60	0.42	0.41
2.5	1.40	0.48	0.46*
2.5	1.33	0.40	0.40
2.5	1.60	0.38	0.38
2.5	1.40	0.35	0.32
3.0	1.33	0.38	0.39*
3.0	1.40	0.36	0.35
3.0	1.60	0.37	0.37
3.5	0.93	0.43	0.43*
3.5	1.67	0.30	0.30
3.5	1.17	0.29	0.27
4.0	1.07	0.39	0.38*
4.0	1.47	0.33	0.33
4.0	1.37	0.41	0.40
4.0	1.53	0.25	0.25

*Final thickness measured 5 minutes after the molding process

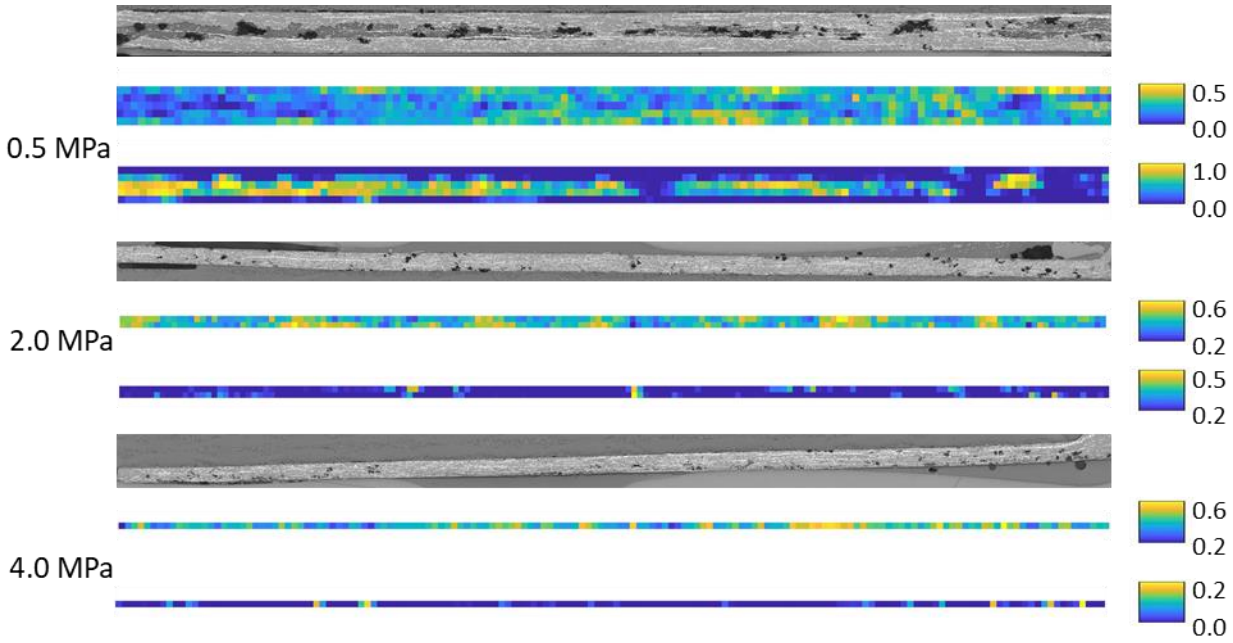

Figure S18. Carded fiber preform local properties across a range of molding pressures

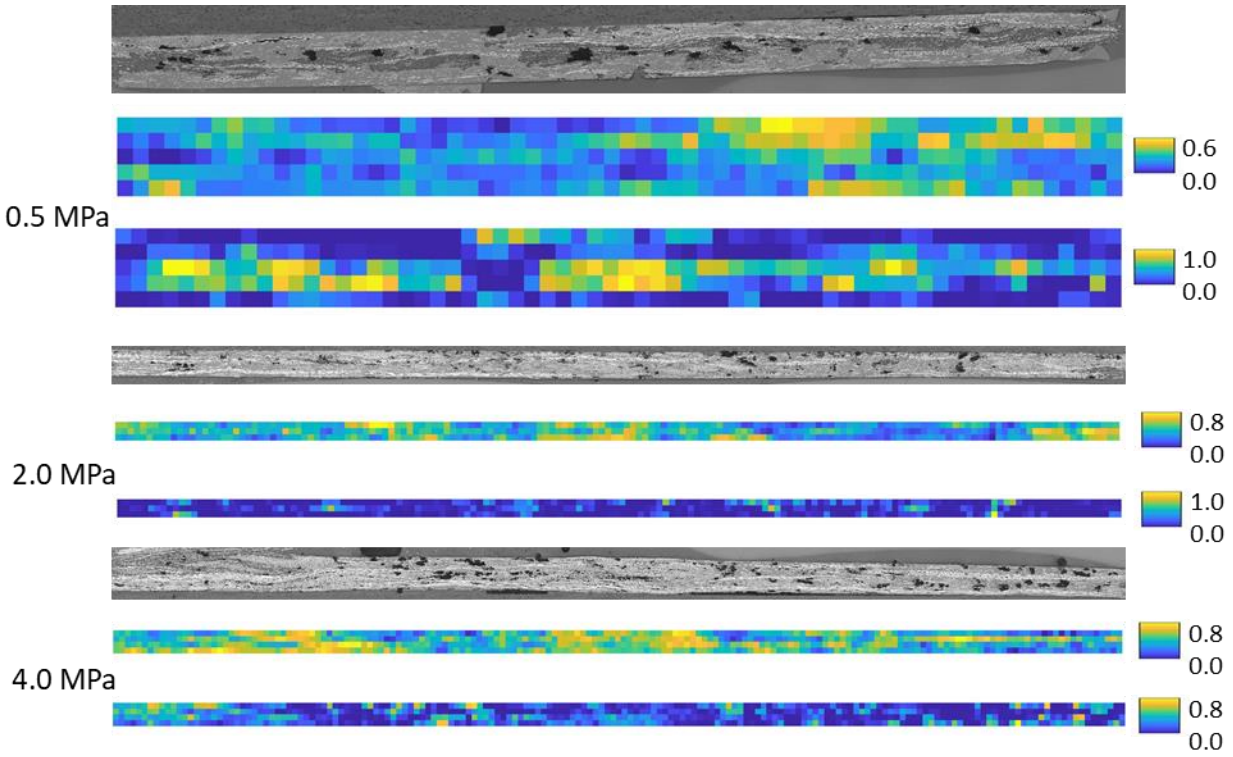

Figure S19. Wet-laid fiber preform local properties across a range of molding pressures

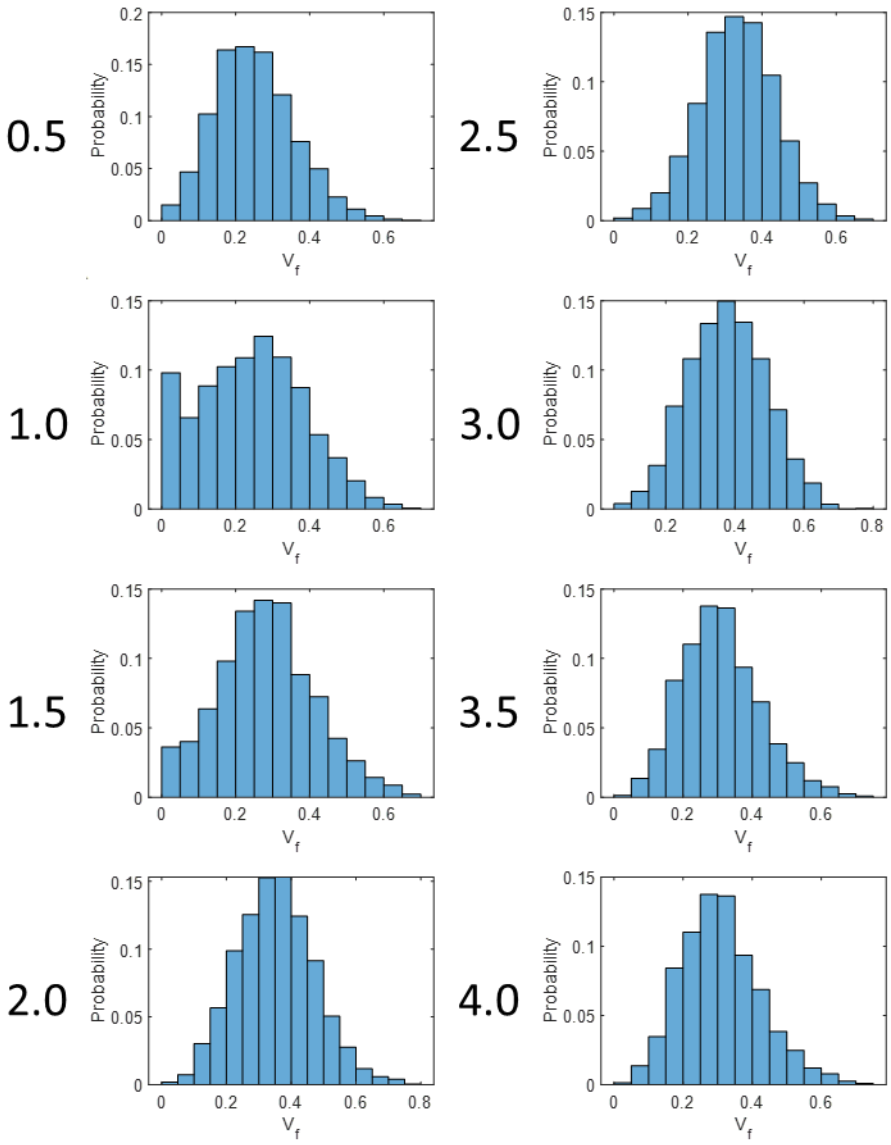

Figure S20. Carded fiber volume fraction distributions

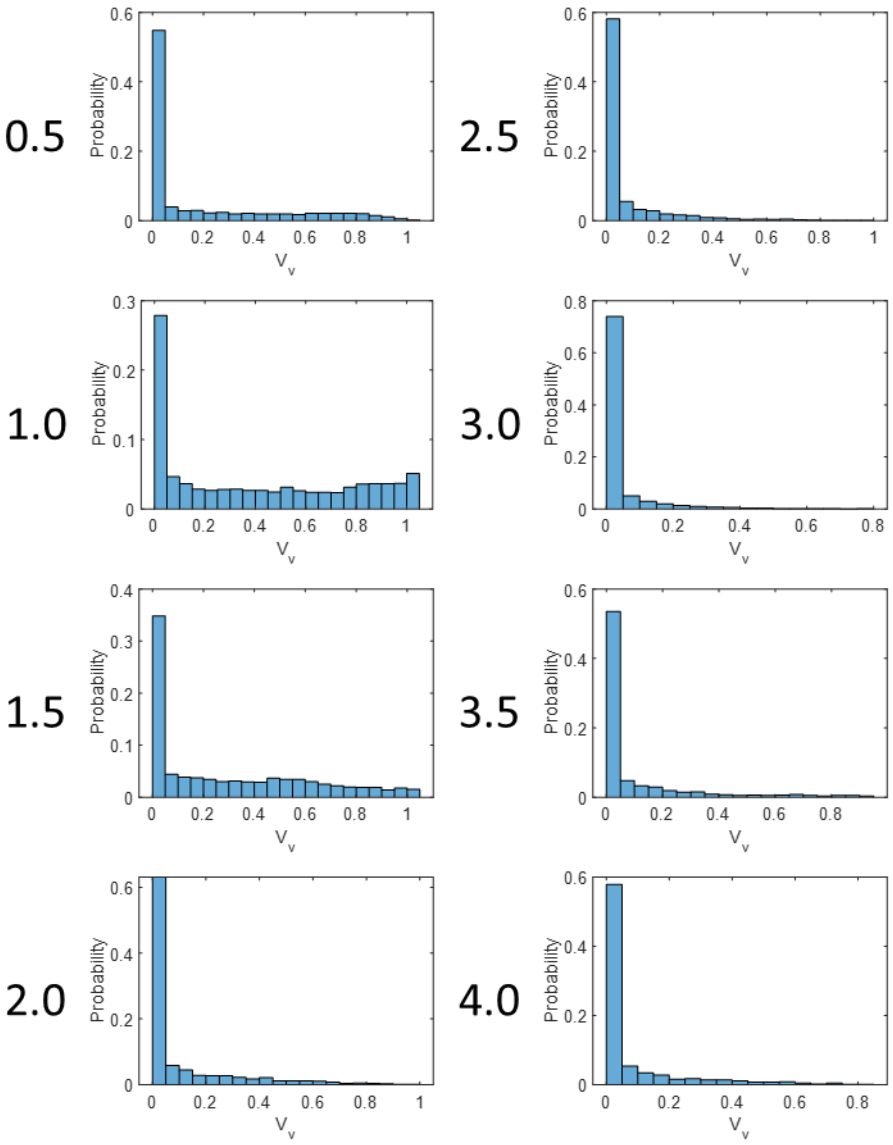

Figure S21. Carded fiber void volume fraction distributions

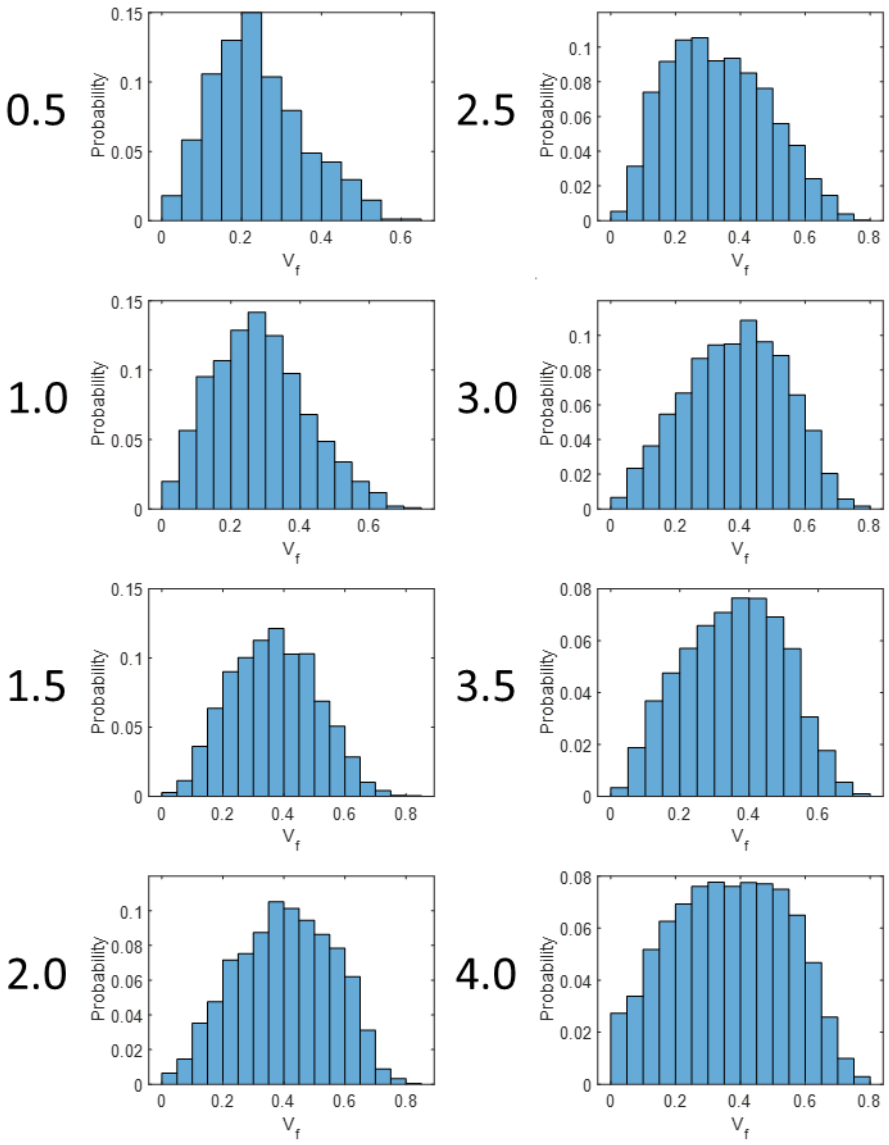

Figure S22. Wet-laid fiber volume fraction distributions

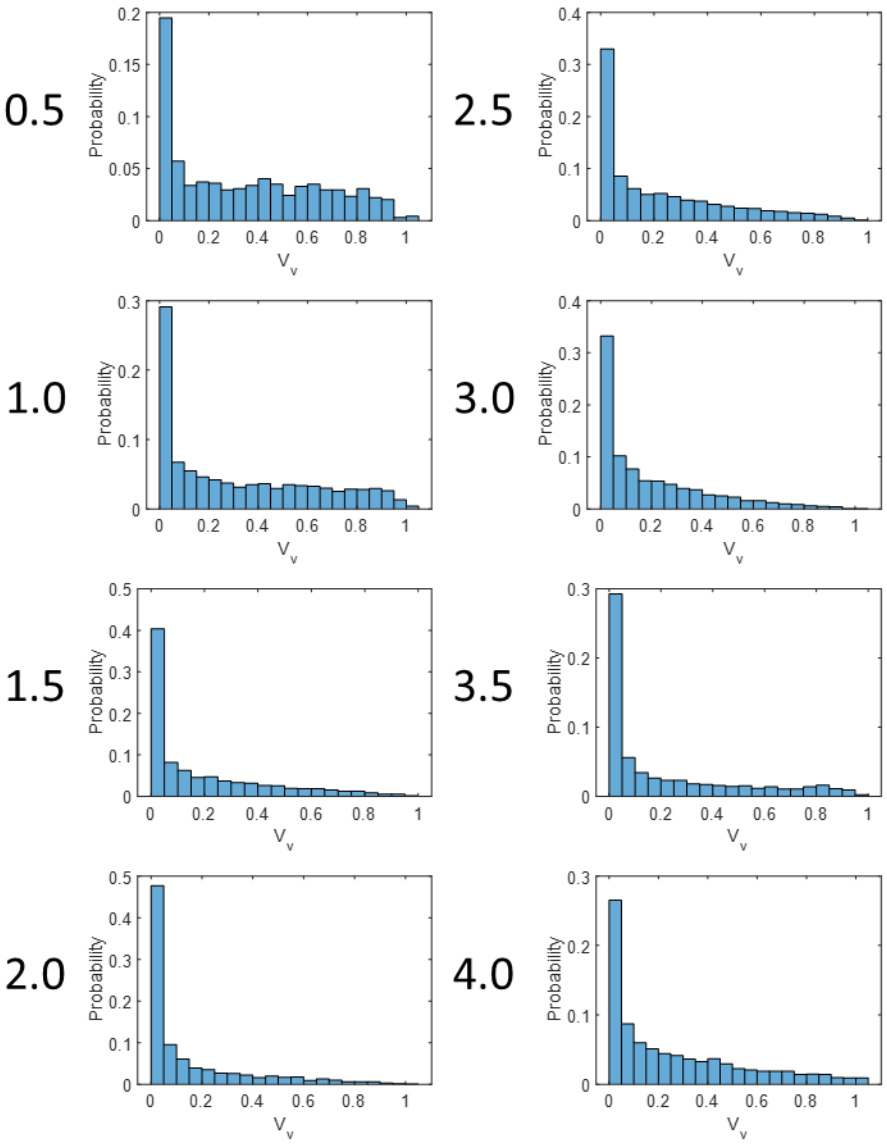

Figure S23. Wet-laid void volume fraction distributions

Supplmentary Information for Chapter VI

SVI-1. Crush Testing Results

Crush testing results can be found in Tables S38-41.

SVI-2. Dynamic Mechanical Analysis Results

The DMA testing results can be found in Table S42.

SVI-3. IZOD Impact Results

The IZOD impact testing results can be found in Table S43.

SVII-4. Particle Size Analysis Results

The particle size analysis results can be found in Table S44.

SVII-5. Impact of Manufacturing Defects

The impact of manufacturing defects are described in table S45.

Table S38. Epoxy crush results

Test Rate (mm min^{-1})	Test Temperature (°C)	Sample Area (mm^2)	Density (g cm^{-3})	SEA (kJ kg^{-1})	Steady State Crush Stress (MPa)
5.08	RT	136.38	1.25	106.35	133.20
		147.50	1.14	111.92	127.62
		147.06	1.14	122.73	139.80
		152.35	1.21	105.83	127.58
		135.33	1.28	100.82	128.59
50.8	RT	153.97	1.17	102.59	119.72
		132.85	1.19	112.97	134.94
		136.36	1.19	112.38	133.79
		132.48	1.24	117.20	145.74
		133.61	1.21	115.70	139.89
		137.30	1.22	97.70	119.60
508	RT	164.14	1.17	107.42	125.53
		140.32	1.19	115.39	137.29
		143.59	1.17	101.97	119.67
		144.85	1.14	125.49	142.60
		142.16	1.17	129.75	152.15
		141.54	1.14	123.78	140.86
		118.10	1.18	126.65	148.58
50.8	-40	160.24	1.05	94.46	98.72
		151.17	1.07	94.84	101.29
		141.25	1.18	102.46	120.75
		144.28	1.11	114.63	126.90
		157.97	1.18	90.01	106.47
50.8	80	165.44	1.10	99.03	108.43
		147.20	1.17	93.77	110.11
		131.84	1.16	91.52	106.29
		131.03	1.26	96.18	121.37
		142.19	1.12	98.79	110.22
50.8	150	157.65	1.07	29.72	31.91
		152.69	1.15	24.35	27.97
		147.63	1.08	32.64	35.12
		145.86	1.08	37.08	39.93
		136.06	1.21	33.28	40.38

Table S39. PPS crush results

Test Rate (mm min^{-1})	Test Temperature (°C)	Sample Area (mm^2)	Density (g cm^{-3})	SEA (kJ kg^{-1})	Steady State Crush Stress (MPa)
5.08	RT	167.10	1.19	85.14	100.97
		162.28	1.20	83.56	100.07
		170.02	1.11	88.97	98.36
		153.55	1.27	86.85	110.70
		127.15	1.47	97.43	142.92
50.8	RT	144.08	1.34	98.61	132.53
		159.08	1.21	90.99	110.47
		158.70	1.26	89.43	113.02
		137.61	1.36	100.07	136.30
		135.50	1.41	98.57	138.88
		171.42	1.16	90.10	104.19
		153.11	1.20	98.79	118.44
508	RT	157.15	1.26	106.63	134.83
		178.03	1.12	91.14	102.18
		146.28	1.38	113.37	156.40
		175.50	1.10	107.78	118.01
		136.98	1.45	129.78	188.35
50.8	-40	151.90	1.27	129.60	164.66
		158.96	1.16	108.55	125.90
		149.87	1.20	111.25	132.95
		140.57	1.29	115.98	149.39
		154.54	1.18	109.93	129.27
50.8	80	146.40	1.28	65.06	83.26
		137.79	1.37	72.65	99.41
		153.01	1.31	75.66	98.92
		144.96	1.38	75.10	103.76
		126.01	1.46	75.91	111.15
50.8	109	159.66	1.17	54.17	63.64
		157.86	1.22	51.99	63.26
		150.19	1.28	53.36	68.55
		138.31	1.34	53.71	71.82
		145.11	1.34	45.73	61.34

Table S40. ABS crush results

Test Rate (mm min^{-1})	Test Temperature (°C)	Sample Area (mm^2)	Density (g cm^{-3})	SEA (kJ kg^{-1})	Steady State Crush Stress (MPa)
5.08	RT	156.34	0.97	59.30	57.75
		144.73	1.09	32.38	35.23
		157.66	1.03	51.82	53.17
		150.00	1.06	43.33	45.78
		162.40	0.96	37.52	35.98
50.8	RT	159.60	1.02	43.37	44.15
		149.08	1.01	47.66	48.07
		156.69	1.01	57.74	58.50
		157.65	0.98	47.43	46.42
		164.50	0.95	49.35	46.83
		165.28	0.95	38.37	36.36
508	RT	138.60	1.15	56.51	64.85
		118.19	1.27	54.82	69.82
		172.19	0.93	52.76	49.33
		149.48	1.07	44.79	47.97
50.8	-40	142.47	1.15	76.43	87.82
		172.84	0.97	63.29	61.59
		158.19	1.06	65.03	69.01
		154.10	1.06	71.55	76.17
		152.14	1.08	73.24	79.10
50.8	80	144.10	1.09	27.78	30.34
		160.21	0.98	32.21	31.71
		134.00	1.14	30.74	34.94
		150.56	1.05	28.52	29.88
		158.09	0.97	31.50	30.46
50.8	109	162.33	1.00	14.19	14.13
		158.47	0.97	15.07	14.58
		165.83	0.97	11.11	10.80
		164.95	1.01	11.87	11.95

Table S41. Machine-direction crush results

Sample Type	Sample Area (mm^2)	Density ($g\ cm^{-3}$)	SEA ($kJ\ kg^{-1}$)	Steady State Crush Stress (MPa)
Epoxy	139.40	1.18	92.22	109.12
	132.13	1.18	86.74	101.95
	135.54	1.18	87.70	103.32
	143.70	1.18	83.92	99.04
	138.71	1.18	88.46	104.50
	140.28	1.18	96.42	113.39
PPS	150.35	1.21	79.82	96.75
	138.81	1.45	76.32	110.77
	144.61	1.38	84.77	116.95
	143.49	1.41	73.04	103.09
	124.75	1.51	72.38	108.97
	148.94	1.27	80.59	102.69
ABS	183.41	0.93	30.97	28.84
	155.23	1.07	35.12	37.63
	146.79	1.14	34.54	39.24
	158.41	1.05	26.52	27.88
	151.73	1.11	34.17	38.02
	153.99	1.06	37.63	39.96

Table S42. DMA results for organosheet composites

Sample	Glass Transition Temperature	Storage Modulus Retained
Epoxy	148.59	53.2%
	150.12	51.7%
	150.82	55.6%
PPS	109.18	85.6%
	107.98	80.6%
	109.14	75.6%
ABS	109.17	66.3%
	108.74	71.4%
	108.49	61.3%

Table S43. IZOD impact testing results

Resin Type	Fiber Type	Impact Resistance J m^{-1}	Impact Resistance J m^{-2}
Epoxy	Neat	29.6	2967.2
		25.2	2521.9
		31.1	3097.6
		27.9	2788.6
		26.0	2589.9
		27.3	2713.8
		26.4	2641.6
		26.4	2660.7
		26.9	2693.0
		28.5	2845.7
Epoxy	Recycled	78.9	7871.6
		84.1	8444.7
		85.6	8446.6
		79.1	7847.8
		86.7	8738.7
		79.5	7884.0
		93.9	9326.2
		91.7	9124.5
		85.7	8563.0
		73.4	7258.3
ABS	Recycled	391.3	39169.4
		317.7	31844.8
		392.2	39029.5
		310.2	30787.4
		466.1	46068.5
		321.9	31722.8
		365.2	36471.6
PPS	Recycled	156.0	15408.9
		142.5	13929.4
		149.4	14510.3
		174.8	17072.8
		151.0	14798.0
		146.2	14436.0
		156.1	15243.9
		166.0	16408.3
		167.8	16379.7
		148.7	14559.9

Table S44. Particle size analysis results

Sample Type	Test Rate (mm min^{-1})	Test Temperature (°C)	> 25 mm	12.5 to 25 mm	4 mm to 12.5 mm	2 mm to 4 mm	0.85 mm to 2 mm	0.5 mm to 0.85 mm	< 0.5 mm
ABS	5.08	RT	95.22%	0.00%	4.47%	0.14%	0.09%	0.02%	0.05%
	50.8	RT	97.96%	0.00%	1.22%	0.28%	0.42%	0.06%	0.06%
	508	RT	99.37%	0.00%	0.00%	0.27%	0.29%	0.03%	0.03%
	50.8	-40	97.20%	0.00%	2.15%	0.22%	0.24%	0.10%	0.09%
	50.8	80	98.55%	0.00%	1.29%	0.07%	0.08%	0.01%	0.01%
	50.8	109	100.00%	0.00%	0.00%	0.00%	0.00%	0.00%	0.00%
PPS	5.08	RT	72.20%	11.18%	14.20%	1.30%	0.99%	0.09%	0.04%
	50.8	RT	82.65%	3.02%	8.57%	4.35%	1.25%	0.10%	0.06%
	508	RT	93.14%	0.00%	3.99%	2.20%	0.60%	0.04%	0.02%
	50.8	-40	84.17%	5.45%	6.98%	2.51%	0.78%	0.06%	0.05%
	50.8	80	95.97%	0.00%	2.35%	1.17%	0.46%	0.04%	0.02%
	50.8	109	99.15%	0.00%	0.00%	0.59%	0.23%	0.02%	0.01%
Epoxy	5.08	RT	59.84%	0.00%	6.35%	20.56%	9.59%	1.65%	2.00%
	50.8	RT	56.91%	0.00%	14.63%	17.51%	7.17%	1.58%	2.21%
	508	RT	30.48%	25.03%	14.63%	19.71%	7.51%	1.24%	1.40%
	50.8	-40	82.60%	0.00%	0.00%	7.29%	6.58%	1.66%	1.87%
	50.8	80	84.78%	0.00%	8.41%	3.70%	1.93%	0.53%	0.65%
	50.8	150	90.58%	0.00%	7.13%	1.01%	0.58%	0.28%	0.42%

Table S45. Impact of manufacturing defects

Sample Type	Rate (mm min^{-1})	Flaw Description	Flaw Severity	Effect	SEA (kJ kg^{-1})	Sample Set Mean SEA (kJ kg^{-1})
Epoxy	508	General porosity	Severe	None	125.5	118.6
	5.08	General porosity	Severe	None	106.4	109.5
	5.08	General porosity	Severe	None	111.9	109.5
	50.8	General porosity; FOD on left	Severe	Buckled near FOD	112.4	109.8
	50.8	General porosity; large void	Severe	Broke on same side as large void	97.7	109.8
	508	General porosity	Severe	None	123.8	118.6
PPS	508	Ductile tearing	Severe	Broke on opposite side of tear	54.4	109.7
	50.8	None	N/A	N/A	98.6	95.2
	50.8	None	N/A	N/A	98.8	95.2
	508	Interlaminar	Mild	None	107.8	109.7
	5.08	Interlaminar; ductile tearing	Mild	None	97.4	88.4
	5.08	Ductile tearing	Mild	Broke across lower half; failed rapidly	-	88.4
ABS	50.8	Interlaminar	Severe	None	47.4	47.3
	5.08	Interlaminar; ductile tearing	Severe	Broke on same side as tear	37.5	44.9
	508	Interlaminar	Mild	None	52.8	52.2
	5.08	Interlaminar	Severe	None	43.3	44.9
	50.8	Interlaminar; ductile tearing	Severe	None	38.4	47.3
	508	Interlaminar; ductile tearing	Severe	Broke on opposite side of tear; failed rapidly	-	52.2

VITA

Philip Barnett attended the University of Illinois for his undergraduate studies in the Department of Aerospace Engineering. As an undergraduate student, he worked for Prof. Scott R. White in the Autonomous Materials Systems research group under the advisement of then PhD candidate Stephen J. Pety. He studied the use of microvascular carbon fiber composites for electric vehicle battery cooling and impact protection, where he manufactured microvascular composites, fabricated PDMS microfluidic devices, and performed crush tests on microvascular sinusoidal composite specimens. His work in the group provided him with the skills to serve as a materials engineer in the development of a deployable microvascular carbon fiber heatsink for solar panel cooling on a small satellite. These experiences ultimately led him to pursue graduate studies focusing on carbon fiber composites.

Upon graduation, Philip began his doctoral studies in Energy Science and Engineering under the advisement of Prof. Dayakar Penumadu at the University of Tennessee as part of the Bredesen Center for Interdisciplinary Research and Graduate Education. During his graduate studies, Philip became well versed in several polymer and composites characterization methods found here. He also participated in the National Science Foundation Innovation Corps program, where he developed a business model and invention disclosure for the commercialization of discontinuous recycled fiber organosheet composites. Philip was a founding member of the University of Tennessee SAMPE (Society for the Advancement of Material and Process Engineering) Student Chapter. This exposure to the industry, as well as his involvement in the Institute for Advanced Composites Manufacturing Innovation (IACMI), has enabled him to pursue industry-relevant research with the potential for significant impact on the field of composite materials.